12-2022

Experimental approaches to evaluating silicate melt properties and trace element fractionation during crystallization at high pressures and high temperatures

Megan D. Mouser
mmouser@vols.utk.edu

Recommended Citation

Mouser, Megan D., "Experimental approaches to evaluating silicate melt properties and trace element fractionation during crystallization at high pressures and high temperatures. " PhD diss., University of Tennessee, 2022.
https://trace.tennessee.edu/utk_graddiss/7628

To the Graduate Council:

I am submitting herewith a dissertation written by Megan D. Mouser entitled "Experimental approaches to evaluating silicate melt properties and trace element fractionation during crystallization at high pressures and high temperatures." I have examined the final electronic copy of this dissertation for form and content and recommend that it be accepted in partial fulfillment of the requirements for the degree of Doctor of Philosophy, with a major in Geology.

Nicholas J. Dygert, Major Professor

We have read this dissertation and recommend its acceptance:

Molly C. McCanta, Bradley J. Thomson, Bhavya Sharma

Accepted for the Council:

Dixie L. Thompson

Vice Provost and Dean of the Graduate School

(Original signatures are on file with official student records.)

Experimental approaches to evaluating silicate melt properties and trace element fractionation during crystallization at high pressures and high temperatures

A Dissertation Presented for the
Doctor of Philosophy
Degree
The University of Tennessee, Knoxville

Megan D. Mouser
December 2022

DEDICATION

I dedicate this to my family; I could not have done this without their endless love and support.

ACKNOWLEDGEMENTS

First, I want to thank my advisor, Nick Dygert, for his support, patience, and guidance over the last five years. I am deeply grateful for the opportunity to work with and learn from him. I could not have imagined a better graduate experience. I am thankful for my committee, Molly McCanta, Brad Thomson, and Bhavya Sharma, for their support during my degree. I would also like to thank those that mentored me from the beginning of my geoscience journey and who were instrumental in getting me where I am today- Aaron Bell, Roy Christoffersen, and Justin Simon.

I would like to thank those who assisted me in the laboratory and with my research- Brendan Anzures, Nadine Grambling, Allan Patchen, Grace Sarabia, and Blake LaDouceur. A special thanks goes out to Ross Hrubiak and the entire High Pressure Collaborative Access Team (HPCAT) at the Advanced Photon Source, Argonne National Laboratory for making my time as a user and an intern a wonderful experience.

My graduate school experience would not have been as enjoyable without the great people in this department. Thank you to all of the faculty, staff, and graduate students for your support over the years. To my dear friends- Wendy Eskuri, Rossina Miller, Louisa Rader, CJ Leight, Jessi Ende, Sam Gwizd, and Cam Hughes, I am so thankful for your friendship. Whether it was pep talks, running too many miles, or watching football on the weekends, all of you kept me going.

And finally, I owe a great deal of gratitude to my family. Mom and Dad, you always believed in me even when I didn’t believe in myself. I truly appreciate everything you have done for me, from your unwavering support and words of encouragement, to driving across the country (multiple times) with me. To my sister Ashley, I am thankful for your constant wisdom, humor, and support. I am grateful for our shared curiosity of the natural world and look forward to many more adventures with you, sharing stories of bird migration and rock formation.

ABSTRACT

Current understanding of the evolution and behavior of silicate materials that form in planetary interiors at high-pressures and high-temperatures largely come from experimental work as natural samples are either rare, or physically inaccessible. Laboratory experiments provide a comprehensive way to constrain the crystallization history, elemental partitioning, and viscosity of different silicate materials at planetary mantle pressure and temperature conditions. This work utilizes two high-pressure experimental techniques, the Paris-Edinburgh apparatus, and the piston cylinder apparatus, to measure physical and chemical properties of silicate materials. The viscosity of reduced, Fe-free silicate liquids, with and without sulfur (S-free and S-bearing), were measured to predict the viscosity of Mercury's magma ocean (Chapter 1). These viscosity measurements were used to create predictive viscosity models. The viscosity models were combined with crystallization models to predict mantle structures for Mercury's solidifying magma ocean. The density of the resulting mantle structures were modeled to predict possible physical processes that could have occurred in Mercury's interior, such as mantle overturn, that could produce the proper source regions for the igneous provinces seen on the surface of Mercury today (Chapter 2). The results of the viscosity measurements revealed differences in the behavior of the S-free and S-bearing liquids, where the sulfur-bearing exhibited lower viscosities than the S-free. Energy-dispersive X-ray Diffraction and Raman spectroscopy measurements were taken on in situ liquids and recovered glasses, respectively, to analyze the liquid and glass amorphous structures between the S-free and S-bearing compositions. The results revealed that sulfur has a depolymerization effect on the silicate structure and that Al causes inherent pressure sensitivity in silicate liquids by affecting the bond length and angles of the silicate structure (Chapter 3). The final project (Chapter 4) includes measuring the trace element partitioning in mafic systems with variable Fe and Al content. This work revealed that while Al does affect the partitioning of 1+, 3+, and 4+ cations into the clinopyroxene structure, in Fe-rich systems, Fe appears to play a role in the partitioning of heavy rare earth elements (3+) onto the M1 site in 6-fold coordination that is not observed in Mg-rich clinopyroxenes.

TABLE OF CONTENTS

LIST OF TABLES

LIST OF FIGURES

LIST OF ATTACHMENTS

Attachment Ch4SupportingTables.xlsx contains supplementary information on the major and trace element data, Tables D1 and D2, related to contents of Chapter 4.

INTRODUCTION

Terrestrial bodies in the Solar System exhibit a range in chemical diversity and geologic processes (e.g., volcanism, impact events) that occurred during early stages of planetary formation. All of the rocky planets in our Solar System are believed to have gone through an early evolutionary stage known as a magma ocean. The magma ocean stage began where there was enough heating of the planetesimal through processes like the decay of short lived isotopes (e.g., ^{26}Al) and impact bombardment, to cause widescale or global melting of the planetary body, ultimately leading to differentiation of the core, mantle, and crust. The compositional structure of the mantle is a direct result from the crystallization that occurs during the cooling of the magma ocean. However, most planetary interiors are dynamic and undergo further physical processes such as mixing and melting post-magma ocean solidification that further modify the chemical structure of the mantle.

The physical properties of the magma ocean liquid and the processes that occur during and post-solidification are critical to understanding the planet's petrogenetic history as well as how the internal chemistry and physical structures influence the igneous surface features seen on planetary surfaces today. This work is composed of four chapters that explore Mercury's early evolution and the trace element partitioning in Fe-rich mafic systems, all of which combine experimental, analytical, and modeling approaches to understand these systems.

Mercury's Magma Ocean and Subsequent Mantle Formation

Mercury has a compositionally diverse surface that currently includes nine geochemical terranes (Vander Kaaden et al., 2017) that differ in composition and age, with the oldest (Heavily Cratered Terrane/Intercratered Plains) at ~4–4.1 Ga and the youngest (Borealis Planitia) at ~3.5–3.8 Ga (Marchi et al., 2013; Byrne et al., 2016). This indicates that there were different periods of volcanic activity on Mercury during the first ~500 million years after magma ocean solidification. The resulting chemical structure of the mantle from the cooling magma ocean will directly influence the compositional reservoirs that are sources for surface volcanism.

The properties of a magma ocean liquid, such as viscosity, control the style of crystallization that will occur in the cooling magma ocean. In silicate systems, polymerization (and thus viscosity) correlate to the number of non-bridging oxygens per tetrahedral unit (NBO/T, Mysen et al., 1981; Mysen 1990; Wang et al., 2014; Kono, 2018). The TO_4 tetrahedral unit is comprised of a tetrahedrally (T) coordinated cation (Si^{4+}, Al^{3+}) and four oxygens (O). A TO_4 unit with four NBO is an isolated unit with no connections to other TO_4 units. A liquid dominated with these isolated units would be low in viscosity as there are little to no bonds to be modified between the TO_4 units (e.g., peridotite, ~2 Pa·s at 1400°C; Dingwell et al., 2004). Conversely, a TO_4 unit with zero NBO, represents a fully polymerized, connected network where the liquid would be high in viscosity (e.g., rhyolite, ~54 Pa·s at 1400°C; Romine and Whittington, 2015). The viscosity of a liquid will evolve with changes to the environment, such as changes in temperature, pressure, or the introduction of crystals, thus it is important to consider how it evolves as the magma body cools and crystallizes. The viscosity and polymerization of a liquid can be evaluated via experimental (e.g., falling sphere viscometry) and analytical (e.g., diffraction, spectroscopy) methods and the results can be used to understand the behavior silicate liquids. Measuring the viscosity of Mercury's magma ocean liquid is critical as it provides constraints in modeling the crystallization styles that would be expected during magma ocean solidification.

Mercury may have formed a graphite flotation crust during early magma ocean solidification (e.g., Vander Kaaden and McCubbin, 2015; Peplowski et al., 2016; Klima et al., 2018). Similar to the process believed to have occurred on the Moon with a plagioclase flotation crust (e.g., Warren 1985; Shearer et al., 2006), a flotation crust on Mercury may have produced a heterogeneous mantle via fractional crystallization of the cooling magma ocean. If this were the case, different physical processes may occur in Mercury's interior that can alter the structure and chemistry after magma ocean solidification. Cumulate mantle overturn is a process where gravitational instabilities develop as a result of inverted density structures (overlying layer is denser than the underlying layer). These gravitational instabilities will occur as downwelling Rayleigh-Taylor instabilities, denser material sinking into the less dense cumulates (e.g., Kesson and Ringwood, 1976; Zhang et al., 2017; Li et al., 2019; Yu et al., 2019). This process may lead to mixing between materials, forming new compositional reservoirs than would not have been produced from the magma ocean solidification. This process of downwelling instabilities is important to consider for Mercury's internal evolution, as a lherzolite (clinopyroxene-bearing) source is needed to form the Heavily Cratered Terrane. A silicate-only mantle may produce gravitational instabilities, but the addition of sulfides in Mercury's interior are an important consideration as their density differences are different than the common, terrestrial mantle silicate minerals (e.g., olivine, pyroxene). Additionally, sulfides like oldhamite have the potential for incorporating heat producing elements (e.g., U, Th, K) in their crystal structure (e.g., Wohlers and Wood, 2015, 2017; Boujibar et al., 2019; Boukaré et al., 2019) that, over millions of years, could lead to significant partial melting of the layer in which they reside. Understanding the processes that could occur in Mercury's mantle and how that influenced early volcanism on the surface will provide important models for beginning to understand Mercury's petrogenetic history.

Trace Element Partitioning in Fe-rich Pyroxenes

Trace element partitioning is an important process for understanding the petrogenesis of igneous rocks, as they can be records of melting and fractionation processes during crystallization. Clinopyroxene is one such mineral that is common in planetary interiors that is useful to study trace element partitioning due to its more distorted M2 site that can house a wider variety of cations with larger radii and valence states. Incompatible elements, such as the rare earth elements (REE) and high field strength elements (HFSE), in general, have higher valence states and larger cation radii than cations found in common mafic minerals (e.g., Mg^{2+}, Fe^{2+}, Ca^{2+}). In order to substitute into a crystallographic site, the incompatible elements need to maintain charge balance, often through a coupled substitution of M2 Ca^{2+} and tetrahedral Si^{4+}, e.g., $Ca^{2+} + Si^{4+} \leftrightarrow REE^{3+} + Al^{3+}$ (e.g., Lundstrom et al., 1998; Schwandt and McKay; 1998; Shearer et al., 2006).

Mg-rich mafic systems have been studied extensively due to their prevalence in mafic systems on Earth. However, Fe-rich mafic systems are common on other terrestrial bodies in our Solar System, such as the Moon, Mars, and meteorites. Understanding how Fe can influence the partitioning of trace elements in pyroxenes in comparison to Mg-rich systems is important for understanding the petrogenetic evolution of Fe-rich magmatic systems in our Solar System.

CHAPTER I.

EXPERIMENTAL INVESTIGATION OF MERCURY’S MAGMA OCEAN VISCOSITY: IMPLICATIONS FOR THE FORMATION OF MERCURY’S MANTLE, DYNAMIC EVOLUTION, AND CRUSTAL PETROGENESIS

A version of this chapter was originally published by Megan D. Mouser, Nicholas Dygert, Brendan A. Anzures, Nadine L. Grambling, Rostislav Hrubiak, Yoshio Kono, Guoyin Shen, and Stephen W. Parman:

Mouser, M. D., Dygert, N., Anzures, B. A., Grambling, N. L., Hrubiak, R., Kono, Y., Shen, G., & Parman, S. W. (2021) Experimental investigation of Mercury's magma ocean viscosity: Implications for the formation of Mercury's cumulate mantle, its subsequent dynamic evolution, and crustal petrogenesis. *Journal of Geophysical Research: Planets, 126,* e2021JE006946. https://doi.org/10.1029/2021JE006946

This research was submitted to the Journal of Geophysical Research: Planets initially in September 2020. It went through three rounds of peer review before acceptance on October 19, 2021. Megan Mouser, the first author, was the corresponding author throughout the submission process of this paper and was in charge of the primary revisions from reviews and co-authors. Megan was the primary individual involved in all aspects of data collection, data processing, and writing. Nick Dygert provided important and constructive edits and assisted with data collection and processing throughout the entirety of this research. Brendan Anzures assisted with data collection, conditioned multiple experimental compositions, and conducted Fourier transform infrared spectroscopy analysis of the experimental samples. Nadine Grambling assisted with the experimental data collection and sample preparation. Rostislav Hrubiak, Yoshio Kono, and Guoyin Shen are the beamline scientist at the Advanced Photon Source, Argonne National Laboratory who assisted in the data collection and provided invaluable knowledge of the experimental process and data processing. Stephen Parman provided important information and advice on Mercurian geochemistry and the experimental compositions.

Abstract

Mercury has a compositionally diverse surface that was produced by different periods of igneous activity suggesting heterogeneous mantle sources. Understanding the structure of Mercury's mantle formed during the planet's magma ocean stage could help in developing a petrologic model for Mercury, and thus, understanding its dynamic history in the context of crustal petrogenesis. We present results of falling sphere viscometry experiments on late-stage Mercurian magma ocean analogue compositions conducted at the Advanced Photon Source, beamline 16-BM-B, Argonne National Laboratory. Owing to the presence of sulfur on the surface of Mercury, two compositions were tested, one with sulfur and one without. The liquids have viscosities of 0.6–3.9 (sulfur-bearing; 2.6–6.2 GPa) and 0.6–10.9 Pa·s (sulfur-free; 3.2–4.5 GPa) at temperatures of 1600–2000°C. We present new viscosity models that enable extrapolation beyond the experimental conditions and evaluate grain growth and the potential for crystal entrainment in a cooling, convecting magma ocean. We consider scenarios with and without a graphite flotation crust, suggesting endmember outcomes for Mercury's mantle structure. With a graphite flotation crust, crystallization of the mantle would be fractional with negatively buoyant minerals sinking to form a stratified cumulate pile according to the crystallization sequence. Without a flotation crust, crystals may remain entrained in the convecting liquid during solidification, producing a homogeneous mantle. In the context of these endmember models, the surface could result from dynamical stirring or mixing of a mantle that was initially heterogeneous, or potentially from different extents of melting of a homogeneous mantle.

1.1. Introduction

Mercury, like other terrestrial planets and the Moon, likely had a magma ocean early in its formation history (e.g., Warren, 1985; Abe, 1997; Solomon and Longhi, 1997; Brown and Elkins-Tanton, 2009; Solomatov, 20015; Vander Kaaden and McCubbin 2015; Boukaré et al., 2019). Constraining the dynamics of Mercury's magma ocean provides a starting point for constructing a petrologic model for Mercury. Convection and viscosity of the magma ocean largely dictate the stratification of the cumulate pile produced during solidification. For given convection vigor, and liquid and crystal density, more viscous liquids keep larger crystals entrained (i.e., suspended in the liquid) compared to lower viscosity liquids, which are therefore more likely to fractionate crystals. Thus, crystal suspension in a convecting magma ocean is efficient or inefficient depending on the magma viscosity, suggesting two endmember possibilities for magma ocean solidification: 1. Formation of a mineralogically stratified cumulate pile by a low viscosity magma ocean (e.g. Shearer et al., 2006; Dygert et al., 2017), or 2. Formation of a well-mixed mantle by a relatively high viscosity magma ocean (Suckale et al., 2012; Solomatov, 2015). Determining where on this spectrum Mercury falls is highly dependent on the viscosity of the magma ocean. Thus, the viscosity of Mercury's magma ocean holds critical importance for understanding the planet's formation and how the interior dynamics produced the unique interior and surface features we see today.

This experimental study focuses on characterization of the viscosity of late stage Mercurian magma ocean liquids and evaluates implications for the efficiency of crystal fractionation during Mercury's magma ocean stage and subsequent dynamic evolution of Mercury's mantle. Falling sphere viscometry experiments tested Mercurian analogue liquids using a Paris-Edinburgh press at the Advanced Photon Source, Argonne National Laboratory. Two compositions (Table 1.1) were investigated: one sulfur-free, and one containing 3 wt% sulfur to reflect the possibility of elevated sulfur in Mercury's magma ocean during solidification (e.g., Namur et al., 2016a). The viscosities of these compositions place constraints on the capacity of Mercury's convecting magma ocean to entrain crystals.

1.1.1. *Formation of a Mercurian Magma Ocean*

Mechanisms for forming partially or completely molten planets are debated; however, the leading theory for Mercury and the Earth-Moon system is that their magma oceans were produced by giant impacts (e.g., Wetherill, 1994; Kortenkamp et al., 2000). It is likely that heat from giant impacts along with thermal input from the young sun, core formation, and the decay of the short-lived isotope ^{26}Al contributed to the existence of terrestrial magma oceans (Flasar and Birch, 1973; Hostetler and Drake, 1980; Solomatov, 2015). Mercury has an unusually large core to mantle ratio in comparison to the other terrestrial planets, which has led researchers to propose that a giant impact origin for a Mercurian magma ocean is feasible, as an impactor could strip away a significant amount of surface silicate and mantle material after core formation (Smith, 1977; Benz et al., 1988; Cameron et al., 1988). If this was the case for Mercury, this would have likely created a magma ocean stage subsequent to initial magma ocean(s) that produced differentiation of the planet (e.g., Benz et al., 2007). Alternative theories to explain Mercury's large core-to-crust ratio invoke the decomposition of its early surface and mantle material through degassing in the high-temperature field of the depleting solar nebula (Cameron, 1985; Fegley and Cameron, 1987), or argue that Mercury's parent material was very metal rich-resembling a Carbonaceous B (Bencubbin) chondrite which has approximately 60 wt% metallic iron (Taylor and Scott, 2003; Brown and Elkins-Tanton, 2009). Here we assume that the giant impact hypothesis is the most likely scenario to produce Mercury's current core to mantle ratio.

1.1.2. *Mercury's Heterogeneous Surface*

The MErcury, Surface, Space, ENvironment, GEochemistry, and Ranging (MESSENGER) mission revealed unique aspects of Mercury including its high surface volatile content. Mercury has 1–4 wt% S, 2.5–5 wt% Na, and 1–2 wt% Fe present on the surface as measured by X-ray spectrometry and gamma-ray spectrometry (Nittler et al., 2011; Evans et al., 2012; Starr et al., 2012; Weider et al., 2012; Peplowski et al., 2014). The sulfur content of Mercurian lavas (1–4 wt%) is much higher than Earth, Mars, or lunar mantle, which are estimated to have <0.1wt% S (Ringwood and Kesson, 1977; King and McLennan, 2010; Namur et al., 2016a). Additionally, the absence of Fe^{3+} charge transfer absorptions in the visible and near infrared (VNIR) spectra indicate low-Fe silicate minerals (Izenberg et al., 2014; Murchie et al., 2015; Riner et al., 2010). The high sulfur, low iron, and large core to mantle ratio indicate that Mercury is very reduced, between 2 and 7 log units below IW (Malavergne et al., 2010; McCubbin et al., 2012; Zolotov et al., 2012, Namur et al., 2016a, 2016b), where IW refers to the iron-wüstite buffer.

Mercury's surface has been revealed to be compositionally heterogeneous, including multiple terranes defined by their geochemical diversity and morphological differences (Vander Kaaden et al., 2017). Some such terranes include the Borealis Planitia (BP), plains associated with large impact basins (e.g., Caloris, Rachmaninoff), and the Intercratered Terrane and Heavily Cratered Terrane (IcT-HCT). Based on crater chronology, the oldest surfaces on Mercury are estimated to be between 4.0–4.1 Ga, with the youngest surfaces aging around 3.5–3.8 Ga (Marchi et al., 2013). The difference in age is thought to have resulted from volcanic resurfacing of Mercury starting around 4 Ga and ceasing around 3.5 Ga (Marchi et al., 2013; Byrne et al., 2016), with volcanic episodes that formed the expansive BP occurring toward the end of and post-late heavy bombardment (Trask and Guest, 1975; Malin, 1976; Solomon et al., 2008; Denevi et al., 2009; Head et al., 2011).

Located in the northern hemisphere, the BP are in general high in Al/Si, and low in Mg/Si, Ca/Si, and S/Si ratios (Weider et al., 2012; Peplowski et al., 2014; Weider et al., 2015; Namur et al., 2016b; Lawrence et al., 2017; Nittler et al., 2019); however, the BP can be further subdivided into a low-Mg region, which exists at latitudes higher than 60°N, and a high-Mg region which encompasses the BP at latitudes of ~30–60°N (Weider et al., 2015; Lawrence et al., 2017) where MgO is estimated to vary by ~8 wt% between the high and low Mg regions (Vander Kaaden et al., 2017). Compared to the BP, the IcP-HCT have high Mg/Si, Ca/Si, S/Si ratios and low Al/Si ratios (Weider et al., 2012; Peplowski et al., 2014; Weider et al., 2015; Namur et al., 2016b; Lawrence et al., 2017; Nittler et al., 2019). Further subdivisions of the IcP-HCT are less defined than the BP, but appear to include a high-Mg region, a high-Mg and high-Ca region, and an intermediate heterogeneous region (Weider et al., 2015; Lawrence et al. 2017) where the MgO may vary by ~5wt% (Vander Kaaden et al., 2017). Impact basin plains are also chemically distinct from each other, with the Caloris basin being more Al/Si enriched than Rachmaninoff, and conversely, Rachmaninoff being more Mg/Si rich than Caloris (Weider et al., 2015; Lawrence et al., 2017). Studying the properties of Mercury's magma ocean may lend insight into the compositional variability of Mercury's surface, which implies heterogeneous mantle sources that may relate to stratification of Mercury's mantle after magma ocean crystallization or processes such as cumulate overturn or the rising of buoyant material into shallower cumulates (Charlier et al., 2013; Tosi et al., 2013a; Namur and Charlier, 2016; Namur et al., 2016b).

1.2. Methods

1.2.1. *Compositions*

Starting materials used are based on assumption of bulk Mercury with a Carbonaceous H chondrite Allan Hills 85085 (ALH 85085)-like composition. ALH 85085 was chosen due to its compositional similarities to Mercury, and higher Al/Si, Mg/Si, and Fe/Si ratios compared to other chondrites (Weisberg et al., 1988); however, the Fe and Na content assumed were modified to better resemble an estimated Mercurian composition (Anzures et al., 2020). We experimentally investigate a residual liquid after 80% crystallization of a Mercurian magma ocean with an ALH 85085 bulk composition because it falls within a proposed Mercurian magma ocean fractionation line (see Fig. 3 in Anzures et al., 2020). This silicate liquid is rich in Mg and has an intermediate silica content, similar to an Fe-free andesite (Table 1.1)

Starting compositions were prepared from a silicon and sulfur-free parent mixture using reagent grade oxide powders homogenized by grinding in ethanol in an agate mortar and pestle for six hours. The parent mixture was decarbonated in an Al crucible for 24 hours at 900°C. After decarbonation, the parent mixture was divided into aliquots. SiO_2 was added to the first aliquot which was then reground to create the S-free experimental starting material. This powder, and the second aliquot were then conditioned to an oxygen fugacity one log unit below the iron-wüstite (IW) buffer in a CO/H_2 gas mixing furnace at Brown University. To the second (SiO_2-free) aliquot, 3 wt% sulfur and a mixture of Si metal and SiO_2 in a molar Si/SiO_2 ratio of 5:95 were added, bringing the effective fO_2 of this composition to near IW-5. The difference in the fO_2 of the compositions is due to the Si metal added to the S-bearing composition to ensure the sulfur would remain in solution. The compositions of these mixtures, based on electron microprobe analysis of glassy experimental run products, are reported in Table 1.1 and Table A1.

Two series of experiments were conducted: those on the ground oxide powders described previously (denoted MMO for S-free and MMOS for S-bearing), and a second series on a sulfur-free composition that was fused in a furnace at 1400°C for four hours in air, reground into a powder, and then prepared using the procedure outlined above. The remainder of the original MMO composition was used to make the fused composition; the fused and unfused are compositionally indistinguishable within uncertainty (measured data are reported in Table A1 in the Appendix). The experiments using the fused composition are named 'FMMO' (Table 1.2).

1.2.2. *Paris-Edinburgh Experiments*

Viscometry experiments were conducted using the VX-3 Paris-Edinburgh (P-E) press at Beamline 16-BM-B, High Pressure Collaborative Access Team (HPCAT) located at the Advanced Photon Source, Argonne National Laboratory. A rhenium sphere (for S-free experiments) or a tungsten carbide (WC) sphere (for S-bearing and some S-free experiments) was placed near the top of a graphite-lined boron nitride capsule packed with the experimental powder (Figure 1.1), additional powder was placed over the sphere to prevent it from adhering to the graphite lid during the experiment. WC spheres were used for S-bearing experiments to prevent reaction of sulfur with rhenium. Experimental temperature is calculated using a thermocouple-calibrated power-temperature curve (Kono et al., 2014) with an estimated uncertainty of ±5%. Once the experiment has been loaded in the press and pressurized, the temperature is incrementally raised by 5°C until the temperature is approximately 300°C below the target condition. Within a few seconds, the current is then ramped to the desired experimental condition, at which point the composition melts and the sphere starts falling. The path of the falling sphere is imaged by X-ray radiography using a high-speed camera (Photron FASTCAM SA3) behind the P-E press (Kono et al., 2014). Imaging of the interior of the experimental cell and the falling sphere is recorded as X-rays pass through the assembly and are attenuated by the sphere, allowing the path of the sphere to be imaged, and its velocity to be measured as a function of time and displacement. In our experiments, the paths of the falling sphere were recorded by a high-speed camera at 250 frames per second (for MMO and FMMO) and 500 fps (MMOS). Depending on the experimental condition, the peak velocities of the falling spheres ranged from 0.012-0.489 mm/s, such that the experimental durations were seconds to minutes. This allowed for collection of at least 500 frames per experiment, sufficient to yield accurate viscosity measurements. Pressure is calculated from X-ray diffraction measurement of MgO in the assembly using an equation of state for MgO (Kono et al., 2010) assuming the experimental liquid experienced a similar condition. The measured uncertainty for MgO is ±0.15 GPa (Kono et al., 2010) but due to potential pressure and/or temperature gradients across the assembly (Kono et al., 2014) we estimate the pressure uncertainty of the run condition to be ±0.5 GPa.

1.2.3. *Calculating Viscosity: Stokes' Law*

The viscosity of the experimental liquids was calculated using the nominal terminal velocity of the falling sphere with a Stokes' law formulation with wall (Faxén, 1922) and end (Maude, 1961) effect corrections (e.g., Kono et al., 2014),

$$\eta = \frac{g_E d^2(\rho_s - \rho_l)W}{18Bv}, \tag{1.1}$$

where g_E is gravitational acceleration on Earth (9.8 m/s^2), d is the diameter of the sphere, ρ_s is the density of the sphere, ρ_l is the density of the liquid, v is the terminal velocity of the falling sphere, and W and B are wall and end effect correction coefficients, respectively. Wall and end effects, measured sphere size, and calculated sphere and liquid density and their associated uncertainties are reported in appendix A (Table A3). The velocity of the falling sphere is determined by calculating the position of the sphere in an image sequence using ImageJ. The velocity values are plotted against displacement (e.g. Figure A2–4). The peak of the velocity-displacement curves, which ideally plateau at the terminal velocity, are interpreted as the terminal velocity.

The densities of the liquid (ρ_l) and sphere (ρ_s) were calculated for each experiment using a third order Birch Murnaghan equation of state to take into consideration the effect of pressure and temperature on the density of the silicate liquid (Ueki and Iwamori, 2016) and the rhenium (Zha et al., 2004; Anzellini et al., 2014) and tungsten carbide (Litasov et al., 2010) spheres. The calculated liquid densities range from 2.78–2.93 g/cm^3 (Table A2) over the range of experimental pressures (1.4–6.2 GPa). Density uncertainties for the sphere calculations are expected to be between 2.5–5% (Litasov et al., 2010; Anzellini et al., 2014). The initial molar volume uncertainty for the liquid is ~5% (Ueki and Iwamori, 2016) which propagates through the liquid density calculation.

Table 1.1. Experimental compositions and Mercurian surface compositions.

S-free Experimental Liquid Composition (wt%)									
	SiO_2	**TiO_2**	**Al_2O_3**	**MgO**	**CaO**	**K_2O**	**Na_2O**	**S**	**Total**
	54.29	1.21	16.63	15.20	11.32	1.30	0.35	0.00	100.30
1σ Std Dev	0.49	0.04	0.16	0.49	0.11	0.06	0.02	0.00	
S-bearing Experimental Liquid Composition (wt%)									
	50.90	1.16	17.22	15.36	11.38	0.43	0.03	2.72	99.21
1σ Std Dev	0.70	0.05	0.26	0.50	0.20	0.03	0.01	0.07	
Borealis Planitia Estimated Composition (wt%)[a]									
	53.67	0.24	4.57	36.89	2.26	0.05	1.97	0.00	99.65
Intercratered Plains/Heavily Cratered Terrane Estimated Composition (wt%)[a]									
	51.98	0.21	4.24	37.64	3.84	0.04	1.29	0.00	99.24

Compositions of S-free and S-bearing experimental liquids as determined by electron microprobe analyses of quenched glasses. The compositions of the analogue magma ocean liquids are not intended to resemble the lavas; these liquids represent a late magma ocean liquid parental to a juvenile cumulate mantle that eventually formed the BP and IcP-HCT sources. Note the BP and IcP-HCT compositions reported here do not include sulfur (1–4 wt%) or reduced iron (1–2 wt%) as measured on Mercury's surface by MESSENGER (Nittler et al., 2011, 2019; Weider et al., 2014). [a]BP and IcP/HCT compositions (Nittler et al., 2019) are shown for comparison.

Table 1.2. Viscometry experiment results.

Experiment	η (Pa·s)	Uncertainty associated with run conditions (Pa·s)	Uncertainty associated with viscosity determinations (Pa·s)	T (°C)	P (GPa)	Preparation
S-free						
MMO6	1.5	±0.3	±0.2	2000	6.2	Unfused
MMO1	0.6	±0.3	±0.1	2000	6.0	Unfused
MMO17	0.9	±0.2	±0.1	2000	5.4	Unfused
MMO16	2.8	±0.2	±0.4	2000	4.8	Unfused
MMO12	2.8	±0.3	±0.6	2000	4.0	Unfused
MMO7	4.5	±0.3	±1.2	1950	4.0	Unfused
MMO2	1.1	±0.2	±0.2	1900	5.5	Unfused
MMO9	6.7	±0.3	±2.6	1850	2.7	Unfused
FMMO9	0.9	±0.4	±0.1	1800	5.6	Fused
FMMO8	2.3	±0.2	±0.4	1800	4.2	Fused
FMMO1	1.6	±0.3	±0.3	1700	2.8	Fused
FMMO3	10.9	±0.4	±4.1	1600	2.6	Fused
S-bearing						
MMOS7	0.7	±0.3	±0.1	2000	4.0	Unfused
MMOS6	0.6	±0.3	±0.1	2000	3.2	Unfused

Table 1.2 Continued

Experiment	η (Pa·s)	Uncertainty associated with run conditions (Pa·s)	Uncertainty associated with viscosity determinations (Pa·s)	T (°C)	P (GPa)	Preparation
MMOS5	0.8	±0.5	±0.1	1900	3.8	Unfused
MMOS10	1.4	±0.6	±0.2	1800	4.5	Unfused
MMOS2	1.6	±0.8	±0.3	1700	3.5	Unfused

Experimental results and nominal pressure and temperature conditions for S-free (MMO and FMMO) and S-bearing (MMOS) experiments. MMO and MMOS refer to experiments testing unfused powder compositions, while FMMO refers to experiments testing pre-fused powder compositions. All S-free experiments were conditioned to IW-1 and all S-bearing experiments were conditioned to IW-5. Estimated uncertainty in run conditions is ±0.5 GPa for pressure and ±5% for temperature. Experimental and calculated uncertainties are discussed further in Section 1.3.

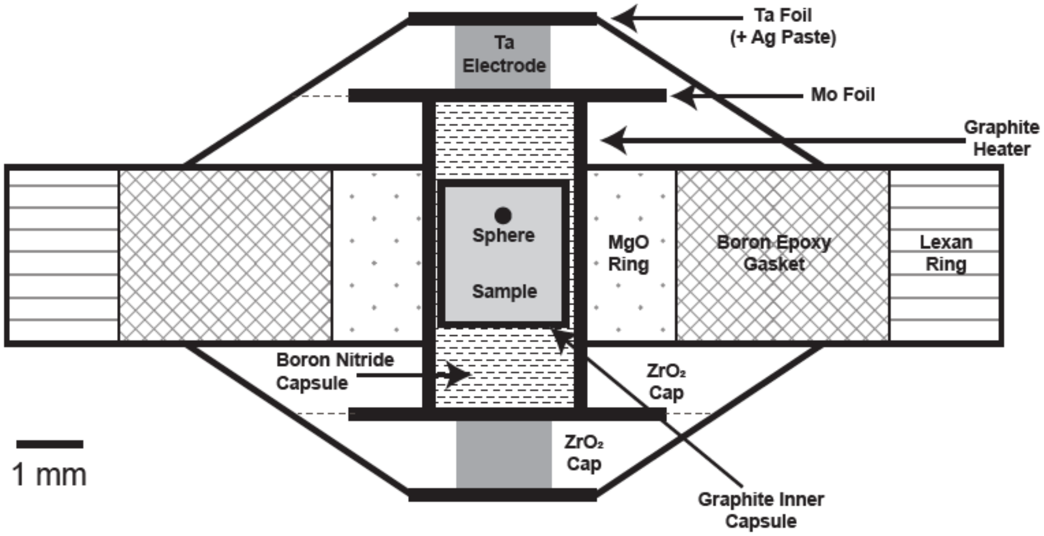

Figure 1.1. Schematic cross section of the experimental assembly used in the Paris-Edinburgh apparatus.

1.2.4. *Analytical Methods*

1.2.4.1. *Electron Probe Micro Analyzer*

Electron probe micro analyzer (EPMA) analysis was conducted on the experimental glasses of experiments MMO1 and MMOS5 (Table 1.1) and FMMO9 (Table A1) to determine the major element composition of the glasses. Analysis was done using the Cameca SX100 electron micro probe at the University of Tennessee. Analytical conditions were an accelerating voltage of 15 kV and a beam current of 30 nA. The glass was analyzed using a defocused 10 μm beam.

1.2.4.2. *Fourier Transform Infrared Spectroscopy*

Fourier transform infrared (FTIR) spectroscopic measurements were conducted on sample MMOS5 to determine water content. MMOS5 thin sections were ground and doubly polished down to 1 μm. Sample thickness was measured using a Mitutoyo digimatic indicator with 0.1 μm precision. Five measurements were made for each sample to test uniformity (chip 1: 55, 69, 69, 70, 68 μm; chip 2: 115, 117, 113, 116, 110 μm). Transmission spectra were collected in the Reflectance Experiment Laboratory (RELAB) at Brown University using a Bruker LUMOS FTIR microscope with a KBR beamsplitter and MCT detector. Glass chips were mounted in a Linkam environment stage with CaF_2 windows and dry air flowing though. The stage was heated to 200°C then cooled to room temperature with dry air flowing for two days to remove absorbed water. Transmission spectra over the wavelength range of 2.5–7 μm (the spectrally transparent range of CaF_2 windows) were taken after heating the sample to 250°C and holding for an hour.

Total water abundance was calculated using the Beer-Lambert Law. Background beneath the absorbance peak between 2500 cm^{-1} and 3800 cm^{-1} was obtained by a fit to the spectrum between 2400 cm^{-1} and 2500 cm^{-1} and spectrum between 3800 cm^{-1} and 4400 cm^{-1}. An absorption coefficient of 62.32 $L \cdot mol^{-1} \cdot cm^{-1}$ for Fe-free andesites was used for the calculation (Mandeville et al., 2002). Based on three analyses of the two chips, the sample has an average water content of 94 ppm (±38 ppm, 1σ). Fourier transform infrared spectra of the analyses is included in appendix A, Figure A1.

1.2.4.3. *Laser Ablation Inductively Coupled Plasma Mass Spectrometry*

Laser ablation inductively coupled plasma mass spectrometry (LA-ICP-MS) measurements were conducted on two glass samples, FMMO3 and a glassed sample of MMO run at 3 GPa and 2000 °C (no viscosity measurement), at the University of Texas at Austin to test for possible boron contamination. Each sample had a grid of measurements taken with 250 μm spacing between each spot. Spot size was 75 μm and data were collected with a laser fluence of 2.03 J/cm^2 at 20 Hz with a 60 second dwell and 30 second gas blank. Analytical reference material was NIST 610, USGS GSE-1G and NIST 612 were used as a secondary reference materials.

The boron concentration in the two samples ranged from ~75 ± 50 ppm (glassed sample of MMO) to ~1790 ± 710 ppm (FMMO3). FMMO3 is this highest viscosity, longer duration experiment (~54 seconds) while the glassed sample was quenched within ~10 seconds after being brought to temperature (Table A2). Therefore, boron concentrations in all experiments reported in this study are expected to fall within this range. While boron was experimentally shown to affect the viscosity of silicate melts at higher concentrations (on the order of wt%, e.g., Brosh et al., 2012; Bartels et al., 2013; Malfait et al., 2014), the concentrations measured here are one to three orders of magnitude lower (Table A2), suggesting boron contamination has a minimal to negligible effect on the viscosity of the experimental liquids investigated in this study.

1.3. Results

Twelve successful falling sphere viscometry experiments using the S-free composition (4 fused and 8 unfused), and five successful S-bearing experiments are reported (all unfused); experimental results are summarized in Table 1.2 and Figure 1.2. A back scattered electron (BSE) image of experiment MMO1 is included in appendix A, Figure A5. The range of viscosities for the S-free experiments was 0.6–10.9 Pa·s at pressures of 2.6–6.2 GPa. The S-bearing experiments have a viscosity range of 0.6–3.9 Pa·s at pressures of 1.4–4.5 GPa. The tested temperature range for both liquids was 1600–2000°C. The S-bearing liquid exhibits lower viscosities than the S-free liquid at all temperature and pressure conditions. Both liquids show viscosity decreasing with increasing pressure, with the S-free liquid exhibiting larger pressure sensitivity over the range of conditions explored. These systematics and the measured viscosities are consistent between experiments run using the fused and unfused starting materials (Figure 1.2a). Compared to other S-free experiments, FMMO1 (1700°C, 2.8 GPa) exhibits a lower viscosity than expected when compared to the rest of the S-free dataset (Figure 1.2a) which we interpret to result from the relatively large uncertainty in experimental pressure and temperature conditions. As it is not representative of the overall dataset, FMMO1 is reported in the tables and figures but not included in the modeling of experimental data.

Uncertainties associated with the experimental measurements include the sphere diameter (±7%), density of liquid and sphere (±5%), and the velocity determination of the falling sphere. The standard deviations of the falling sphere velocity range from ±2% up to ±20%, depending on the experiment. Experiments with higher viscosities have higher velocity uncertainties than low viscosity experiments (e.g., compare Figure A2e; l, MMO1 and FMMO3). These compounded uncertainties in the viscosity measurements are reported as the “uncertainty associated with viscosity determinations” (Table 1.2).

Using the viscosity data obtained from these experiments (Table 1.2, but excluding outlying experiment FMMO1), we parameterized Arrhenius relations to model the viscosity of the liquids by simultaneous nonlinear regression of the experimental observations to determine activation energy (*E*), pre-exponential factor (*A*), and activation volume (*V*):

$$\eta = A \times exp\left(\frac{E+PV}{RT}\right), \tag{1.2}$$

where η is the viscosity in Pa·s, *A* is the pre-exponential factor, *E* is the activation energy in J/mol, *P* is the pressure in pascals, *V* is the activation volume in m^3/mol, *R* is the universal gas constant (8.314 J/mol K), and *T* is the temperature in K.

Models for the S-free and S-bearing compositions were parameterized separately, as the experimentally determined viscosities differ (Figure 1.2). The determined *A*, *E*, and *V* values for both models are presented in Table 1.3. To establish the quality of the fit for the S-free and S-bearing models, model predicted viscosities are compared to the measured viscosity for each experiment in Figure 1.3. Within the exception of the outlying experiment (FMMO1), the models predict the viscosity of these compositions within a factor of two of the measured values. Generalized predictive models for silicate liquids (Hui and Zhang, 2007; Giordano et al., 2008; Sehlke and Whittington, 2016) and slag liquids (Riboud et al., 1981; Browning et al., 2003; Mills et al., 2011) are compared to our viscosity data and models in appendix A, Figures A6 and A7. The silicate models consistently underestimate the experimental determinations by up to several orders of magnitude (Figure A6). The slag models better reproduce the viscosity of the S-bearing melt but underestimate the S-free melt viscosity (Figure A7).

The estimated experimental temperature uncertainty is ±5% of the nominal run temperature and pressure uncertainty is approximately ±0.5 GPa. Uncertainties based on deviations from the nominal run conditions were estimated by producing a synthetic dataset of 500 perturbed experimental conditions with a 1σ Gaussian distribution about the nominal run conditions. A distribution of viscosities was then calculated using Eq (1.2). The standard deviation of the synthetic viscosities is reported as the “uncertainty associated with run conditions” (Table 1.2).

Viscosities predicted using the Arrhenius models are shown as a function of temperature and pressure in Figure 1.4. Consistent with the experimental results presented in Figure 1.2, the models show that the S-free composition has a higher viscosity than the S-bearing composition, except when extrapolated to low temperatures and high pressures, where the viscosities converge. At low pressures, the liquid viscosities are sub-parallel as a function of temperature (Figure 1.4). At high pressures, the activation volume term dominates the S-free model, resulting in low temperature sensitivity. This is consistent with the trends in the experimental data (Figure 1.2) which suggest that at high pressures the S-free liquid becomes weakly temperature sensitive.

In Figure 1.5, our predictive models are compared to those for other silicate melts (peridotite, Liebske et al., 2005; alkali basalt, Giordano and Dingwell, 2003; andesite, Vetere et al., 2006; and a lunar magma ocean ferrobasaltic liquid, Dygert et al., 2017), and experiments on enstatite liquid (Cochain et al., 2017). In general, the MMO compositions have higher viscosities than the mafic liquids shown (Figure 1.5). The S-free MMO liquid is most comparable to an andesite; the S-bearing liquid best resembles an alkali basalt. The relatively high viscosity of these Mercurian liquids compared to primitive liquids (e.g., peridotite) is to be expected for an 80% crystallized, late-stage magma ocean liquid enriched in Si, and that is thus polymerized compared to the basalt and peridotite.

1.4. Discussion

1.4.1. *Structural Control on the Viscosity of Experimental Liquids*

The viscometry experiments demonstrate different viscosities, as well as temperature and pressure sensitivities for the S-free and S-bearing compositions. The S-free composition shows a consistent, relatively large decrease in viscosity with both increasing pressure and temperature (Figure 1.2a; 1.4). The S-bearing composition shows a more modest decrease in viscosity at the different pressure and temperature conditions, but it does exhibit some pressure and temperature sensitivities as well (Figures 1.2c; 1.4). At all tested pressure and temperature conditions, the S-free composition exhibits a higher viscosity than the S-bearing composition.

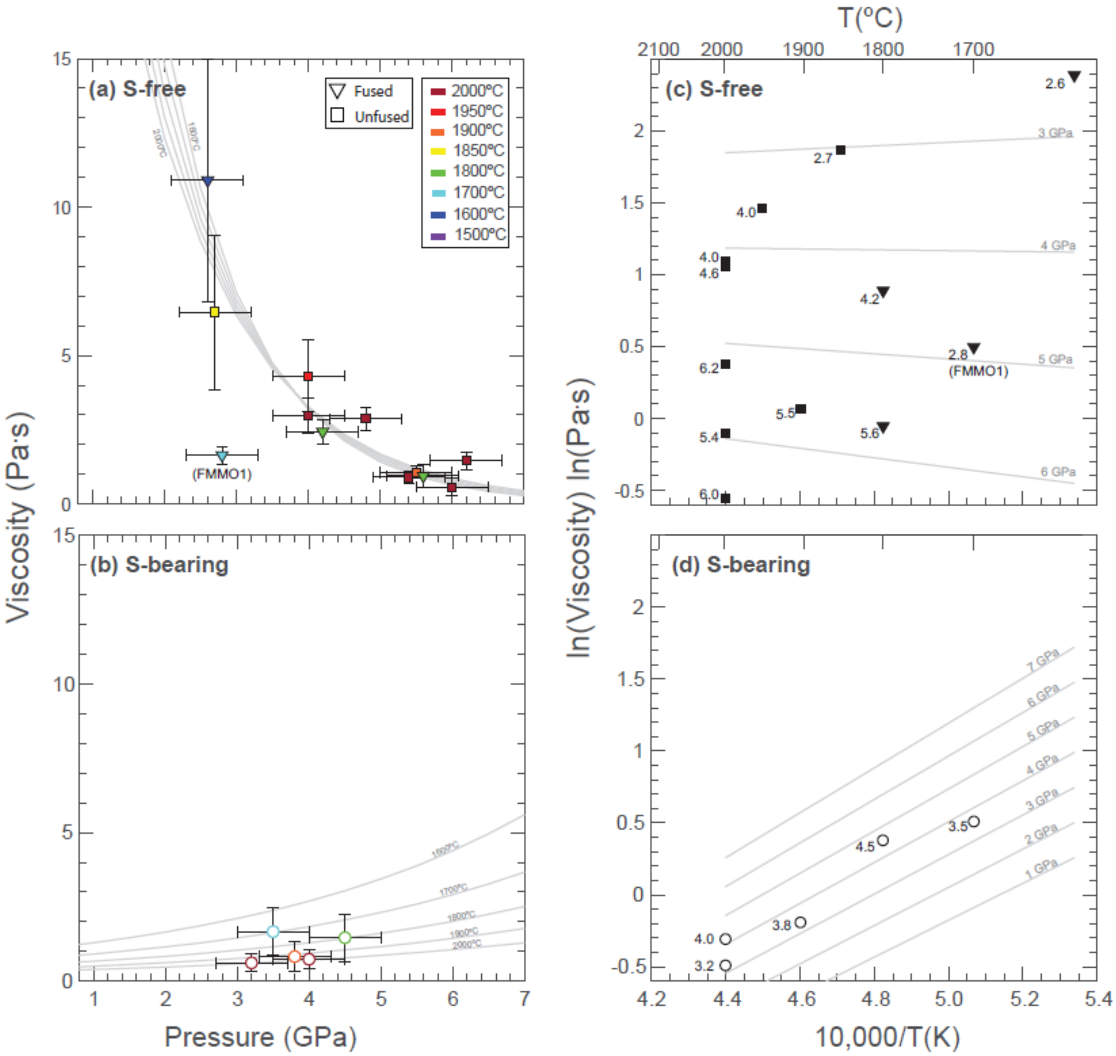

Figure 1.2. Experimental viscosity results. Experimentally determined viscosities for (a; c) S-free (unfused- filled squares and fused- filled triangles) and (b; d) S-bearing (open circles) MMO compositions. In (a; b) the results are plotted as a function of pressure on a linear scale. Symbol color indicates experimental temperature. In (c; d) the log of the viscosity is plotted against 10,000 × inverse temperature with experimental pressures (in GPa) indicated next to each observation. Gray lines indicate model predictions (Eq (1.2); Table 1.3) at constant temperature (a; b) and constant pressure (c; d) for each data set. Note the y-axis scales are the same in (a) and (b); and (c) and (d). Error bars shown are based on whichever is larger, the uncertainty associated with the viscosity determinations or the run conditions (Table 1.2, Section 1.3). Outlying experiment in the S-free dataset, FMMO1, is indicated in (a; c).

Table 1.3. Viscosity model parameters.

	ln(*A*)	***E* (J/mol)**	***V* (m^3/mol)**
S-free	$1.31^{+1.41}_{-0.58}$	$0.48 \times 10^5\ \ \pm 1.0 \times 10^5$	$-1.2 \times 10^{-5} \pm 1.0 \times 10^{-5}$
S-bearing	$-6.60^{+1.84}_{-0.15}$	$1.03 \times 10^5 \pm 1.0 \times 10^5$	$-3.8 \times 10^{-6} \pm 1.0 \times 10^{-6}$

S-Free and S-bearing model parameters determined for the pre-exponential term (*A*), the activation energy (*E*), and the activation volume (*V*) in Eq (1.2).

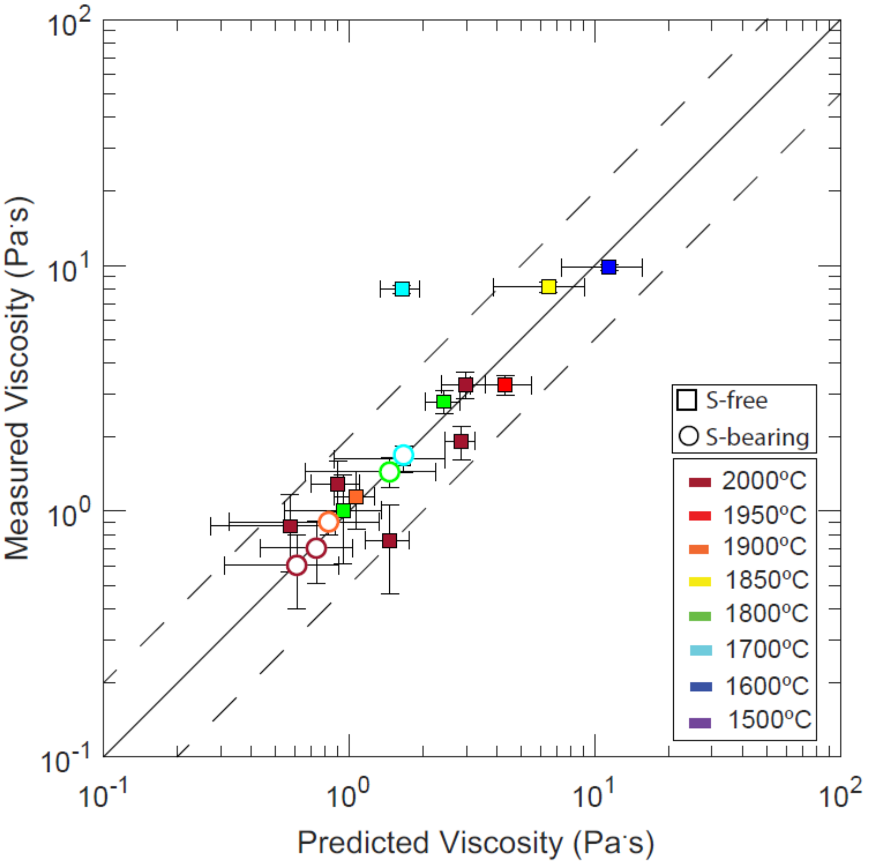

Figure 1.3. Viscosity model fit. Comparison between viscosity model predictions (Eq (1.2), x axis) and experimentally determined observations (y axis). S-free experiments are shown as squares, and S-bearing experiments are shown as circles. Symbol color corresponds to nominal experimental temperature, black solid line is 1:1; dashed lines are 1:2 and 2:1.

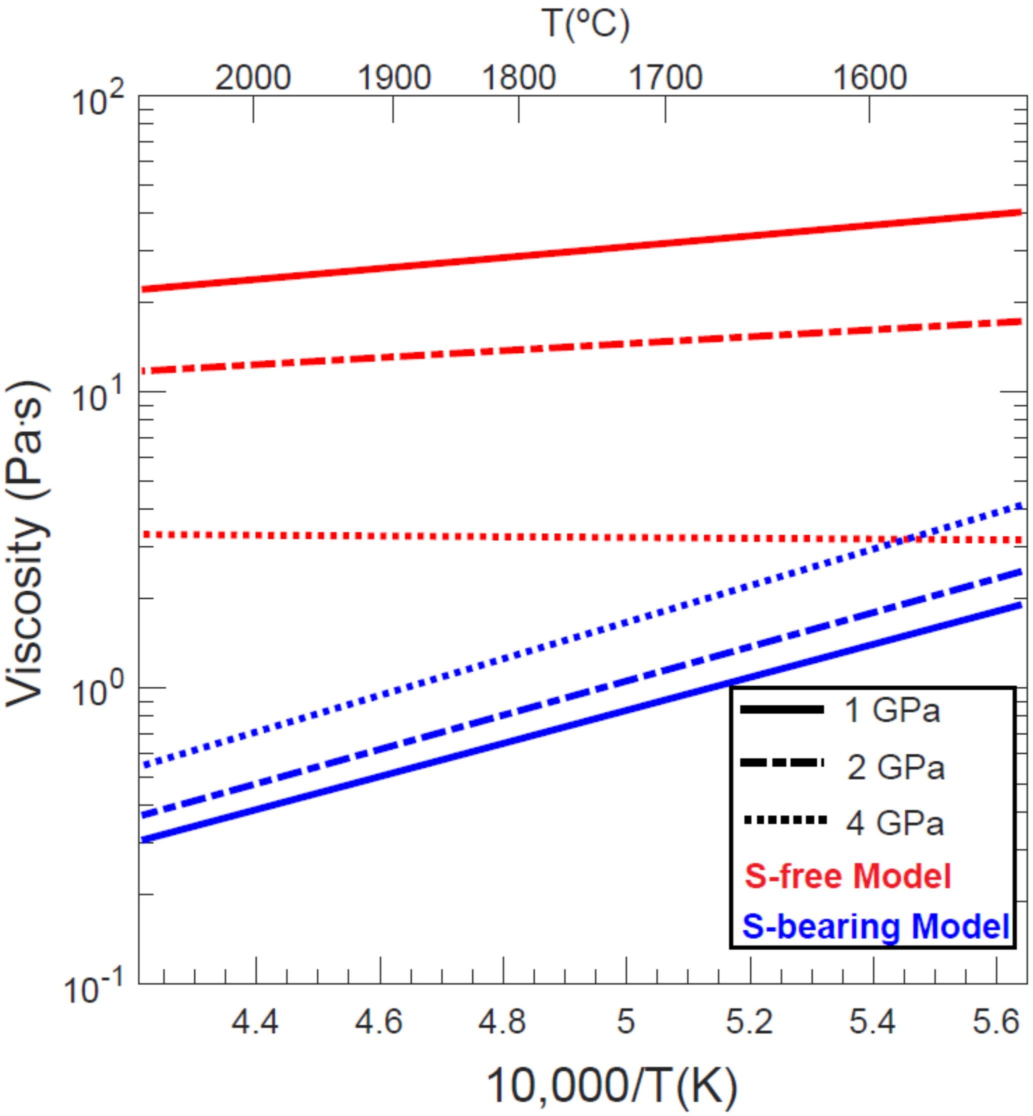

Figure 1.4. Viscosity models at different pressure and temperature conditions. Viscosities predicted using the S-free (red) and S-bearing (blue) models (Eq (1.2); 1.3) at 1, 2, and 4 GPa for a range of temperatures (1500°C to 2100°C, shown as 10,000 × inverse temperature on the x axis).

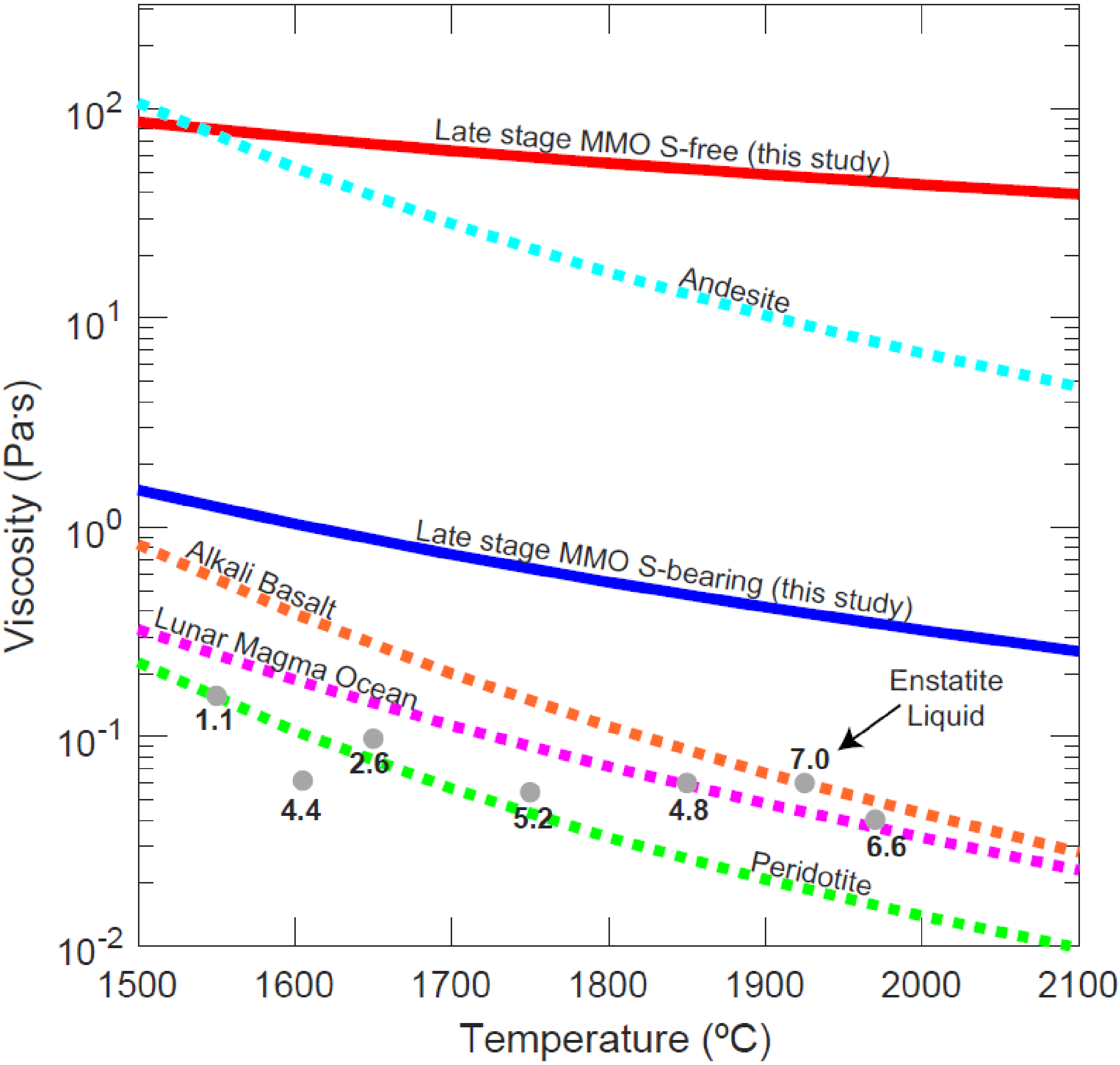

Figure 1.5. Viscosity models compared to other silicate viscosity models. Comparison of the late-stage Mercury magma ocean viscosity model predictions (Eq (1.2); Table 1.3) for the S-free and S-bearing compositions (red and blue lines, respectively) to viscosity models for andesite (Vetere et al., 2006), alkali basalt (Giordano and Dingwell, 2003), the lunar magma ocean ferrobasalt (Dygert et al., 2017), and peridotite liquid (Liebske et al., 2005) at 0.1 GPa. Gray circles show enstatite liquid viscosity measurements (Cochain et al., 2017) with the corresponding pressures (in GPa) next to each data point. The liquid enstatite data may be representative of the viscosity of the Mercurian magma ocean before significant solidification.

First, we address lower viscosities of the S-bearing experiments compared to the S-free experiments, which suggests that the presence of sulfur in reduced andesitic liquids decreases viscosity. This result is somewhat surprising, because in silicate liquids under low oxygen fugacity conditions, sulfur is thought to exist as an anion (S^{2-}) that complexes with metal cations (e.g., Anzures et al., 2020). The addition of sulfur to a silicate liquid may disrupt existing Mg- and Ca-bearing structural networks through the formation of MgS and CaS species (Fogel, 1997; McCoy et al., 1999; Namur et al., 2016a; Anzures et al., 2020). Isolation of network modifying Mg and Ca in sulfide species would polymerize the melt by forming networks dominated by tetrahedrally coordinated Si and Al. This sulfide complexing acts to increase the activity of SiO_2 as sulfide complexes "remove" network modifying cations from silicate structures (Anzures et al., 2020). However, this expectation is complicated by the fact that the compositions explored here were conditioned at two very different fO_2s, the S-free at IW-1, and S-bearing at IW-5. Highly reducing conditions are known to decrease the valence states of Ti and Si (e.g., Schreiber, 1977; Boujibar et al., 2019). Decreasing the valence states of these cations (which may be tetrahedrally coordinated under higher fO_2s) would increase their coordination states, turning them from network formers into network modifiers and disrupting existing polymerized structures.

The presence of S^{2-} should hypothetically increase polymerization of the S-bearing melt, however, our viscometry data indicate the opposite occurs. Across the range of experimental conditions explored, reduction of Ti and Si may overwhelm whatever polymerizing effect sulfur has on the S-bearing silicate liquid establishing its lower viscosity. Further experimentation and structural characterization are needed to disentangle their competing effects on viscosity. We note that preliminary experiments reported in appendix A (Table A4, Figure A8) suggests that fO_2 may exert a second-order control on viscosity in S-free systems.

Another important consideration is the inverse dependence of viscosity on pressure, which is exhibited by the S-free composition (Figure 1.2). Traditionally, this has been attributed to changes in the coordination state of Al^{3+} in the melt as pressure increases, which has been suggested for albitic and peridotitic melts (e.g., Kushiro, 1976; Liebske et al., 2005). The inverse pressure dependence we observe may be a result of Al coordination change; however, further characterization is needed to evaluate this interpretation. We note that depolymerized melts are less sensitive to changes in pressure than polymerized melts, because depolymerized melt structures can rearrange without breaking multiple bridging oxygen bonds, owing to the fact that TO_4 tetrahedra (T being the tetrahedrally coordinated cation; e.g. Al^{3+}, Si^{4+}) are already largely disconnected (Wang et al., 2014). Because our melts are moderately siliceous, the apparent inverse pressure dependence may be expected.

In silicate melts, the amount of Al present may also control melt viscosity as Al coordination is thought to change from tetrahedral to octahedral at high Al concentrations. This coordination change causes a turnover in viscosity for high-Al melts because Al acts as a depolymerizing network modifier in octahedral coordination (Bottinga and Weill, 1972). Our Al-bearing experiments have significantly higher viscosities than Al-free compositions under the conditions explored, (Figure A8) demonstrating that such a coordination turnover was not reached in our experiments or does not reduce viscosity below Al-free compositions.

1.4.2. *Solidification Timescale for Mercury's Magma Ocean*

The cooling rate of magma oceans controls convection vigor and in part determines the efficiency of crystal fractionation. Therefore, an important consideration for any analysis of magma ocean crystallization (and cumulate pile formation) is the magma ocean's cooling history (e.g., Martin and Nokes, 1988; Tonks and Melosh, 1990; Elkins-Tanton et al., 2011; Solomatov, 2015; Dygert et al., 2017; Boukaré et al., 2018; 2019). In the absence of an atmosphere, cooling rate is largely determined by the presence or absence of a flotation crust and the surface area to volume ratio of the magma ocean. If a magma ocean initially cooling as a blackbody forms a flotation crust during solidification, then convection of the system will be dampened because heat conduction through a stagnant lid dramatically reduces heat flux (e.g. Shearer et al., 2006; Elkins-Tanton, 2012; Solomatov, 2015). Depending on composition and thickness, the presence of a flotation crust extends the solidification timescale by many orders of magnitude (e.g., Elkins-Tanton et al., 2011). A thin graphite crust has been proposed to have formed during later stages of Mercury's magma ocean solidification (Vander Kaaden and McCubbin, 2015); thus, it is important to consider implications of such a crust for Mercury's solidification dynamics.

To evaluate consequences of possible solidification timescales, we considered Mercurian magma oceans with and without a flotation crust. For a magma ocean without a flotation crust, the cooling rate was estimated by calculating the time required to dissipate latent and specific heat released from the solidifying magma ocean liquid by blackbody radiation across the surface of the planet. Radiogenic heat production caused by short lived isotopes like ^{26}Al is ignored here because we assume that short lived isotope systems are dead at the time of a late-stage magma ocean solidification. Additionally, heat contribution from long lived isotope systems such as U, Th, and K are ignored here as their contribution of heat flix from core solidification is similarly negligible (see appendix A for a demonstration; Table A5). For a scenario without a flotation crust or atmosphere, the solidification timescale (τ_{NC}) is calculated using Eq (1.3) (e.g., Eq (43) Solomatov, 2015),

$$\tau_{NC} = \frac{(L_H \times 0.2M) + (C_P \times \Delta T_m \times 0.2M)}{4\pi\sigma r^2 T^4}, \tag{1.3}$$

where L_H is the latent heat of the magma ocean liquid (4×10^5 J/kg), M is the mass of the magma ocean (after 80% crystallization; 0.2 is the remaining fraction of liquid), C_P is specific heat of the magma ocean liquid (1405 J/kg K), ΔT_m is the temperature difference during solidification (assumed to be 200°C), σ is the Stefan-Boltzmann constant, and r is the radius of Mercury, and T is the temperature of the magma ocean (1350°C).

The solidification timescale of a magma ocean with a flotation crust is strongly controlled by the composition and thickness of the crust (e.g., Minear and Fletcher, 1978; Hakim et al., 2019). Workers have proposed the possibility of sulfide rich (Boukaré et al., 2019) and graphite (Vander Kaaden and McCubbin, 2015; Peplowski et al., 2016; Klima et al., 2018) flotation crusts on Mercury, however, for this analysis we consider the latter scenario. The solidification timescale for Mercury's magma ocean with a graphite flotation crust (τ_c) was estimated by dividing latent and specific heat by the steady state flux of heat conducted through a graphite flotation crust:

$$\tau_C = \frac{(L_H \times 0.2M) + (C_P \times \Delta T_m \times 0.2M)}{\left(\frac{\Delta T_C \kappa C_{Pg} \rho_g}{z}\right) A_p}, \tag{1.4}$$

where ΔT_c is the temperature difference between the magma ocean liquid and the surface of the crust, κ is the thermal diffusivity of graphite (1.2×10^{-3} m^2/s (Hofmeister et al., 2014)), C_{Pg} is the thermal heat capacity of graphite, ρ_g is the density of graphite, z is the thickness of the graphite crust, and A_p is the surface area of Mercury. The thickness of Mercury's graphite flotation crust is dependent on the amount of carbon present during solidification (Vander Kaaden and

McCubbin, 2015). Estimates suggest the range in graphite crust thickness could be between 1 m and 21 km but depends on the amount of carbon originally present in the primordial material (Vander Kaaden and McCubbin, 2015). Remote sensing analysis of Mercury's surface supports the graphite flotation crust theory, suggesting an average of 2.5 wt% carbon enrichment in the HCT and indicating some craters may have as much as 4 wt% carbon present (e.g., Peplowski et al., 2016; Klima et al., 2018).

The thickness of the crust greatly impacts the solidification timescale of the cooling magma ocean. A thicker flotation crust will lead to a longer solidification time, while a thinner flotation crust will lead to a shorter solidification time. In this analysis we consider a graphite flotation crust thicknesses of 100 m and 1 km. Compared to the 1 km scenario, which results in a solidification timescale of ~3,000 years, the 100 m thick crust decreases the solidification timescale by an order of magnitude. For the remainder of the analysis, we assume a 1 km thick graphite flotation crust; analysis for the 100 m scenario is included in appendix A (Figure A9).

1.4.3. *Grain Size*

In addition to the liquid viscosity and convection vigor, grain size is an important parameter in determining the efficiency of crystal entrainment in a convecting magma ocean. The ranges of predicted timescales for solidification of Mercury's late magma ocean were converted into cooling rates and used to calculate upper bound grain sizes for magma ocean cumulates using grain growth laws (Figure 1.6). These are upper bound calculations because they assume that grains grow continuously throughout the final 20% magma ocean solidification considered here. We explore the growth of common igneous minerals; forsteritic olivine (Karato, 1989), pyroxene (Walker et al., 1976), and Ca-rich plagioclase (Walker et al., 1978) where details regarding the experiments, crystal growth rates, and growth models can be found in the respective references. For cooling rates and timescales relevant to Mercury's magma ocean, we predict maximum grain sizes of a centimeter (cm) in a non-flotation crust scenario and up to tens of meters in size for the flotation crust scenario. The calculation is instructive but obviously unrealistic because in convecting magma oceans, very large grains will float or sink in accordance with their buoyancy, and high crystallinities significantly impede convective transport, resulting in sedimentation (Suckale et al., 2012). Nonetheless, the analysis demonstrates that in a slow cooling magma ocean, the crystal sizes are significantly larger than in a fast-cooling magma ocean, and that in fast cooling Mercurian magma oceans maximum grain sizes are on the order of centimeters.

1.4.4. *Crystal Suspension in Mercury's Magma Ocean and its Dependence on Grain Size and Crystallinity*

Mineralogical stratification of planetary mantles formed by magma ocean solidification is largely determined by whether crystallizing grains sink or float during crystallization (according to their buoyancy in the liquid) or remain viscously entrained in the convecting magma ocean liquid. To place constraints on the efficiency of crystal fractionation from Mercury's magma ocean, we calculated critical grain sizes for entrainment of relevant minerals as a function of magma ocean viscosity. The critical grain size is calculated assuming that the magma ocean's capacity to retain crystals in suspension depends on the potential for viscous dissipation from crystal settling, and work conducted by the convecting magma ocean liquid on entrained crystals (Solomatov, 2015):

$$d_f = \left(\frac{18\alpha\eta Q_R A_{planet} L}{f g_M C_P \Delta\rho^2 \phi X}\right)^{\frac{1}{2}}, \tag{1.5}$$

where α is the thermal expansion for silicates in K^{-1}, Q_R is the surface heat flux in W/m^2, A_{planet} is the surface area of the planet in m^2, L is the depth of the magma ocean in m, f is a hindered settling function (a value of 0.15 is assumed), g_M is the gravitational acceleration on Mercury (3.7 m/s^2), C_P is the thermal heat capacity (1450 J/kg K), ϕ is the crystal fraction (0.1 assumed), and X is the volume of the magma ocean in m^3. Using this equation, the boundary between fractionation and entrainment of a mineral at different viscosities can be calculated. In Figure 1.7, the colored lines represent critical grain size regime boundaries. For positively buoyant minerals such as graphite, grains larger than the critical values will float, grains smaller than the critical sizes will be entrained in the liquid. Plagioclase is shown with graphite; however, it is likely the plagioclase will be neutrally or negatively buoyant in the liquid (e.g., Riner et al., 2009; Figure 1.8a). For negatively buoyant minerals (orthopyroxene, clinopyroxene, and olivine), grains larger than the critical values will sink; grains smaller than the critical values will remain entrained in the convecting liquid.

For grains to remain entrained in the liquid, the ratio of buoyancy stress to weight per unit area of particles must exceed some critical value (Solomatov et al., 1993). Viscous traction cannot re-entrain particles that settled out onto the bottom of a magma ocean (Martin and Nokes, 1988), but convection can re-entrain particles from the crests of sediment dunes that may accumulate during crystallization (Solomatov et al., 1993). Analysis of the critical grain size for entrainment using Eq (1.5) considers the energy balance of a convecting magma ocean and settling crystals in the liquid. Solomatov et al. (1993) consider the effects of viscous and buoyancy stresses on particles in sediment dunes on the magma ocean floor (their Eq (5)). This model recovers critical grain sizes that differ from predictions of Eq (1.5) by only a factor of two, arguably a negligible difference considering the uncertainties in the model assumptions and input parameters. Tank experiments by Lavorel and Le Bars (2009) supported the scaling relation proposed by Solomatov et al. (1993), while numerical simulations by Patočka et al. (2020) that do not consider re-entrainment suggested that particle settling is more efficient. Clearly, more work on this important topic is needed. Here we proceed with our analysis based on Eq (1.5).

The viscosity of the system will change as crystallization progresses; therefore, we must consider how the viscosity may evolve as a slurry forms during solidification. We model the effective viscosities of crystal-liquid suspensions using an effective viscosity equation (Einstein, 1906; Roscoe, 1952) to predict the viscosity of the system at various crystallinities, from 2.5–50%:

$$\eta_{eff} = \eta^0 (1 - j\phi)^{-2.5}, \tag{1.6}$$

where η^0 is the viscosity of the pure liquid in Pa·s, j is a geometric constant (for random close crystal packing, 1.61), and ϕ is the crystal fraction.

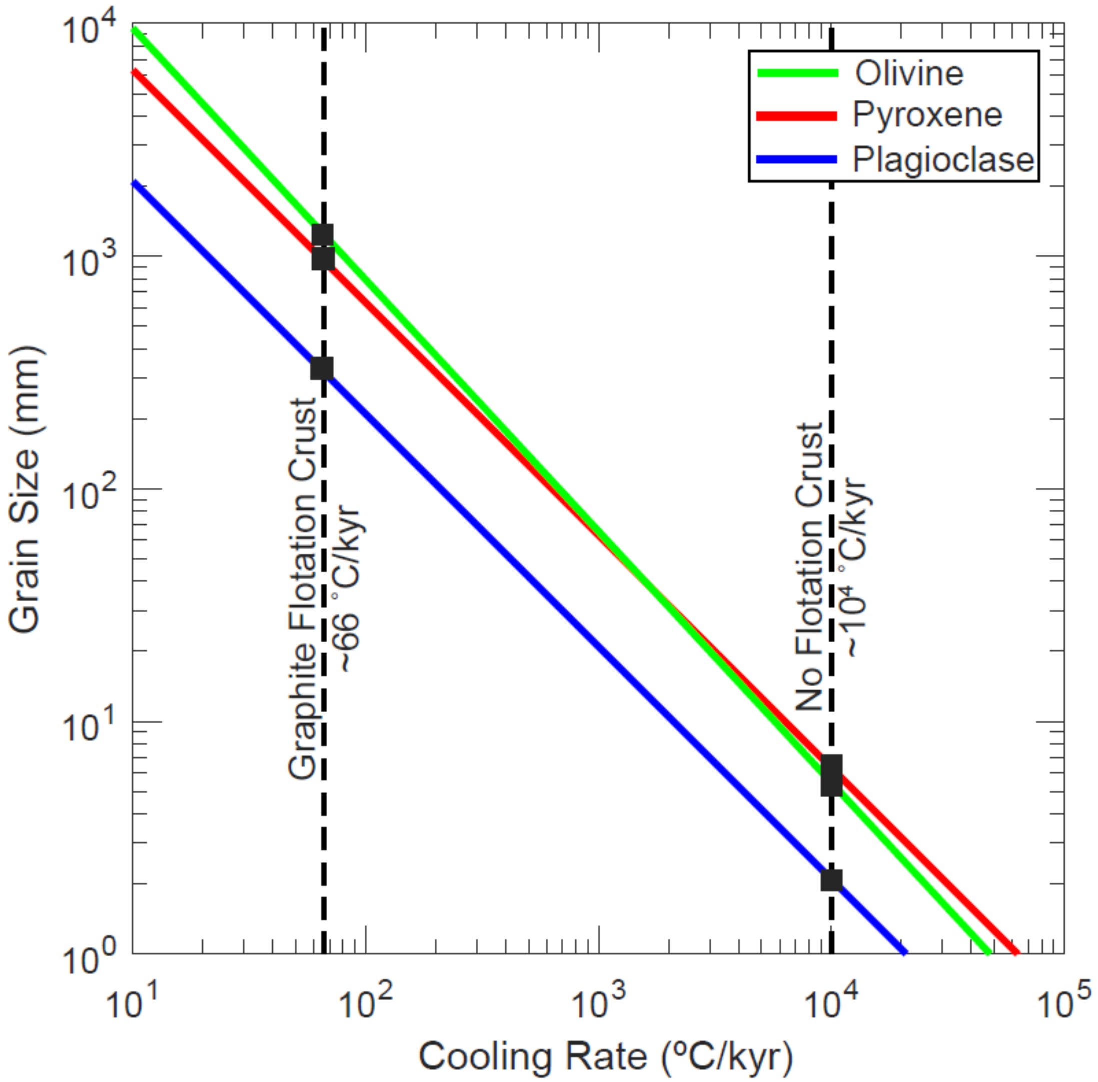

Figure 1.6. Grain size and cooling rate. Grain sizes of olivine (green), pyroxene (red), and plagioclase (blue) predicted for cooling rates relevant to solidification of a late stage (80% crystallized) Mercurian magma ocean calculated using experimentally parameterized grain growth laws (Walker et al., 1976; Walker et al., 1978; Karato, 1989). Dashed lines indicate the predicted cooling rates and grain sizes for Mercury's magma ocean in scenarios with and without a flotation crust, assuming crystals grow continuously in the convecting liquid. By assuming perfectly efficient crystal entrainment, the dashed lines indicate upper bounds on possible grain sizes. Black squares indicate these maximum grain sizes for each mineral at the given cooling rate.

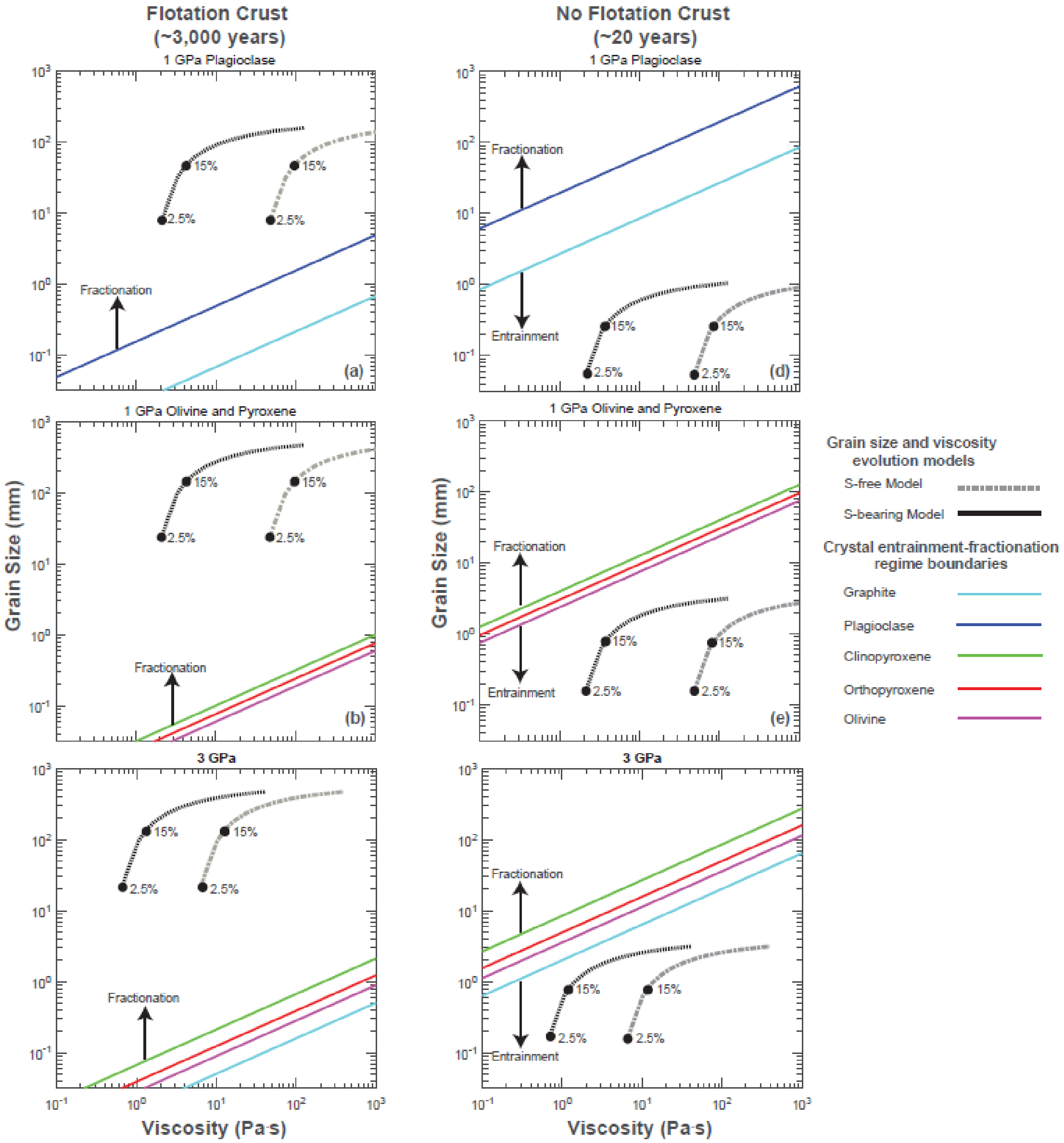

Figure 1.7. Crystal behavior in an evolving magma ocean. Scenarios for solidification of an 80% crystallized Mercurian magma ocean (a-c) with a graphite flotation crust, and (d-f) without a flotation crust. Colored lines show entrainment-fractionation regime boundaries for clinopyroxene, orthopyroxene, olivine, plagioclase, and graphite calculated using the model of Solomatov (2015) (Eq (41) in Solomatov, 2015; Eq (1.5) here), which assumes that the magma ocean's capacity to retain crystals in suspension depends on a balance between the potential for viscous dissipation by crystal settling, and work conducted by the convecting magma ocean liquid on entrained crystals. Dash-dotted lines show viscosities predicted for liquid-crystal suspensions with crystal fractions ranging from 2.5–50% (Einstein, 1906; Roscoe, 1952), with 2.5% and 15% crystal fractions indicated. These paths show the possible evolution of magma ocean viscosities starting from crystal-free melts, constrained by the S-free and S-bearing models at temperatures of 1300°C (1 GPa) and 1400°C (3 GPa). In (a; d) plagioclase and graphite in the magma ocean are shown at 1 GPa. Above the regime boundary for graphite, the mineral will

fractionate by floating, and below the lines it will remain suspended in the liquid. Plagioclase may be neutrally to negatively buoyant in this scenario (Figure 8a) so it will likely either remain suspended or fractionate by sinking. In (b; e) negatively buoyant minerals in the magma ocean are shown at 1 GPa. Above the respective regime boundaries, the minerals will fractionate by sinking, and below the boundaries they will stay suspended in the liquid. In (c; f), crystallization in scenarios with and without a flotation crust are explored at 3 GPa. These models suggest that crystal fractionation will be efficient in scenarios with a flotation crust, and that crystals may be entrained in the convecting magma ocean liquid in scenarios without a flotation crust (see section 1.4.4). Note that in (c; f) the S-free and S-bearing models are shown but produce similar viscosities at higher pressures which results in overlap.

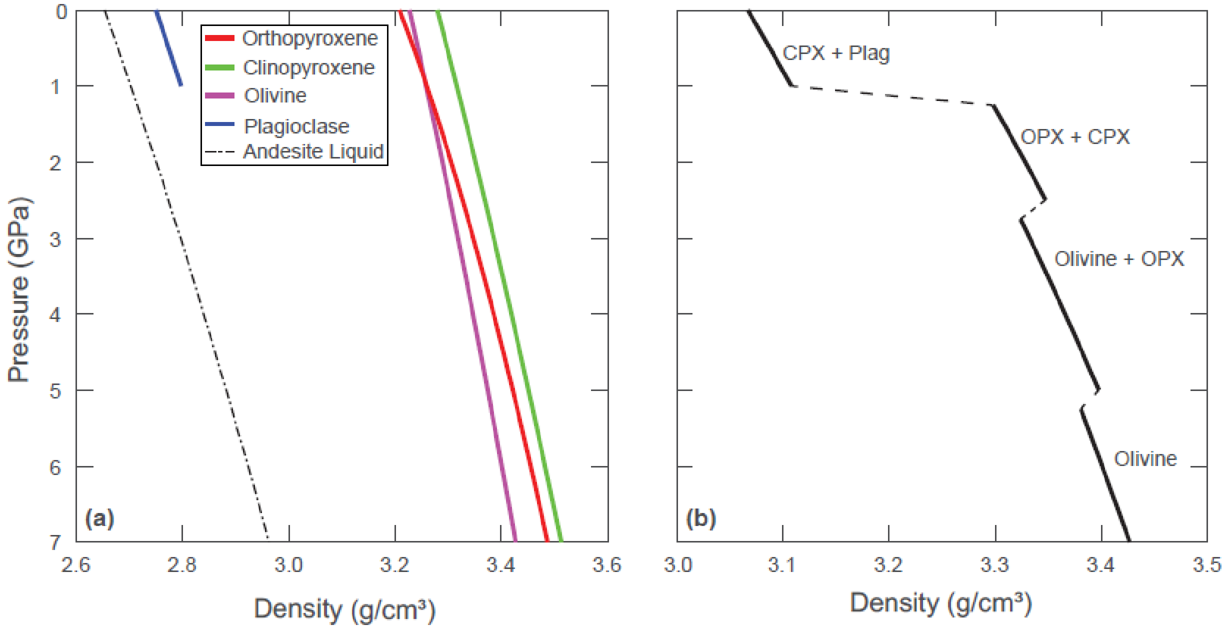

Figure 1.8. Density profiles of silicate minerals. Calculated profile of (a) individual mineral and liquid densities in Mercury's interior (Eq (1.7)); and (b) potential cumulate layers produced in a scenario for magma ocean solidification with a flotation crust. Note the inverted density structure, demonstrating potential for forming gravitational instabilities. Plagioclase is plotted to the higher extent of its possible pressure stability. Bulk modulus (k_T), pressure derivative of the bulk modulus (k'_T), and initial molar volume (V_0) values for the density calculations of enstatite, diopside, forsterite, albite, and the andesitic liquid were obtained from the following sources: Hugh-Jones and Angel, 1997; Jackson et al., 1999; Elkins-Tanton et al., 2003; Schutt and Lesher, 2006; Tenner et al., 2007; Tajčmanová et al., 2015; and Ueki and Iwamori, 2016. Modal proportions assumed for each layer in (b) are the following: harzburgite, 50% forsterite and 50% enstatite; pyroxenite, 50% enstatite and 50% diopside; gabbro, 60% diopside and 40% albite.

If crystal entrainment is assumed to be perfectly efficient in the convecting magma ocean liquid, we can calculate grain sizes throughout the solidification process using the grain growth laws described in Section 1.4.3. Assuming unimpeded crystal entrainment, the effects of viscosity and grain size evolution for crystal entrainment are shown in Figure 7 (dotted and dash-dotted lines). The left column represents scenarios with no flotation crust and the right column represents scenarios with a graphite flotation crust. Colored lines represent the entrainment-fractionation boundaries for mantle relevant igneous minerals (orthopyroxene, clinopyroxene, olivine, plagioclase, and graphite). Dotted and dash-dotted lines show viscosities predicted for liquid-crystal suspensions with crystal fractions ranging from 2.5–50%, with 2.5% and 15% indicated on the crystallization paths. At high crystallinities, collisions amongst grains lead to clumping, which would make crystal entrainment inefficient (Elkins-Tanton, 2012; Suckale et al., 2012). In the models presented in Figure 1.7 (a-f), three crystallization regimes are present: entrainment, fractionation, and intermediate cases.

1.4.4.1. *Entrainment*

This region of “entrainment’ is indicated in Figure 1.7 and happens below the critical grain size boundary for all minerals. In this case of crystal entrainment, all grains will be small enough with respect to the magma viscosity and convection vigor to be entrained in the liquid. In scenarios where physical properties favor crystal entrainment, we may anticipate the formation of a compositionally homogeneous Mercurian mantle. In this instance the cumulate phases would be mixed together in the convecting liquid instead of settling into a cumulate pile or floating to form a crust.

1.4.4.2. *Fractionation*

Fractionation is indicated throughout Figure 1.7 according to the critical grain size boundaries. Positively buoyant minerals (graphite) are less dense than the liquid and thus will float once the grain sizes are above the critical grain size boundary. Plagioclase in this system is slightly negatively buoyant, so it is expected to sink in cases that favor fractionation. More negatively buoyant minerals (orthopyroxene, clinopyroxene, and olivine) have densities much greater than the liquid (Figure 1.8a) so once crystal sizes are above the critical grain size regime boundary for each mineral, they will fractionate by sinking.

1.4.4.3. *Mixed Regime*

The region between fractionation and entrainment regime boundaries must also be considered. For example, in Figure 1.7a, above the plagioclase boundary, both plagioclase and graphite will fractionate from the liquid. Below the graphite boundary, both plagioclase and graphite will be entrained. Between the plagioclase and graphite regime boundaries, there is the apparent potential for graphite to fractionate and plagioclase to remain entrained. The efficiency of crystal fractionation under these intermediate conditions depends on the crystal load in the convecting slurry. Suspensions with solid phase proportions of more than ~10% experience clumping which significantly reduces the efficiency of fractionation, promoting formation of clots of multiple phases that sink or float depending on their bulk density (Suckale et al., 2012). Viscous dissipation associated with crystal fractionation produces heat, which may dampen convection of the magma ocean liquid, promoting crystal settling and perhaps eliminating the possibility of these mixed regime scenarios.

1.4.5. *Implications of a Flotation Crust, or Lack Thereof, for the Mercurian Mantle*

Here we evaluate the crystallization of Mercury's magma ocean in two scenarios: without a flotation crust and with a graphite flotation crust. In a scenario without a flotation crust (Figures 1.7d-f), taking the regime boundaries and grain growth calculations at face value, at higher pressure (i.e., deeper in the magma ocean; Figure 1.7f) crystallization will proceed in the entrainment regime. With continued solidification, the magma ocean evolves toward fractionation, but it is unlikely that the flotation-entrainment regime boundaries will be crossed as our grain growth models provide upper bounds on grain size (see Section 1.4.3). As solidification proceeds and the magma ocean shallows (Figure 1.7d-f), plagioclase becomes stable. At the anticipated grain sizes crystallization continues in the entrainment regime and evolves toward fractionation. Again, we do not anticipate crossing the boundary into the fractionating regime as the grain growth models provide upper bounds on reasonable grain sizes. We note that in scenarios where the liquid approaches crystal loads of ~10%, crystal clots comprising mixtures of multiple phases are expected to form and sink (Suckale et al., 2012). We conclude that in a scenario without a flotation crust, Mercury's cumulate mantle would most likely be a compositionally homogeneous lherzolite, with some mineralogical stratification possible depending on the cumulate sequence, convection vigor, and grain growth rates (Figure 1.9a).

In a scenario with a graphite flotation crust (Figure 1.7a-c), because both the olivine and pyroxene and plagioclase crystallization paths lie entirely in the fractionation regime at all depths and temperatures; the solidification is fractional, with the exception of early plagioclase growth at low pressures (Figure 1.7a). In this scenario, we would expect the mantle to be compositionally heterogeneous and stratified according to the magma ocean's crystallization sequence (Figure 1.9b). Fractional crystallization is anticipated because the amount of time for crystallization is relatively long, and convection in the system is less vigorous.

The preceding analysis suggests that if Mercury did not have a flotation crust, most crystals would remain entrained in the liquid, ultimately forming a homogeneous lherzolitic mantle. Distinct magmas would be produced from melting a lherzolitic source to different extents, for example, before and after exhaustion of clinopyroxene from the source assemblage (Charlier et al., 2013; Namur et al., 2016b), or at different pressures (Boujibar et al., 2015). If Mercury's magma ocean produced a flotation crust, the resulting mantle would be compositionally stratified (Figure 1.9b). Although experimental work is needed to constrain phase equilibria in possible Mercurian magma ocean-relevant systems, we may reasonably assume the following stratigraphy (from bottom to top) for a heterogeneous cumulate mantle: dunite (olivine), harzburgite (olivine + orthopyroxene), pyroxenite (orthopyroxene + clinopyroxene), gabbro (clinopyroxene + plagioclase), and finally the graphite flotation crust. Sulfides may or may not be present in the cumulate mantle as well, but their stability and compositions are largely unknown (e.g., Boukaré et al., 2019). This mineralogy is in general agreement with studies investigating Mercury's interior and volcanic source compositions (e.g., Stockstill-Cahill et al., 2012; Vander Kaaden and McCubbin, 2016), but as elaborated on below, the mineral stratification is inconsistent with volcanic source compositions which require pyroxene-bearing Mg-rich sources (forsteritic olivine, Mg-rich pyroxene). To achieve appropriate assemblages requires additional physical processing.

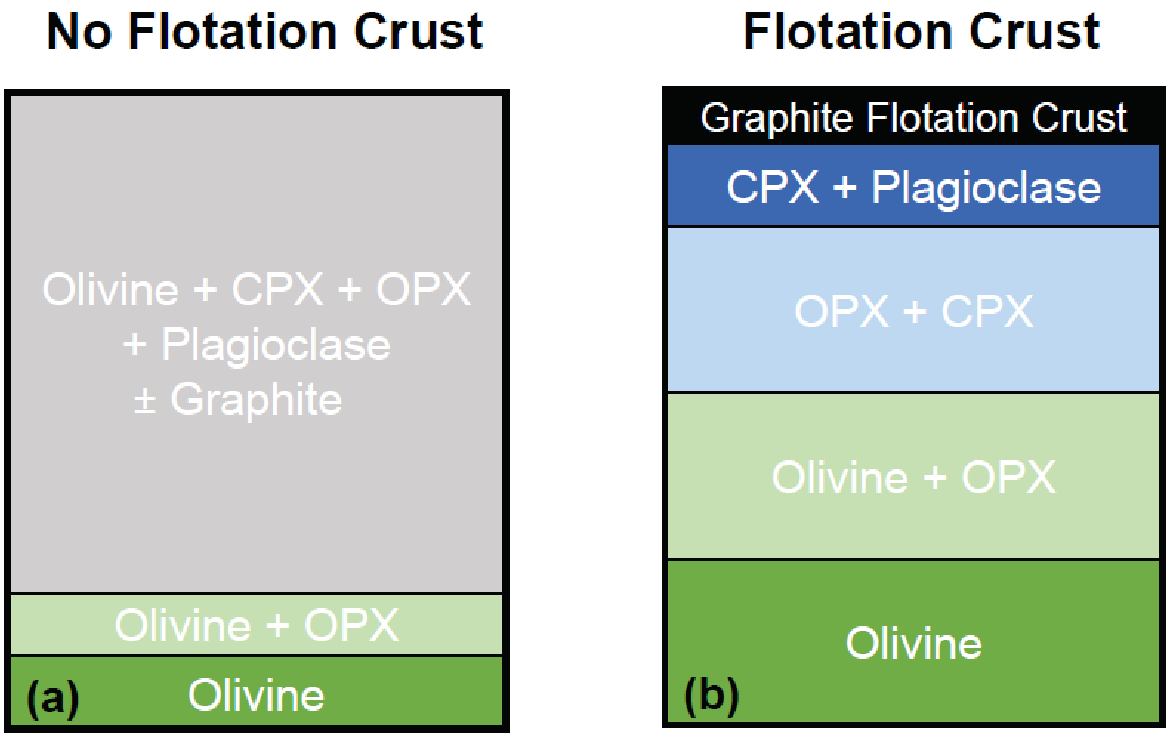

Figure 1.9. Proposed Mercurian mantle structures. Hypothetical cumulate piles produced in end-member crystallization scenarios for Mercurian magma oceans (a) without and (b) with a flotation crust. Accessory sulfides could have been present at some depth in Mercury's cumulate mantle as well, but as their compositions and stabilities are unknown, here we focus on silicates.

1.4.6. *Formation of Downwelling Rayleigh-Taylor Instabilities in Mercury's Mantle*

If the Mercurian mantle was heterogeneous (a seemingly unavoidable scenario if the magma ocean had a flotation crust) the mantle source for the IcP-HCT could not have been exclusively a direct product of magma ocean solidification. The composition of the IcP-HCT suggests a clinopyroxene-bearing lherzolite source composition, while the BP is believed to be sourced from a clinopyroxene-free (or clinopyroxene-poor) harzburgite composition. These source compositions are inferred from the Ca/Si and Mg/Si ratios of the surface volcanics, where the BP has lower Ca/Si and Mg/Si ratios and the IcP-HCT have high Ca/Si and Mg/Si ratios (Weider et al., 2012; Peplowski et al., 2014; Weider et al., 2015; Namur et al., 2016b; Lawrence et al., 2017; Nittler et al., 2019). The proposed mantle stratigraphy for Mercury in a flotation crust scenario (Figure 1.9b) does not have a lherzolitic (orthopyroxene + clinopyroxene + olivine) layer which would melt to produce the IcP-HCT. To produce an apparent lherzolitic source, some mechanism is required to mix melts derived from multiple layers in the cumulate pile, or to physically mix the cumulate layers to make a lherzolitic source. Convective mixing of a stratified mantle may be produced by thermally driven convection, or a process known as cumulate mantle overturn, where Rayleigh-Taylor instabilities composed of relatively dense, late magma ocean cumulates sink into less dense, underlying layers in the cumulate pile (e.g., Hess and Parmentier, 1995). Cumulate overturn can only occur if an overlying layer in the cumulate pile is denser than the underlying layer. In this case, the gravitationally unstable overlying layer would sink into the layers beneath, mixing late and early cumulates to form the lherzolitic mantle source.

A Mercurian cumulate pile composed of (from bottom to top) layered olivine, olivine and orthopyroxene, orthopyroxene and clinopyroxene (Figures 1.9b), would have inverted, gravitationally unstable density structures because in Fe-poor systems, pyroxene (especially high-Ca pyroxene) is denser than olivine. Note here we neglect consideration of sulfide-bearing layers in the cumulate pile (Boukaré et al., 2019), which should also be considered when sufficient experimental data exists to evaluate their effect on the density structure and mechanical properties of the cumulate pile.

To demonstrate the potential for cumulate mantle overturn on Mercury, we calculated the density of each layer in the Mercurian cumulate pile as a function of pressure and temperature assuming the stratigraphy presented in Figure 1.9b. The densities of each layer were determined using a Birch-Murnaghan equation of state to calculate the molar volume of each phase as a function of pressure and temperature:

$$P = \frac{3}{2}k_T\left[\left(\frac{V_0}{V_F}\right)^{\frac{7}{3}} - \left(\frac{V_0}{V_F}\right)^{\frac{5}{3}}\right]\left\{1-\left(\frac{3}{4}\right)(4-k'_T)\left[\left(\frac{V_0}{V_F}\right)^{\frac{2}{3}}-1\right]\right\}, \tag{1.7}$$

where P is the pressure in Pa, k_T is the isothermal bulk modulus of a mineral, k'_T is the pressure derivative of k_T, V_0 is the initial molar volume of a mineral, and V_F is the molar volume at pressure. To scale the bulk modulus for temperature variation with depth in Mercury's mantle, the following expression for k_T is used:

$$k_T = k_{T_{298}} + \left(\frac{\partial k_T}{\partial T}\right)_P (T-298)\ , \tag{1.8}$$

which considers the variation of the bulk modulus as a function of temperature (T) from a reference value, $k_{T_{298}}$, and the isobaric bulk modulus at constant pressure. When calculating densities, we assumed adiabatic P-T variation in Mercury's cumulate mantle with a slope of 0.1°C/km and a reference (potential) temperature of 1300°C. Steeper thermal gradients exaggerate the anticipated density contrast for the cumulate mantle. Using Eq (1.8) and (1.9), we solved iteratively for *V* for each individual mineral over a range of mantle relevant temperature (~1300–1400°C) and pressure conditions (0–7 GPa). Using the molar volume values, density was solved by dividing the molar mass of a mineral by the molar volume values acquired from Eq (1.8). The results from these density calculations are shown in Figure 1.8 which plots the density profiles of individual phases (a) and the respective cumulate layers (b).

In Figure 1.8b, the pyroxenite (clinopyroxene and orthopyroxene) and harzburgite (orthopyroxene and olivine) layers have a higher density than their respective underlying layers at ∼2.5 and 5 GPa. The invert- ed stratigraphy presented in Figure 1.8b suggests that at least localized density-driven cumulate mixing is possible among these layers by formation of dense downwelling Rayleigh-Taylor instabilities. Gravitational instabilities that form at localized density inversions may persist with depth as they sink, as suggested by the pure phase densities (Figure 1.8a); alternatively, mixing produced by sinking at the lithological boundaries could neutralize the density inversions. Instability formation also depends on the thermal conditions in the interior (e.g., Tosi et al., 2013), and the potential presence of other minerals (e.g., sulfides; Boukaré et al., 2019). If the pyroxenite layer was to sink (overturn) and mix with the underlying harzburgite, or sink more deeply into the dunite, it would create a lherzolitic composition (clinopyroxene + orthopyroxene + olivine). This gravitational mixing would produce an appropriate lherzolitic source for formation of the IcP-HCT; further analysis should be conducted to understand the potential for and implications of cumulate overturn in Mercury's mantle in future studies.

1.4.6.1. *Crustal Petrogenesis*

Finally, we consider what the present-day surface of Mercury implies about evolution of Mercury’s mantle in the context our predictions for magma ocean solidification. The younger BP are compositionally distinct from the older IcP-HCT, having come from a harzburgitic source while the IcP-HCT has a lherzolitic source (Charlier et al., 2013; Namur et al., 2016b; Nittler et al., 2019). We may assume that the mantle sources and/or the volcanic mechanisms which formed these regions were different. As previously discussed, if the mantle was heterogeneous as it would be in scenarios with a flotation crust on Mercury’s magma ocean, then a lherzolitic composition could not be a direct product of magma ocean solidification. Our cumulate density analysis suggests that density-driven overturn of late magma ocean cumulates is possible which would create a lherzolitic source by mixing distinct layers in the cumulate pile. Alternatively, a lherzolitic source could have been produced by thermally driven mantle convection, or an apparent lherzolitic source could be produced by mixing of magmas from distinct layers in the cumulate pile. If the mantle was more homogeneous (as in the scenario without a flotation crust), high extents of partial melting of an initially lherzolitic source (beyond clinopyroxene exhaustion) could potentially have formed the BP (Charlier et al., 2013); however, it is unclear how depletion in both Ca and Mg in a mantle source could be achieved through increasing extents of partial melting.

1.5. Conclusions

We experimentally conducted falling sphere viscometry experiments using the Paris-Edinburgh apparatus to constrain the viscosity of S-free and S-bearing Mercurian magma ocean analogue compositions. The S-bearing experiments have lower viscosities. Both compositions exhibit inverse viscosity dependence with pressure, but the S-free composition shows more sensitivity to variations in pressure. Using the experimental observations, we parameterized pressure and temperature sensitive predictive models for the viscosity of our Mercurian magma ocean liquids. These late-stage Mercurian magma ocean analogue liquid viscosities are similar to andesite and alkali basalt for the sulfur-free and sulfur-bearing melts, respectively.

Applying the viscosity models in a crystal entrainment-fractionation analysis, we make predictions for crystallization regime (batch vs. fractional) in Mercury's convecting magma ocean in scenarios with and without a flotation crust. Models without a flotation crust produce a homogeneous lherzolitic mantle due to the crystallization process being in the entrainment regime. Models with a flotation crust are in the fractionation regime and produce a mineralogically stratified Mercurian mantle without a lherzolitic layer in the cumulate pile.

Mercury's surface has multiple geologic terranes, one of which, Borealis Planitia, is inferred to have a harzburgite source composition, while regions like the Intercratered Plains-Heavily Cratered Terrane are believed to have come from a lherzolitic mantle source. In scenarios where Mercury had a flotation crust, formation of a lherzolitic mantle source may require mantle mixing of late and early magma ocean cumulates by thermally driven convection or density-driven sinking of late magma ocean cumulates into underlying layers in the cumulate pile.

Depending on the crystallization sequence, our analysis suggests that overturn of Mercury's mantle may have been possible in scenarios with a flotation crust. On the other hand, if the magma ocean cooled without a flotation crust, the mantle would have a dominantly homogeneous lherzolitic mineralogy due to crystal entrainment being the primary crystallization mode during cooling. Confirming the presence or absence of a flotation crust on Mercury, establishing its thickness and composition, and placing experimental constraints on the crystallization sequence of Mercury's magma ocean are needed to further refine models for the dynamic evolution of Mercury's mantle.

1.6. Acknowledgments

This work benefited from discussions with Tim Grove, Molly McCanta, and Francis McCubbin. We thank Ralph Milliken for assistance with FTIR measurements, Nathan Miller for LA-ICP-MS measurements, and Allan Patchen for assistance with EPMA analyses. This research was supported by the UT-ORNL Science Alliance and NASA grant 80NSSC18K0249 to ND. Experiments were performed at HPCAT (Sector 16), Advanced Photon Source (APS), Argonne National Laboratory. HPCAT operations are supported by DOE-NNSA's Office of Experimental Sciences. The Advanced Photon Source is a U.S. Department of Energy (DOE) Office of Science User Facility operated for the DOE Office of Science by Argonne National Laboratory under Contract No. DE-AC02-06CH11357. Falling-sphere viscometry experiment image stacks used to calculate the viscosities for each experiment can be found in Zenodo repository (Mouser et al., 2021).

References

Abe, Y. (1997). Thermal and chemical evolution of the terrestrial magma ocean. *Physics of the Earth and Planetary Interiors, 100(1-4),* 27-39. https://doi.org/10.1016/S0031-9201(96)03229-3

Anzellini, S., Dewaele, A., Occelli, F., Loubeyre, P., & Mezouar, M. (2014). Equation of state of rhenium and application for ultra high pressure calibration. *Journal of Applied Physics, 115*, 043511. https://doi.org/10.1063/1.4863300

Anzures, B. A., Parman, S. W., & Milliken, R. E., Namur, O., Cartier, C., & Wang, S. (2020). Effect of Sulfur Speciation on Chemical and Physical Properties of Very Reduced Mercurian Melts. *Geochimica et Cosmochimica Acta*, *286*, 1-18. https://doi.org/10.1016/j.gca.2020.07.024

Benz, W., Anic, A., Horner, J., & Whitby, J. A. (2007). The Origin of Mercury. *Space Science Reviews, 132 (2-4),* 189-202. https://doi.org/10.1007/s11214-007-9284-1

Benz, W., Slattery, W. L., & Cameron, G. W. (1988). Collisional stripping of Mercury’s mantle. *Icarus*, *74(3),* 516-528. https://doi.org/10.1016/0019-1035(88)90118-2

Bottinga, Y., & Weill, D. F. (1972). The Viscosity of Magmatic Silicate Liquids: A Model for Calculation. *American Journal of Science*, *272(5),* 438-475. https://doi.org/10.2475/ajs.272.5.438

Boujibar, A., Habermann, M., Righter, K., Ross, D. K., Pando, K., Righter, M., Chidester, B. A., & Danielson, L. R. (2019). U, Th, and K partitioning between metal, silicate, and sulfide and implications for Mercury’s structure, volatile content, and radioactive heat production. *American Mineralogist*, *104*, 1221-1237. https://doi.org/10.2138/am-2019-7000

Boujibar, A., Righter, K., Pando, K., & Danielson, L. (2015). The origin of the compositional diversity of Mercury’s surface constrained from experimental melting of enstatite chondrites. *European Planetary Science Congress 2015, 10*, EPSC2015-517.

Boukaré, C.-E., Parman, S. W., Parmentier, E. M., & Anzures, B. A. (2019). Production and Preservation of Sulfide Layering in Mercury’s Mantle. *Journal of Geophysical Research: Planets*, *124*, 3354-3372. https://doi.org/10.1029/2019JE005942

Boukaré, C.-E., Parmentier, E. M., & Parman, S. W. (2018). Timing of mantle overturn during magma ocean solidification. *Earth and Planetary Science Letters, 491*, 215-225, https://doi.org/10.1016/j.epsl.2018.03.037

Brown, S. M., & Elkins-Tanton L. T. (2009). Compositions of Mercury’s earliest crust from magma ocean models. *Earth and Planetary Science Letters, 286(3-4),* 446-455. https://doi.org/10.1016/j.epsl.2009.07.010

Browning, G. J., Bryant, G. W., Hurst, H. J., Lucas, J. A., & Wall, T. F. (2003). An Empirical Method for the Prediction of Coal Ash Slag Viscosity. *Energy & Fuels, 17*, 731-737. https://doi.org/10.1021/ef020165o

Byrne, P. K., Ostrach, L. R., Fassett, C. I., Chapman, C. R., Denevi, B. W., Evans, A. J., Klimczak, C., Banks, M. E., Head, J. W., & Solomon, S. C. (2016). Widespread effusive volcanism on Mercury likely ended by about 3.5 Ga. *Geophysical Research Letters, 43(14)*, 7408-7416. https://doi.org/10.1002/2016GL069412

Cameron, A. G. W. (1985). The partial volatilization of Mercury. *Icarus, 64(2),* 285-294. https://doi.org/10.1016/0019-1035(85)90091-0

Cameron, A. G. W., Fegley Jr., B., Benz, W. & Slattery, W. E. (1988). The Strange Density of Mercury: Theoretical Considerations. In M.S. Matthews, C. Chapman, F. Vilas (Eds.), *Mercury.* (pp. 692-708) University of Arizona Press, Tuscon.

Charlier, B., Grove, T. L., & Zuber, M. T. (2013). Phase equilibria of ultramafic compositions on Mercury and the origin of the compositional dichotomy. *Earth and Planetary Science Letters, 363,* 50-60. https://doi.org/10.1016/j.epsl.2012.12.021

Cochain, B., Sanloup, C., Leroy, C., & Kono, Y. (2017) Viscosity of mafic magmas at high pressures. *Geophysical Research Letters, 44,* 818-826. https://doi.org/10.1002/2016GL071600

Denevi, B. W., Robinson, M. S., Solomon, S. C., Murchie, S. L., Blewett, D. T., Domingue, D. L., McCoy, T. J., Ernst, C. M., Head, J. W., Watters, T. R., & Chabot, N. L. (2009). the Evolution of Mercury's Crust: A Global Perspective from MESSENGER. *Science, 324,* 613-617. https://doi.org/10.1126/science.1172226

Dingwell, D. B., Courtial, P., Giordano, D., & Nichols, A. R. L. (2004). Viscosity of peridotite liquid. *Earth and Planetary Science Letters, 226,* 127-138. https://doi.org/10.1016/j.epsl.2004.07.017

Dygert, N., Lin, J., Marshall, E. W., Kono, Y., & Gardner, J. E. (2017). A low viscosity lunar magma ocean forms a stratified anorthitic flotation crust with mafic poor and rich units. *Geophysical Research Letters, 44(22),* 11282-11291. https://doi.org/10.1002/2017GL075703

Einstein, A. (1906). Eine neue Bestimmung der Moleküldimensionen. (Doctoral dissertation). Retrieved from ETH Zurich Research Collection. (https://doi.org/10.3929/ethz-a-000565688). Zurich, Switzerland: University of Zurich.

Elkins-Tanton, L. T. (2012). Magma Oceans in the Inner Solar System. *Annual Reviews of Earth and Planetary Sciences, 40,* 113-139. https://doi.org/10.1146/annurev-earth-042711-105503

Elkins-Tanton, L. T., Burgess, S., & Yin, Q. (2011). The lunar magma ocean: Reconciling the solidification process with lunar petrology and geochronology. *Earth and Planetary Science Letters, 304(3-4),* 326-336. https://doi.org/10.1016/j.epsl.2011.02.004

Elkins-Tanton, L. T., Parmentier, E. M., & Hess, P. C. (2003). Magma ocean fractional crystallization and cumulate overturn in terrestrial planets: Implications for Mars. *Meteoritics & Planetary Science, 38(12),* 1753-1771. https://doi.org/10.1111/j.1945-5100.2003.tb00013.x

Evans, L. G., Peplowski, P. N., Rhodes, E. A., Lawrence, D. J., McCoy, T. J., Nittler, L. R., Solomon, S. C., Sprague, A. L., Stockstill-Cahill, K. R., Starr, R. D., Weider, S. Z., Boynton, W. V., Hamara, D. K., & Goldsten, J. O. (2012). Major-element abundances on the surface of Mercury: Results from the MESSENGER Gamma-Ray Spectrometer. *Journal of Geophysical Research, 117,* E00L07. https://doi.org/10.1029/2012JE004178

Faxén, H. (1922). Der Widerstand gegen die Bewegung einer starren Kugel in einer zähen Flüssigkeit, die zwischen zwei parallelen ebenen Wänden eingeschlossen ist. *Annalen der Physik, 373(10),* 89-119. https://doi.org/10.1002/andp.19223731003

Fegley Jr., B., & Cameron, A. G. W. (1987). A vaporization model for iron/silicate fractionation in the Mercury protoplanet. *Earth and Planetary Science Letters, 82(3-4),* 207-222. https://doi.org/10.1016/0012-821X(87)90196-8

Flasar, M., & Birch, F. (1973). Energetics of Core Formation: A Correction. *Journal of Geophysical Research, 78(26),* 6101-6103. https://doi.org/10.1029/JB078i026p06101

Fogel, R. (1997). On the significance of diopside and oldhamite in enstatite chondrites and aubrites. *Meteoritics and Planetary Science, 32(4),* 577-591. https://doi.org/10.1111/j.1945-5100.1997.tb01302.x

Giordano, D., & Dingwell, D. B. (2003). Viscosity of hydrous Etna basalt: implications for Plinian-style basaltic eruptions. *Bulletin of Volcanology, 65,* 8-14. https://doi.org/10.1007/s00445-002-0233-2

Giordano, D., Russell, J. K., & Dingwell, D. B. (2008). Viscosity of magmatic liquids: A model. *Earth and Planetary Science Letters, 271*, 123-134. https://doi.org/10.1016/j.epsl.2008.03.038

Hakim, K., van den Berg, A., Vazan, A., Höning, D., van Westrenen, W., & Dominik, C. (2019). Thermal evolution of rocky exoplanets with a graphite outer shell. *Astronomy & Astrophysics, 630,* A152. https://doi.org/10.1051/0004-6361/201935714

Hauck II, S. A., Dombard, A. J., Phillips, R. J., & Solomon, S. C. (2004). Internal and tectonic evolution of Mercury. *Earth and Planetary Science Letters, 222*, 713-728. https://doi.org/10.1016/j.epsl.2004.03.037

Head, J. W., Chapman, C. R., Strom, R. G., Fassett, C. I., Denevi, B. W., Blewett, D. T., Ernst, C. M., Watters, T. R., Solomon, S. C., Murchie, S. L., Prockter, L. M., Chabot, N. L., Gillis-Davis, J. J., Whitten, J. L., Goudge, T. A., Baker, D. M. H., Hurwitz, D. M., Ostrach, L. R., Xiao, Z., Merline, W. J., Berber, L., Dickson, J. L., Oberst, J., Byrne, P. K., Klimczak, C., & Nittler, L. R. (2011). Flood Volcanism in the Northern High Latitudes of Mercury Revealed by MESSENGER. *Science, 333,* 1853-1855. https://doi.org/10.1126/science.1211997

Hess, P. C. & Parmentier, E. M. (1995). A model for the thermal and chemical evolution of the Moon's interior: implications for the onset of mare volcanism. *Earth and Planetary Science Letters, 134(3-4),* 501-514. https://doi.org/10.1016/0012-821X(95)00138-3

Hofmeister, A. M., Dong, J., & Branlund, J. M. (2014). Thermal diffusivity of electrical insulators at high temperatures: Evidence for diffusion of bulk phonon-polaritons at infrared frequencies augmenting phonon heat conduction. *Journal of Applied Physics, 115,* 163517. https://doi.org/10.1063/1.4873295

Hostetler, C. J., & Drake, M. J. (1980). On the early global melting of the terrestrial planets. *Proceedings of the Lunar and Planetary Science Conference, 11,* 1915-1929.

Hugh-Jones, D. A., & Angel, R. J. (1997). Effect of Ca^{2+} and Fe^{2+} on the equation of state of $MgSiO_3$ orthopyroxene. *Journal of Geophysical Research, 102(B6),* 12,333-12340. https://doi.org/10.1029/96JB03485

Hui, H., & Zhang, Y. (2007). Toward a general viscosity equation for natural anhydrous and hydrous silicate melts. *Geochimica et Cosmochimica Acta, 17,* 403-416. https://doi.org/10.1016/j.gca.2006.09.003

Izenberg, N. R., Klima, R. L., Murchie, S. L., Blewett, D. T., Holsclaw, G. M., McClintock, W. E., Malaret, E., Mauceri, C., Vilas, F., Sprague, A. L., Helbert, J., Domingue, D. L., Head III, J. W., Goudge, T. A., Solomon, S. C., Hibbitts, C. A., & Dyar, M. D. (2014). The low-iron, reduced surface of Mercury as seen in spectral reflectance by MESSENGER. *Icarus, 228,* 364-374. https://doi.org/10.1016/j.icarus.2013.10.023

Jackson, J. M., Sinogeikin, S. V., & Bass, J. D. (1999). Elasticity of $MgSiO_3$ orthoenstatite. *American Mineralogist, 84(4),* 677-680. https://doi.org/10.2138/am-1999-0421

Karato, S. (1989). Grain growth kinetics in olivine aggregates. *Tectonophysics, 168(4),* 225-273. https://doi.org/10.1016/0040-1951(89)90221-7

King, P. L., & McLennan, S. M. (2010). Sulfur on Mars. *Elements, 6(2),* 107-112. https://doi.org/10.2113/gselements.6.2.107

Klima, R. L., Denevi, B. W., Ernst, C. M., Murchie, S. L., & Peplowski, P. N. (2018). Global Distribution and Spectral Properties of Low-Reflectance Material on Mercury. *Geophysical Research Letters, 45(7),* 2945-2953. https://doi.org/10.1002/2018GL077544

Kono, Y., Irifune, T., Higo, Y., Inoue, T., & Barnhoorn, A. (2010). P-V-T relation of MgO derived by simultaneous elastic wave velocity and in situ X-ray measurements: A new pressure scale for the mantle transition region. *Physics of the Earth and Planetary Interiors, 183(1-2),* 196–211. https://doi.org/10.1016/j.pepi.2010.03.010

Kono, Y., Park, C., Kenny-Benson, C., Shen, G., & Wang, Y. (2014). Toward comprehensive studies of liquids at high pressures and high temperatures: Combined structure, elastic wave velocity, and viscosity measurements in the Paris–Edinburgh cell. *Physics of the Earth and Planetary Interiors, 228,* 269-280. https://doi.org/10.1016/j.pepi.2013.09.006

Kortenkamp, S. J., Kokubo, E., & Weidenschilling, S. J. (2000). Formation of planetary embryos. In R. M. Canup, K. Righter (Eds.), *Origin of the Earth and Moon*. (pp. 85–100) University of Arizona Press, Tucson.

Kushiro, I. (1976). Changes in Viscosity and Structure of Melt of NaAlSi2O8 Composition at High Pressures. *Journal of Geophysical Research, 81(35),* 6347-6350. https://doi.org/10.1029/JB081i035p06347

Lawrence, D. J., Peplowski, P. N., Beck, A. W., Feldman, W. C., Frank, E. A., McCoy, T. J., Nittler, L. R., & Solomon, S. C. (2017). Compositional terranes on Mercury: Information from fast neutrons. *Icarus, 281,* 32-45. https://doi.org/10.1016/j.icarus.2016.07.018

Lavorel, G. & Le Bars, M. (2009). Sedimentation of particles in a vigorously covecting fluid. *Physical Review, 80,* 046324. https://doi.org/10.1103/PhysRevE.80.046324

Liebske, C., Schmickler, B., Terasaki, H., Poe, B. T., Suzuki, A., Funakoshi, K., Ando, R., & Rubie, D. C. (2005). Viscosity of peridotite liquid up to 13 GPa: Implications for magma ocean viscosities. *Earth and Planetary Science Letters, 240(3-4),* 589-604. https://doi.org/10.1016/j.epsl.2005.10.004

Litasov, K. D., Shatskiy, A., Fei, Y., Suzuki, A., Ohtani, E., & Funakoshi, K. (2010). Pressure-volume-temperature equation of state of tungsten carbide to 32 GPa and 1673 K. *Journal of Applied Physics, 108,* 053513. https://doi.org/10.1063/1.3481667

Lovering, J. F., and Morgan J. W. (1964). Uranium and thorium abundances in stony meteorites: 1. The chondritic meteorites. *Journal of Geophysical Research, 69(10),* 1979-1988. https://doi.org/10.1029/JZ069i010p01979

Malavergne, V., Toplis, M. J., Berthet, S., & Jones, J. (2010). Highly reducing conditions during core formation on Mercury: Implications for internal structure and the origin of a magmatic field. *Icarus, 206(1),* 119-209. https://doi.org/10.1016/j.icarus.2009.09.001

Malin, M. C. (1976). Observations of Intercrater Plains on Mercury. *Geophysical Research Letters, 3(10),* 518-584. https://doi.org/10.1029/GL003i010p00581

Mandeville, C. W., Webster, J. D., Rutherford, M. J., Taylor, B. E., Timbal, A., & Faure, K. (2002). Determination of molar absorptivities for infrared absorption bands of H2O in andesitic glasses. *American Mineralogist, 87,* 813-821.

Marchi, S., Chapman, C. R., Fassett, C. I., Head, J. W., Bottke, W. F., & Strom, R. G. (2013). Global resurfacing of Mercury 4.0-4.1 billion years ago by heavy bombardment and volcanism. *Nature, 498,* 59-61. https://doi.org/10.1038/nature12280

Martin, D., & Nokes, R. (1988). Crystal settling in a vigorously convecting magma chamber. *Letters to Nature, 332,* 534-536. https://doi.org/10.1038/332534a0

Maude, A. D. (1961). End effects in a falling-sphere viscometer. *British Journal of Applied Physics, 12(6)*, 293. https://doi.org/10.1088/0508-3443/12/6/306

McCoy, T. J., Dickinson, T. L., & Lofgren, G. E. (1999). Partial melting of the Indarch (EH4) meteorite: A textural, chemical, and phase relations view of melting and melt migration. *Meteoritics & Planetary Science, 34*, 735-746. https://doi.org/10.1111/j.1945-5100.1999.tb01386.x

McCubbin, F. M., Riner, M. A., Vander Kaaden, K. E., & Burkemper, L. K. (2012). Is Mercury a volatile-rich planet? *Geophysical Research Letters, 39(9),* 1-5. https://doi.org/10.1029/2012GL051711

Mills, K. C., Yuan, L., & Jones, E. T. (2011). Estimating the physical properties of slags. *The Journal of The Southern African Institute of Mining and Metallurgy, 111,* 649-658.

Minear, J. W. & Fletcher, C. R. (1978). Crystallization of a lunar magma ocean. *Proceedings of the Lunar and Planetary Science Conference 9th*, 263-283.

Mouser, M., Dygert, N., Anzures, B., Grambling, N., Hrubiak, R., Kono, Y., Shen, G., & Parman, S. (2021). Data Annex to Experimental investigation of Mercury's magma ocean viscosity: Implications for the formation of Mercury's cumulate mantle, its subsequent dynamic evolution, and crustal petrogenesis. https://doi.org/10.5281/zenodo.5182174

Murchie, S. L., Klima, R. L., Denevi, B. W., Ernst, C. M., Keller, M. R., Domingue, D. L., Blewett, D. T., Chabot, N. L., Hash, C. D., Malaret, E., Izenberg, N. R., Vilas, F., Nittler, L. R., Gillis-Davis, J. J., Head, J. W., & Solomon, S. C. (2015). Orbital multispectral mapping of Mercury with the MESSENGER Mercury Dual Imaging System: Evidence for the origins of plains units and low-reflectance material. *Icarus, 254,* 287-305. https://doi.org/10.1016/j.icarus.2015.03.027

Namur, O., & Charlier, B. (2016). Silicate mineralogy at the surface of Mercury. *Nature Geoscience, 10,* 9-12. https://doi.org/10.1038/NGEO2860

Namur, O., Charlier, B., Holtz, F., & Cartier, C. (2016a). Sulfur solubility in reduced mafic melts: Implications for the speciation and distribution of sulfur on Mercury. *Earth and Planetary Science Letters, 448,* 102-114. https://doi.org/10.1016/j.epsl.2016.05.024

Namur, O., Collinet, M., Charlier, B., Grove, T., Holtz, F., & McCammon, C. (2016b). Melting processes and mantle sources of lavas on Mercury. *Earth and Planetary Science Letters, 439*, 117-128. https://doi.org/10.1016/j.epsl.2016.01.030

Nittler, L. R., Chabot, N. L., Grove, T. L., & Peplowski, P. N. (2019). The Chemical Composition of Mercury. In S.C. Solomon, L. R. Nittler, B. J. Anderson (Eds.), *Mercury: The view after MESSENGER.* (pp. 30-51) Cambridge Planetary Science.

Nittler, L. R., Starr, R. D., Weider, S. Z., McCoy, T. J., Boynton, W. V., Ebel, D. S., Ernst, C. M., Evans, L. G., Goldsten, J. O., Hamara, D. K., Lawrence, D. J., McNutt Jr., R. L., Schlemm II, C. E., Solomon, S. C., & Sprague, A. L. (2011). The Major-Element Composition of Mercury's Surface from MESSENGER X-ray Spectrometry. *Science, 333*, 1847-1850. https://doi.org/10.1126/science.1211567

Patočka, V., Calzavarini, E., & Tosi, N. (2020). Settling of inertial particles in turbulent Rayleigh-Bernard convection. *Physical Review Fluids, 5*, 114304. https://doi.org/10.1103/PhysRevFluids.5.114304

Peplowski, P. N., Evans, L. G., Stockstill-Cahill, K. R., Lawrence, D. J., Goldsten, J. O., McCoy, T. J., Nittler, L. R., Solomon, S. C., Sprague, A. L., Starr, R. D., & Weider, S. Z. (2014).

Enhanced sodium abundance in Mercury's north polar region revealed by the MESSENGER Gamma-Ray Spectrometer. *Icarus, 228,* 86-95. https://doi.org/10.1016/j.icarus.2013.09.007

Peplowski, P. N., Klima, R. L., Lawrence, D. J., Ernst, C. M., Denevi, B. W., Frank, E. A., Goldsten, J. O., Murchie, S. L., Nittler, L. R., & Solomon, S. C. (2016). Remote sensing evidence for an ancient carbon-bearing crust on Mercury. *Nature Geoscience Letters, 9,* 273-276. https://doi.org/10.1038/NGEO2669

Riner, M. A., Lucey, P. G., Desch, S. J., & McCubbin, F. M. (2009). Nature of opaque components on Mercury: Insights into a Mercurian magma ocean. *Geophysical Research Letters, 36,* L02201. https://doi.org/10.1029/2008GL036128

Riner, M. A., McCubbin, F. M., Lucey, P. G., Taylor, G. J., & Gillis-Davis, J. J. (2010). Mercury surface composition: Integrating petrologic modeling and remote sensing data to place constraints on FeO abundance. *Icarus, 209,* 301-313. https://doi.org/10.1016/j.icarus.2010.05.018

Ringwood, A. E., & Kesson, S. E. (1977). Basaltic magmatism and the bulk composition of the Moon II. Siderophile and Volatile Elements in Moon, Earth and Chondrites: Implications for Lunar Origins. *The Moon, 16,* 425-464. https://doi.org/10.1007/BF00577902

Riboud, P. V., Roux, Y., Lucas, L-D., & Gaye, H. (1981). Improvement of Continuous Casting Powders. *Fachber Huttenprax Metallweiterverarb,19(10),* 859-869.

Romine, W. L. & Whittington, A. G. (2015). A simple model for the viscosity of rhyolites as a function of temperature, pressure and water content. *Geochimica et Cosmochimica Acta, 170,* 281-300. https://doi.org/10.1016/j.gca.2015.08.009

Roscoe, R. (1952). The viscosity of suspensions of rigid spheres. *British Journal of Applied Physics, 3(8),* 267-269. https://doi.org/10.1088/0508-3443/3/8/306

Ruedas, T. (2017). Radioactive heat production of six geologically important nuclides. *Geochemistry, Geophysics, Geosystems, 18,* 3530-3541. https://doi.org/10.1002/2017GC006997

Schreiber, H. D. (1977). Redox states of Ti, Zr, Hf, Cr, and Eu in basaltic magmas: An experimental study. *Proceedings of the Lunar and Planetary Science Conference, 8,* 1785-1807.

Schutt, D. L., & Lesher, C. E. (2006). Effects of melt depletion on the density and seismic velocity of garnet and spinel lherzolite. *Journal of Geophysical Research, 11,* B05401. https://doi.org/10.1029/2003JB002950

Sehlke, A., & Whittington, A. (2016). The viscosity of planetary tholeiitic melts: A configurational entropy model. *Geochimica et Cosmochimica Acta, 191,* 277-299. https://doi.org/10.1016/j.gca.2016.07.027

Shearer, C. K., Hess, P. C., Wieczorek, M. A., Pritchard, M. E., Parmentier, E. M., Borg, L. E., Longhi, J., Elkins-Tanton, L. T., Neal, C. R., Antonenko, I., Canup, R. M., Halliday, A. N., Grove, T. L., & Hager, B.H. (2006). Thermal and Magmatic Evolution of the Moon. *Reviews in Mineralogy and Geochemistry, 60,* 365-518. https://doi.org/10.2138/rmg.2006.60.4

Smith, J. V. (1977). Mineralogy of the planets: a voyage of space and time. *Philosophical Transactions of the Royal Society of London, 286,* 433-437.

Solomatov, V. S., Olsen, P., & Stevenson, D. J. (1993). Entrainment from a bed of particles by thermal convection. *Earth and Planetary Science Letters, 120(3-4),* 387-393. https://doi.org/10.1016/0012-821X(93)90252-5

Solomatov, V. (2015). Magma Oceans and Primordial Mantle Differentiation. *Treatise on Geophysics, 9,* 97-113. https://doi.org/10.1016/B978-044452748-6.00141-3

Solomon, S. C., & Longhi, J. (1997). Magma oceanography: 1. Thermal evolution. *Proceedings of the Lunar Science Conference, 8,* 583-599.

Solomon, S. C., McNutt Jr., R. L., Watters, T. R., Lawerence, D. J., Feldman, W. C., Head, J. W., Krimigis, S. M., Murchie, S. L., Phillips, R. J., Slavin, J. A., & Zuber, M. T. (2008). Return to Mercury: A Global Perspective on MESSENGER's First Mercury Flyby. *Science, 321,* 59-62. https://doi.org/10.1126/science.1159706

Suckale, J., Elkins-Tanton, L. T., & Sethian, J. A. (2012). Crystals stirred up: 2. Numerical insights into the formation of the earliest crust on the Moon. *Journal of Geophysical Research, 117,* 1-21. https://doi.org/10.1029/2012JE004067

Starr, R. D., Schriver, D., Nittler, L. R., Weider, S. Z., Byrne, P. K., Ho, G. C., Rhodes, E. A., Schlemm II, C. E., Solomon, S. C., & Trávníček, P. M. (2012). MESSENGER detection of electron-induced X-ray fluorescence from Mercury's surface. *Journal of Geophysical Research, 11,* E00L02. https://doi.org/10.1029/2012JE004118

Stockstill-Cahill, K. R., McCoy, T. J., Nittler, L. R., Weider, S. Z., & Hauck II, S. A. (2012). Magnesium-rich crustal compositions on Mercury: Implications for magnesium from petrologic modeling. *Journal of Geophysical Research, 117,* E00L15. https://doi.org/10.1029/2012JE004140

Tajčmanová, L., Vrijmoed, J., & Moulas, E. (2015). Grain-scale pressure variations in metamorphic rocks: implications for the interpretation of petrographic observations. *Lithos, 216-217,* 338-351. https://doi.org/10.1016/j.lithos.2015.01.006

Taylor, G. J., & Scott, E. R. D. (2003). Mercury. In Heinrich D. Holland, Karl K. Turekian (Eds.) *Treaties on Geochemistry.* (pp. 477-485) Elsevier Ltd. https://doi.org/10.1016/B0-08-043751-6/01071-9

Tenner, T. J., Lange, R. A., & Downs, R. T. (2007). The albite fusion curve re-examined: New experiments and the high-pressure density and compressibility of high albite and $NaAlSi_3O_8$ liquid. *American Mineralogist, 92(10),* 1573-1585. https://doi.org/10.2138/am.2007.2464

Tonks, W. B., & Melosh, H. J. (1990). The physics of crystal settling and suspension in a turbulent magma ocean. In N. E. Newsom, J. H. Jones (Eds.), *Origin of the Earth*. (pp.151-174) Oxford University Press, New York.

Tosi, N., Grott, M., Plesa, A.-C., & Breuer, D. (2013a). Thermochemical evolution of Mercury's interior. *Journal of Geophysical Research: Planets, 118,* 2474-2487. https://doi.org/10.1002/jgre.20168

Tosi, N., Plesa, A.-C., & Breuer, D. (2013b). Overturn and evolution of a crystallized magma ocean: A numerical parameter study for Mars. *Journal of Geophysical Research: Planets, 118,* 1512-1528. https://dio.org/10.1002/jgre.20109

Trask, N. J., & Guest, J. E. (1975). Preliminary Geologic Terrain Map of Mercury. *Journal of Geophysical Research, 80(17),* 2461-2477. https://doi.org/10.1029/JB080i017p02461

Ueki, K., & Iwamori, H. (2016). Density and seismic velocity of hydrous melts under crustal and upper mantle conditions. *Geochemistry, Geophysics, Geosystems, 17(5),* 1799-1814. https://doi.org/10.1002/2015GC006242

Vander Kaaden, K. E., & McCubbin F. M. (2015). Exotic crust formation on Mercury: Consequences of a shallow, FeO-poor mantle. *Journal of Geophysical Research: Planets, 120(2),* 195-209. https://doi.org/10.1002/2014JE004733

Vander Kaaden, K. E., & McCubbin, F. M. (2016). The origin of boninites on Mercury: An experimental study of the northern volcanic plains lavas. *Geochimica et Cosmochimica Acta, 173,* 246-263. https://doi.org/10.1016/j.gca.2015.10.016

Vander Kaaden, K. E., McCubbin, F. M., Nittler, L. R., Peplowski, P. N., Weider, S. Z., Frank, E. A., & McCoy, T. J. (2017). Geochemistry, mineralogy, and petrology of boninitic and komatiitic rocks on the mercurian surface: Insights into the mercurian mantle. *Icarus, 285*, 155-168. https://doi.org/10.1016/j.icarus.2016.11.041

Vetere, F., Behrens, H., Holtz, F., & Neuville, D. R. (2006). Viscosity of andesitic melts—New experimental data and a revised calculation model. *Chemical Geology, 228(4),* 233–245. https://doi.org/10.1016/j.chemgeo.2005.10.009

Walker, D., Kirkpatrick, R. J., Longhi, J., & Hays, J. F. (1976). Crystallization history of lunar picritic basalt sample 12002: Phase-equilibria and cooling-rate studies. *Geological Society of America Bulletin, 87(5),* 646-656. https://doi.org/10.1130/0016-7606(1976)87<646:CHOLPB>2.0.CO;2

Walker, D., Powell, M. A., Lofgren, G. E., & Hays, J. F. (1978). Dynamic crystallization of a eucrite basalt. *Proc. Lunar Planet. Sci. Conf. 9th*, 1396-1391.

Wang, Y., Sakamaki, T., Skinner, L. B., Jing, Z., Yu, T., Kono, Y., Park, C., Shen, G., Rivers, M. L., & Sutton, S. R. (2014). Atomistic insight into viscosity and density of silicate melts under pressure. *Nature Communications, 5,* 3241. https://doi.org/10.1038/ncomms4241

Warren, P. H. (1985). The Magma Ocean Concept and Lunar Evolution. *Annual Reviews Earth and Planetary Science, 13,* 201-240. https://doi.org/10.1146/annurev.ea.13.050185.001221

Weider, S. Z., Nittler, L. R., Starr, R. D., McCoy, T. J., Stockstill-Cahill, K. R., Byrne, P. K., Denevi, B. W., Head, J. W., & Solomon, S. C. (2012). Chemical heterogeneity on Mercury's surface revealed by the MESSENGER X-Ray Spectrometer. *Journal of Geophysical Research: Planets, 117,* E00L05. https://doi.org/10.1029/2012JE004153

Weider, S. Z., Nittler, L. R., Starr, R. D., Crapster-Pregont, E. J., Peplowski, P. N., Denevi, B. W., Head, J. W., Byrne, P. K., Hauck II, S. A., Ebel, D. S., & Solomon, S. C. (2015). Evidence for geochemical terranes on Mercury: Global mapping of major elements with MESSENGER's X-Ray Spectrometer. *Earth and Planetary Science Letters, 416,* 109-120. https://doi.org/10.1016/j.epsl.2015.01.023

Weisberg, M. K., Prinz, M., & Cherukupalli, E. N. (1988). Petrology of ALH85085: a chondrite with unique characteristics. *Earth and Planetary Science Letters, 91(1-2),* 19-32. https://doi.org/10.1016/0012-821X(88)90148-3

Wetherill, G. W. (1994). Provenance of the terrestrial planets. *Geochimica et Cosmochimica Acta 58(20),* 4513-4520. https://doi.org/10.1016/0016-7037(94)90352-2

Zha, C-S., Bassett, W. A., & Shim, S-H. (2004). Rhenium, an *in situ* pressure calibration for internally heated diamond anvil cells. *Review of Scientific Instruments, 75,* 2409-2418. https://doi.org/10.1063/1.1765752

Zhao, C., Lodders, K., Bloom, H., Chen, H., Tian, Z., Koefoed, P., Petö, M. K., Wang, K. (2020). Potassium isotopic compositions of enstatite meteorites. *Meteoritics and Planetary Science, 55(6),* 1404-1417. https://doi.org/10.111/maps/13358

Zolotov, M. Y., Sprague, A. L., Hauck II, S. A., Nittler, L. R., Solomon, S. C., & Weider, S. Z. (2012). The redox state, FeO content, and origin of sulfur-rich magmas on Mercury.

Journal of Geophysical Letters: Planets, *118*, 138-146. https://doi.org/10.1029/2012JE004274

Appendix A

Table A1. Compositional data for experiment FMMO9.

<table>
<tr><th colspan="10">EPMA Glass Composition (wt%) FMMO9</th></tr>
<tr><th></th><th>SiO_2</th><th>TiO_2</th><th>Al_2O_3</th><th>MgO</th><th>CaO</th><th>K_2O</th><th>Na_2O</th><th>S</th><th>Total</th></tr>
<tr><td></td><td>52.21</td><td>1.16</td><td>15.94</td><td>16.84</td><td>11.19</td><td>1.28</td><td>0.37</td><td>0.00</td><td>99.01</td></tr>
<tr><td>1σ Std Dev</td><td>1.55</td><td>0.15</td><td>2.73</td><td>4.82</td><td>1.41</td><td>0.33</td><td>0.25</td><td>0.00</td><td></td></tr>
<tr><th colspan="10">EPMA Glass Composition (wt%) MMO1</th></tr>
<tr><td></td><td>54.29</td><td>1.21</td><td>16.63</td><td>15.20</td><td>11.32</td><td>1.30</td><td>0.35</td><td>0.00</td><td>100.30</td></tr>
<tr><td>1σ Std Dev</td><td>0.49</td><td>0.04</td><td>0.16</td><td>0.49</td><td>0.11</td><td>0.06</td><td>0.02</td><td>0.00</td><td></td></tr>
</table>

Electron microprobe analysis of experiment FMMO9 and MMO1 (data reported in main text) conducted using a Cameca SX100 Electron Probe Micro Analyzer at the University of Tennessee using a 15kV beam and a 25 µm spot size. This experiment was not quenched and exhibits crystalline features resulting in larger standard deviations than experiment MMO1 reported in the main text. Nonetheless, the data demonstrate consistency between the fused (FMMO) and unfused (MMO) starting compositions.

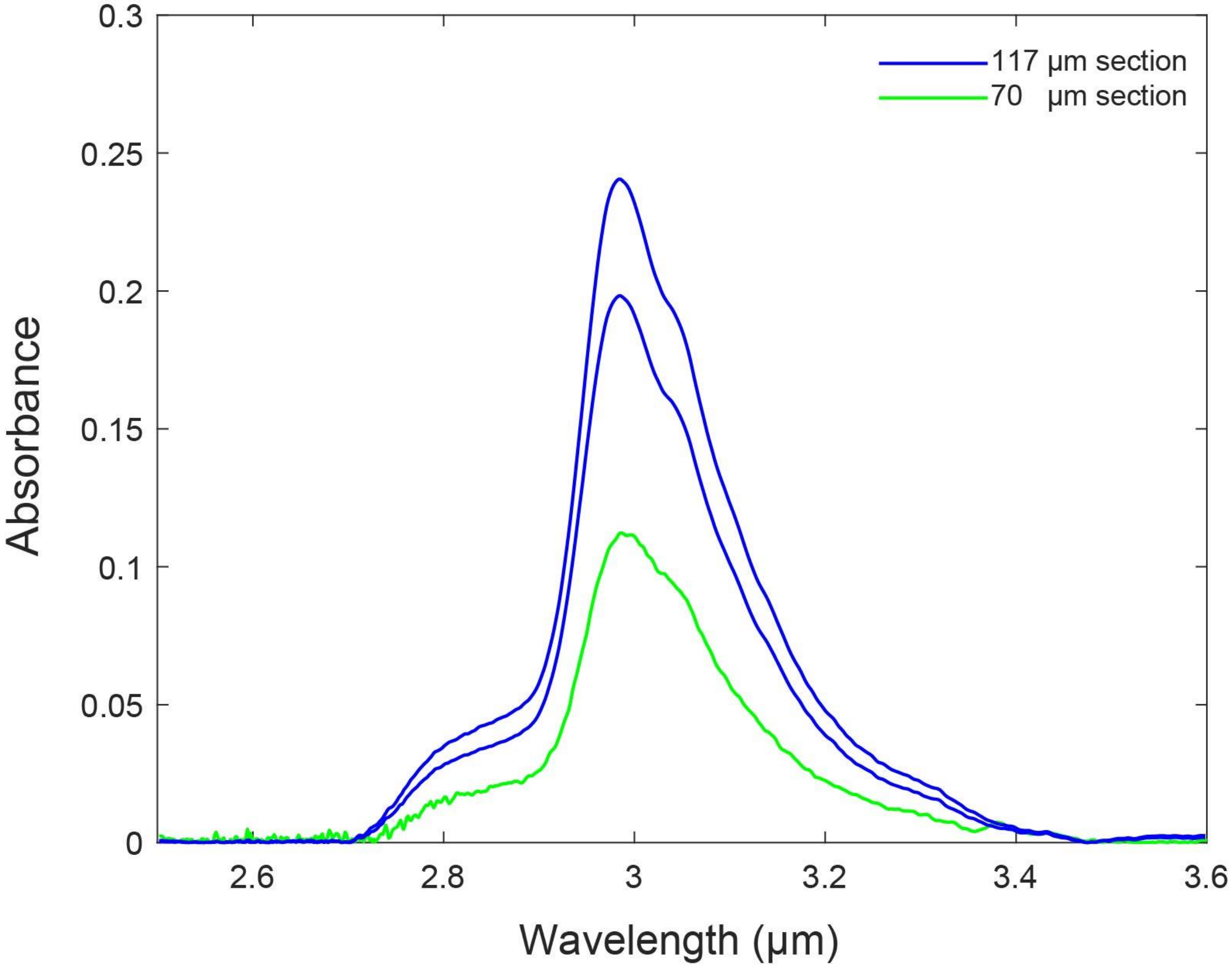

Figure A1. Background subtracted Fourier transform infrared (FTIR) spectra of experiment MMOS5. Two sections of the glassy sample were measured, one 117µm thick (blue lines) and the other 70 µm thick (green line). The average H_2O concentration is 94 ± 38 ppm. See main text for analytical and data processing methods.

Table A2. Boron analysis results for MMO experiments.

	MMO Glass	FMMO3	Secondary Standard (GSE-1G)	Secondary Standard (NIST612)
Pressure (GPa)	3.0	2.6	-	-
Temperature (°C)	2000	1600	-	-
Experimental Duration (seconds)	~10	54.5	-	-
Boron Concentration (ppm)	77.6 ± 50.7	1790.8 ± 710.6	330.0 ± 1.4	34.3 ± 7.9
Number of Spot Analyses	12	16	6	6
Preferred Boron Concentration (ppm)	-	-	330.0	34.3

Experimental run conditions and LA-ICP-MS boron measurements for experiment FMMO3 and a glassed sample of MMO. Boron concentrations of two secondary standards shown for comparison with the analysis of the experimental samples.

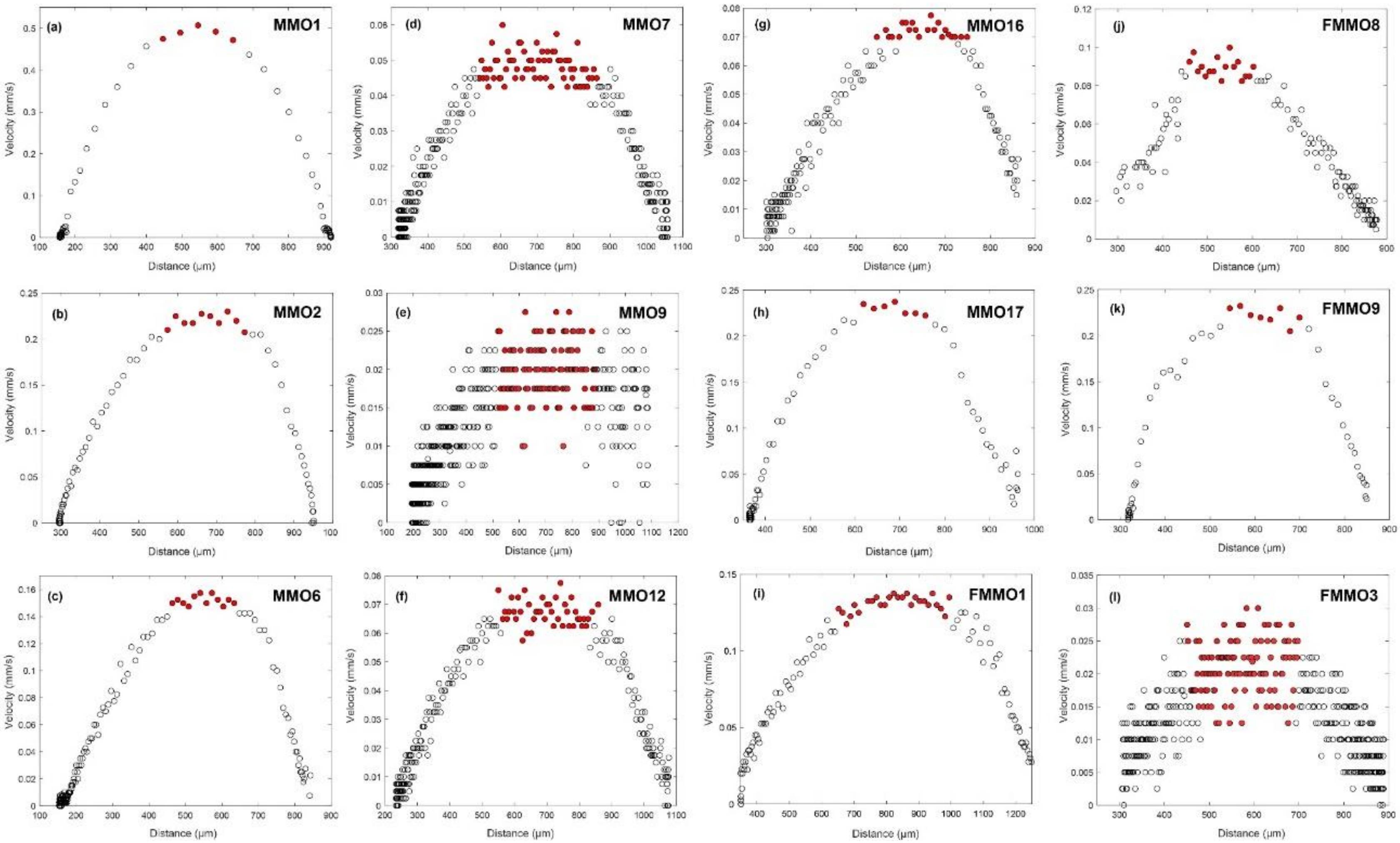

Figure A2. Velocity profiles of S-free experiments. Circles are 5-point velocities obtained from red points indicate the apparent terminal velocity averaged for the viscosity calculations.

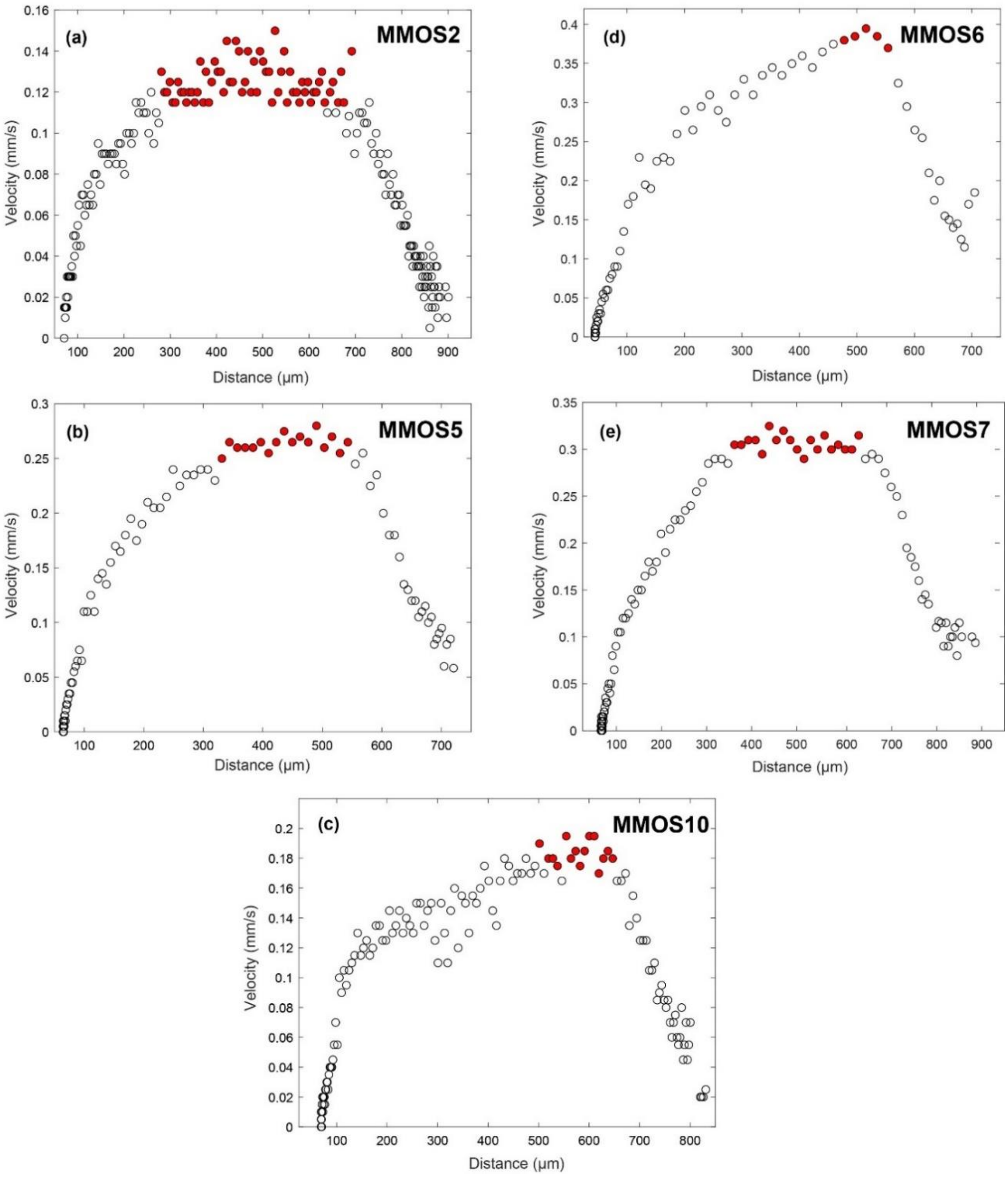

Figure A3. Velocity profiles of S-bearing experiments. Circles are 5-point averages of velocities obtained from the original dataset. The red points indicate the apparent terminal velocity averaged for the viscosity calculations.

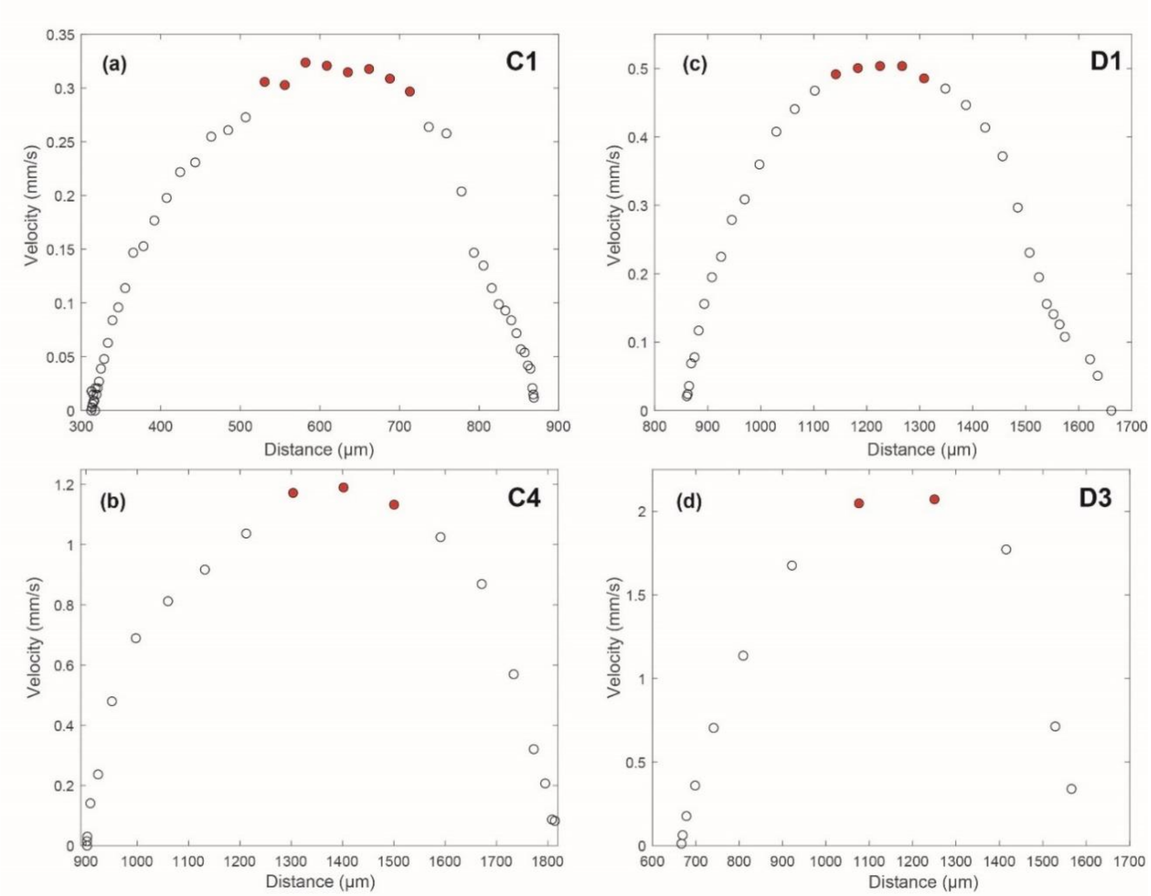

Figure A4. Velocity profiles of C and D experiments. Circles are 5-point averages of velocities obtained from the dataset. Red points indicate apparent terminal velocity averaged for calculation of viscosity. C and D experiments discussed further in Tables A2 and A3 and Figure A7.

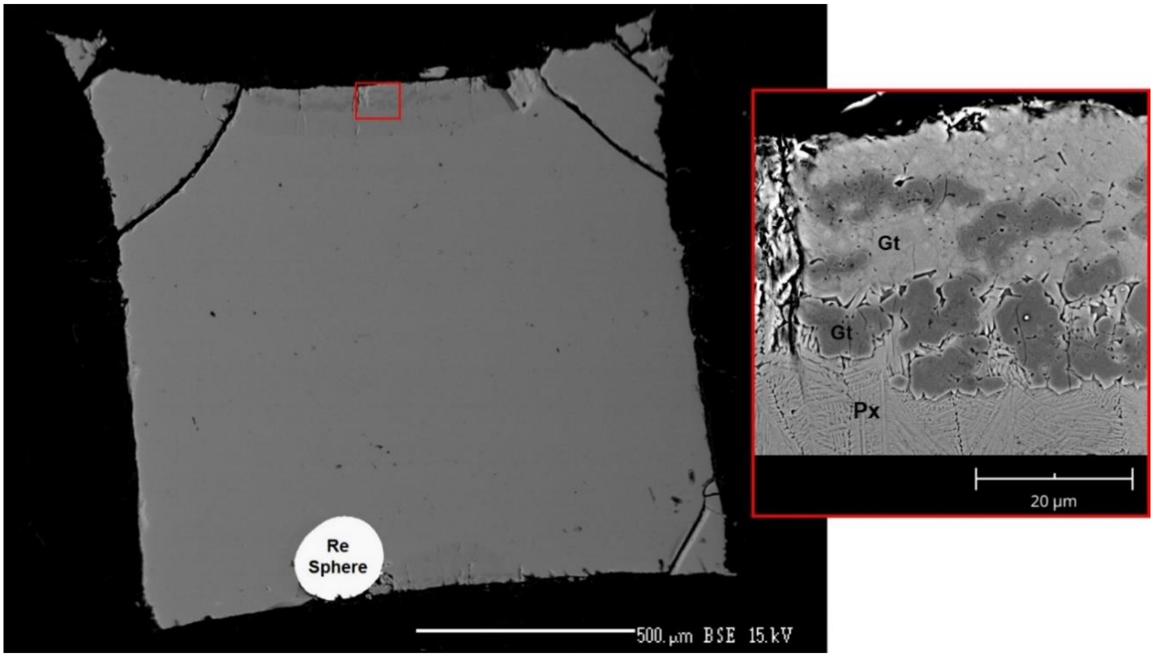

Figure A5. BSE images of experiment MMO1. This experiment was sectioned for imaging and analysis by scanning electron microscope and electron microprobe. Image inset shows a lens of garnet (Gt) and pyroxene (Px), which is present at the top and bottom walls of the experiment. A rind of pyroxene adjacent to this crystalline region exhibits a feathery texture indicating growth during the quench process. Aside from these thin crystalline regions at the assembly walls, the experiment is a homogeneous glass. The measured composition of the glass is reported in Table 1.1 in the main text.

Table A3. Additional experimental parameters.

Experiment	Sphere Composition	Sphere Density (g/cm^3)	Sphere Diameter (mm)	Liquid Density (g/cm^3)	Wall Effect (W)	End Effect (B)
S-free						
MMO1	Rhenium (Re)	21.35	0.20	2.93	0.72	1.08
MMO2	Rhenium (Re)	21.32	0.18	2.89	0.74	1.07
MMO6	Rhenium (Re)	21.36	0.18	2.94	0.75	1.07
MMO7	Rhenium (Re)	21.23	0.17	2.84	0.76	1.07
MMO9	Rhenium (Re)	21.15	0.12	2.78	0.83	1.05
MMO12	Tungsten Carbide (WC)	17.04	0.19	2.84	0.73	1.08
MMO16	Tungsten Carbide (WC)	17.03	0.20	2.88	0.72	1.08
MMO17	Tungsten Carbide (WC)	17.03	0.20	2.90	0.72	1.08
FMMO1	Tungsten Carbide (WC)	17.05	0.20	2.79	0.72	1.08
FMMO3	Tungsten Carbide (WC)	17.05	0.21	2.78	0.70	1.09
FMMO8	Tungsten Carbide (WC)	17.04	0.20	2.85	0.72	1.08
FMMO9	Tungsten Carbide (WC)	17.02	0.20	2.91	0.72	1.08
S-bearing						
MMOS2	Tungsten Carbide (WC)	17.05	0.20	2.82	0.72	1.08
MMOS5	Tungsten Carbide (WC)	17.04	0.21	2.83	0.71	1.08
MMOS6	Tungsten Carbide (WC)	17.05	0.21	2.81	0.71	1.08
MMOS7	Tungsten Carbide (WC)	17.04	0.21	2.84	0.71	1.09
MMOS10	Tungsten Carbide (WC)	17.04	0.22	2.86	0.69	1.09
Al-free						
C1	Tungsten Carbide (WC)	17.06	0.19	2.75	0.73	1.08
C4	Tungsten Carbide (WC)	17.06	0.19	2.75	0.73	1.08
D1	Tungsten Carbide (WC)	17.06	0.20	2.75	0.72	1.08

Table A3 Continued

Experiment	Sphere Composition	Sphere Density (g/cm^3)	Sphere Diameter (mm)	Liquid Density (g/cm^3)	Wall Effect (W)	End Effect (B)
Al-free						
D3	Tungsten Carbide (WC)	17.04	0.20	2.83	0.72	1.08

Sphere composition, density, and size along with liquid density, wall effect (Faxén, 1922) and end effect (Maude, 1961) for the experiments reported in the main text and in appendix A and used in the viscosity calculations. The densities for the spheres and liquids were calculated using a third order Birch-Murnaghan equation of state (Eq (1.8) and (1.9) in main text) to determine the pressure and temperature effect on rhenium (Zha et al., 2004; Anzellini et al., 2014), tungsten carbide (Litasov et al., 2010), and the liquid (Ueki and Iwamori, 2016). Uncertainties for the density calculations for the sphere and liquid are approximately ±5% (Litasvo et al., 2010; Anzellini et al., 2014; Ueki and Iwamori, 2016). Uncertainty related to the sphere diameter is approximately 7%.

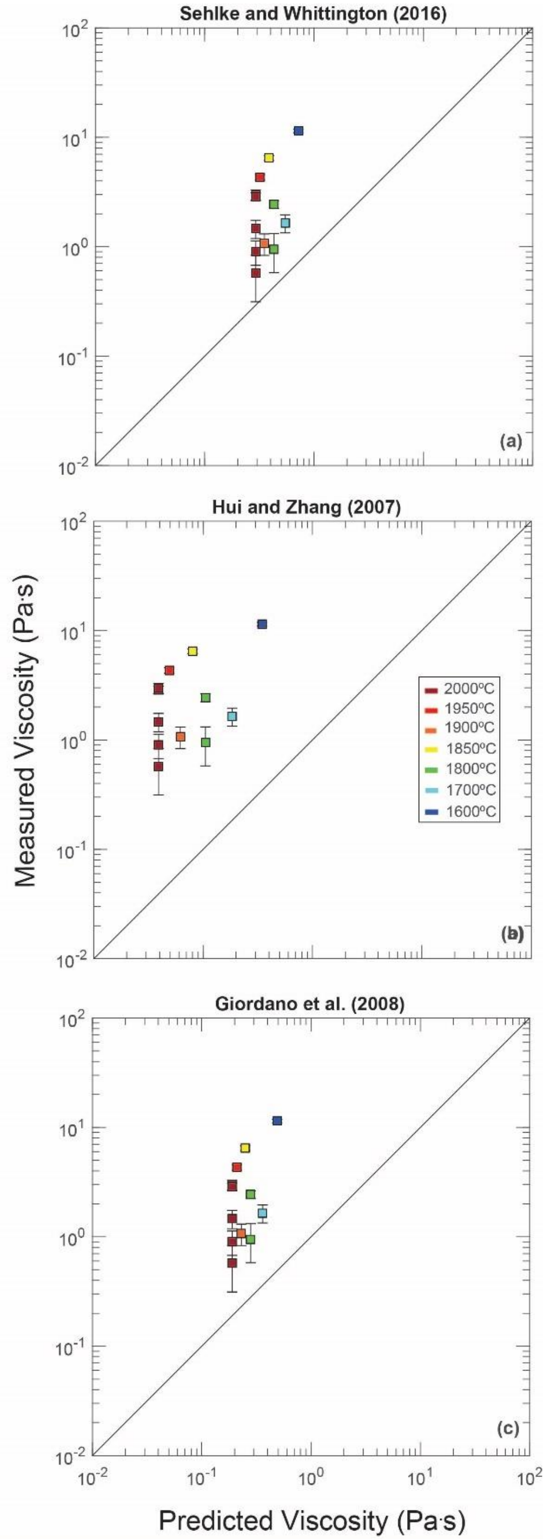

Figure A6. Measured S-free viscosities compared to predictions of the viscosity models of Sehlke and Whittington (2016) (a); Hui and Zhang (2007) (b); and Giordano et al. (2008) (c), which are parameterized using data relevant to terrestrial geologic systems.

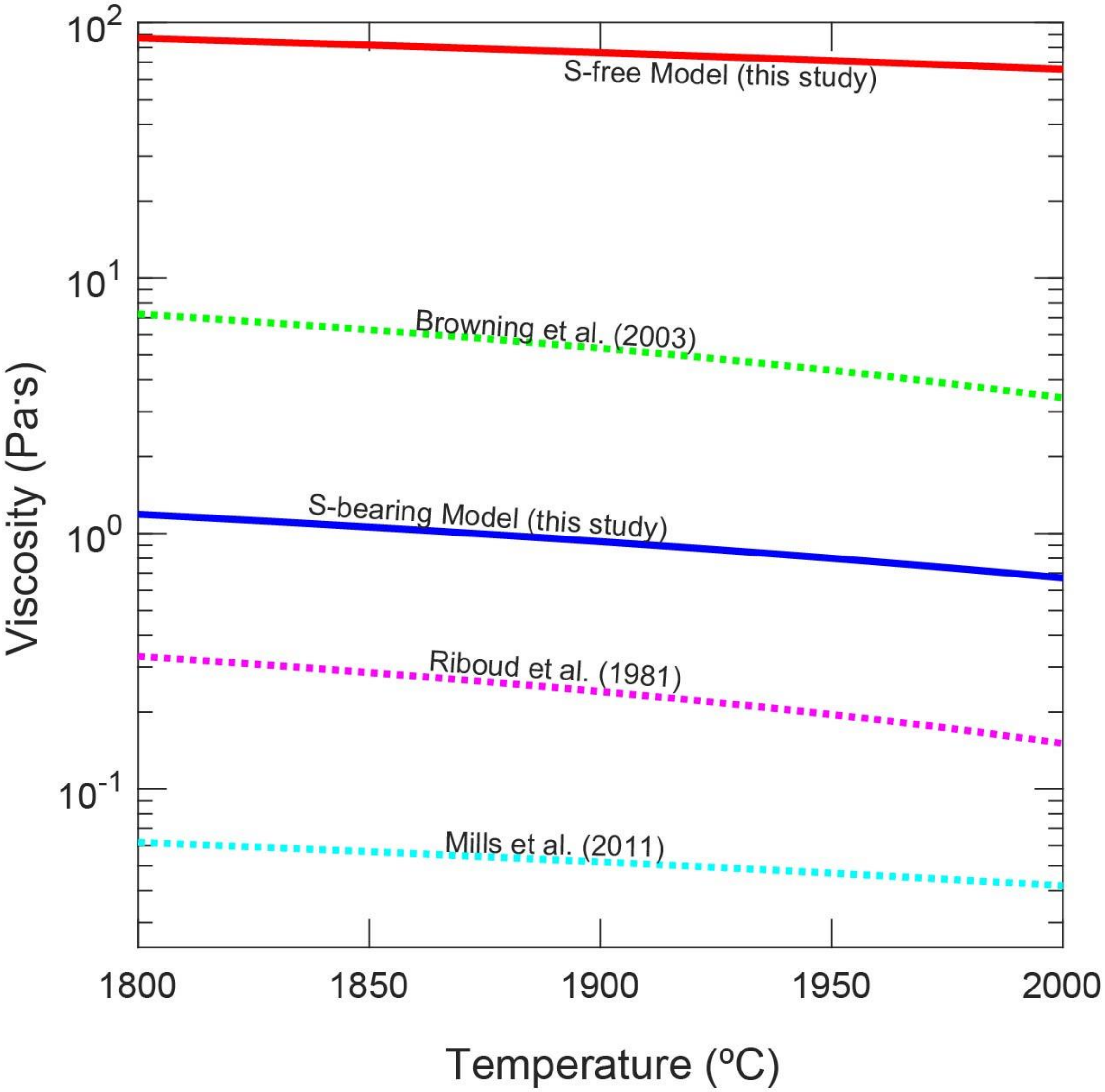

Figure A7. Viscosities calculated using the S-free and S-bearing models (solid lines, this study) compared to viscosities calculated using models for slags from Riboud et al., (1981); Browning et al. (2003), and Mills et al. (2011) at atmospheric pressure.

Experiments testing aluminum-free compositions

Two additional magma ocean analogue compositions were tested to evaluate the possible influences of oxidation state and Al on viscosity. These Al-free compositions were prepared by first homogenizing reagent grade oxide powders in ethanol with a mortar and pestle for six hours. The compositions were decarbonated in a furnace for 24 hours at 900°C. Next, the compositions were placed in platinum crucibles and fused in a box furnace in air at 1400°C for 4 hours. The fused compositions were reground and conditioned to IW-1 and IW-4.5 (C and D, respectively) using a CO/H_2 and CO_2/CO gas mixtures respectively at Brown University (Table A2).

Table A4. C and D experimental compositions.

Bulk Compositions (wt% oxide)										
	SiO_2	**TiO_2**	**Al_2O_3**	**MgO**	**CaO**	**K_2O**	**Na_2O**	**S**	**Total**	**fO_2**
C	64.0	1.4	0.0	18.1	13.2	2.7	0.5	0.0	100	IW-1
D	64.0	1.4	0.0	18.1	13.2	2.7	0.5	0.0	100	IW-4.5

Nominal compositions of decarbonated C and D powders calculated based on measured weights of oxide and carbonate constituents. C was conditioned to IW-1 and D was conditioned to IW-4.5.

Table A5. C and D viscosity results.

Experiment	**η (Pa·s)**	**T (°C)**	**P (GPa)**	**fO_2**
C1	0.63	1500	2.0	IW-1
C4	0.17	1700	2.0	IW-1
D1	0.43	1600	2.0	IW-4.5
D3	0.10	1900	3.8	IW-4.5

Experimental results for experiments on C and D compositions. Uncertainties in nominal run conditions are approximately ±0.5 GPa for pressure and ±5% for temperature.

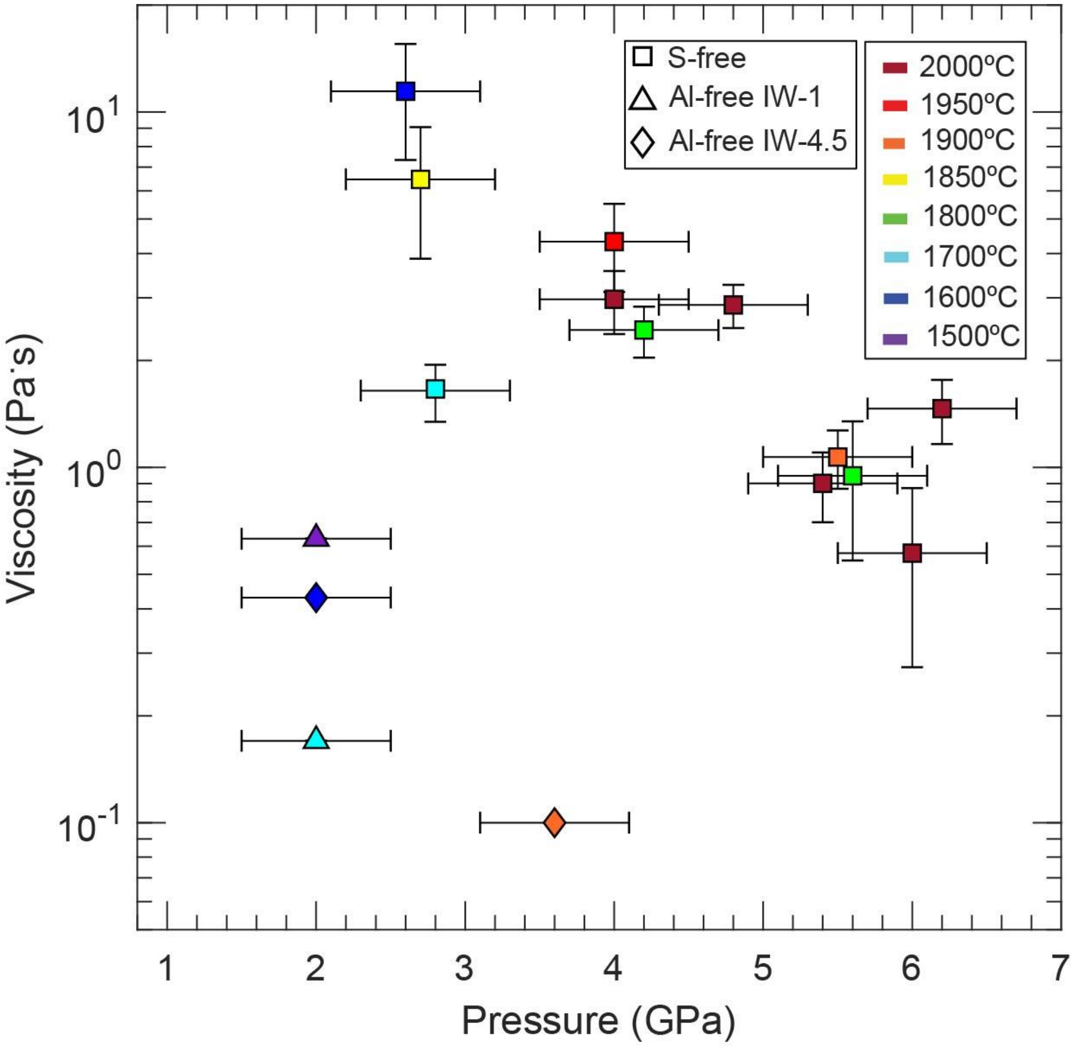

Figure A8. Results of experiments on aluminum-free starting composition C (triangles, iron-wüstite -1) and D (diamonds, iron-wüstite -4.5) compared to S-free viscosity data (squares). We infer that Al is dominantly a network former in this system as the Al free experiments have lower viscosities than Al-bearing experiments.

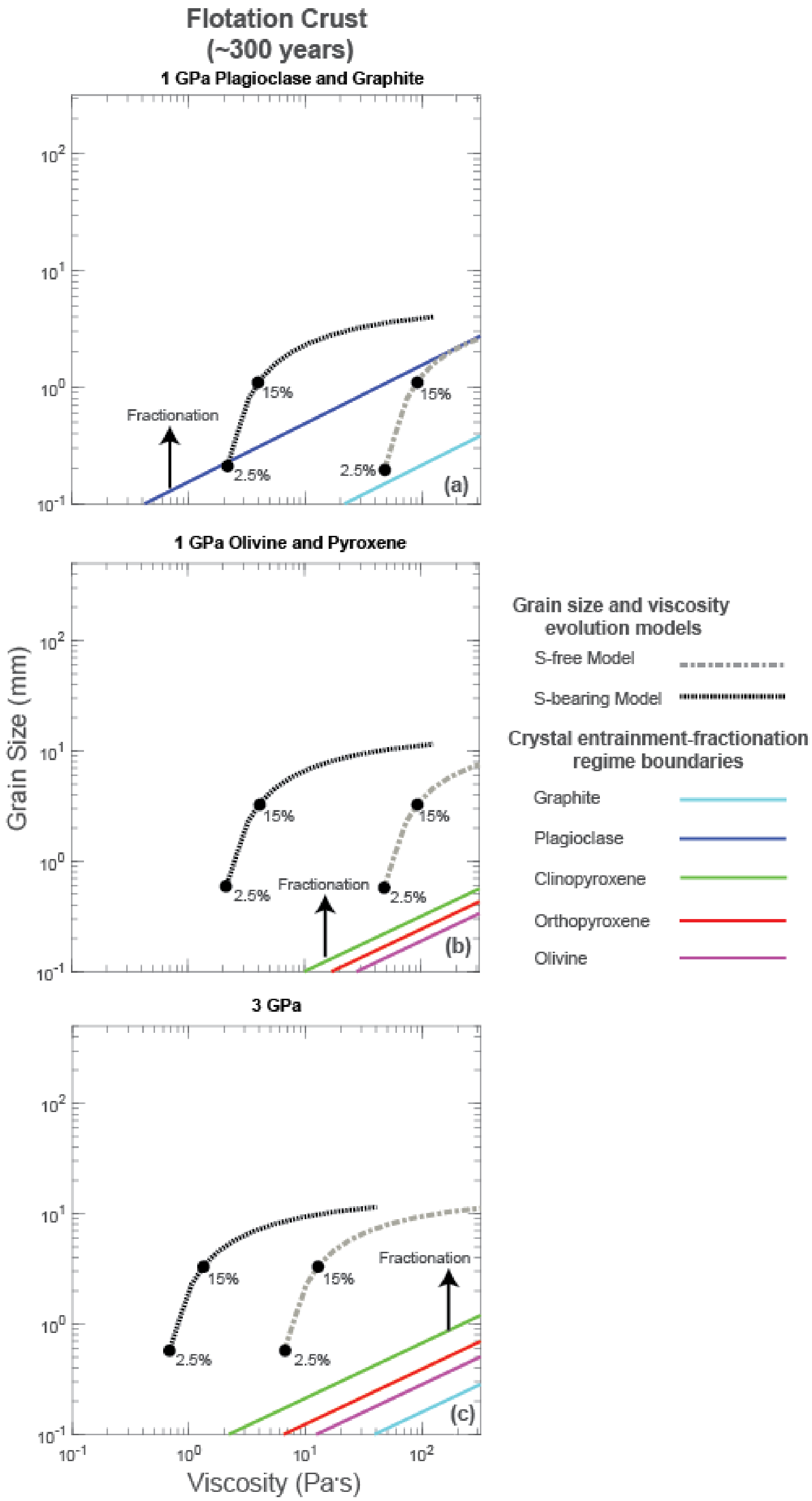

Figure A9. Scenario for continued solidification of an 80% crystallized magma ocean with a 100 m graphite flotation crust where the solidification timescale is 300 years. The analysis follows that detailed in Sections 1.4.2-1.4.4 and Figure 1.7 in the main text.

Contributions of core heat flux and radioactive decay to the magma ocean solidification timescale

Heat produced from radioactive decay and core heating are ignored in the main text (Eq 1.3-1.4) due to their negligible contribution to the heat budget (Table A5). The solidification timescale for a scenario without a flotation crust including contributions from radioactive decay and core heating is calculated as follows:

$$\tau_{NC} = \frac{(L_H \times 0.2M) + (Q_{core} \times A_{core} \times \tau_{NC}) + (C_P \times \Delta T_m \times 0.2M) + (H_t \times M_P)}{4\pi\sigma r^2 T^4}, \qquad \text{(A1.1)}$$

where L_H is the latent heat of the magma ocean liquid (4×10^5 J/kg), M is the mass of the magma ocean (after 80% crystallization; 0.2 is the remaining fraction of liquid), Q_{core} is the core heat flux for Mercury (50 mW/m^2 or less, depending on the timing of magma ocean formation (Hauck et al., 2004)), A_{core} is the surface area of the core, C_P is specific heat of the magma ocean liquid (1405 J/kg K), ΔT_m is the temperature difference during solidification (assumed to be 200°C), M_P is the mass of Mercury, σ is the Stefan-Boltzmann constant, and r is the radius of Mercury, and T is the temperature of the magma ocean (1350°C). This calculation assumes efficient transport of thermal energy from core solidification and radioactive decay in the Mercurian mantle to the magma ocean, maximizing possible contributions of these sources.

The radiogenic heat contribution (H_t) to the solidification timescale is calculated from the following:

$$H_t = (\Delta C_{238U} \times Q_{238U}) + (\Delta C_{235U} \times Q_{235U}) + (\Delta C_{232Th} \times Q_{232Th}) + (\Delta C_{40K} \times Q_{40K}), \qquad \text{(A1.2)}$$

where H_t is the total heat produced from the decay of long-lived radiogenic isotopes ^{238}U, ^{235}U, ^{232}Th, and ^{40}K per unit mass and is determined by determining the difference in concentration of the radioactive isotope, ΔC, from the initial amount to after a given period of time (e.g., here, τ_{NC}), multiplied by the heat produced from the decay of each isotope, Q, (Ruedas, 2017). Assumed initial concentrations for each isotope are from U, Th, and K abundances in enstatite chondrites (Lovering and Morgan, 1964; Zhao et al., 2020). For relevant solidification timescales, contributions of the core heat flux and decay of long-lived radioisotopes are insignificant, even assuming efficient contributions from core heat and radioactive decay in the mantle (Table A5). For a late stage (~80% crystallized) magma ocean without a flotation crust, the solidification timescale would be on the order of 20 years.

For the scenario with a flotation crust, the equation would be:

$$\tau_C = \frac{(L_H \times 0.2M) + (Q_{core} \times A_{core} \times T_C) + (C_P \times \Delta T_m \times 0.2M) + (H_t \times M_P)}{\left(\frac{\Delta T_C \kappa C_{Pg} \rho_g}{z}\right) A_{planet}}, \qquad \text{(A1.3)}$$

where ΔT_c is the temperature difference between the magma ocean liquid and the surface of the crust, κ is the thermal diffusivity of graphite (1.2×10^{-3} m^2/s (Hofmeister et al., 2014)), C_{Pg} is the thermal heat capacity of graphite, ρ_g is the density of graphite, z is the thickness of the graphite crust, and A_{planet} is the surface area of Mercury. Again, this model assumes efficient transport of thermal energy from core solidification through the mantle to the magma ocean, and efficient transport of thermal energy from radioactive decay in the mantle to the magma ocean, maximizing the possible contributions of those sources.

Table A6. Effect of heat contribution to solidification timescale.

	Flotation Crust	**No Flotation Crust**
	Time (years)	**Time (years)**
Latent Heat (LH)	1870	11.1
LH + Core Heat (QH)	1870	11.1
LH + QH + Specific Heat (CP)	3220	19.2
LH + QH + CP + Radioactive Heat	3220	19.2

Solidification timescales calculated using Supplementary Eqs (A1.1-A1.3) demonstrating the negligible effects of core heating and long-lived radioactive decay to the solidification time.

Table A7. Table of variables used.

Symbol	Term	Value and/or Units
η	Viscosity	Pa s
g	Gravitational acceleration (Earth)	9.8 m/s^2
d	Sphere diameter	m
ρ_s	Sphere density	g/m^3
ρ_l	Liquid density	g/m^3
W	Wall effect	-
B	End effect	-
v	Terminal velocity	m/s
A	Pre-exponential factor	-
E	Activation energy	J/mol
P	Pressure	Pa
V	Activation volume	m^3/mol
R	Universal gas constant	8.314 J/mol K
T	Temperature	K
τ_x	Solidification timescale	yr
L_H	Latent heat	4.0 x 10^6 J/kg
M	Mass of magma ocean	1.28 x 10^{23} kg
Q_{core}	Core heat flux	0.05 W/m^2
A_{core}	Surface area of core	4.07 x 10^{13} m^2
C_P	Specific heat	1450 J/kg K
ΔT_x	Temperature difference across a boundary	K
σ	Stefan-Boltzmann constant	5.67 x 10^{-8} W/m^{2}K^4
r	Radius of Mercury	2,439,700 m
H_t	Total heat produced by radioactive decay	J
ΔC_x	Change in isotopic concentration from radioactive decay	ppm
Q_x	Heat produced by decay of a quantity of a radioisotope	J/ppm
κ	Thermal diffusivity of graphite	1.2 x 10^{-3} m^2/s
C_{Pg}	Thermal heat capacity of graphite	720 J/kg K
ρ_g	Density of graphite	2.26 g/m^3
A_p	Surface area of Mercury	74.8 x 10^9 m
z	Graphite crust thickness	m
d_f	Critical grain size	m
α	Coefficient of thermal expansion for silicates	3 x10^{-5} K^{-1}
Q_R	Surface heat flux	10^6 W/m^2
L	Depth of magma ocean	m
f	Hindered settling function	0.15
g_M	Gravitational acceleration (Mercury)	3.7 m/s^2

Table A7 Continued

Symbol	**Term**	**Value and/or Units**
$\Delta\rho$	Density difference between liquid and crystal	g/m^3
ϕ	Crystal fraction	0.1 (Eq. 1.5); 0.025-0.5 (Eq. 1.6)
X	Volume of magma ocean (80%)	8.1 x 10^{18} m^3
η_{eff}	Effective viscosity	Pa s
η^o	Initial viscosity	Pa s
j	Geometric constant (Eq 7)	1.61
k_T	Isothermal bulk modulus	GPa
V_0	Initial molar volume	cm^3/mol
V_F	Molar volume at pressure	cm^3/mol
k_{T298}	Isothermal bulk modulus at reference temperature	GPa
${\frac{\delta k_T}{\delta T}}_P$	Isobaric bulk modulus at constant pressure	GPa/K
k'_T	Pressure derivative of k_T	-

Variables used in equations in the main text and appendix A. The x subscript is used to denote specific radioisotopes, see specific equations for more detail.

CHAPTER II.

ON THE POTENTIAL FOR CUMULATE MANTLE OVERTURN IN MERCURY

Abstract

Mercury has a compositionally diverse surface exhibiting geochemical terranes which represent different time periods of igneous activity, suggesting a diversity of mantle source compositions. It is likely that Mercury's juvenile mantle formed after fractional solidification of a magma ocean, which produced distinct mineralogical horizons with depth. To produce the diversity of observed volcanic terranes, dynamic mixing of materials from distinct mantle horizons is required. One process that could dynamically mix the juvenile cumulate pile is cumulate mantle overturn, where dense layers in shallow planetary mantles sink into deeper, less dense layers as Rayleigh-Taylor instabilities. To promote cumulate overturn, gravitationally unstable density stratification is a requisite starting condition; solidification of the Mercurian magma ocean is likely to have produced such a density inversion, with relatively dense clinopyroxene-bearing pyroxenite layers atop lower density dunite and harzburgite layers. Sulfides are present in abundance on Mercury's surface and would be additional mantle phase(s) if they are indigenous to the planet's interior. Sulfides have variable densities; they could potentially enhance the formation of gravitational instabilities or prevent them from developing at all. Exploring a range of physically reasonable mantle density and viscosity structures, we evaluate the potential for cumulate mantle overturn in Mercury, and present predictions of the possible timing, scale, and rate of overturn for plausible physical parameter combinations. Our analysis suggests that overturn is possible in Mercury's mantle during the first ~100 Myr after magma ocean solidification. Cumulate mantle overturn provides a mechanism for producing the mantle sources that would melt to form surface compositions on Mercury and may control the spatial scale of volcanic provinces observed on the surface today.

2.1. Introduction

Interpretations of geochemical and morphological features on Mercury's surface suggest it is comprised of multiple terranes related to distinct volcanic episodes. Major terranes include Borealis Planitia (BP) in the northern hemisphere, which has a high-Mg and a low-Mg region within (Weider et al., 2016; Lawrence et al., 2017); the Heavily Cratered Terrane and Intercratered Terrane (HCT-IcP) which includes subdivisions of a high-Mg, high-Mg and Ca, and an intermediate region; and the smooth volcanic plains associated with impact basins, such as Caloris and Rachmaninoff, which vary in Mg content (Weider et al., 2016; Lawrence et al., 2017). Ages of the terranes estimated by crater counting indicate distinct periods of volcanic history on Mercury from 3.7 to 2.5 Ga for BP and 4.1 to 4.0 Ga for the HCT-IcP (Neukum et al., 2001; Marchi et al., 2009, 2013; Le Feuvre and Wieczorek, 2011l; Ostrach et al., 2015). This diverse surface (e.g., Figure 1 in Vander Kaaden et al., 2017) suggests diverse mantle sources in Mercury's interior to produce the various surface compositions. The two largest terranes, the BP and HCT/IcP, differ in their Ca and Mg content where the more Ca-rich HCT/IcP requires a lherzolitic (clinopyroxene-bearing) mantle source while the more Ca-depleted BP requires a harzburgitic (clinopyroxene-free) mantle source (Charlier et al., 2013; Namur et al., 2016a; Nittler et al., 2019).

A recent experimental study constrained the viscosity of Mercurian magma ocean liquids and found that the structure of the mantle produced is largely controlled by the presence or absence of a flotation crust during Mercury's magma ocean stage (Mouser et al., 2021). Flotation crusts dramatically reduce heat flux, dampening convection, and prolonging solidification. Low reflectance material on Mercury's surface is interpreted to be the remnant of a graphite flotation crust (Murchie et al., 2015; Vander Kaaden and McCubbin, 2015; Peplowski et al., 2016; Klima et al., 2018). Estimates suggest the range in graphite crust thickness could have been between 1 m and 21 km with the lower bound reflecting a bulk Mercurian carbon content comparable to a CK chondrite, ~0.22 wt% C, and upper bound being comparable to a CI chondrite with ~2.4 wt% C (Vander Kaaden and McCubbin, 2015). These predictions are supported by remote sensing analysis of Mercury's surface which suggests an average of 2.5 wt% carbon enrichment in the HCT (e.g., Klima et al., 2018; Peplowski et al., 2016). Mouser et al. (2021) estimated the final 20% of magma ocean solidification occurred over 3,000 and 300 years for 1 km and 100 m thick graphite flotation crusts on Mercury, respectively, compared to 20 years for a case without a flotation crust. By forming a conductive thermal barrier, a Mercurian flotation crust would promote growth of cumulate minerals to relatively large grain sizes. Reduced heat flux would dampen convection limiting viscous re-entrainment of minerals that settled out on the magma ocean floor, promoting fractional crystallization. Thus, we anticipate that Mercury's juvenile cumulate mantle, produced by near-fractional solidification of the magma ocean, was mineralogically stratified according to the magma ocean's liquid line of descent (e.g., Brown and Elkins-Tanton, 2009; Elkins-Tanton, 2012; Mouser et al., 2021). However, the mantle structure produced from these fractional crystallization models does not create the required lherzolitic source composition to form the HCT/IcP, suggesting additional physical processes must occur to achieve the different source compositions, such as cumulate mantle overturn, described below.

The proposed stratified Mercurian mantle and subsequent mantle evolution may be analogous to the evolution of Earth's Moon. The Moon is believed to have produced a stratified mantle during magma ocean cooling with a flotation crust, resulting in a dense, shallow layer that precipitated at the end of magma ocean solidification (~95-99% crystallization; Shearer and Papike, 1999) from a residual liquid highly enriched in incompatible elements such as potassium, rare earth elements (REEs), phosphorous, uranium, and thorium, with a distinctive geochemical signature referred to as KREEP (Warren, 1985). Evidence for this layer, rich in dense ilmenite ($FeTiO_3$), is inferred from the enrichment of Ti and a KREEPy trace element pattern in many lunar basalt samples (e.g., Kesson and Ringwood, 1976). Ilmenite, and other solidification products of the KREEP-forming residual liquid (e.g., hedenbergite, $FeCaSi_2O_6$) would have been much denser than the underlying cumulates, promoting the formation of gravitational instabilities (Rayleigh-Taylor instabilities) that sank into the interior as a viscous solid (e.g., Kesson and Ringwood, 1976; Zhang et al., 2017; Li et al., 2019; Yu et al., 2019). While silicate minerals in Mercury are expected to lack iron, reducing their density relative to lunar liquids, we demonstrate below that density inversions in Mercury's mantle analogous to those in the lunar mantle are possible, such that denser material sank into less dense underlying material as Rayleigh-Taylor instabilities. Here we present the results of an analysis of the potential for gravitationally driven redistribution of shallow and deep cumulates of a stratified Mercurian mantle and explore implications of the overturn for Mercury's surface compositions.

2.2. Compositional and Density Structure of Mercury’s Mantle

We assume Mercury’s mantle mineralogy is comprised of forsterite (Mg_2SiO_4), enstatite ($MgSiO_3$), diopside ($MgCaSi_2O_6$), albite (at lower pressures, $NaAlSi_3O_8$), and possibly sulfides (e.g., oldhamite, heideite, troilite, etc.). The surface of Mercury exhibits a low Fe content (1-2 wt%, e.g., Nittler et al., 2011; Evans et al., 2012; Starr et al., 2012; Weider et al., 2012), and experimental studies suggest that the Mercury’s fO_2 is very low, IW-2 to IW -7, where IW refers to the iron wüstite buffer, (Malavergne et al., 2010; McCubbin et al., 2012; Zolotov et al., 2012; Namur et al., 2016a, 2016b); thus, we assume magnesian endmember silicates for the mantle mineralogy. Informed by experiments on lunar systems (e.g., Lin et al., 2017; Charlier et al., et al., 2018; Rapp and Draper 2018) we assume a hypothetical, compositionally stratified cumulate pile for Mercury with the following mineralogy, from bottom to top: dunite (forsterite), harzburgite (forsterite and enstatite), pyroxenite (enstatite and diopside), and gabbro (diopside and plagioclase feldspar). Of the minerals being considered, clinopyroxene is the densest and therefore in appropriate proportions the layer bearing clinopyroxene could be denser than an underlying layer without clinopyroxene. Enstatite is also denser than olivine at pressures greater than 1 GPa. Thus, conditions favorable for forming gravitational instabilities may be produced by pyroxene-bearing layers overlying pyroxene-free or pyroxene-poor layers.

The presence of sulfur on the surface of Mercury, approximately 1-4 wt% (Namur et al., 2016a) suggests the possible presence of sulfide minerals, in the Mercurian interior. Sulfides have long been proposed as components of the regolith on Mercury (Sprague et al., 1995); however, MESSENGER data revealed the diversity of possible sulfides present, primarily oldhamite (CaS) and troilite (FeS), with possible minor amounts of alabandite (MnS) and caswellsilverite ($NaCrS_2$) (e.g., Weider et al., 2016; Vander Kaaden et al., 2017). Oldhamite may be an important phase dictating the distribution of trace elements in Mercury’s interior, as it has been noted in multiple studies on enstatite chondrites and aubrites that oldhamite is a primary trace element reservoir, especially for REEs and heat producing elements (HPEs) (e.g., Murrell and Burnett 1982; Murrell and Burnett, 1986; Floss et al., 1990; Lodders, 1996; Barrat et al., 2014). Owing to its favorable structure for partitioning of large and highly charged cations, oldhamite has been observed to have high U concentrations in reduced natural samples. Other sulfides observed in reduced meteorites (e.g., djerfisherite) are rich in K. Therefore, enrichment of parent isotopes for long lived radioisotope systems (U, Th, K, etc.) may lead to significant heat production in sulfide rich regions of Mercury’s mantle, depending on the sulfide species (e.g., Wohlers and Wood, 2015; Wohlers and Wood 2017; Boujibar et al., 2019; Boukaré et al., 2019).

Mercury’s sulfur content, low fO_2, and high Mg (enstatite) content, are comparable to enstatite chondrites and aubrites which are are often used as analogues for Mercurian material (e.g., Burbine et al., 2010; Udry et al., 2019; Steenstra and van Westrenen, 2020; Wilbur et al., 2022). Sulfides that have been identified in aubrites are listed in Table 2.1, with enstatite chondrites containing similar sulfides (e.g., Mason 1966; Keil, 1968).

Table 2.1. Sulfides in aubrite meteorites (and their atmospheric-pressure densities as solids).

Sulfide	Formula	Density at atmospheric pressure (g/cm^3)
Troilite[a,b]	FeS	4.61
Oldhamite[a,c]	$(Ca,Mg)S$	2.60
Daubrelite[a,c]	$Fe^{2+}Cr^{3+}{}_2S_4$	3.81
Caswellsilverite[d]	$NaCrS_2$	3.21
Heideite[e]	$(Na,Cr)_{1+x}(Ti,Fe)_2S_4$	4.10
Niningerite[f]	MgS	3.22
Djerfisherite[g]	$K_6Na(Fe,Cu,Ni)_{25}S_{26}Cl$	3.52
Ferroan Alabandite[a,d,h]	$(Fe,Mn)S$	3.95
Wassonite[i]	TiS	4.45

Originally observed by [a]Watters and Prinz, 1979; [b]Olsen et al., 1977; [c]Graham et al., 1977; [d]Okada and Keil, 1982; [e]Keil and Brett, 1974; [f]McCoy, 1998; [g]Ramdohr, 1963; [h]Keil, 1968, [i]Nakamura-Messenger et al., 2012.

The densities of possible Mercurian mantle phases, including silicates and sulfides, were estimated using a Birch-Murnaghan Equation of state (Eq. 2.1–2) by calculating the molar volume of individual phases as a function of pressure and temperature.

$$P = \frac{3}{2} k_T \left[\left(\frac{V_0}{V_F}\right)^{\frac{7}{3}} - \left(\frac{V_0}{V_F}\right)^{\frac{5}{3}} \right] \left\{ 1 - \left(\frac{3}{4}\right) (4 - k'_T) \left[\left(\frac{V_0}{V_F}\right)^{\frac{2}{3}} - 1 \right] \right\}, \qquad (2.1)$$

where P is the pressure in Pa, k_T is the isothermal bulk modulus of a mineral, V_0 is the initial molar volume of a mineral, V_F is the molar volume at pressure, and k'_T is the pressure derivative of k_T. To scale the bulk modulus for temperature variation with depth in Mercury's mantle, the following expression for k_T is used:

$$k_T = k_{T_{298}} + \left(\frac{\partial k_T}{\partial T}\right)_P (T - 298) , \qquad (2.2)$$

which considers the variation of the bulk modulus as a function of temperature (T) from a reference value, $k_{T_{298}}$, and the isobaric bulk modulus at constant pressure. The pressure range considered was 0–7 GPa (7 GPa representing the probable base of Mercury's silicate mantle), and the temperature range was calculated assuming an adiabatic gradient of 0.1°C/km with a reference temperature of 1300°C (Mouser et al., 2021).

The bulk modulus, pressure derivative of the bulk modulus, and the initial molar volume were considered for the following minerals and liquids: enstatite, diopside, forsterite, albite, oldhamite (solid and liquid), troilite (solid and liquid), andesite liquid, and peridotite liquid. Table 2.2 reports parameter assumptions for each mineral. The results of the individual mineral density calculations, as well as peridotite and andesite liquids (shown for reference) are presented in Figure 2.1. The density profile for the cumulate mantle is shown in Figure 2.2. Modal mineralogy proportions for each layer assumed are: dunite, 100% forsterite; harzburgite, 45–50% forsterite, 45–50% enstatite, and ± 0–10% sulfide; pyroxenite, 45–50% enstatite, 45–50% diopside, and ± 0–10% sulfide; gabbro, 60% diopside and 40% plagioclase.

2.2.1. Density of a Silicate-only Mantle

The proposed mantle structure for Mercury in the scenario that its magma ocean fractionally solidified (i.e., if it had a graphite flotation crust) is shown in Figure 2.2. Using Eq (2.1), the densities of the respective layers were calculated. Figure 2.2a shows the density profile of the silicate mantle without sulfides. Between pyroxenite and harzburgite and the harzburgite and the dunite layers, there are density inversions (i.e., the overlying layer is denser than the underlying layer). The density differences at these interfaces demonstrate that gravitational instabilities could develop, causing the overlying layers to flow ("overturn") into underlying layers to achieve gravitational stability. This process would promote redistribution of material among the layers and could promote formation of a more homogeneous Mercurian mantle.

Table 2.2. Parameters used for density calculations.

Material	k_{T298}	V_0	k'_T	$(\partial Kt/\partial T)_P$
Forsterite [(a,b)]	129.0	43.6	5.37	-0.0224
Enstatite [(c,d,e)]	105.5	31.292	10.2	-0.0370
Diopside [(b)]	113.0	66.4	4.8	-0.0200
Plagioclase (albite) [(f)]	56.4	100.9	3.9	--
Oldhamite *s* [(g.h)]	56.7	27.72	4.9	-0.01170[†]
Oldhamite *l* [(g,h,i)]	45.6[*]	27.72	49.0	-0.00104[*]
Troilite *s* [(h,j)]	54.3	18.2	4.0	-0.01170
Troilite *l* [(h,i)]	45.6	18.2	5.0	-0.00104
Andesite Liquid [(k)]	17.2	25.84	6.3	-0.00110
Peridotite Liquid [(l)]	24.3	13.7	5.2	-0.00160

Note plagioclase only considered changes in pressure; *s* denotes solid, *l* denotes liquid. [†]Assumed value (from solid troilite). [*]Values are from liquid troilite used to predict the density of liquid oldhamite. [a]Holland and Powell (1998); [b]Bertka and Fei (1998); [c]Jackson et al., 2015; [d]Schutt and Lesher, 2006; [e]Angel and Hugh-Jones, 1994; [f]Tenner et al., 2007; [g]Smyth and McCormick, 1995; [h]Robie et al., 1967; [i]Sanloup et al., 2000; [j]Urakawa et al., 2004; [k]Malfait et al., 2014; [l]Sakamaki et al., 2010.

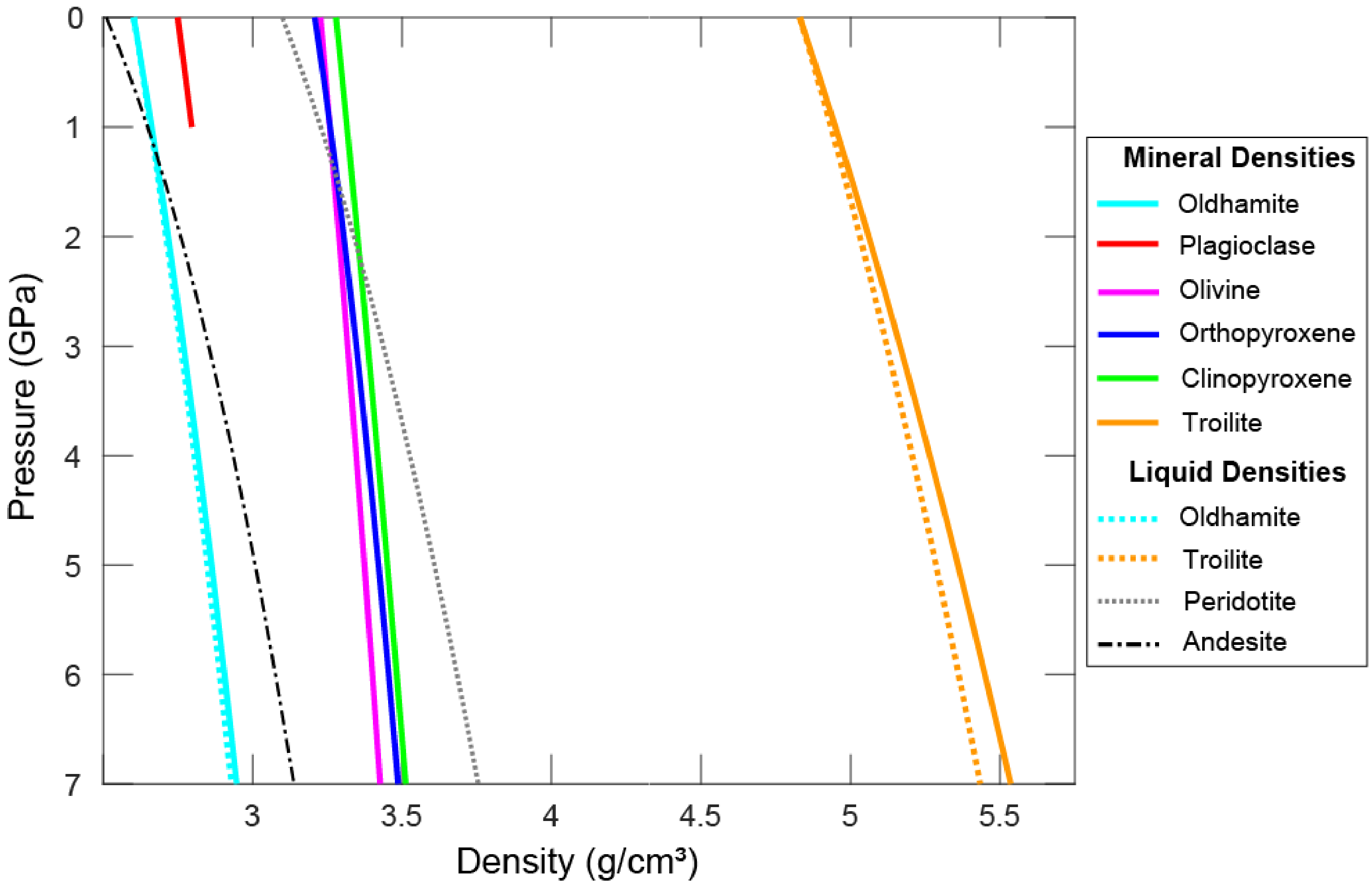

Figure 2.1. Calculated densities of individual minerals and liquids in Mercury's interior from 0 to 7 GPa. Plagioclase is plotted to the higher extent of its possible pressure stability.

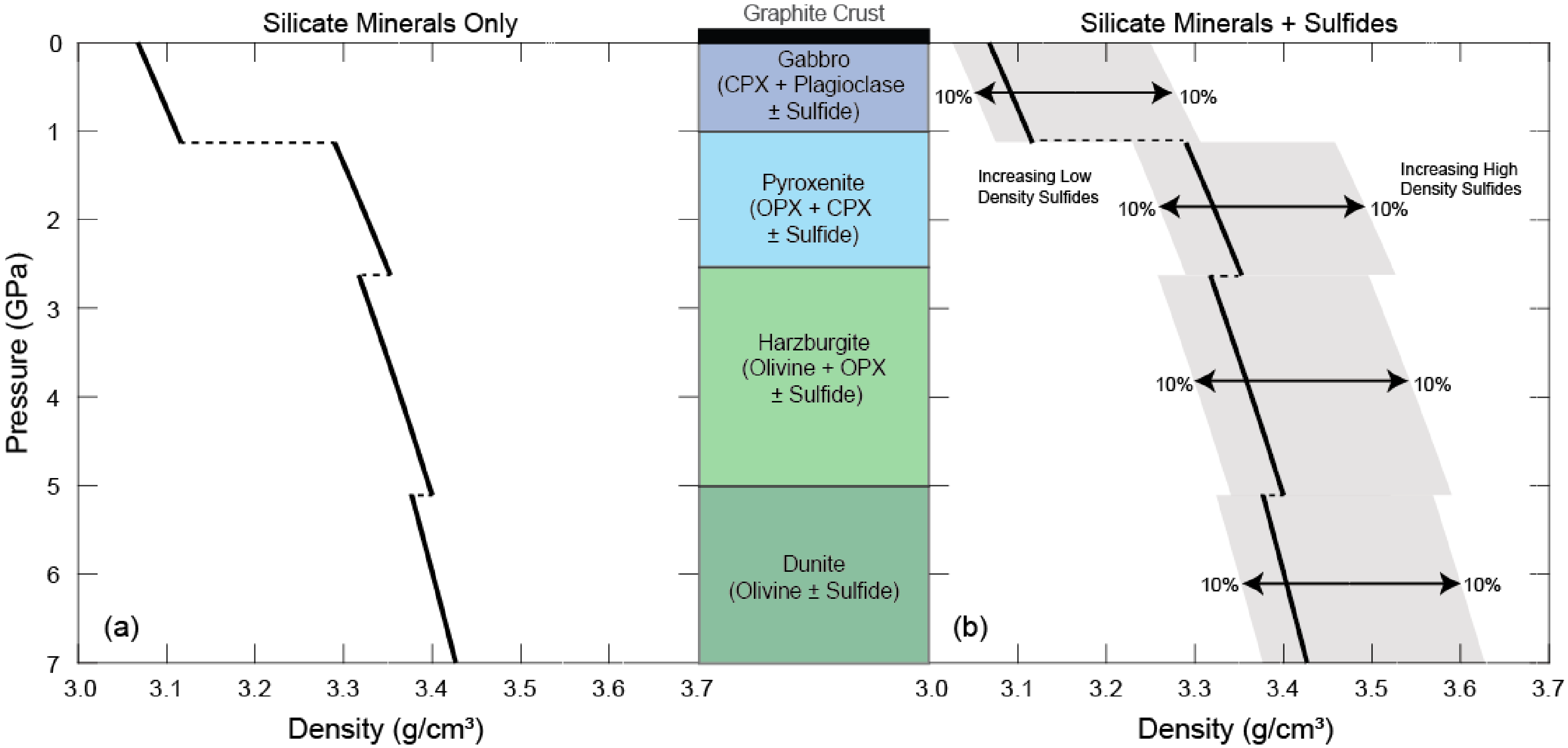

Figure 2.2. Calculated density profiles of potential cumulate layers produced in a scenario for magma ocean solidification with a flotation crust with proposed pre-overturn stratigraphy shown in the center. (a) The scenario with silicate minerals only; and (b) the scenario with sulfides present. The gray areas in (b) show the density range of heavy and light sulfides in the silicate layer ranging from 0% (central black line) up to 10% (indicated by arrow). Note the inverted density structure in the silicate minerals only case, demonstrating potential for forming gravitational instabilities. Potential sulfide minerals in the mantle may be assumed from reduced meteorites (Table 2.1), but the phases that would precipitate from a reduced Mercurian magma ocean liquid are largely unknown.

2.2.2. Density of a Sulfide-bearing Mantle

The abundance of sulfur on Mercury's surface indicates sulfides may play a role in the interior mineralogy. Carbonaceous impactors have been suggested as an alternative mechanism to achieve the carbon content on the surface (e.g., Syal et al., 2015) as opposed to a graphite flotation crust. This hypothesis may be similarly invoked as an alternative explanation for the sulfur content on the surface; however, in this study, we assume surficial sulfur originates from the planet's interior. Experimental data shows that sulfur solubility in silicate liquids is increased at low oxygen fugacities (e.g., Mavrogenes and O'Neill, 1999; Berthet et al., 2009; Anzures et al., 2020) suggesting that sulfides may have precipitated from Mercury's magma ocean along with the silicates. Below, the potential for sulfide in the pyroxene bearing and dunite layers is used to assess the implications of sulfide on the density of the layers.

2.2.2.1. A Mantle with Dense Sulfides

The addition of dense sulfides (e.g., troilite) to a layer in Mercury's cumulate mantle would significantly affect the layer density owing to liquid troilite's >1 g/cm^3 density excess compared to mantle silicates (Figure 2.1). Low abundances, such as 1–2%, may increase the bulk density of the layer by a small amount (~0.1 g/cm^3; Figure 2.2b). At larger proportions, such as ~10%, the bulk density is increased by up to 0.2 g/cm^3 compared to cases with no sulfide present (Figure 2.2b). The impact of the sulfides on the potential for forming Rayleigh-Taylor instabilities is determined by the layer in which they are present. Abundant, dense sulfides in deeper layers (e.g., harzburgite or dunite) would neutralize formation of gravitational instabilities from shallower layers dominated by silicates. If dense sulfides were more abundant in shallower layers (e.g., pyroxenite) they would enhance the potential for forming gravitational instabilities.

2.2.2.2. A Mantle with Low-density Sulfides

The density difference between less dense sulfides (e.g., oldhamite) and common silicate minerals is ~0.5 g/cm^3 (Figure 2.1). While not as impactful as the denser sulfides, in sufficient quantities, the presence of light sulfides could affect the density of the silicate layers. At ~10% sulfide the density of an otherwise silicate-bearing layer would decrease by ~0.1g/cm^3 (Figure 2.2b). Alkali- and Ca-bearing sulfides (e.g., oldhamite, djerfisherite, caswellsilverite) are unlikely to precipitate at greater depths as their saturation in residual magma ocean liquid depends on the build-up of alkali elements which occurs later in the crystallization sequence. For this reason, it is unlikely that these less dense sulfides would exist at great depth (e.g., in the dunite layer, Figure 2.2), however; the phase equilibria relationships of sulfides at varying conditions in potential Mercurian magma ocean liquids are largely unknown at this time. Similar to the dense sulfide case, the layers that sulfides are present in will affect the density stratification. Light sulfides in the harzburgite would further increase the gravitational instability. If they are more abundant in the pyroxenite, it is possible that light sulfides would neutralize the instability that would otherwise be present (this possibility is discussed further in section 2.5). Light sulfides may also have a large effect on the distribution of heat-producing elements in Mercury's cumulate mantle.

Whether or not sulfides are present in Mercury's mantle, according to the density calculations presented, formation of gravitational instabilities is possible between the pyroxene-bearing layers and between the harzburgite and dunite (Figure 2.2). Gravitational mixing between the middle layers (harzburgite and pyroxenite layers) would create a lherzolitic source, which is expected to be the source of the HCT-IcP (Charlier et al., 2013; Namur et al., 2016a; Nittler et al., 2019).

2.3. Experimental Sulfide Crystallization in Mercury's Magma Ocean

A crystallization experiment was conducted on a sulfur-bearing, Fe-free, late-stage Mercurian magma ocean composition ('MMOS' composition of Mouser et al., 2021) to determine possible sulfides in Mercury's upper mantle. The experiment was conducted in a 150-ton end-loaded piston cylinder apparatus at the University of Tennessee. The experimental composition was packed inside a graphite lined Mo capsule in an assembly using a NaCl cell as a confining medium. The experiment was run at 1 GPa, ramping to an assumed liquidus temperature of 1400°C at 70°C/min, maintained at that condition for one hour before cooling to 1000°C at 2°C/min. The recovered experiment was mounted in epoxy and polished for analysis on the SX100 scanning electron microscope at the University of Tennessee.

Backscattered electron images of the experiment are shown in Figure 2.3. This experiment crystallized enstatite, diopside, and plagioclase as the major phases, with sulfides and quartz in the interstitial regions. The composition of the sulfides was determined using energy dispersive X-ray spectroscopy (EDS). Ca-bearing and Ti-bearing sulfides were observed (Figure 2.3). Since this experimental composition represents a late stage magma ocean liquid, CaS would be expected to precipitate at this later stage due to the stability and build-up of alkali elements. Ti-sulfides are not as abundant as CaS in the experiment but were still observed in several locations suggesting they would also precipitate from the late stage magma ocean, depending on its Ti content.

2.4. Potential for Sulfide-localized Heat Production and Mobility in the Mantle

Sulfide rich material that may have existed in Mercury's mantle could have concentrated heat producing elements (HPEs) such as U, Th, and K in phases such as oldhamite due their higher affinity for trace elements over silicate materials (Murrell and Burnett, 1986; Floss et al., 1990; Lodders, 1996). The increased presence of HPEs in the mantle may cause sulfide-rich layers to heat and even become partially molten which could promote the migration of sulfide rich material through the mantle via percolation. By concentrating heat in the HPE-rich layer, the sulfide would additionally promote thermal expansion, lowering the layer density (e.g., see density differences of olivine and clinopyroxene with depth in scenarios with positive and negative thermal gradient, Figure B1). The possible heat production from an HPE-rich sulfide layer was determined by calculating the total heat production from ^{238}U, ^{235}U, ^{230}Th, and ^{40}K over time, assuming the radioisotope are concentrated in the sulfides. The initial concentration of the isotopes were determined first by calculating the total decay of each isotope over the last 4.5 billion years:

$$d_x(\%) = \frac{100}{2^{n_x}}, \tag{2.3}$$

where *d* is the percent of decay of the isotope, *x* represents the radioisotope of interest, and *n* is the number of half-lives that have occurred since 4.5 Ga. The initial concentration (C_0) of isotope *x* can be determined by:

$$C_0 = (d_x \times C_x) + C_x, \tag{2.4}$$

where C_x represents present day isotopic abundances in an assumed bulk-Mercury relevant material (Table 2.3). Using this initial value, the concentration of each isotope can be modeled over time using the decay equation:

$$\Delta C_x = C_0 - (C_0 \times e^{-\lambda_x t}), \tag{2.5}$$

where ΔC_x is the concentration of radioisotope *x*, after *t* period of time in seconds. λ_x is the decay constant for isotope *x* (Table 2.3). Relevant time periods for early mantle evolution were considered. Once the concentration for each isotopic system has been determined, the heat produced from all radioisotopes can be calculated using the following equation:

$$H_t = \left[\left(\frac{\Delta C_{238U} \times N_a \times E_{238U}}{M_{238U}}\right) + \left(\frac{\Delta C_{235U} \times N_a \times E_{235U}}{M_{235U}}\right) + \left(\frac{\Delta C_{232Th} \times N_a \times E_{232Th}}{M_{232Th}}\right) + \left(\frac{\Delta C_{40K} \times N_a \times E_{40K}}{M_{40K}}\right)\right], \tag{2.6}$$

Where H_t is the total energy produced from the decay of all radioisotopes considered, N_a is Avogadro's number, M_x is the molar mass of element *x*, and E_x is the heat produced from the decay of each atom of element *x* (Table 2.3). The final step is to find the temperature produced from the decay reactions over time:

$$T = \frac{H_t \times \frac{M_p}{M_l}}{C_p \times M_p}, \tag{2.7}$$

Where *T* is temperature, M_p and M_l are the mass of the planet and layer, respectively, and C_p is the specific heat for pyroxenite. The ratio of the mass of the layer to the mass of the planet is used to evaluate the endmember scenario where all U, Th, and K are concentrated in a sulfide-rich layer. The temperature produced over time in a sulfide-rich layer of varying thicknesses is presented in Figure 2.4.

This rapid increase in temperature in a concentrated layer could be enough to promote partial melting of the sulfide rich material for any of the investigated layer thicknesses. In the event the layer became significantly molten, as is the case for thinner layers (Figure 2.4), the low density sulfides would percolate upward to shallower layers according to their buoyancy. Melting of the sulfide-bearing silicate layer would promote some melting along the interface of underlying and overlying layers, potentially leading to limited mixing between cumulate horizons.

The possibility of a partially molten sulfide rich layer suggests the potential for sulfide mobility and redistribution in the mantle. Multiple experimental studies on mafic silicate melts in a cumulate, such as olivine, found that at higher melt fractions, the more connected the melt networks are between grain boundaries, thus enhancing permeability through the cumulate (e.g., Riley and Kohlstedt., 1991; Faul, 1997; Lambart et al., 2012). In scenarios where the liquid is primarily a metal or a sulfide, studies that have examined the process of molten iron moving through solid silicates (e.g., olivine aggregates) found that the addition of sulfur to the liquid Fe decreases the dihedral angle between the molten liquid and olivine crystals (e.g., Gaetani and Grove, 1999; Takafuji et al., 2004), which may enhance the mobility of the Fe-S liquid. However, at low melt fractions, sulfide melts may not be highly mobile (Riley and Kohlstedt., 1991; Faul, 1997; Barnes et al., 2008; Lambart et al., 2012). Oxygen fugacity conditions are also known to affect sulfide mobility (Gaetani and Grove, 1999). While we do not expect the sulfide rich material in Mercury to be primarily molten Fe-S, the molten (or partially molten) sulfide rich material may be redistributed in shallower regions of the mantle.

2.5. Revised Mantle Density Structure

Considering the low fO_2 environment and stability of the different sulfides, we evaluate what we consider the most probable density scenarios. In the case of high density, Fe-rich sulfides, the highest concentration would likely be lower in the mantle, increasing the density of deeper cumulates (Figure 2.5). As for low density sulfides (e.g., like oldhamite), it is more likely that they would precipitate in shallower cumulates, effectively decreasing the density (Figure 2.5). However, the distribution of small sulfides between silicate phases in our experiment indicates oldhamite and Ti-sulfide were among the last phases to precipitate. If our experimental liquid represent a good analog for Mercury's late magma ocean, we infer that sulfides would have precipitated in the uppermost layer in Mercury's mantle (gabbro). If they did precipitate earlier in Mercury's solidification sequence, heat production would promote partial melting and upward migration according to their density. It is also important to note the magma ocean crystallization experiment presented in Section 2.3 demonstrates that other sulfides may precipitate shallower in the mantle along with CaS and, in the case of Ti-bearing sulfides, have high densities that neutralize some of the low density effects CaS might have.

2.6. Mantle Viscosity

The viscosity structure of a planetary mantle is an important parameter to understanding different geochemical and geophysical processes that occur, such as cumulate mixing and convective flow (King, 1995). Constraining mantle viscosity on Earth has been approached by multiple techniques, such as measuring glacial rebound (e.g., Peltier, 1976; Mitrovica and Peltier, 1991, 1992), post-seismic rebound (e.g., Gourmelen and Amelung, 2005), experimentally measuring rheological properties (e.g., Hirth and Kohlstedt, 2004; Dygert et al., 2016), and applying flow laws and paleopiezometers to natural materials (e.g., Hansen and Warren, 2015; Dygert et al., 2019). Viscosity studies have found that for Earth's mantle, the steady state viscosity is on the order of ~10^{20} Pa·s but determinations vary among studies by several orders of magnitude (Hager, 1991; Paulson et al., 2007; Freed et al., 2012). On other planetary bodies (the Moon, Mars), the mantle viscosity can be constrained in models that consider, for example, seismic data, tidal forces, and topographic and gravitational constraints, where the viscosities are predicted to be similar to that of Earth's mantle (e.g., Harada et al., 2014; Matsumoto et al., 2015; Khan et al., 2021).

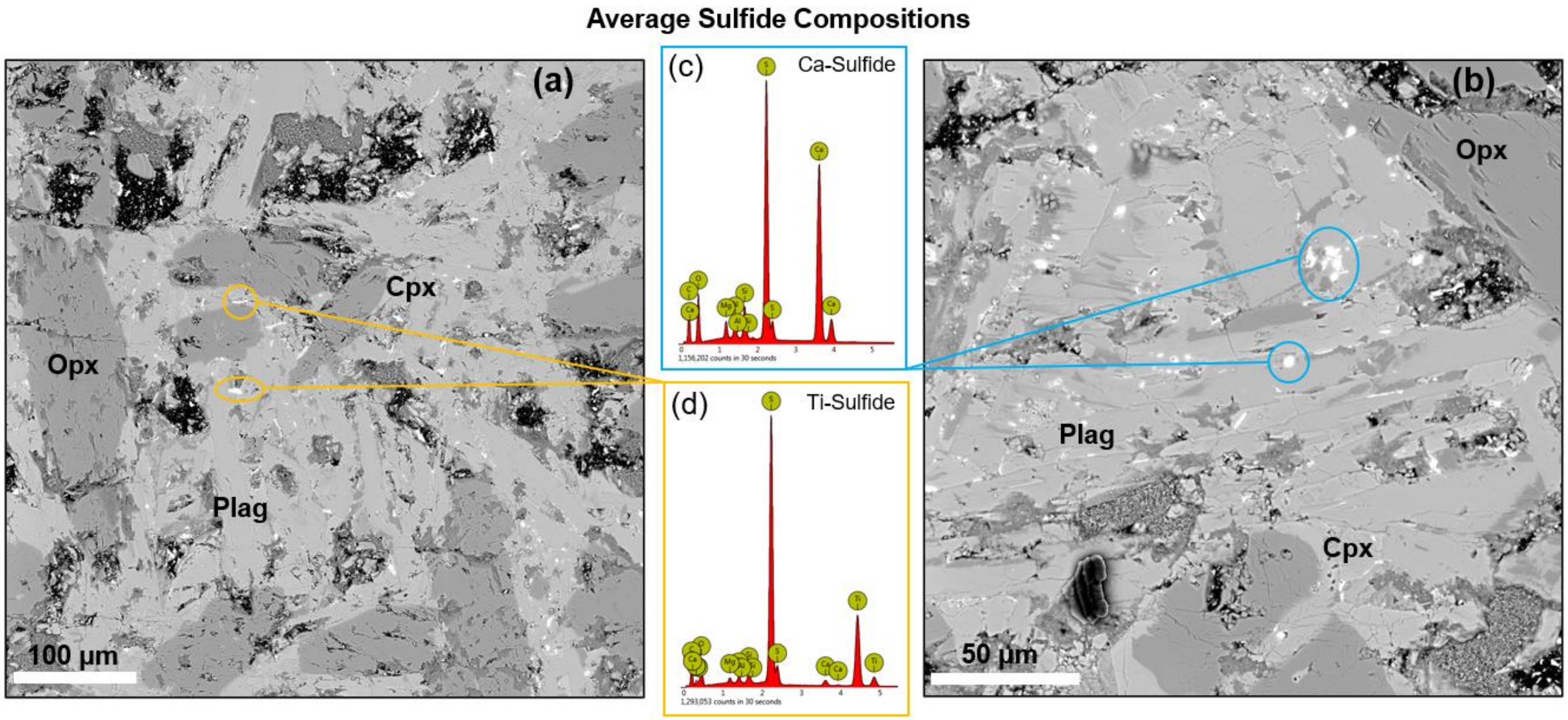

Average Sulfide Compositions

Figure 2.3. Select backscattered electron images of the Mercurian magma ocean crystallization experiment(a,b) and EDS spectra of sulfides (c,d). (b;c) highlight Ca-bearing sulfides, and (a;d) highlight Ti-bearing sulfides.

Table 2.3. Parameters used for temperature calculation, Eqs (2.3-2.7).

Heat Production Analysis Parameters	
C_x (present day, mg/kg)[a,b]	^{238}U: 7.99×10^{-9} ^{235}U: 5.76×10^{-11} ^{232}Th: 2.90×10^{-8} ^{40}K: 6.00×10^{-8}
M_x (kg/mol)	^{238}U: 0.238 ^{235}U: 0.235 ^{232}Th: 0.232 ^{40}K: 0.039
E_x (J/atom)[c]	^{238}U: 7.63×10^{-12} ^{235}U: 7.11×10^{-12} ^{232}Th: 6.48×10^{-12} ^{40}K: 1.08×10^{-12}
λ_x (sec^{-1})	^{238}U: 3.13×10^{-17} ^{235}U: 4.93×10^{-18} ^{232}Th: 1.57×10^{-18} ^{40}K: 1.77×10^{-17}
N_a (atom/mol)	6.02×10^{23}
C_p (J/kg°C)[d]	1000
Effective layer density (kg/m^3)	3258.93
M_p (kg)	3.28×10^{23}
V_p (m^3)	6.08×10^{19}

Present day isotopic abundances in enstatite chondrites, after scaling the element abundance by the proportion of each isotope. Specific heat capacity value is for a pyroxenite. [a]Barrat et al., 2014; [b]Zhao et al., 2019; [c]Rudeas, 2017; [d]Čermák and Rybach, 1982.

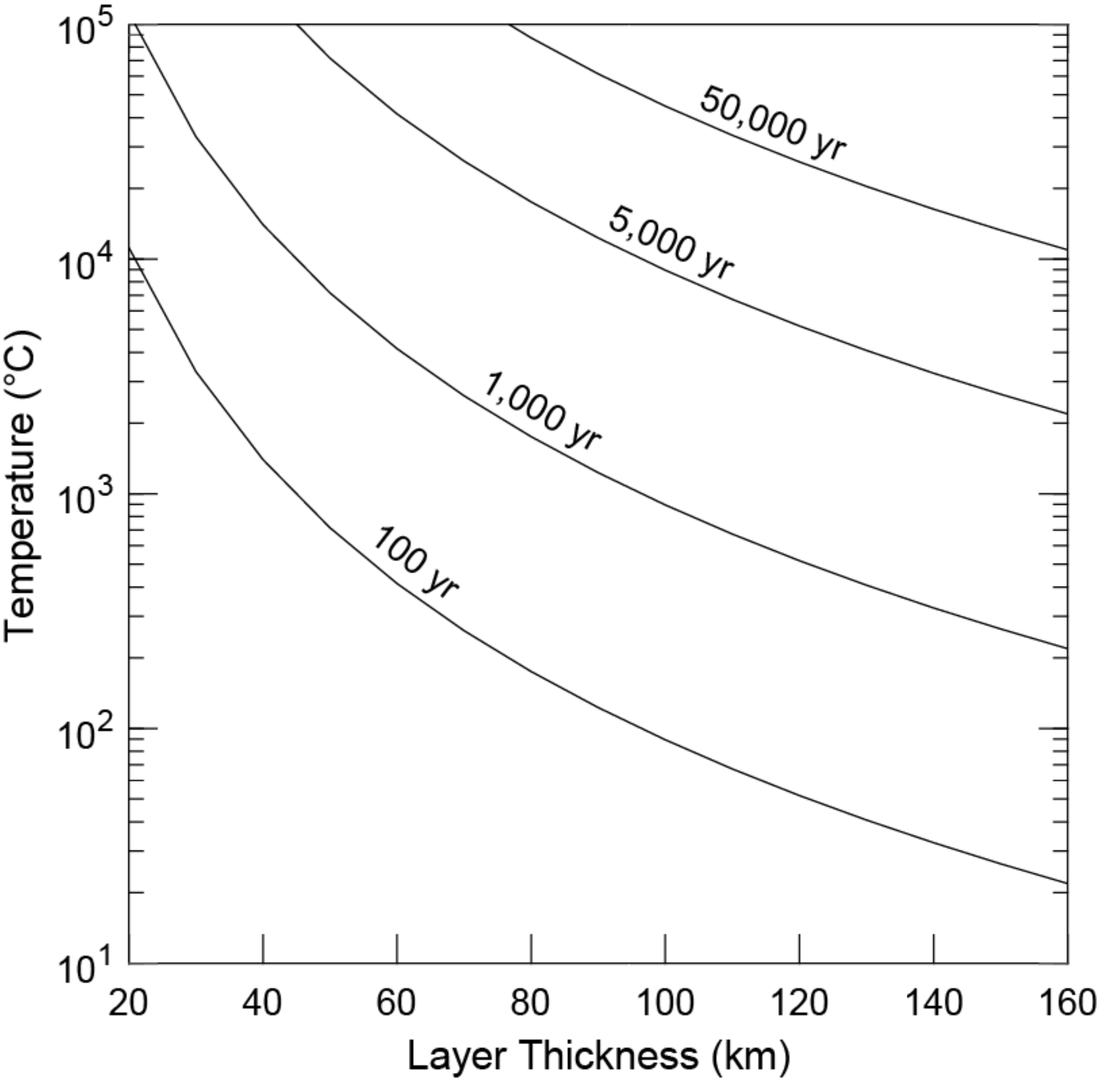

Figure 2.4. Nominal temperature increase in an HPE-bearing pyroxenite layer produced from the decay of ^{238}U, ^{235}U, ^{232}Th, and ^{40}K over 50,000 years, assuming an effective density reported in Table 2.3.

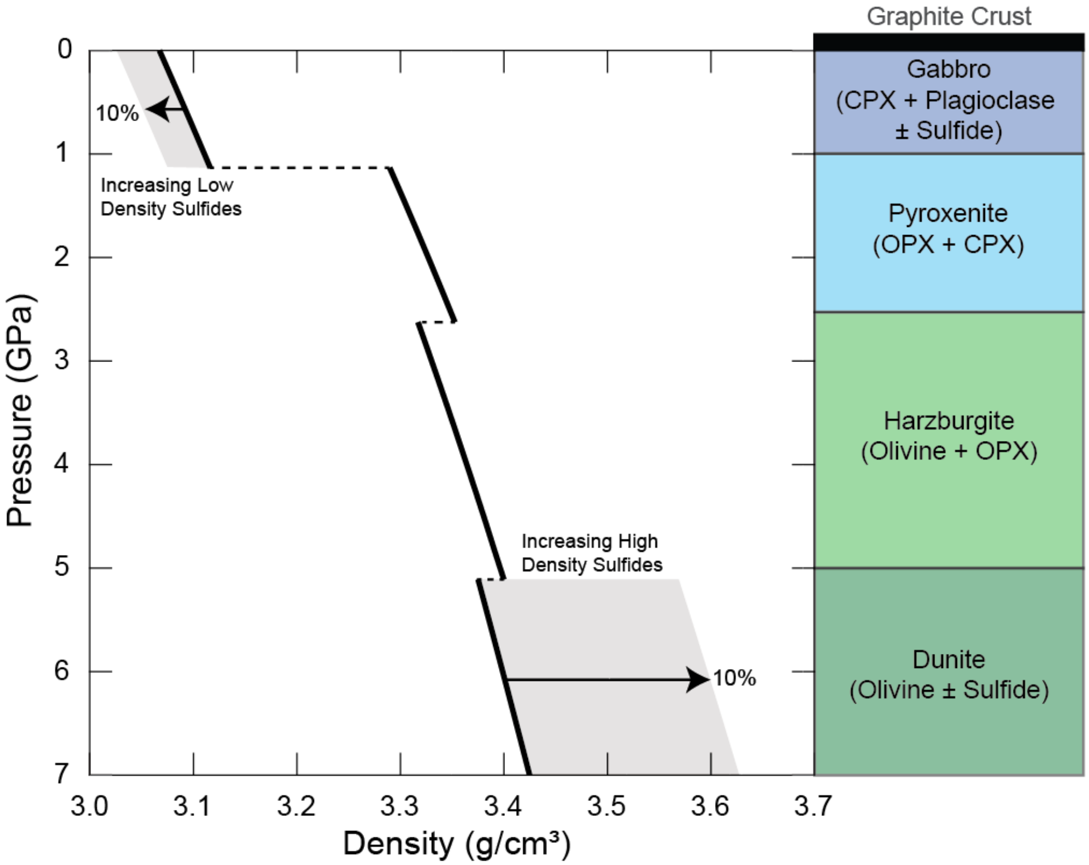

Figure 2.5. Anticipated mantle structure after considering likely formation horizons of sulfides in Mercury's mantle.

The composition and fO_2 conditions of the mantle cumulates can affect the strength and therefore the viscosity of the mantle. Increased Fe has been shown to weaken mantle silicates, such as olivine and garnet, thus decreasing the viscosity compared to more Mg-rich silicates (e.g., Katayama and Karato, 2008; Zhao et a., 2009; Bollinger et al., 2015). In addition to Fe, the presence of sulfur may have an effect on the viscosity of olivine (Hauck et al., 2004). Finally, an increase in fO_2 conditions has been observed to decrease the viscosity of dunite in deformation experiments (Keefner et al., 2011).

In addition to the effects that Fe, S, and fO_2 have on mantle silicates, it is also important to consider the effect of HPEs on the mantle viscosity. Any HPE-rich sulfide-bearing silicate layer will likely have a lower viscosity due to the possible partial melting that may occur over time. The assumed low Fe content of Mercury's mantle and the low fO_2 conditions would likely increase the viscosity relative to an Fe-rich, more oxidized mantle. Owing to the aforementioned uncertainties, we consider a range of viscosities potentially relevant to Mercury's silicate mantle for pyroxene-rich and pyroxene-poor layers (10^{23}-10^{20} Pa·s).

2.7. Gravitational Instabilities in Mercury's Mantle

The composition and saturation depths of sulfides in the Mercurian mantle are uncertain, thus, we consider a range of density differences relevant to scenarios with and without high and low density sulfides (Figures 2.2a and 2.5). The thick black line in Figure 2.2a shows the density profile for the reference case of a sulfide-free mantle. Clinopyroxene (~50%) in the pyroxenite would cause the layer to be denser than the underlying harzburgite layer, promoting formation of gravitational instabilities. In addition to the density structure, the scale and sinking rate of the instability depends on the viscosity structure of the mantle. We evaluate outcomes for a variety of possible mantle viscosity structures (Table 2.4).

2.7.1. *Instability Wavelength*

Unstable density stratification is a minimal requirement for forming gravitational instabilities. If such instabilities produced diverse source compositions in Mercury's mantle that melted to form surface terranes, the spatial scales of formation and growth need to be considered. For example, to form a lherzolite capable of producing the broad HCT-IcP terranes, the overlying pyroxenite or harzburgite layer must produce small enough diapirs that sink in a reasonable time scale (thousands to millions of years) to effectively form a new mixture. One or a few large diapirs would not create a well-mixed layer; instead, the downwelling diapirs would sink to a gravitationally stable depth in Mercury's interior, failing to form mixtures, except perhaps along the diapir boundaries. The wavelength of the downwelling instabilities that form (i.e., the diapir scale) can be calculated as a function of the viscosity contrast between adjacent mantle layers and the overlying dense layer thickness (Whitehead, 1988; Hess and Parmentier, 1995):

$$\lambda = 2.9 \times h \left(\frac{\mu_2}{\mu_1}\right)^{1/3}, \tag{2.8}$$

where λ is the wavelength of the instability, h is the thickness of the dense overlying layer, $\mu_{overlying}$ is the viscosity of the overlying layer, and $\mu_{underlying}$ is the viscosity of the underlying layer. As a reference case, we start with mantle relevant baseline assumptions for a viscosity of the overlying pyroxenite layer (10^{21} Pa·s) and an underlying harzburgite layer (10^{20} Pa·s) (e.g., Zaho et al., 2009; Hansen and Warren, 2015; Dygert et al., 2019); however, we consider other viscosity conditions for the overlying pyroxenite layer (10^{20}, 10^{21}, 10^{22}, 10^{23} Pa·s). It is possible that Mercury's deep mantle may have lower viscosities on the order of 10^{13}–10^{18} Pa·s, based on modeling from the planet's obliquity and tidal dissipation (Steinbrügge et al., 2020). When the viscosities of the two layers are approximately equal, the instability wavelengths will be hundreds of km, depending on the thickness of the pyroxenite layer, where the wavelength increases with thicker layers. When $\mu_{overlying} > \mu_{underlying}$, instabilities will be smaller than if the viscosities are equal and when $\mu_{overlying} < \mu_{underlying}$, the instabilities will be larger than when the viscosities are equal (Figure 2.6). A higher $\mu_{overlying}/\mu_{underlying}$ ratio would theoretically lead to many small instabilities to form, potentially promoting more widespread mixing of cumulates (Hess and Parmentier, 1995). A lower $\mu_{overlying}/\mu_{underlying}$ ratio is more likely to lead to fewer, or possibly a single large diapir to form, potentially leading to little or highly localized cumulate mixing (Hess and Parmentier, 1995).

2.7.2. *Instability Formation Timescale*

If Mercurian mantle sources formed by Rayleigh-Taylor instabilities produced surface volcanics, the instability formation timescale must be consistent with the inferred ages of the volcanic provinces. The instability growth timescale *(t)* can be estimated as (Whitehead, 1988; Hess and Parmentier, 1995):

$$t = \frac{6.5(\mu_2)^{2/3}(\mu_1)^{1/3}}{\Delta\rho g_M h}, \tag{2.9}$$

where $\Delta\rho$ is the density difference between the overlying and underlying layers in kg/m^3, and g_M is the surface gravitational acceleration on Mercury (~3.7 m/s^2). In addition to varying layer viscosities, we consider a range of density differences according to the possible influence of sulfides on cumulate mantle density. We assume a $\Delta\rho$ range of 100–400 kg/m^3. While the density contrasts being considered here are constant, compressible materials have been observed to enhance growth rates of instabilities (e.g., Baker, 1983; Berstein and Book, 1983); as minerals are elastic solids, instabilities may form faster than what is reported here.

The viscosity effect on the overturn timescale is significant. The greater the viscosity contrast, the faster the Rayleigh-Taylor instability growth timescale will be (Figure 2.7). When $\mu_{overlying} < \mu_{underlying}$, the overturn growth timescale would be 0.4-12.9 Myr, depending on layer thickness and density contrast, while $\mu_{overlying} > \mu_{underlying}$ will result in 0.2-129 Myr. In a case where $\mu_{overlying} << \mu_{underlying}$, as in an HPE-bearing mantle, the formation timescale would be at least two orders of magnitude shorter than presented in Figure 2.7.

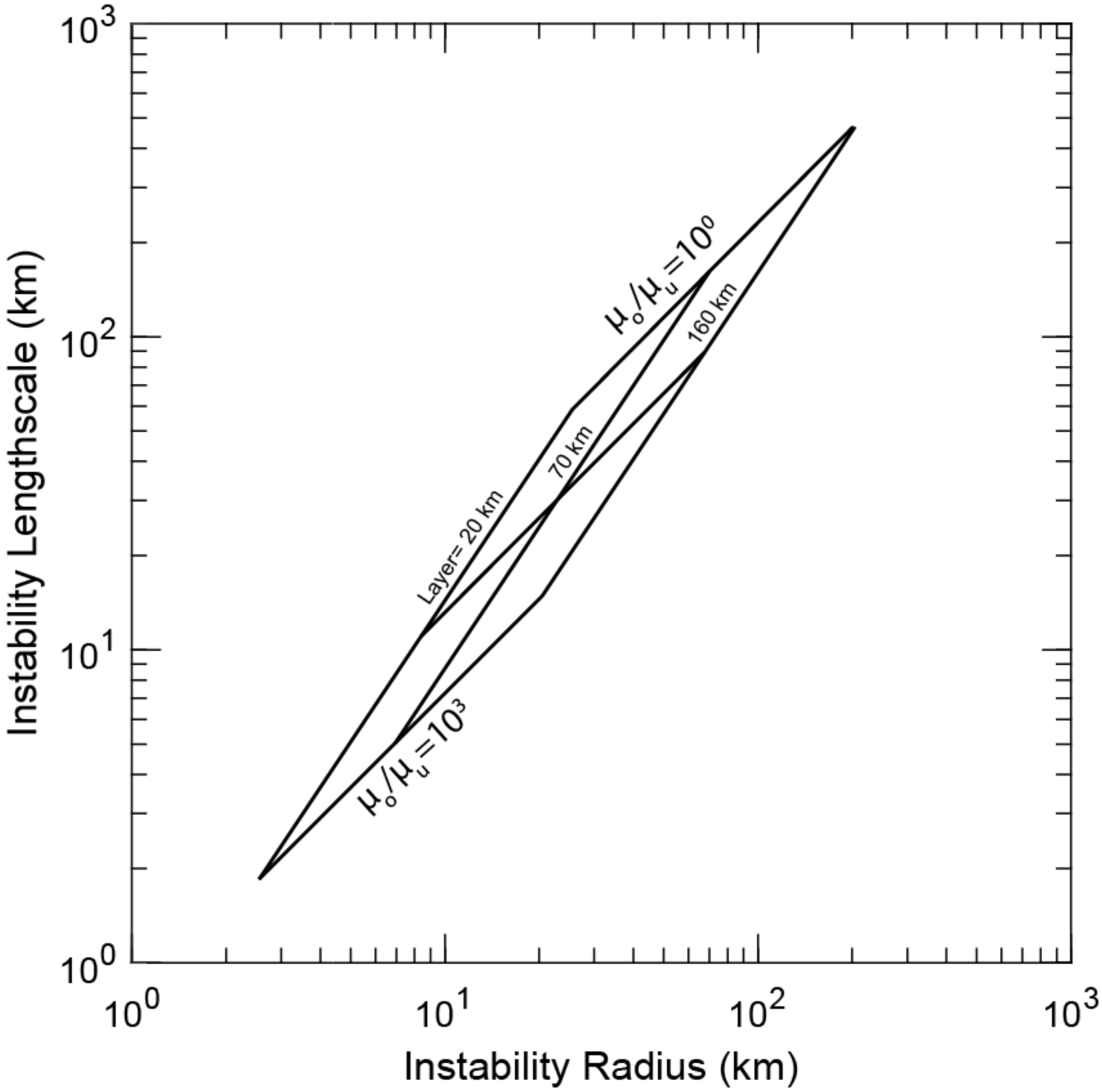

Figure 2.6. Instability lengthscale and radius at different viscosity contrasts, $\mu_{overlying}/\mu_{underlying}$ (μ_o/μ_u)= 10^3 and $\mu_{overlying}/\mu_{underlying}$ (μ_o/μ_u)= 10^1. The range of layer thicknesses (20-160 km) considered is indicated on the figure.

Table 2.4. Parameters assumed in overturn scaling analysis.

Overturn Model Parameters	
Pyroxenite Viscosity ($\mu_{overlying}$)	$10^{20–23}$ Pa·s
Harzburgite Viscosity ($\mu_{underlying}$)	$10^{20–21}$ Pa·s
Layer Thickness (h)	20–160 km
Density Contrast ($\Delta\rho$)	100, 400 kg/m^3
Gravitational Acceleration (g_M)	3.7 m/s^2

2.7.3. *Instability Sinking Velocity*

The velocity at which the diapirs settle is important to consider because if a diapir has a fast sinking velocity, the diapir and the layer it is passing through will initially form mixed body composed of the high and low density materials, but then unmix as the dense diapir sinks to the core-mantle boundary, perhaps before melting can occur (Hess and Parmentier, 1995). On the other hand, if the sinking rate is too slow, mixing can never occur, as the dense material is immobile. The diapir sinking velocity can be estimated using an expression for Stokes' settling of spheres of finite viscosity in a viscous medium (e.g., Hess and Parmentier, 1995):

$$V = \frac{1}{3}\frac{\Delta\rho g_M a}{\mu_{underlying}}\left(\frac{\mu_{underlying}+\mu_{overlying}}{\mu_{underlying}+\frac{2}{3}\mu_{overlying}}\right), \qquad (2.10)$$

where V is the settling velocity, and a is the diapir radius. The diapir radius can be estimated according to the instability wavelength with the following equation (Hess and Parmentier, 1995):

$$a = \left(\frac{3\lambda^2 h}{4\pi}\right)^{1/3}, \qquad (2.11)$$

Faster settling velocities are associated with scenarios where the density contrast between layers is larger, $\mu_{underlying} \geq \mu_{overlying}$ (Figures 2.8-2.9); the scale of the instability and layer thickness of the overlying layer will also influence the settling velocity, with thicker layers leading to slower settling velocities (Figure 2.7). In cases where $\mu_{underlying} << \mu_{overlying}$, the settling velocities are at least two orders of magnitude faster than in the cases presented in Figures 2.8 and 2.9, as could be possible in an HPE-bearing silicate mantle.

2.8. Evolution of Mercury's Interior

2.8.1. *Silicate Mantle*

In the case of Mercury's mantle being comprised of silicate minerals only, the density difference between layers is likely to be a few percent (e.g., Figure 2.2a), ~100 kg/m^3 at the interface between the layers. In this scenario, the instability formation timescale between overlying and underlying layers is longer than in the scenario with a larger density difference between layers. Scaling analysis suggests instability formation timescale to be between 1 and 100 Myr, depending on layer thickness and viscosity differences (longer timescales relating to thinner layers and smaller viscosity contrasts). Additionally, the sinking velocities for the instabilities are slower than cases with a larger density contrast, on the order of 1.7×10^{-1} to 1.9×10^{3} km/Myr. Given these parameters sinking could mix late materials ~20km to the core mantle boundary in 100 Myr. Depending on the lateral extent of the mixing and the sinking velocity, over thousands to tens of millions of years, there could be enough mixing to achieve the different volcanic source compositions.

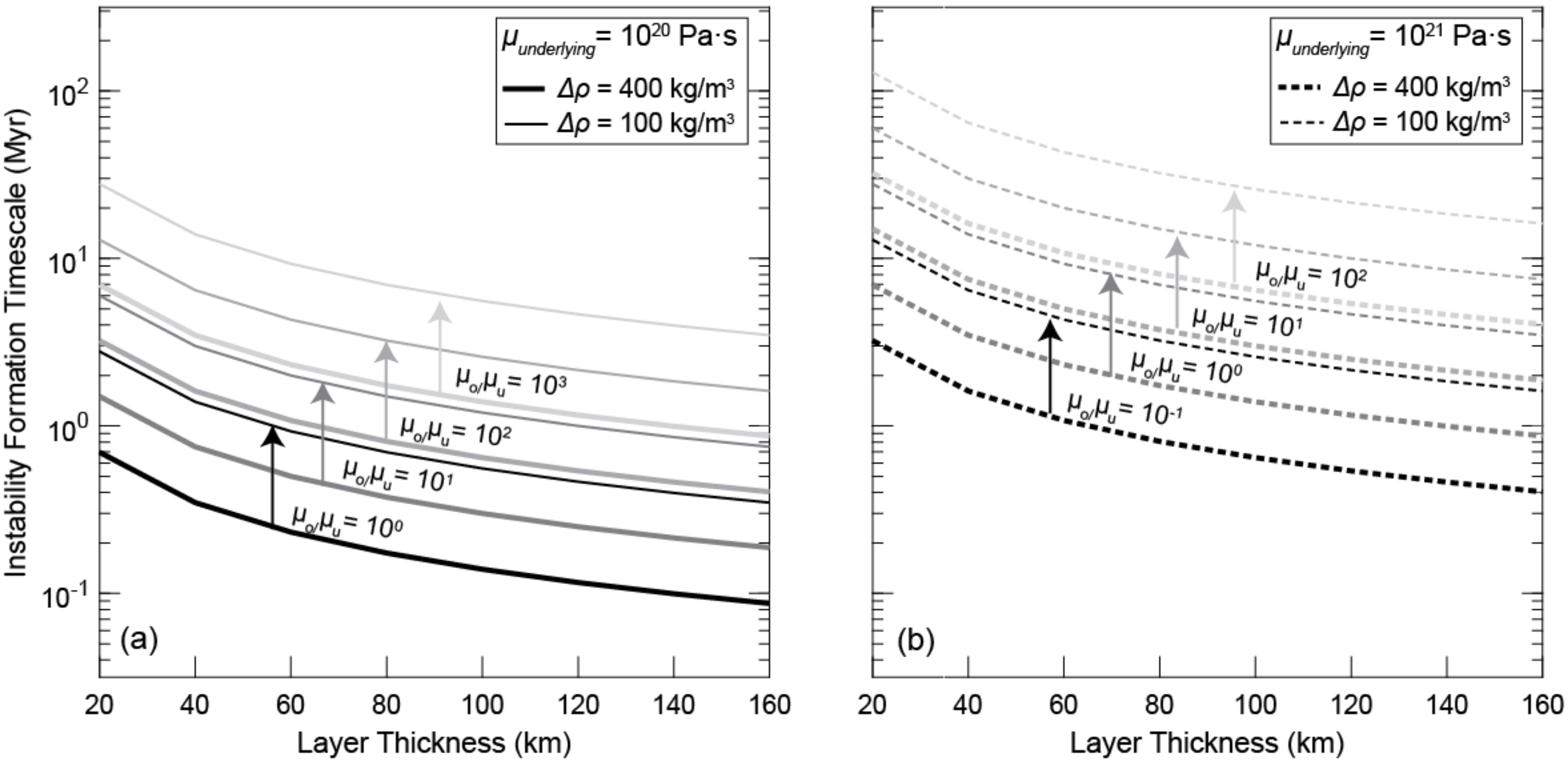

Figure 2.7. Instability formation timescale versus layer thickness for (a) an underlying harzburgite viscosity ($\mu_{underlying}$) of 10^{20} Pa·s, and (b) 10^{21} Pa·s. Dashed lines indicate harzburgite viscosity of 10^{21} Pa·s, while solid lines indicate harzburgite viscosity of 10^{20} Pa·s. The dark gray to light gray lines show changing $\mu_{overlying}$ values from 10^{20} to 10^{23} Pa·s, shown as a ratio of $\mu_{overlying}/\mu_{underlying}$ (μ_o/μ_u). Additionally, the thick to thin lines show the variation of $\Delta\rho$ for each $\mu_{overlying}$ scenario.

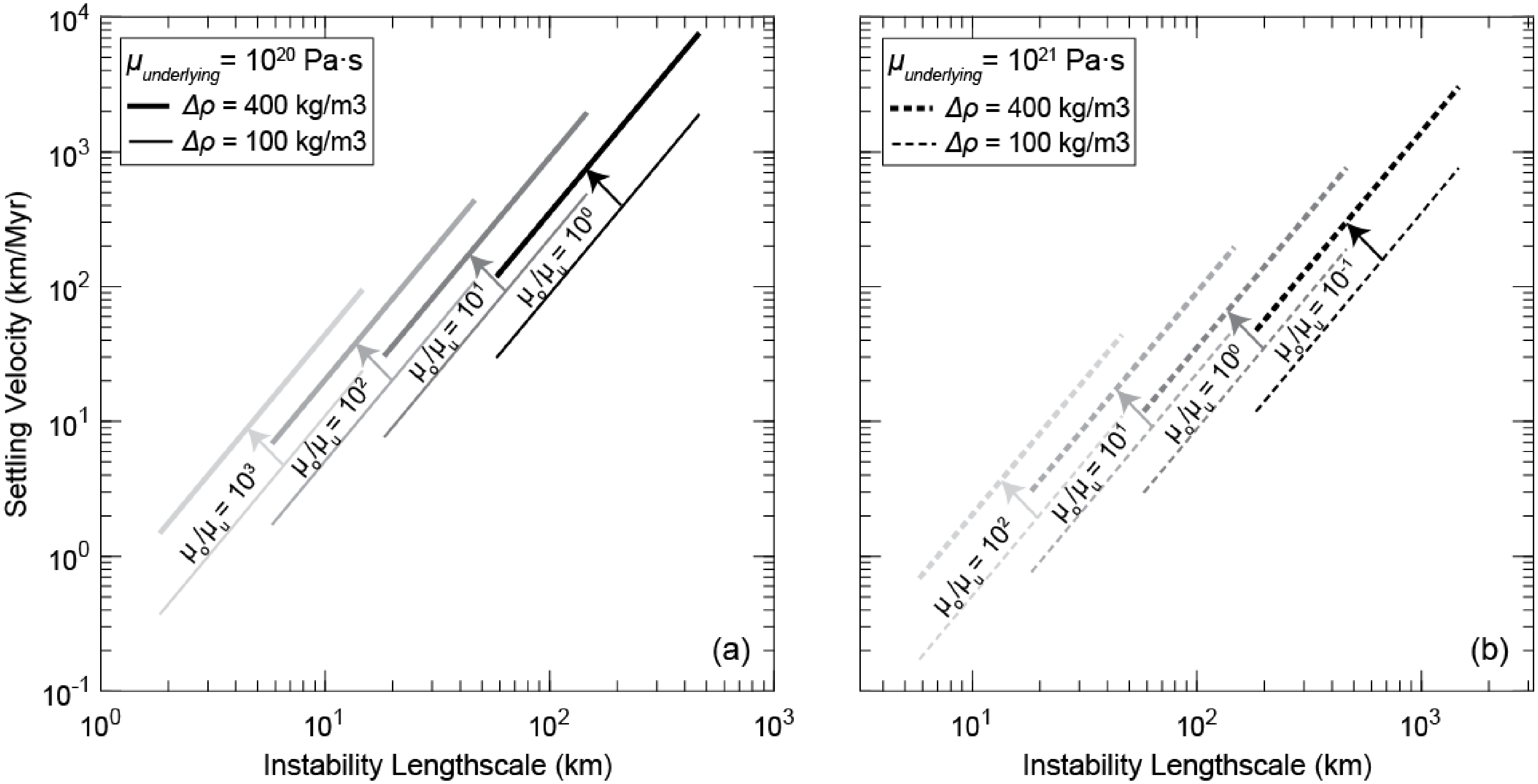

Figure 2.8. Settling velocity versus instability length for (a) an underlying harzburgite viscosity ($\mu_{underlying}$) of 10^{20} Pa·s in solid lines, and (b) 10^{21} Pa·s in dashed lines. The dark gray to light grey lines show changing $\mu_{overlying}$ values from 10^{20} to 10^{23} Pa·s, shown as a ratio of $\mu_{overlying}/\mu_{underlying}$ (μ_o/μ_u). Additionally, the thick to thin lines show the variation of $\Delta\rho$ for each $\mu_{overlying}$ scenario.

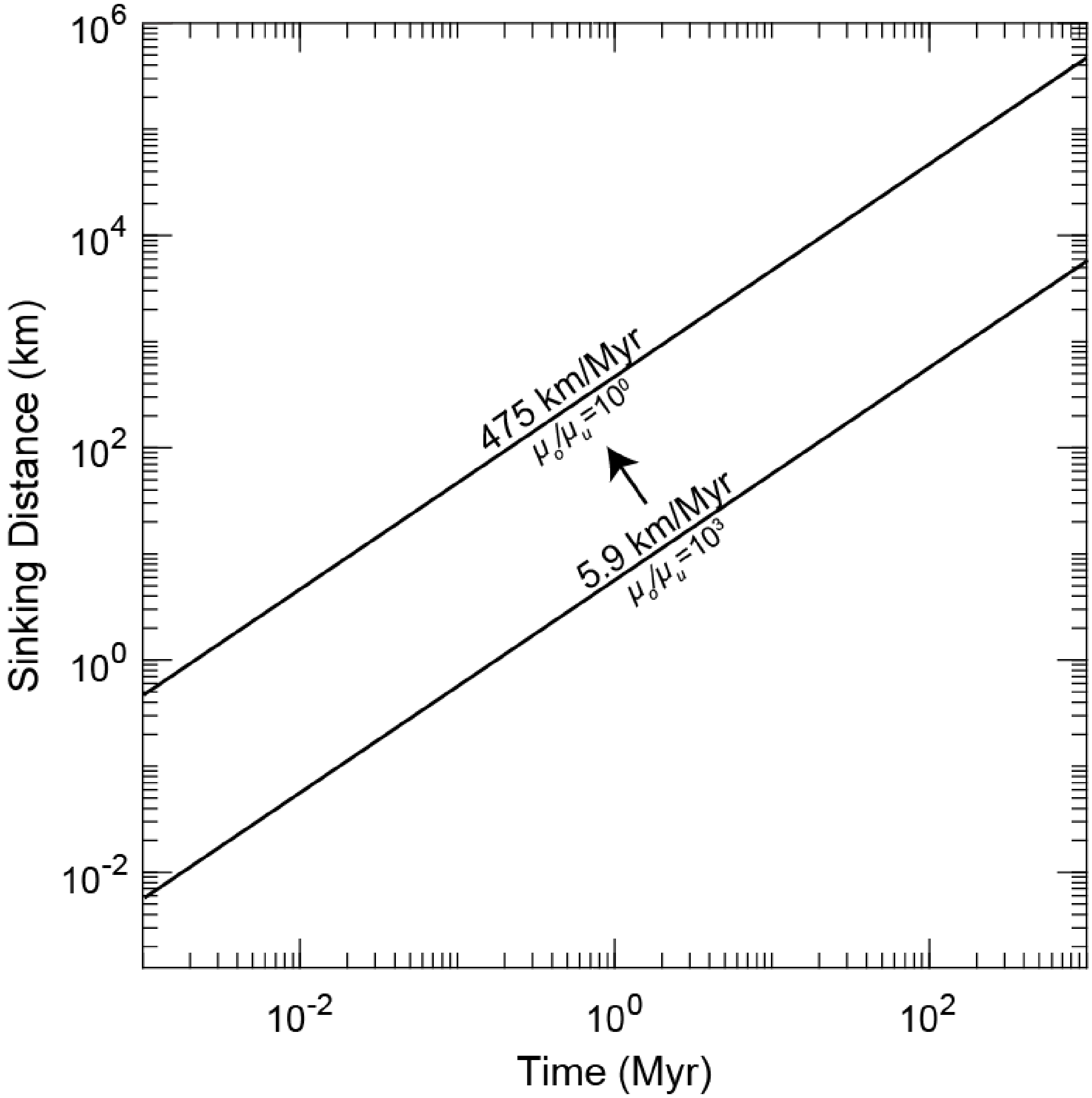

Figure 2.9. Sinking depth for downwelling cumulates over time for an 80 km thick layer, $\Delta\rho$=100 g/cm^3. Gray region indicates the range of possible sinking depths for the parameters considered here. μ_o/μ_u is the ratio of overlying and underlying layer viscosities, $\mu_o/\mu_u = 10^{23}/10^{20}$ Pa·s and $\mu_o/\mu_u = 10^{20}/10^{20}$ Pa·s

2.8.2. ***Silicate and Sulfide Mantle***

If denser sulfides are present in deeper layers, there is the possibility they neutralize any instabilities (Figure 2.2). Conversely if they are present in shallower layers, they could further enhance any existing gravitational instabilities (Figure 2.2). Boukaré et al. (2019) predicted that at fO_2s >IW-3, sulfides (perhaps troilite) will precipitate earlier from the magma ocean and thus may be anticipated lower in the subsequent cumulate mantle. At fO_2s of <IW-6, less dense (alkali-bearing) sulfides may be expected to precipitate later in the crystallization sequence, thus being concentrated at shallower depths in the mantle, although this is dependent on the bulk sulfur and alkali element content (Boukaré et al., 2019). The crystallization experiment discussed in Section 2.3 showed Ca-bearing and, to a lesser extent, Ti- bearing sulfides precipitating from a late magma ocean composition. If low density HPE-bearing sulfides precipitate later in the crystallization sequence, they would likely remain in shallower regions of the mantle, having little influence on layers that may form gravitational instabilities (Figure 2.5).

Dense sulfides (e.g., troilite) would enhance existing gravitational instabilities if present in shallower layers. If this is the case, the large density contrast between a dense overlying layer and a less dense underlying layer will lead to a faster instability formation (~0.1-10 Myr) and downwelling velocities (6.8×10^{-1} to 7.6×10^{3} km/Myr) than in a smaller density contrast scenario such as in the silicate-only scenario where settling velocities may be up to orders of magnitude longer. Over 100 Myr, mixing of initially shallow and deep materials may be possible. However, the extent of the instability (settling velocity, formation timescale, etc.) will also depend on parameters such as layer thickness and the viscosities of the layers. Importantly, the gravitational instabilities are contingent upon the location and amount of sulfide precipitated in the mantle. More work on the stability of sulfides in Mercury’s mantle, precipitation depths and modal abundances is needed to better constrain this parameter.

2.9. Implications for Mercury’s Surface Geochemistry

The analysis presented in this work showed a magma ocean that cooled and solidified with a flotation crust would produce a mineralogically stratified mantle with an unstable density configuration. The analysis demonstrates that under a variety of reasonable physical conditions (viscosity, density, and layer thicknesses) forming instabilities that produce cumulate mantle overturn timescales of (~0.1–100 Myr) is feasible. Such an overturn timescale is consistent with ages of formation of Mercury’s distinct surface geochemical terranes, e.g., 3.7–2.5 Ga for BP and 4.1–4.0 Ga for HCT (Neukum et al., 2001; Marchi et al., 2009, 2013; Le Feuvre and Wieczorek, 2011; Ostrach et al., 2015).

2.9.1. ***Borealis Planitia***

The BP has a low-Mg region at high latitudes (>60°N) and a high-Mg region at latitudes of ~30-60°N (Weider et al., 2016; Lawrence et al., 2017). Between the high- and low-Mg regions, the Mg content is estimated to vary by ~8 wt% (Vander Kaaden et al., 2017). This variability within a single geologic unit may be associated with heterogeneity within the mantle source.

The BP are believed to be the result of effusive volcanism (Head et al., 2011; Stockstill-Cahill et al., 2012; Ostrach et al., 2015) and resemble large terrestrial flood basalt features in composition and morphology (e.g., Weider et al., 2012; Vander Kaaden and McCubbin, 2016). The BP exhibits spatial and temporal geochemical variations, therefore, terrestrial basaltic sources with lateral geochemical variations, such as Hawaii and the Siberian and Deccan traps, may be useful analogues to understanding the geochemical variations in the BP. The Siberian and Deccan flood basalts exhibit spatial chemical variations (e.g., Fedorenko et al., 1996; Sen, 2001) that may be the result of fractionation, crustal assimilation, magma mixing, and/or sulfide separation. Short-term geochemical variations of major elements in Hawaiian basalts (Kea and Loa volcanic tracks) are also attributed to shallow melting processes, while long term variations are often attributed to heterogeneities in the source region (e.g., Ren et al., 2005; Bianco et al., 2011; Hofmann and Farnetani, 2013). The Hawaiian plume is proposed to have a bimodal structure that may source from chemically heterogeneous areas within its source region of the Earth's mantle (e.g., Hofmann and Farnetani, 2013). Since the BP exhibits chemical variations on the latitudinal scale, a possible solution could be heterogeneities within its own source region. This compositional heterogeneity may indicate that regions of the mantle remain not fully mixed or mixing occurring in specific locations in Mercury's interior. Wang et al. (2022) suggested that thermal anomalies may have existed in Mercury's interior as a result of large impactors which may cause partial melting to varying degrees therefore contributing to surface composition heterogeneity.

2.9.2. *Homogeneous and Heterogeneous Mantle Scenario*

The overturn analysis suggests that there are many possible outcomes, one being that many small diapirs that form, in another, a single (or few) larger diapirs form. The former scenario, with many small diapirs, would likely result in a more homogeneous mantle. This is in large part controlled by the viscosity differences between the overlying and underlying layers, where a larger viscosity difference will result in many small diapirs forming (Hess and Parmentier, 1995). In this case, the downwelling material would be more widespread throughout the mantle, effectively mixing with the previously underlying cumulates (Figure 2.10).

The single or few diapir scenario would likely result in a more heterogeneous mantle (Figure 2.10). This case correlates to faster settling velocity which, in addition to fewer instabilities forming, leads to a shorter time period for cumulate mixing during downwelling. This process would also lead to less widespread mixing throughout the mantle, potentially resulting in incongruent mixing throughout the mantle as suggested in models proposing asymmetry in lunar mantle during cumulate mantle overturn (e.g., Zhong et al., 2000; Zhang et al., 2013).

2.10. Conclusions

We analyzed a hypothetical mantle structure for Mercury and how the density structure would vary with the presence or absence of sulfides. The proposed mantle structure suggests less dense, alkali-bearing sulfides precipitating in the upper mantle and dense sulfides precipitating in the lower mantle. Ca- and alkali-bearing sulfides may be an important component of heat production in the mantle as they are reservoirs for heat producing elements. If these HPEs are concentrated in specific sulfide-bearing layers, they may be capable of hundreds to thousands of degrees of heating over thousands of years, which would promote partial melting in the mantle.

The proposed silicate mantle structure suggests a density instability between the denser pyroxenite and less dense harzburgite layers, which may promote mixing between the layers via denser material flowing into the less dense material in Rayleigh-Taylor instabilities. In all scenarios evaluated, the instability formation could occur within 100 Myr, depending on mineralogy, density, and viscosity structure of Mercury's mantle. Given these results and the estimated time of igneous activity on Mercury (HCT: 4.1–4.0 Ga, BP: 3.7–2.5 Ga, Neukum et al., 2001; Marchi et al., 2009; Le Feuvre and Wieczorek, 2011; Ostrach et al., 2015) we infer that cumulate mixing by the growth of Rayleigh-Taylor instabilities could have occurred enough to form surficial volcanic provinces. The compositionally diverse surface we see today could be a direct consequence of Mercury's interior structure after cumulate mantle overturn.

2.11. Acknowledgements

The authors gratefully acknowledge NASA grant 80NSSC18K0249 which supported this work.

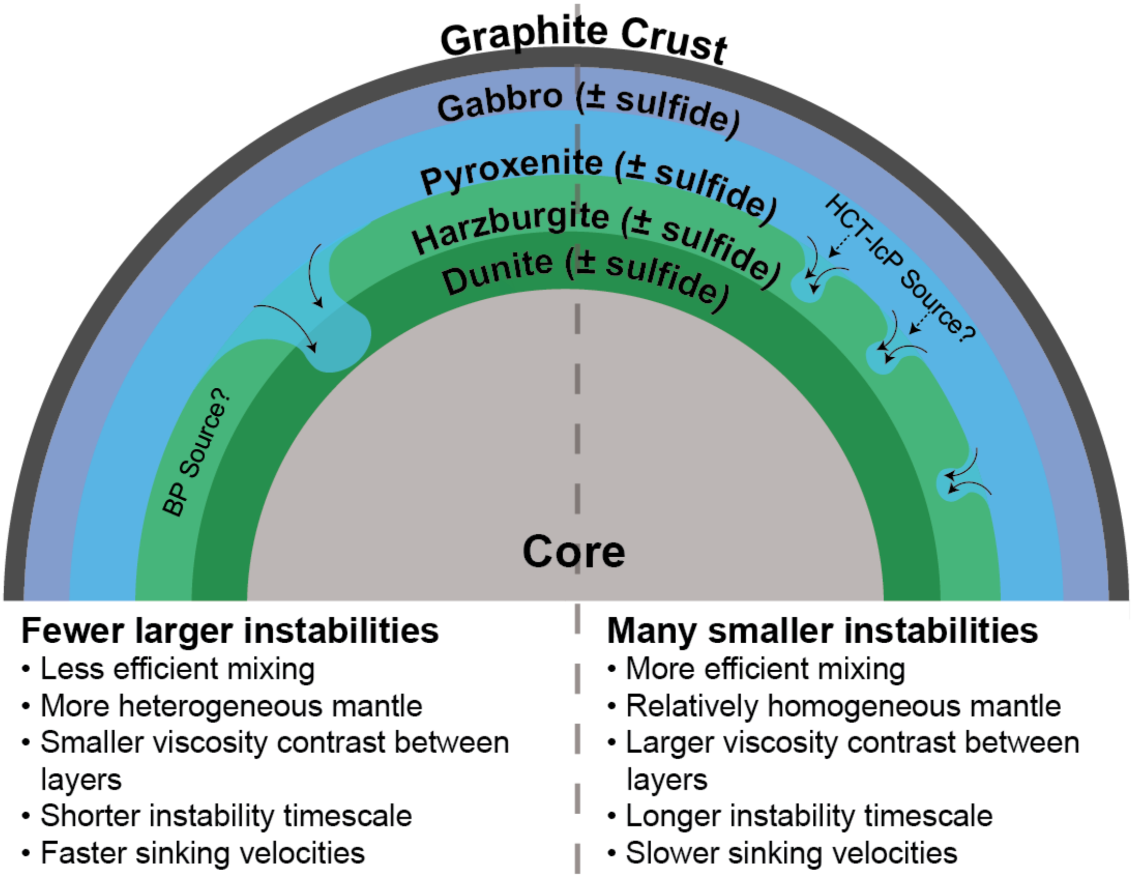

Figure 2.10. Hypothetical cross-section of Mercury's juvenile mantle after magma ocean solidification with a graphite flotation crust. The left side of the figure illustrates a scenario in which there are fewer, larger instabilities that form which promotes inefficient mixing of the mantle material resulting in a heterogeneous mantle composition. The right side of the figure shows a scenario with many smaller instabilities which promotes more efficient mixing of mantle material and may result in a relatively homogeneous mantle composition. Possible source compositions for the BP and HCT-IcP are indicated on the figure where BP could source from a harzburgite-rich layer and the HCT-IcP could source from the mixing between the pyroxenite and harzburgite layers to produce a lherzolitic composition.

References

Anzures, B. A., Parman, S. W., Milliken, R. E., Namur, O., Cartier, C., & Wang, S. (2020). Effect of sulfur speciation on chemical and physical properties of very reduced mercurian melts. *Geochimica et Cosmochimica Acta, 286,* 1-18. https://doi.org/10.1016/j.gca.2020.07.024

Baker, L. (1983). Compressible Rayleigh-Taylor instability. *The Physics of Fluids, 26,* 950-952. https://doi.org/10.1063/1.864245

Barnes, S. J., Fiorentini, M. L., Austin, P., Gessner, K., Hough, R. M., & Squelch, A. P. (2008). Three-dimensional morphology of magmatic sulfides sheds light on ore formation and sulfide melt migration. *Geology, 36,* 655-658. https://doi.org/10.1130/G24779A.1

Barrat, J.-A., Zanda, B., Jambon, A., & Bollinger, C. (2014). The lithophile trace elements in enstatite chondrites. *Geochimica et Cosmochimica Acta, 128,* 7194. https://doi.org/10.1016/j.gca.2013.11.042

Berthet, S., Malavergne, V., & Righter, K. (2009). Melting of the Indarch meteorite (EH4 chondrite) at 1 GPa and variable oxygen fugacity: Implications for early planetary differentiation processes. *Geochimica et Cosmochimica Acta, 73(20),* 6402-6420. https://doi.org/10.1016/j.gca.2009.07.030

Bertka, C. M. & Fei, Y. (1998). Density profile of an SNC model martian interior and the moment-of-inertia factor of Mars. *Earth and Planetary Science Letters, 157,* 79-88. https://doi.org/10.1016/S0012-821X(98)00030-2

Bernstein, I. B. & Book, D. L. (1983). Effect of compressibility on the Rayleigh-Taylor instability. *The Physics of Fluids, 26,* 453-458. https://doi.org/10.1063/1.864158

Bianco, T. A., Ito, G., van Hunen, J., Ballmer, M. D., & Mahoney, J. J. (2011). Geochemical variations at intraplate hot spots caused by variable melting of a veined mantle plume. *Geochemistry, Geophysics, Geosystems, 12,* Q0AC13. https://doi.org/10.1029/2011GC003658

Bollinger, C., Merkel, S., Cordier, P., & Raterron, P. (2015). Deformation of forsterite polycrystals at mantle pressure: Comparison with Fe-bearing olivine and the effect of iron on its plasticity. *Physics of the Earth and Planetary Interiors, 240,* 95-104. https://doi.org/10.1016/j.pepi.2014.12.002

Boujibar, A., Habermann, M., Righter, K., Ross, D. K., Pando, K., Righter, M., & Danielson, L. R. (2019). U, Th, and K partitioning between metal, silicate, and sulfide and implications for Mercury's structure, volatile content, and radioactive heat production. *American Mineralogist,* 104, 1221-1237. https://doi.org/10.2138/am-2019-7000

Boukaré, C.-E., Parman, S. W., Parmentier, E. M., & Anzures, B. A. (2019). Production and Preservation of Sulfide Layering in Mercury's Mantle. *Journal of Geophysical Research: Planets, 124,* 3354-3372. https://doi.org/10.1029/2019JE005942

Brown, S. M. & Elkins-Tanton, L. T. (2009). Compositions of Mercury's earliest crust from magma ocean models. *Earth and Planetary Science Letters, 286,* 446-455. https://doi.org/10.1016/j.epsl.2009.07.010

Burbine, T. H., McCoy, T. J., Nittler, L. R., Benedix, G. K., Cloutis, E. A., & Dickinson, T. L. (2010). Spectra of extremely reduced assemblages: Implications for

Mercury. *Meteroitics & Planetary Science, 37,* 1233-1244. https://doi.org/10.1111/j.1945-5100.2002.tb00892.x

Byrne, P. K., Ostrach, L. R., Fassett, C. I., Chapman, C. R., Denevi, B. W., Evans, A. J., Klimczak, C., Banks, M. E., Head, J. W., & Solomon, S. C. (2016). Widespread effusive volcanism on Mercury likely ended by about 3.5 Ga. *Geophysical Research Letters, 43(14),* 7408-7416. https://doi.org/10.1002/ 2016GL069412

Čermák, V. & Rybach L. (1982). Thermal Properties. In Hellwege, K.-H. ed., Landolt-Bornstien numerical data and functional relationships in science and technology: new Series, Group V. Geophysics and Space Research, V. 1 Physical properties of Rocks, Subvolume a: Springer-Verlag, Berlin, P. 305-371 (in English and German).

Charlier, B., Grove, T. L., & Zuber, M. T. (2013). Phase equilibria of ultramafic compositions on Mercury and the origin of the composition- al dichotomy. Earth and Planetary Science Letters, 363, 50–60. https://doi.org/10.1016/j.epsl.2012.12.021

Charlier, B., Grove, T. L., Namur, O., Holtz, F. (2018). Crystallization of the lunar magma ocean and the primordial mantle-crust differentiation of the Moon. *Geochimica et Cosmochimica Acta*, *234*, 50-69. https://doi.org/10.1016/j.gca.2018.05.006

Dygert, N., Hirth, G., & Liang, Y. (2016). A flow law for ilmenite in dislocation creep: Implications for lunar cumulate mantle overturn. *Geophysical Research Letters, 43,* 532-540. https://doi.org/10.1002/2015GL066546

Dygert, N., Bernard, R. E., & Behr, W. M. (2019). Great Basin Mantle Xenoliths Record Active Lithospheric Downwelling Beneath Central Nevada. *Geochemistry, Geophysics, Geosystems, 20,* 751-772. https://doi.org/10.1029/2018GC007834

Elkins-Tanton, L. T. (2012). Magma Oceans in the Inner Solar System. *Annual Reviews of Earth and Planetary Sciences, 40,* 113-139. https://doi.org/10.1146/annurev-earth-042711-105503

Evans, L. G., Peplowski. P. N., Rhodes, E. A., Lawrence, D. J., McCoy, T. J., Nittler, L. R., Solomon, S. C., Sprague, A. L., Stockstill-Cahill, K. R., Starr, R. D., Weider, S. Z., Boynton, W. V., Hamara, D. K., & Goldsten, J. O. (2012). Major-element abundances on the surface of Mercury: Results from the MESSENGER Gamma-Ray Spectrometer. *Journal of Geophysical Research: Planets, 117,* E00L07. https://doi.org/10.1029/2012JE004178

Faul, U. H. (1997). Permeability of partially molten upper mantle rocks from experiments and percolation theory. *Journal of Geophysical Research, 102,* 10299-10311. https://doi.org/10.1029/96JB03460

Fedorenko, V. A., Lightfoot, P. C., Naldrett, A. J., Czamanske, G. K., Hawkesworth, C. J., Wooden, J. L., & Ebel, D. S. (1996). Petrogenesis of the Flood-Basalt Sequence at Noril'sk, North Central Siberia. *International Geology Review, 38,* 99-135. https://doi.org/10.1080/00206819709465327

Floss, C., Strait, M. M., & Crozaz, G. (1990). Rare earth elements and the petrogenesis of aubrites. *Geochimica et Cosmochimica Acta*, *54*, 3553-3558. https://doi.org/10.1016/0016-7037(90)90304-4

Freed, A. M., Hirth, G., & Behn, M. D. (2012). Using short-term postseismic displacements to infer the ambient deformation conditions of the upper mantle. *Journal of Geophysical Research: Solid Earth, 117,* B01409. https://doi.org/10.1029/2011JB008562

Gaetani, G. A. & Grove, T. L. (1999). Wetting of mantle olivine by sulfide melt: implications for Re/Os ratios in mantle peridotite and late-stage core formation. *Earth and Planetary Science Letters*, *169*, 147-163. https://doi.org/10.1016/S0012-821X(99)00062-X

Gourmelen, A. & Amelung, F. (2005). Postseismic Mantle Relaxation in the Central Nevada Seismic Belt. *Science, 310*, 1473-1476. https://doi.org/10.1126/science.1119798

Graham, A. L., Easton, E. J., & Hutchison, R. (1977). The Mayo Belwa meteorite: a new enstatite chondrite fall. *Mineralogical Magazine, 41(320),* 487-492. https://doi.org/10.1180/minmag.1977.041.320.10

Hager, B. H. (1991). Mantle viscosity: A comparison of models from postglacial rebound and from the geoid, plate driving forces, and advancing heat flux. In R. Sabadini, K. Lambeck, & E. Boschi (Eds.), *Glacial Isostacy, Sea-level and Mantle Rheology, NATO ASI Series (Series C: Mathematical and Physical Sciences).* Dordrecht: Springer.

Hansen, L. N. & Warren, J. M. (2015). Quantifying the effect of pyroxene on deformation of peridotite in a natural shear zone. *Journal of Geophysical Research- Solid Earth, 120,* 2717-2738. https://doi.org/10.1002/2014JB011584

Harada, Y., Goossens, S., Matsumoto, K., Yan, J., Ping, J., Noda, H., & Haruyama, J. (2014). Strong tidal heating in an ultralow-viscosity zone at the core-mantle boundary of the Moon. *Nature Geoscience, 7,* 569-572. https://doi.org/10.1038/ngeo2211

Hauck II, S. A., Dombard, A. J., Phillips, R. J., Solomon, S. C. (2004). Internal and tectonic evolution of Mercury. *Earth and Planetary Science Letters, 222,* 713-728. https://doi.org/10.1016/j.epsl.2004.03.037

Head, J. W., Chapman, C. R., Strom, R. G., Fassett, C. I., Denevi, B. W., Blewett, D. T., Ernst, C. M., Watters, T. R., Solomon, S. C., Murchie, S. L., Prockter, L. M., Chabot, N. L., Gillis-Davis, J. J., Whitten, J. L., Goudge, T. A., Baker, D. M. H., Hurwitz, D. M., Ostrach, L. R., Xiao, Z., Merline, W. J., Kerber, L., Dickson, J. L., Oberst, J., Byrne, P. K., Klimczak, C., Nittler, L. R. (2011). Flood Volcanism in the Norther High Latitudes of Mercury Revealed by MESSENGER. *Science, 333*, 1853-1856. https://doi.org/10.1126/science.1211997

Hess, P. C. & Parmentier, E. M. (1995). A model for the thermal and chemical evolution of the Moon's interior: implications for the onset of mare volcanism. *Earth and Planetary Science Letters, 134(3-4),* 501-514. https://doi.org/10.1016/0012-821X(95)00138-3

Hirth, G. and Kohlstedt, D. (2004). Rheology of the Upper Mantle and the Mantle Wedge: A View from the Experimentalists. In Inside the Subduction Factory, J. Eiler (Ed.). https://doi.org/10.1029/138GM06

Hofmann, A. W. & Farnetani, C. G. (2013). Two views of Hawaiian plume structure. *Geochemistry, Geophysics, Geosystems, 14,* 5308-5322. https://doi.org/10.1002/2013GC004942

Holland, T. J. B. & Powell, R. (1998). An internally consistent thermodynamic data set for phases of petrological interest. *Journal of Metamorphic Geology, 16,* 309-343. https://doi.org/10.1111/j.1525-1314.1998.00140.x

Hugh-Jones, D. A. & Angel, R. J. (1997). Effect of Ca2+ and Fe2+ on the equation of state of MgSiO3 orthopyroxene. *Journal of Geophysical Research, 102(B6),* 12,333-12340. https://doi.org/10.1029/96JB03485

Jackson, J. M., Sinogeikin, S. V., & Bass, J. D. (1999). Elasticity of MgSiO3 orthoenstatite. *American Mineralogist, 84(4),* 677-680. https://doi.org/10.2138/am-1999-0421

Katayama, I. & Karato, S-I. (2008). Effects of water and iron content on the rheological contrast between garnet and olivine. *Physics of the Earth and Planetary Interiors, 166*, 57-66. https://doi.org/10.1016/j.pepi.2007.10.004

Keefner, J. W., Mackwell, S. J., Kohlstedt, D. L., Heidelbach, F. (2011). Dependence of dislocation creep of dunite on oxygen fugacity: Implications for viscosity variations in Earth's mantle. *Journal of Geophysical Research: Solid Earth, 116,* B05201. https://doi.org/10.1029/2010JB007748

Keil, K. (1968). Mineralogical and chemical relationships among enstatite chondrites. *Journal of Geophysical Research, 73(22),* 1896-1977. https://doi.org/10.1029/JB073i022p06945

Keil, K. & Brett, R. (1974). Heideite, $(Fe,Cr)_{1+X}(Ti,Fe)_2S_4$, a new mineral in the Bustee enstatite achondrite. *American Mineralogist, 59,* 465-470.

Kesson, S. E. & Ringwood, A. E. (1976). Mare basalt petrogenesis in a dynamic Moon. *Earth and Planetary Science Letters, 30,* 155-163. https://doi.org/10.1016/0012-821X(76)90241-7

Khan, A., Ceylan, S., Van Driel, M., Giardini, D., Lognonné, P., Schmerr, H. S. N. C., Stahler, S. C., Duran, A. C., Huang, Q., Kim, D., Biroquet, A., Charalambous, C., Clinton, J. F., Davis, P. M., Drilleau, M., Karakostas, F., Lekic, V., McLennan, S. M., Maguire, R. R., Michaut, C., Panning, M. P., Pike, W. T., Pinot, B., Plasman, M., Scholz, J-R., Widmer-Schnidrig, R., Spohn, T., Smrekar, S. E., & Banerdt, W. B. (2021). Upper mantle structures of Mars from InSight seismic data. *Science, 373,* 434-438. https://doi.org/10.1126/science.abf2966

King, S. D. (1995). Models of mantle viscosity. In T. J. Ahrens (Eds.), *Mineral Physics & Crystallography: A Handbook of Physical Constants* (pp. 227-236). American Geophysical Union.

Klima, R. L., Denevi, B. W., Ernst, C. M., Murchie, S. L., & Peplowski, P. N. (2018). Global Distribution and Spectral Properties of Low-Reflectance Material on Mercury. *Geophysical Research Letters, 45,* 2945-2953. https://doi.org/10.1002/2018GL077544

Lambart, S., Laporte, D., Provost, A., Schiano, P. (2012). Fate of Pyroxenite-derived Melts in the Periodtitic Manlte: Thermodynamic and Experimental Constraints. *Journal of Petrology, 53,* 4551-476. https://doi.org/10.1093/petrology/egr068

Le Feuvre, M. & Wieczorek, M. A. (2011). Nonuniform cratering of the Moon and a revised crater chronology of the inner Solar System. *Icarus, 214(1),* 1-20. https://doi.org/10.1016/j.icarus.2011.03.010

Li, H., Zhang, N., Liang, Y., Wu, B., Dygert, N. J., Huang, J., & Parmentier, E. M. (2019). Lunar Cumulate Mantle Overturn: A Model Constrained by Ilmenite Rheology. *Journal of Geophysical Research: Planets, 124(5),* 1357-1378. https://doi.org/10.1029/2018JE005905

Lin, Y., Tronche, E. J., Steendtra, E. S., van Westrenen, W. (2017). Experimental constraints on the solidification of a nominally dry lunar magma ocean. *Earth and Planetary Science Letters*, *471*, 104-116. https://doi.org/10.1016/j.epsl.2017.04.045

Lodders, K. (1996). An experimental and theoretical study of rare-earth-element partitioning between sulfides (FeS, CaS) and silicate and applications to enstatite achondrites. *Meteoritics & Planetary Science*, *31*, 749-766. https://doi.org/doi.org/10.1111/j.1945-5100.1996.tb02110.x

Malavergne, V., Toplis, M. J., Berthet, S., & Jones, J. (2010). Highly reducing conditions during core formation on Mercury: Implications for internal structure and the origin of a magnetic field. *Icarus, 206*, 199-209. https://doi.org/10.1016/j.icarus.2009.09.001

Malfait, W. J., Seifert, R., Petitgirard, S., Mezouar, M., & Sanchez-Valle, C. (2014). The density of andesitic melts and compressibility of dissolved water in silicate melts at crustal and upper mantle conditions. *Earth and Planetary Science Letters*, *393,* 31-38. https://doi.org/10.1016/j.epsl.2014.02.042

Mason, B. (1966). The enstatite chondrites. *Geochimica et Cosmochimica Acta, 30(1),* 23-39. https://doi.org/10.1016/0016-7037(66)90089-5

Marchi, S., Chapman, C. R., Fassett, C. I., Head, J. W., Bottke, W. F., & Strom, R. G. (2013). Global resurfacing of Mercury 4.0-4.1 billion years ago by heavy bombardment and volcanism. *Nature*, *498*, 59-61. https://doi.org/10.1038/nature12280

Marchi, S., Mottola, S., Cremonese, G., Massironi, M., & Martellato, E. (2009). A new chronology for the Moon and Mercury. *The Astronomical Journal*, *137(6),* 4936-4948. https://doi.org/10.1088/0004-6256/137/6/4936

Matsumoto, K., Yamada, R., Kikuchi, F., Kamata, S., Ishihara, Y., Iwata, T., Hanada, H., & Sasaki, S. (2015). Internal structure of the Moon inferred from Apollo seismic data and selenodetic data from GRAIL and LLR. *Geophysical Research Letters*, *42*, 7351-7358. https://doi.org/10.1002/2015GL065335

Mavrogenes, J. A., & O'Neill, H. St.C. (1999). The relative effects of pressure, temperature and oxygen fugacity on the solubility of sulfide in mafic magmas. *Geochimica et Cosmochimica Acta, 63(7-8),* 1173-1180. https://doi.org/10.1016/S0016-7037(98)00289-0

McCoy, T. J. (1998). A pyroxene-oldhamite clast in Bustee: Igneous aubritic oldhamite and a mechanism for the Ti enrichment in aubritic troilite. *Antarctic Meteorite Research, 11,* 32-48.

Mitrovica, J. X. & Peltier, W. R. (1991). A complete formalism for the inversion of post-glacial rebound data: resolving power analysis. *Geophysical Journal International*, *104*, 267-288. https://doi.org/10.1111/j.1365-246X.1991.tb02511.x

Mitrovica, J. X. & Peltier, W. R. (1992). A comparison of methods for the inversion of viscoelastic relaxation spectra. *Geophysical Journal International, 108*, 410-414. https://doi.org/10.1111/j.1365-246X.1992.tb04623.x

Mouser, M. D., Dygert, N., Anzures, B. A., Grambling, N. L., Hrubiak, R., Kono, Y., Shen, G., & Parman, S. W. (2021). Experimental investigation of Mercury's magma ocean viscosity: Implications for the formation of Mercury's cumulate mantle, its subsequent dynamic evolution, and crustal petrogenesis. *Journal of Geophysical Research: Planets, 126*, e2021JE006946. https://doi.org/10.1029/2021JE006946

Murchie, S. L., Klima, R. L., Denevi. B. W., Ernst, C. M., Keller, M. R., Domingue, D. L., Blewett, D. T., Chabot, N. L., Hash, C. D., Malaret, E., Izenberg, N. R., Vilas, F., Nittler, L. R., Gillis-Davis, J. J., Head, J. W., & Solomon, S. C. (2015). Orbital multispectral mapping of Mercury with the MESSENGER Mercury Dual Imaging System: Evidence for the origins of plains units and low-reflectance material. *Icarus*, *254*, 287-305. https://doi.org/10.1016/j.icarus.2015.03.027

Murrell, M., & Burnett, D. (1982). Actinide microdistributions in the enstatite meteorites. *Geochimica et Cosmochimica Acta, 46*, 2453-2460. https://doi.org/10.1016/0016-7037(82)90368-4

Murrell, M. T. & Burnett, D. S. (1986). Partitioning of K, U, and Th between sulfide and silicate liquids: Implications for radioactive heating of planetary cores. *Journal of Geophysical Research: Solid Earth, 91*, 8126-8136. https://doi.org/10.1029/JB091iB08p08126

Nakamura-Messenger, K., Clement, S. J., Rubin, A. E., Choi, B-G., Zhang, S., Rahman, Z., Oikawa, K., & Keller, L. P. (2012). Wassonite: A new titanium monosulfide mineral in the Yamato 691 enstatite chondrite. *American Mineralogist, 97*, 807-815. https://doi.org/10.2138/am.2012.3946

Namur, O., Collinet, M., Charlier, B., Grove, T., Holtz, F., & McCammon, C. (2016a). Melting processes and mantle sources of lavas on Mercury. *Earth and Planetary Science Letters*, *439*, 117-128. https://doi.org/10.1016/j.epsl.2016.01.030

Namur, O., Charlier, B., Holtz, F., & Cartier, C. (2016b). Sulfur solubility in reduced mafic melts: Implications for the speciation and distribution of sulfur on Mercury. *Earth and Planetary Science Letters*, *448*, 102-114. https://doi.org/10.1016/j.epsl.2016.05.024

Nittler, L. R., Chabot, N. L., Grove, T. L., & Peplowski, P. N. (2019). The chemical composition of Mercury. In S. C. Solomon, L. R. Nittler, & B. J. Anderson (Eds.), Mercury: The View after MESSENGER (pp. 30–51). Cambridge Planetary Science.

Nittler, L. R., Starr, R. D., Weider, S. Z., McCoy, T. J., Boynton, W. V., Ebel, D. S., Ernst, C. M., Evans, L. G., Goldsten, J. O., Hamara, D. K., Lawrence, D. J., McNutt Jr., R. L., Schlemm II, C. E., Solomon, S. C., & Sprague, A. L. (2011). The Major-Element Composition of Mercury's Surface from MESSENGER X-ray Spectrometry. *Science, 333,* 1847-1850. https://doi.org/10.1126/science.1211567

Neukum, G., Oberst, J., Hoffmann, H., Wagner, R., & Ivanov, B. A. (2001). Geologic evolution and cratering history of Mercury. *Planetary and Space Science. 49(14-15),* 1507-1521. https://doi.org/10.1016/S0032-0633(01)00089-7

Okada, A. & Keil, K. (1982). Caswellsilverite, $NaCrS_2$ a new mineral in the Norton County enstatite achondrite. *American Mineralogist, 67,* 137-136.

Olsen, E. J., Bunch, T. E., Jarosewich, E., Noonan, A. F., & Huss, G. I. (1977). Happy Canyon: A new type of enstatite chondrite. *Meteoritics, 12,* 109-123.

Ostrach, L. R., Robinson, M. S., Whitten, J. L., Fassett, C. I., Strom, R. G., Head, J. W., & Solomon, S. C. (2015) Extent, age, and resurfacing history of the northern smooth plains on Mercury from MESSENGER observations. *Icarus, 250,* 602-622. https://doi.org/10.1016/j.icarus.2014.11.010

Paulson, A., Zhong, S., & Wahr, J. (2007). Inference of mantle viscosity from GRACE and relative sea level data. *Geophysical Journal International, 171,* 497-508. https://doi.org/10.1111/j.1365-246X.2007.03556.x

Peltier, W. R. (1976). Glacial-Isostatic Adjustment- II. The Inverse Problem. *Geophysical Journal International, 46,* 669-705. https://doi.org/10.1111/j.1365-246X.1976.tb01253.x

Peplowski, P. N., Klima, R. L., Lawrence, D. J., Ernst, C. M., Denevi, B. W., Frank, E. A., Goldsten, J. O., Murchie, S. L., Nittler, L. R., & Solomon, S. C. (2016) Remote sensing evidence for an ancient carbon-bearing crust on Mercury. *Nature Geoscience, 9,* 273-276. https://doi.org/10.1038/ngeo2669

Ramdohr, P. (1963). The Opaque Minerals in Stony Meteorites. *Journal of Geophysical Research, 68(7),* 2011-2036. https://doi.org/10.1029/JZ068i007p02011

Rapp, J. F. & Draper, D. S. (2018). Fractional crystallization of the lunar magma ocean: Updating the dominant paradigm. *Meteoritics & Planetary Science, 53,* 1432-1455. https://doi.org/10.1111/maps.13086

Ren, Z-Y., Ingle, S., Takahashi, E., Hirano, N., & Hirata, T. (2005). The chemical structure of the Hawaiian mantle plume. *Nature, 436,* 837-840. 837–840 (2005). https://doi.org/10.1038/nature03907

Riley Jr., G. N., & Kohlstedt, D. L. (1991). Kinetics of melt migration in upper mantle-type rocks. *Earth and Planetary Science Letters, 105,* 500-521. https://doi.org/10.1016/0012-821X(91)90188-N

Robie, R. A., Bethke, P. M., & Beardsley, K. M. (1967). Selected X-ray crystallographic data, molar volumes and densities of minerals and related substance. US Geological Survey Bulletin No. 1248.

Rudeas, T. (2017). Radioactive heat production of six geologically important nuclides. *Geochemistry, Geophysics, Geosystems, 18,* 3530-3541. https://doi.org/10.1002/2017GC006997

Sakamaki, T., Ohatani, E., Urakawa, S., Suzuki, A., & Katayama, Y. (2010). Density of dry peridotite magma at high pressure using an X-ray absorption method. *American Mineralogist, 95,* 144-147. https://doi.org/10.2138/am.2010.3143

Sanloup, C., Guyot, P. G., Fiquet, G., Mezouar, M., & Martinez, I. (2000). Density measurements of liquid Fe-S alloys at high-pressure. *Geophysical Research Letters*, *27*, 811-814. https://doi.org/10.1029/1999GL008431

Schutt, D. L. & Lesher, C. E. (2006). Effects of melt depletion on the density and seismic velocity of garnet and spinel lherzolite. *Journal of Geophysical Research, 11,* B05401. https://doi.org/10.1029/2003JB002950

Sen, G. (2001). Generation of Deccan Trap magmas. *Journal of Earth System Science, 110,* 409-431. https://doi.org/10.1007/BF02702904

Shearer, C. K., & Papkie, J. J. (1999). Magmatic evolution of the Moon. *American Mineralogist*, *84*, 1469-1494. https://doi.org/10.2138/am-1999-1001

Smyth, J. R. & McCormick, T. C. (1995). Crystallographic Data for Minerals. *Mineral Physical and Crystallography: A Handbook of Physical Constants* (eds. T.J. Ahrens), pp. 1-17. American Geophysical Union, Washington, D.C.

Sprague, A. L., Hunten, D. M., & Lodders, K. (1995). Sulfur at Mercury, Elemental at the Poles and Sulfides in the Regolith. *Icarus, 118,* 211-215. https://doi.org/10.1006/icar.1995.1186

Starr, R. D., Schriver, D., Nittler, L. R., Weider, S. Z., Byrne, P. K., Ho, G. C., Rhodes, E. A., Schlemm II, C. E., Solomon, S. C., & Trávníček, P. M. (2012). MESSENGER detection of electron-induced X-ray fluorescence from Mercury's surface. *Journal of Geophysical Research, 11,* E00L02. https://doi.org/10.1029/2012JE004118

Steenstra, E. S. & van Westrenen, W. (2020). Geochemical constrains on core-mantle differentiation in Mercury and the aubrite parent body. *Icarus, 340,* 113621. https://doi.org/10.1016/j.icarus.2020.113621

Steinbrügge, G., Dumberry, M., Rivoldini, A., Schubert, G., Cao, H., Schroeder, D. M., Soderland, K. M. (2020). Challenges on Mercury's Interior Structure Posed by the New Measurements of its Obliquity and Tides. *Geophysical Research Letters, 48,* e2020GL089895. https://doi.org/10.1029/2020GL089895

Stockstill-Cahill, K. R., McCoy, T. J., Nittler, L. R., Weider, S. Z., & Hauck II, S. A. (2012). Magnesium-rich crustal compositions on Mercury: Implications for magmatism from petrologic modeling. *Journal of Geophysical Research, 117,* E00L15. https://doi.org/10.1029/2012JE004140

Syal, M. B., Schultz, P. H., & Riner, M. A. (2015). Darkening of Mercury's surface by cometary carbon. *Nature Geoscience, 8,* 352-356. https://doi.org/10.1038/ngeo2397

Takafuji, N., Hirose, K., Ono, S., Xu, F., Mitome, M., & Bando, Y. (2004). Segregation of core melts by permeable flow in the lower mantle. *Earth and Planetary Science Letters, 224,* 249-257. https://doi.org/10.1016/j.epsl.2004.05.016

Tenner, T. J., Lange, R. A., & Downs, R. T. (2007). The albite fusion curve re-examined: New experiments and the high-pressure density and compressibility of high albite and NaAlSi3O8 liquid. *American Mineralogist, 92(10),* 1573-1585. https://doi.org/10.2138/am.2007.2464

Udry, A., Wilbur, Z. E., Rahib, R. R., McCubbin, F. M., Vander Kaaden, K. E., McCoy, T. J., Ziegler, K., Gross, J., DeFelice, C., Combs, L., & Turrin, B. D. (2019). Reclassification of four aurbites as enstatite chondrite impact melts: Potential geochemical analogs for Mercury. *Meteoritics & Planetary Science, 54,* 785-810. https://doi.org/10.1111/maps.13252

Urakawa, S., Someya, K., Terasaki, H., Katsura, T., Syo, Y., Funakoshi, K-i., Utsumi, W., Katayama, Y., Sueda, Y-i., & Irifune, T. (2004). Phase relationships and equations of state for FeS at high pressures and temperatures and implications for the internal structure of Mars. *Physics of Earth and Planetary Interiors, 143-144,* 469-479. https://doi.org/10.1016/j.pepi.2003.12.015

Vander Kaaden, K. E., & McCubbin F. M. (2015). Exotic crust formation on Mercury: Consequences of a shallow, FeO-poor mantle. *Journal of Geophysical Research: Planets, 120(2),* 195-209. https://doi.org/10.1002/2014JE004733

Vander Kaaden, K. E., & McCubbin, F. M. (2016). The origin of boninites on Mercury: An experimental study of the northern volcanic plains lavas. *Geochimica et Cosmochimica Acta*, *173,* 246-263. https://doi.org/10.1016/j.gca.2015.10.016

Vander Kaaden, K. E., McCubbin, F. M., Nittler, L. R., Peplowski, P. N., Weider, S. Z., Frank, E. A., & McCoy, T. J. (2017). Geochemistry, mineralogy, and petrology of boninitic and komatiitic rocks on the mercurian surface: insights into the mercurian mantle. *Icarus*, *285*, 155-168. https://doi.org/10.1016/j.icarus.2016.11.041

Wang, Y., Xiao, Z., & Xu, R. (2022). Multiple Mantle Sources of High-Magnesium Terranes on Mercury. *Journal of Geophysical Research: Planets,* e2022JE007218. https://doi.org/10.1029/2022JE007218

Warren, P. H. (1985). The magma ocean concept and lunar evolution. *Annual Review of Earth and Planetary Sciences*, *13,* 201-240.

Watters, T. R. & Prinz, M. (1979). Aubrites: Their origin and relationship to enstatite chondrites. *Proceedings of the Lunar and Planetary Science Conference 10th*, 1073-1093.

Weider, S. Z., Nittler, L. R., Murchie, S. L., Peplowski, P. N., McCoy, T. J., Kerber, L., Klimczak, C., Ernst, C. M., Goudge, T. A., Starr, R. D., Izenberg, N. R., Klima, R. L., & Solomon, S. C. (2016). Evidence from MESSENGER for sulfur- and carbon-driven explosive volcanism on Mercury. *Geophysical Research Letters, 43(8),* 3653-3661. https://doi.org/10.1002/2016GL068325

Weider, S. Z., Nittler, L. R., Starr, R. D., McCoy, T. J., Stockstill-Cahill, K. R., Byrne, P. K., Denevi, B. W., Head, J. W., & Solomon, S. C. (2012). Chemical heterogeneity on Mercury's surface revealed by the MESSENGER X-Ray Spectrometer. *Journal of Geophysical Research: Planets*, *117,* E00L05. https://doi.org/10.1029/2012JE004153

Whitehead, J. A. (1988). Fluid Models of Geological Hotspots. *Annual Reviews of Fluid Mechanics*, *20,* 61-87. https://doi.org/10.1146/annurev.fl.20.010188.000425

Wilbur, Z. E., Udry, A., McCubbin, F. M., Vander Kaaden, K. E., DeFelice, C., Ziegler, K., Ross, D. K., McCoy, T. J., Gross, J., Barnes, J. J., Dygert, N., Zeigler, R. A., Turrin, B. D., & McCoy, C. (2022). The effects of highly reduced magmatism revealed through aubrites. *Meteoritics & Planetary Science*, 1-34. https://doi.org/10.1111/maps.13823

Wohlers, A., & Wood, B. J. (2015). A Mercury-like component of early earth yields uranium in the core and high mantle ^{142}Nd. *Nature, 520,* 337. https://doi.org/10.1038/nature14350

Wohlers., A., & Wood, B. J.(2017). Uranium, thorium, and REE partitioning into sulfide liquids: Implications for reduced S-rich bodies. *Geochimica et Cosmochimica Acta, 205*, 226-244. https://doi.org/10.1016/j.gca.2017.01.050

Yu, S. Tosi, N., Schwinger, S., Maurice, M., Breuer, D., & Xiao, L. (2019). Overturn of Ilmenite-Bearing Cumulates in a Rheologically Weak Lunar Mantle. *Journal of Geophysical Research: Planets, 124(2),* 418-436. https://doi.org/10.1029/2018JE005739

Zhang, N., Dygert, N., Liang, Y., & Parmentier, E. M. (2017). The effect of ilmenite viscosity on the dynamics and evolution of an overturned lunar cumulate mantle. *Geophysical Research Letters, 44(13),* 6543-6552. https://doi.org/10.1002/2017GL073702

Zhang, N., Parmentier, E. M., & Liang, Y. (2013). A 3-D numerical study of the thermal evolution of the Moon after cumulate mantle overturn: The importance of rheology and core solidification. *Journal of Geophysical Research: Planets, 118,* 1789-1804. https://doi.org/10.1002/jgre.20121

Zhao, C., Lodders, K., Bloom, H., Chen, H., Tian, Z., Koefoed, P., Peto, M. K., Wang, K. (2019). Potassium isotopic compositions of enstatite meteorites. *Meteoritics & Planetary Science*, *55,* 1404-1417. https://doi.org/10.1111/maps.13358

Zhao, Y.-H., Zimmerman, M. E., & Kohlstedt, D. L. (2009). Effect of iron content on the creep behavior of olivine: 1. Anhydrous conditions. *Earth and Planetary Science Letters*, *287*, 229-240. https://doi.org/10.1016/j.epsl.2009.08.006

Zhong, S., Parmentier, E. M., & Zuber, M. T. (2000). A dynamic origin for the global asymmetry of lunar mare basalts. *Earth and Planetary Science Letters, 177,* 131-140. https://doi.org/10.1016/S0012-821X(00)00041-8

Zolotov, M. Y., Sprague, A. L., Hauck II, S. A., Nittler, L. R., Solomon, S. C., & Weider, S. Z. (2012). The redox state, FeO content, and origin of sulfur-rich magmas on Mercury. *Journal of Geophysical Letters: Planets, 118,* 138-146. https://doi.org/10.1029/2012JE004274

Appendix B

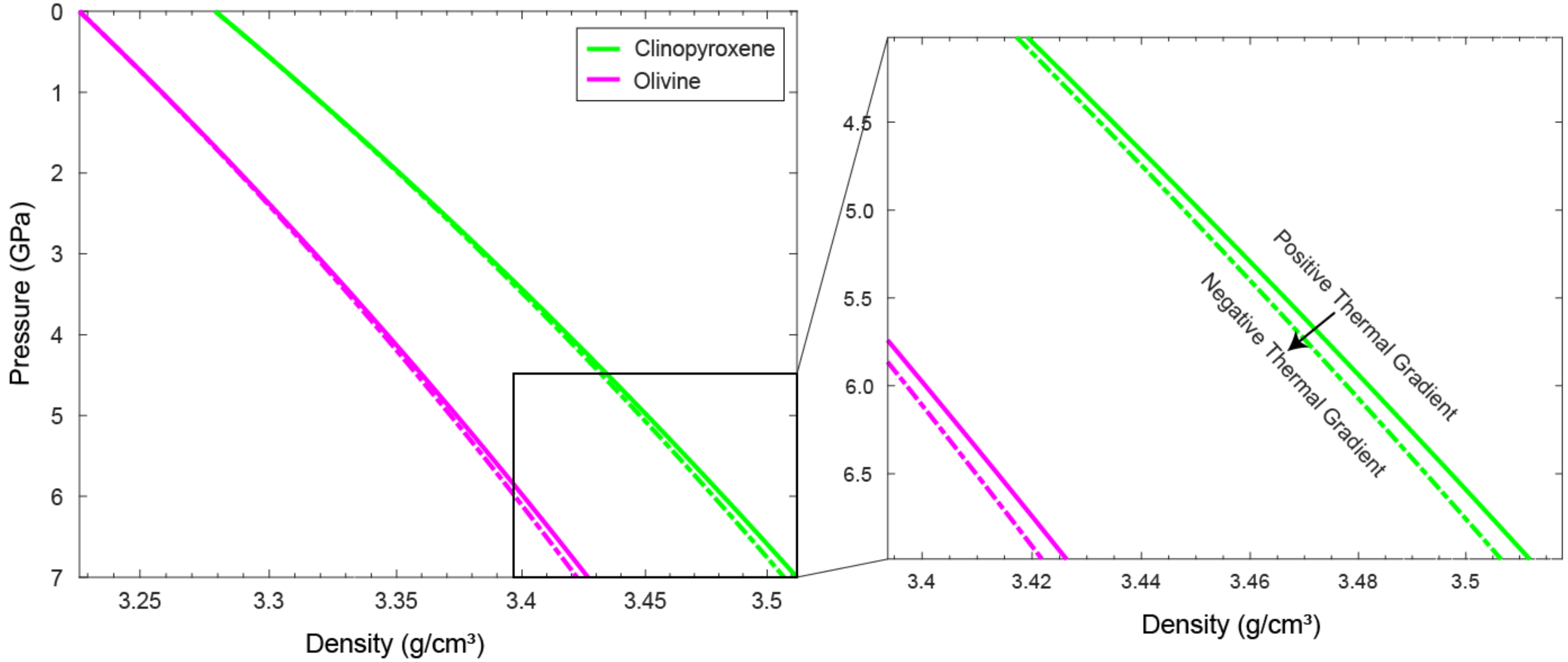

Figure B1. Density of olivine and clinopyroxene with a positive thermal gradient (solid line) at 0.1°C/km, and a negative thermal gradient (dashed line) at -0.1°C/km. Note the density differences increasing at greater depths.

CHAPTER III.

STRUCTURAL ANALYSIS OF REDUCED, FE-SILICATE MELTS AND GLASSES UTILIZING MULTI-ANGLE ENERGY-DISPERSIVE X-RAY DIFFRACTION AND RAMAN SPECTROSCOPY

Abstract

Silicate liquid viscosity is important for understanding physical processes such as volcanism and crystallization behavior of magma bodies and depends on the structure of the liquid. This study utilizes two distinct methods (X-ray diffraction and spectroscopy) to study the structural and chemical variations in silicate liquids at the atomic to meso-scale under different pressure and temperature conditions. Fe-free andesite liquids with compositional variations (i.e., presence or absence of S, Al), were characterized by multi-angle energy-dispersive X-ray diffraction (EDXD). Comparison of the structural information with liquid viscosities measured in a previous study elucidate structural controls on viscosity. EDXD analysis revealed that temperature effects the liquids by increasing bond lengths between tetrahedrally coordinated cations and subsequently increasing bond angles within the tetrahedral units. In Al-bearing liquids, the bond lengths and angles are greater than in Al-free systems, owing to the size difference between Al and Si as cations. Quenched glasses of the experimental compositions analyzed by Raman spectroscopy reveal differences in the structure of the tetrahedral networks between sulfur-free and sulfur-bearing compositions. The sulfur-bearing samples exhibited greater abundance of more isolated silicon tetrahedra (or *Q* species) than the sulfur-free glass, indicating a general lower degree of polymerization in the sulfur-bearing glass.

3. 1. Introduction

The study of silicate melts at different pressure and temperature conditions is important for understanding the dynamic behavior of magma bodies and thus the crystallization process for natural systems. Physical properties, such as viscosity, can be experimentally measured and applied to our understanding of a magmatic system. Viscosity is a critical component to understanding the evolution of a magma body as it controls crystal growth and mobility. In highly viscous systems, crystal mobility may be minimal where the crystals have longer residence times in the liquid. In low viscosity systems, crystals may readily settle out of the liquid, resulting in fractional crystallization. Understanding the viscosity and structure of these silicate liquids is a critical step to modeling the evolution of igneous systems. A previous study measured the viscosity of Fe-free silicate liquids that varied in composition, with and without aluminum and sulfur. The viscosity data revealed that the sulfur-bearing liquid was lower in viscosity at all tested pressure and temperature conditions than the sulfur-free liquid. This work explores the structure of these silicate liquids, both via in situ liquid measurements and on recovered glasses, to understand how their structure correlates to the different viscosities.

Studying the structure of silicate melts can be achieved through different methods, such as the analysis of quenched glasses or in situ analysis of liquids. Energy-dispersive X-ray diffraction (EDXD) is one such method that has been widely used un experimental work to study a variety of materials relevant to geology and material science, in situ. This method utilizes a primary white light X-ray beam where the photons scattered by the sample are detected and analyzed via solid state X-ray detector (SSD) (Nishikawa and Iijima, 1984). Applying the EDXD technique to high-pressure experimental set-ups has been achieved on the Paris-Edinburgh apparatus (Morard et al., 2007; Perrillat et al., 2010; Yamada et al., 2011; Kono et al., 2014). The Paris-Edinburgh press located at Beamline 16-BM-B, Advanced Photon Source (APS), Argonne National Laboratory is equipped to collect EDXD data at a range of angles relative to the incident beam (up to 39.5°) providing a more comprehensive analysis of the sample. Analysis at 16-BM-B has been successful in applications to simple systems, such as SiO_2 or iron alloys (e.g., Yamada et al., 2011; Kono et al., 2014; Sakamaki et al., 2014; Shibazaki et al., 2015; Harke et al., 2017), and limited exploration in more complex systems (e.g., alkali basalt, Bonechi et al., 2021) but the exploration of other complex geologically-relevant systems, conducted at 16-BM-B or elsewhere, is lacking.

The most common ways to study the structure of a melt are through ex-situ analysis of quenched melts, or glasses, (e.g., by infrared spectroscopy, Raman spectroscopy, etc.) on of an experiment conducted at controlled pressure and temperature conditions. While these methods are convenient to study glasses, samples quenched at atmospheric conditions may not preserve high-pressure structures (Williams and Jeanloz, 1988; Kubicki et al., 1992). Nonetheless, paring Raman analysis of experimental glasses with EDXD could provide support in evaluating interpretations of EDXD spectra, and reveal features that cannot be resolved by EDXD. Here we present the structural results of four synthetic multi-component melts using the multi-angle X-ray diffraction technique on the Paris-Edinburgh press and Raman spectroscopy on recovered experimental glasses with paired viscometric characterization to understand the driving factors behind the differences in liquid viscosity at high-temperatures and high-pressures.

3.1.1. *Importance of Composition on the Melt Structure*

All aspects of melt chemistry are important for determining melt structure, the bridging of network forming (Si^{4+}, Al^{3+}) cations, and network disruption by modifying cations (e.g., Mg^{2+}, Fe^{2+}, Na^{+}, Ca^{2+}, H^{+}) is thought to have the greatest control over the melt behavior. The tetrahedrally coordinated cation (T) in silicate melts determines the degree of polymerization, or degree of connectivity of the tetrahedral units, of the melt and it determines and thereby viscosity of the melt. A conventional method for evaluating the degree of polymerization is dividing the ratio of non-bridging oxygens (NBO; the oxygen not shared between TO_4 complexes) by the number of tetrahedra; NBO/T (Mysen et al., 1981; Mysen 1990; Wang et al., 2014; Kono, 2018). A low viscosity melt with a low degree of polymerization will have a high NBO/T value indicating that there is a higher abundance of tetrahedra not sharing oxygens. Conversely, a melt with a lower NBO/T value has more tetrahedral units sharing oxygens and is thus a more polymerized (viscous) melt. Polymerization affects the pressure sensitivity of melt viscosity; depolymerized melts are less sensitive to changes in pressure because their tetrahedral structures are largely isolated such that they can rearrange without breaking multiple bonds (Wang et al., 2014), thus their change in viscosity tends to be minimal at different pressures when compared to a highly polymerous and viscous liquid.

Al plays a unique role in melts since it can act as a network former and/or a network modifier. At low pressures, Al^{3+} acts as a network former and partitions into the tetrahedral site in the TO_4 structure. Excess Al will depolymerize the melt as the excess Al will go from tetrahedral to octahedral coordination by forming longer and weaker bonds than in tetrahedral coordination (Bottinga and Weill, 1972; Waff, 1975; Mysen et al., 1981; Scarfe and Cronin, 1986; Suzuki et al., 2002). Network modifying Al in octahedral coordination depolymerizes the melt (Bottinga and Weill, 1972). A possible coordination change of Al has been documented in experimental viscosity work on peridotites (e.g., Xue et al., 1991; Yarger et al., 1995; Liebske et al., 2005) showing a change in the viscosity behavior around 6 GPa, indicating the increase in pressure may also cause a coordination change. The change is coordination is possible at lower pressures, approximately 2.2 GPa, but requires a highly aluminous melt (Riebling, 1966). Additionally, the presence of metal cations will influence the polymerization of the melt. The strength of the metal cations affects the strength of the Al-O bonds, and the energy associated with these bonds will control the stability of the TO_4 complex (Mysen et al., 1981). Thus, Al's influence in a melt is largely determined by composition and pressure.

Other notable compositional factors are volatiles (e.g., OH^-), alkali cations, and sulfur. Volatile elements are important to the polymerization of the melt as they will act as network modifiers by bonding with previously shared oxygens, breaking up existing TO_4 unit linkages. Water is an effective network modifier in the form of OH^- where it is 3 to 5 times stronger than H_2O in the melt (Tomozawa et al., 1983; Deubener et al., 2003; Reinsch et al., 2016). OH- is highly effective in reducing melt viscosity (Stopler, 1982), where up to a few wt% of OH- can decrease the viscosity of a silicate liquid by at least an order of magnitude when compared to an anhydrous melt (e.g., Dingwell and Mysen, 1985; Richet et al., 1996; Whittington et al., 2001; Giordano et al., 2004).Sulfur, on the other hand, is believed to act as a network former in reduced systems. In reduced systems, sulfur is expected to be an anion, S^{2-}, and thus complex with network modifying elements such as Mg or Fe, forming MgS and FeS species (e.g., Fogel, 1997; McCoy et al., 1999; Namur et al., 2016; Anzures et al., 2020). This process of isolating network modifying cations would theoretically promote the formation of TO_4 networks, thus polymerizing and increasing the viscosity of the melt.

3.2. Methods

3.2.1. *Compositions*

Four Fe-free andesitic compositions (MMO, MMOS, C, and D) were tested to observe the effect of variation of the different compositional components described in the introduction. Each composition was prepared by grinding reagent grade oxide powders in ethanol in an agate mortar and pestle for 6 hours. After grinding, they were decarbonated in a box furnace at 900°C for 24 hours. After decarbonation, the compositions were conditioned in a gas mixing furnace at Brown University. Compositions MMOS and D are reduced to low oxygen fugacities (fO_2) of IW-5 and IW-4.5, respectively, where IW refers to the iron wüstite buffer and compositions MMO and C were conditioned to fO_2s of IW-1 (Table 3.1). The addition of Si metal instead of SiO_2 in MMOS resulted in the fO_2 being the lowest out of the tested compositions, for more details on this composition preparation, review the methods section in Mouser et al. (2021). These mixes have variable Al and S content, MMOS is the only composition to have sulfur and C and D do not have Al (Table 3.1). The water content of recovered experimental glasses of the MMO and MMOS compositions were measured via Fourier transform infrared spectroscopy (FTIR), revealing that water is a negligible factor (~94 ppm) in these compositions (Mouser et al., 2021).

3.2.2. *Multi-angle Energy-dispersive X-ray Diffraction Data Collection*

Multi-angle energy-dispersive X-ray diffraction (EDXD) for each synthetic composition was collected using the Paris-Edinburgh press at APS. The powder compositions were placed in a graphite lined boron nitride capsule. Once the experiment is loaded in the Paris-Edinburgh press and pressurized, the temperature is incrementally raised by a few degrees until it reaches a predicted superliquidus temperature. The temperature of the experiment is calculated using a thermocouple-calibrated current-temperature curve (Kono et al., 2014) with an estimated uncertainty of ±5%. Pressure is calculated from X-ray diffraction measurement of MgO in the assembly using an equation of state for MgO (Kono et al., 2010). The measured uncertainty for MgO is ±0.15 GPa (Kono et al., 2010) but due to potential pressure and/or temperature gradients across the assembly, the estimated pressure uncertainty of the run condition is approximately ±0.5 GPa (Mouser et al., 2021). Once the desired temperature has been achieved, the experiment is set up to first, conduct a falling-sphere viscometry observation, and second, collect multi-angle EDXD data at ten different 2θ angles over a period of approximately two hours. Pressure, temperature, and measured viscosities for each sample are reported in Figure 3.1 and Table 3.2.

To maintain precise control over of the 2θ angle movements, the set up includes a large Huber Stage that holds a Ge solid state detector (SSD) that rotates horizontally from 3° to 35° (Kono et al., 2014). The primary incident slits and the clean-up slits are located near the X-ray source where they define the position of the beam onto the sample (Figure 3.2). The detector slits are located in the front of the detector to accommodate for diffracted X-rays (Kono et al., 2014). A tungsten beam stop, located opposite from the X-ray source, blocks the beam after it has passed through the sample which removes secondary background scatter (Kono et al., 2014).

3.2.3. *EDXD Data Processing*

Sample selection for EDXD analysis was made by critically assessing the experimental liquid diffraction data collected on high-pressure high-temperature experiments of compositions MMO, MMOS, C, and D. Samples that were used exhibited no crystalline peaks in the individual angle spectrums (Table 3.2). Analysis of each experiment was conducted with aEDXD, a program developed at 16-BM-B to view and process multi-angle energy-dispersive X-ray diffraction data. aEDXD analysis procedure is based on Keiko and Takao (1984) and details of the data processing can be found in Yamada et al. (2011). The aEDXD software combines spectral files from the different 2θ angles to interpret the different features (e.g., structure factor, distribution function) of the liquid. Figure C1 in Appendix C is an example of sample D3 spectra before smoothing and cutting peaks associated with components in the experimental assembly. Figure C2 shows spectra from each sample after smoothing and peak cutting. An example of a fully crystalline spectra is included in the Appendix, Figure C3.

Table 3.1. Measured compositions for MMOS, MMO, C, and D and their respective oxygen fugacities (*f*O_2) relative to the iron-wüstite buffer.

Compositions (wt% oxide)										
	SiO_2	**TiO_2**	**Al_2O_3**	**MgO**	**CaO**	**K_2O**	**Na_2O**	**S**	**Total**	***f*O_2**
MMO	52.8	1.2	17.4	15.0	10.9	2.2	0.4	0.0	99.9	IW-1
MMOS	51.4	1.1	16.9	14.5	10.5	2.2	0.4	3.0	100.0	IW-5
C	64.0	1.4	0.0	18.1	13.2	2.7	0.5	0.0	99.9	IW-1
D	64.0	1.4	0.0	18.1	13.2	2.7	0.5	0.0	99.9	IW-4.5

Note that FMMO9 and MMO6 both use the same ‘MMO’ composition as defined in Mouser et al. (2021).

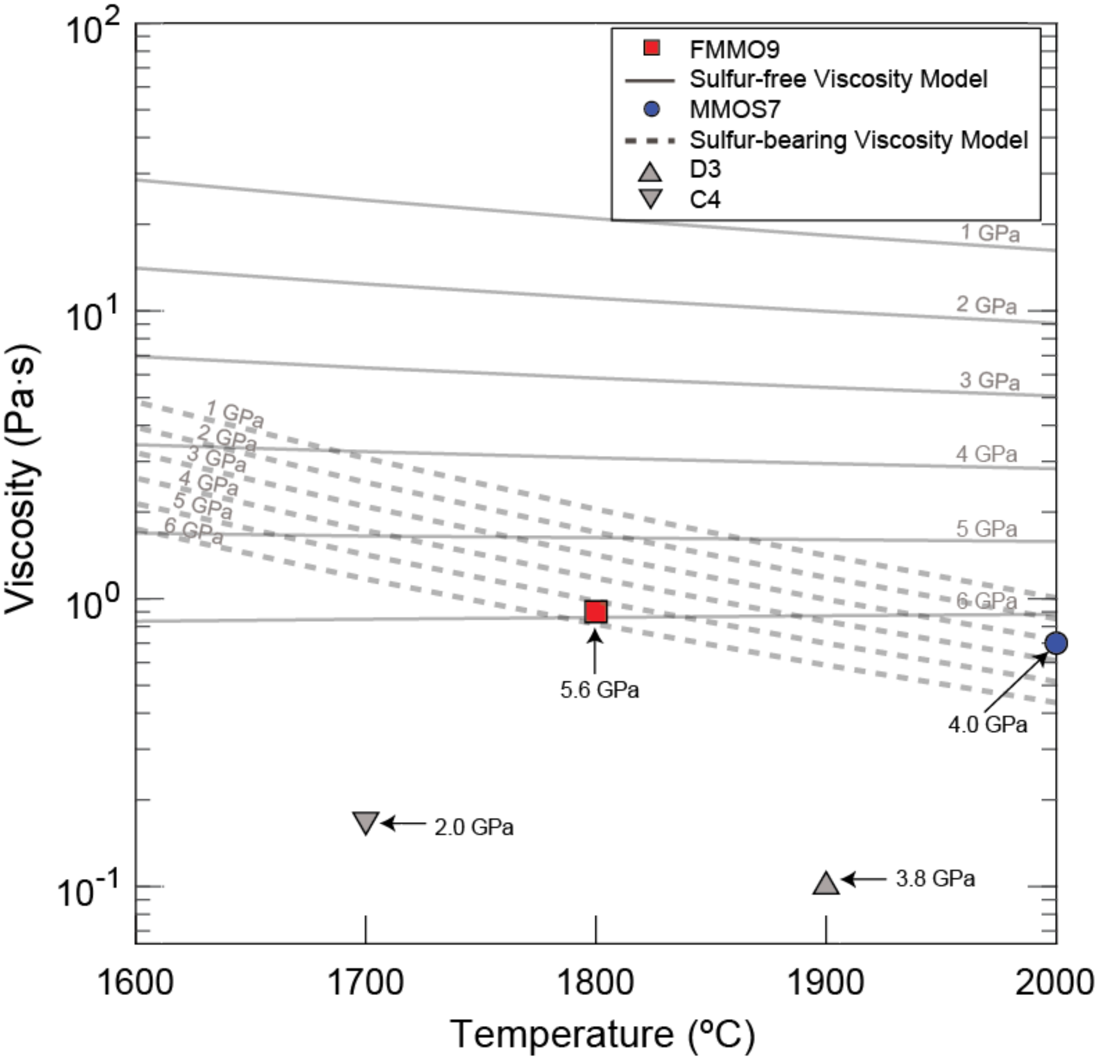

Figure 3.1. Predicted viscosities for (Al-bearing) sulfur-free and sulfur-bearing liquids at different pressure and temperature conditions using viscosity models from Mouser et al. (2021) plotted with the viscosities of MMOS7, FMMO9, C4, and D3. Pressures considered for the models and the experimental pressures are indicated on the figure.

Table 3.2. Experimental conditions and viscosities for each experimental sample.

	Pressure (GPa)	Temperature (°C)	Viscosity (Pa·s)	Descriptive Terms
FMMO9	5.6 ± 0.5	1800 ± 90	0.90 ± 0.1	Al-bearing, S-free
MMOS7	4.0 ± 0.5	2000 ± 100	0.70 ± 0.1	Al-bearing, S-bearing
C4	2.0 ± 0.5	1700 ± 85	0.17 ± 0.2	Al-free
D3	3.8 ± 0.5	1900 ± 95	0.10 ± 0.2	Al-free
MMO6	6.2 ± 0.5	2000 ± 100	Unmeasured	Al-bearing, S-free

Experimental data for FMMO9, MMOS7, C4, and D3 are reported in Mouser et al. (2021). Viscosity was not measured for the MMO6 experiment which is only used for Raman analysis in this work. See discussion in Mouser et al. (2021) for detail on the pressure, temperature, and viscosity uncertainty calculations.

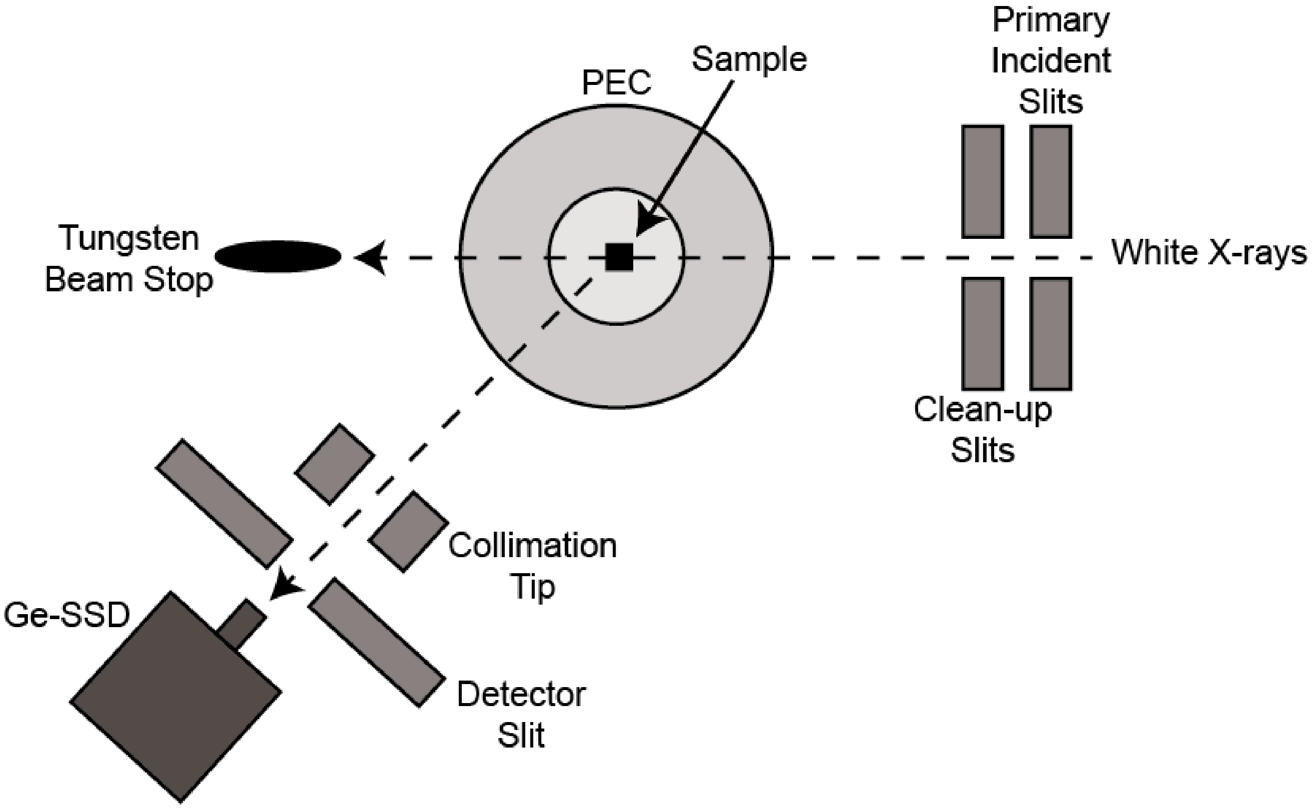

Figure 3.2. The multi-angle EDXD set up with the Paris-Edinburgh apparatus at Beamline 16-BM-B.

3.2.4. *Scanning Electron Microscope*

Experimental samples were mounted in epoxy and polished to determine the glass or crystalline state of the experiment via backscattered electron imaging on the PhenomXL scanning electron microscope (SEM) at the University of Tennessee. If the sample was determined to be a quenched glass, it was used for Raman analysis. Of the experiments with multi-angle EDXD data, only MMOS7 quenched to a glass (Figure C4). Owing to the slow cooling routine employed at the beamline, experiments FMMO9, C4, and D3 quenched with crystalline features. For comparison with MMOS7, a sulfur-free quenched glass (Figure C5) without a reported viscosity (MMO6) was also analyzed for Raman spectroscopy (no EDXD data exist for MMO6).

3.2.5. *Raman Spectroscopy*

Raman spectra were collected on a confocal Raman apparatus at the Department of Chemistry, University of Tennessee. Analyses were conducted with a 532-nm excitation wavelength and a Ti-U inverted microscope with a 0.45 numerical aperture and a 20x objective. Spectra were collected in two frames with a 20 second exposure time for each frame. A laser power of 5 mW was used. Spectra of the epoxy the that the samples were mounted in were collected prior to the glass spectra to provide a background correction to remove the epoxy signal. Included in the Raman set-up is a charged coupled device (CCD) which is sensitive to interactions with high energy particles that cause spikes in the spectrum (Whitaker and Hayes, 2018), therefore, the spectra were also corrected for cosmic ray flux.

The epoxy and cosmic ray flux corrected raw data files were imported to Data Exploration, Visualization, and Analysis for Spectroscopy (DEVAS), a web based program with tools to process and model spectra (Carey et al., 2017). Preprocessing for the spectra included applying a baseline correction, normalizing to 1555 cm^{-1} (atmospheric O_2). The morphological weighted penalized least squares (MPLS) baseline correction was used on the MMOS7 data, and the asymmetric least squares (ALS) baseline correction was used on the MMO6 data. These baseline corrections were selected based on their ability to retain important spectral features.

3.3. Results

3.3.1. *EDXD*

Melt structure analysis by EDXD utilizes on two characterizing descriptions: the structure factor, *s(q)*, where *q* is the scattering vector, and the distribution function, *d(r)*, where *r* is the radial distance. The structure factor is a quantitative description of how material scatters X-ray radiation, relating the diffracted intensity per atom to that produced by a single scattering unit. In other words, it yields information about the atomic positions of atoms on the network scale and provides important information on the polymerization and connectivity of TO_4 units in the melt. The structure is defined by the following equations:

$$s(q) = \frac{I_{coh}(q) - \sum_i f_i(q)^2}{\{\sum_i f_i(q)\}^2}\,, \tag{3.1}$$

where q is determined by:

$$q = \frac{4\pi E sin\theta}{12.398}, \tag{3.2}$$

E is the X-ray energy in keV, θ is the scattering angle, I_{coh} is the coherent scattering intensity of the radiation source through the material. Thus, q defines the elastic scattering of the particle energy on a structural unit in the liquid, given in units of Å^{-1} (e.g., Waseda, 1980). f is the atomic scattering factor, which considers each chemical component (i) in the melt. f can be defined for the scattering of an atom by the following:

$$f(q) = \sum_{j=1}^{4} a_j \exp\left(-b_j s^2\right) + c, \tag{3.3}$$

where a_j, b_j, and c are atomic-dependent parameters (parameters can be found in Ibers and Hamilton (1984)), and s is defined as $\frac{q}{4\pi}$.

The distribution function is the Fourier transform of the structure factor which allows features on the local scale (e.g., bond angles) to be analyzed. The distribution factor is defined by the following equation:

$$G(r) = \frac{2}{\pi}\sum_m K_m^2 \int_0^{\infty}\{s(q) - 1\} q sin(qr) dq, \tag{3.4}$$

Where K is the effective number of electrons for each atom (summed for all components) and r describes the radial distance of atoms.

3.3.1.1. *Structure Factor*

The structure factors for the measured samples are presented in Figure 3.3. These data are presented up to 7 Å^{-1} because beyond that point, the spectra are featureless due to the lack of long-range order in the melts (e.g., Zotov et al., 1989). The intensity of the curves presents differently among the four samples, due to the differences in structure related to experimental pressure, temperature, and sample composition. There are different "range orders" that define the tetrahedral connectivity in liquids, glasses, and crystalline materials: long range, intermediate (or medium) range, and short-range order. The short-range order is representative of a radial distance of ~2 Å^{-1} from the point of reference tetrahedral unit, intermediate range order extends out to distance of ~10–20 Å^{-1} beyond the reference tetrahedral units; and the long-range order is at distances greater than 20 Å^{-1} representing continuous bonding over long distances (e.g., Wright, 1990; Henderson, 2005). Liquids and glasses, in general, exhibit similar bonding, showing features through the intermediate range order, as they do not have the same continuity (long range order) with distance from the reference atom that crystalline materials do (Cormier et al., 1996).

Two features identified in the structure factor are the first sharp diffraction peak (FSDP) and the principal peak (PP). The FSDP reflects the intermediate range order of the liquid, and for these silicate materials, is represented by the TO_4 network. The FSDP is known to be sensitive to pressure (e.g., Elliott, 1991; Sakamaki, 2018), representing a decrease in distances between structures which correlates to internal changes to the TO_4 units (discussed further in the distribution factor section). The pressure sensitivity in the FSDP presents as a shift in the peak q position to higher values at increasing pressures which has been observed in silicates as a result of densification (e.g., SiO_2 glass, Inamura et al., 2001). The structure factors of our experiments exhibit a FSDP around 1.8–2 Å^{-1}, with small variations in peak *q* position among samples. The *q* positions for the FSDP values in all samples show a systematic positive correlation with increasing pressure (Table 3.3, Figure 3.4a) suggesting the same pressure-density correlation observed in Inamura et al. (2001). There is a lack of correlation of FSDP with temperature (Figure 3.4b), likely due to temperature not having the same density correlation as with pressure.

The principal peak of a liquid's structure may indicate the degree of periodicity of the tetrahedral networks in the liquid or how connected the TO_4 network is. A more intense principal peak is the result of more extended short to intermediate range ordering (Zn- and Ge-bearing glasses- Salmon et al., 2005; Er-O liquids- Koyama et al., 2020) . The principal peak for the new data are between 4.20–4.65 Å^{-1}, which is similar to other reported principal peaks for silicate materials (e.g., ~4.2 Å^{-1} for forsterite and enstatite liquid, Wilding et al., 2008; 4.5 Å^{-1} for albite liquid, Yamada et al., 2011). There is a correlation with decreasing PP *q* position and increasing temperature seen in both compositional series (Figure 3.4d), suggesting a decrease in the periodicity in the silicate structure at increasing temperatures. The lack of correlation of PP with pressure (Figure 3.4c), suggests it is not sensitive to structure densification as appears to be the case with the FSDP.

3.3.1.2. *Distribution Function*

The distribution function defines the local bond information in the silicate network. There are three ranges that are represented in the distribution function: Range I (1.5–3 Å)- the identity of the structural units present, Range II (3–5.5 Å)- the connection of adjacent structural units, and Range III (5–10+ Å)- the network topology (three-dimensionality of connected units) (e.g., Wright, 1990; Wright et al., 1991; Henderson, 2005). Additionally, the locations of certain peaks (e.g., representing T-O, O-O, and T-T bond lengths) can be used to determine the bond angles of the connected TO_4 units.

The distribution function of the four samples are shown in Figure 3.5. In Figure 3.5 and in Table 3.4, the locations of the T-O, T-T, and O-O bonds are shown and listed. The T-O bonds for all samples exist in Range I, which is representative of the tetrahedral structural units. The peak location for the T-O bonds are ~1.67 Å for all samples, which is similar to T-O locations measured in other silicates (e.g., 1.63 Å for albite liquid, Yamada et al., 2011; 1.59 Å for Si glass and 1.63 Å for orthoclase glass, Zotov et al., 1989; ~1.7 for alkali basalt, Bonechi et al., 2022). The T-T bonds have slight variations among the samples, 3.13–3.32 Å, but fall within Range II representing the connections of the tetrahedral cations of different tetrahedral units. These values are also similar to reported T-T bonds for other silicates (3.12 Å for albite liquid, Yamada et al., 2011; 3.08 Å for Si glass and 3.15 Å for orthoclase glass, Zotov et al., 1989; ~3.15 for alkali basalt, Bonechi et al., 2022). The final reported bond length, O-O, was only reported for MMOS7 where a soft peak in the spectra appeared around 2.50 Å. The O-O peak was not observed in the other samples, perhaps being masked by other features in these complex systems and therefore not visible. The O-O location in MMOS7 at 2.55 Å is similar to other reported O-O values in silicates (2.60 Å for albite liquid, Yamada et al., 2011; 2.64 Å for Si glass, Zotov et al., 1989). The *d(r)* spectra above 5 Å loses significant structure, which may be a result of the complex, usually multiple parings, that are above 4 Å (e.g., Zotov et al., 1989), thus only features in Ranges I and II are discussed here.

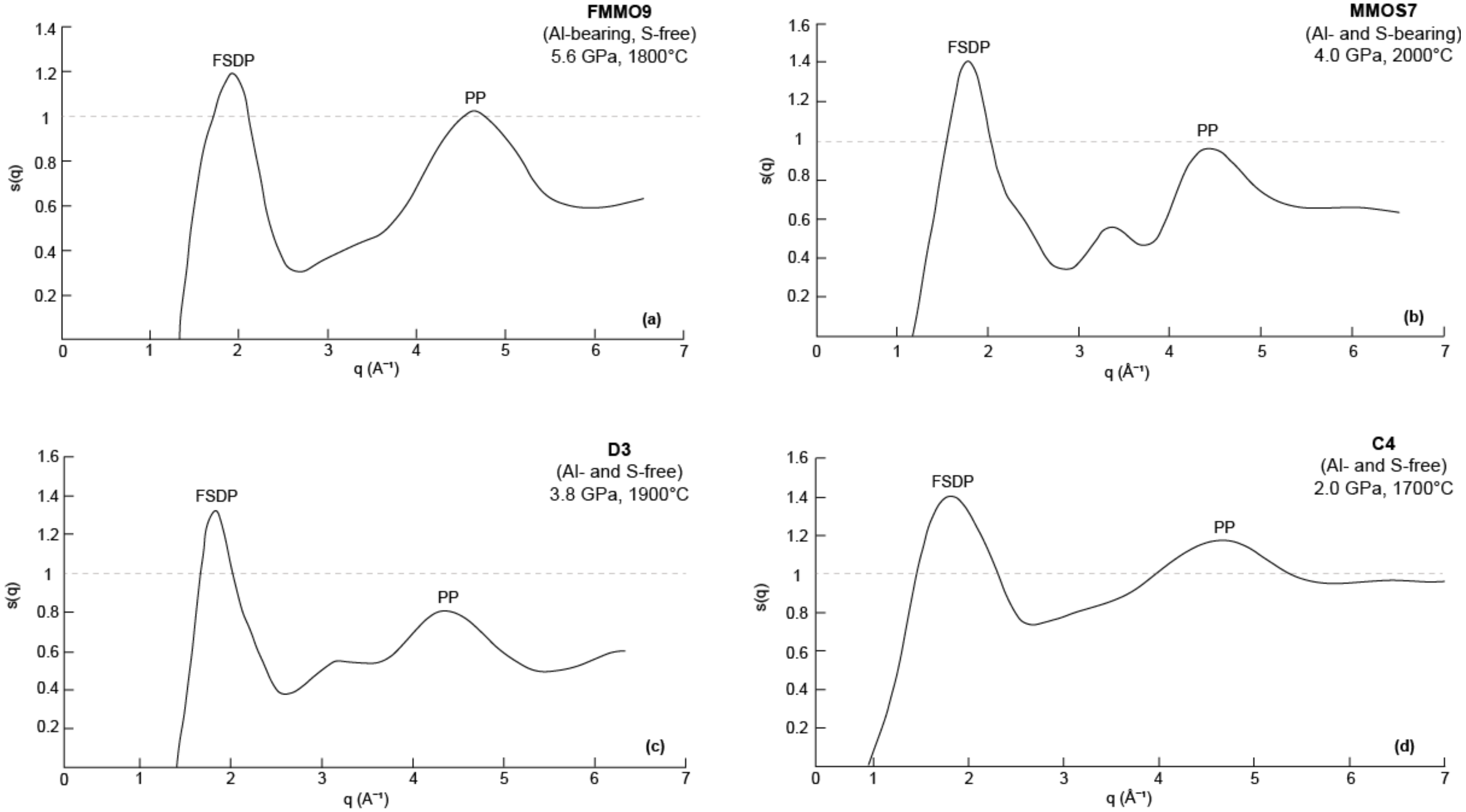

Figure 3.3. Structure factor for (a) FMMO9, (b) MMOS7, (c) D3, and (d) C4. FSDP= first sharp diffraction peak, PP= principal peak.

Table 3.3. Locations of the first sharp diffraction peak (FSDP) and the principal peak (PP) in each experiment.

	First Sharp Diffraction Peak (Å^{-1})	**Principal Peak (Å^{-1})**
FMMO9	2.05	4.58
MMOS7	1.88	4.20
C4	1.80	4.67
D3	1.89	4.50

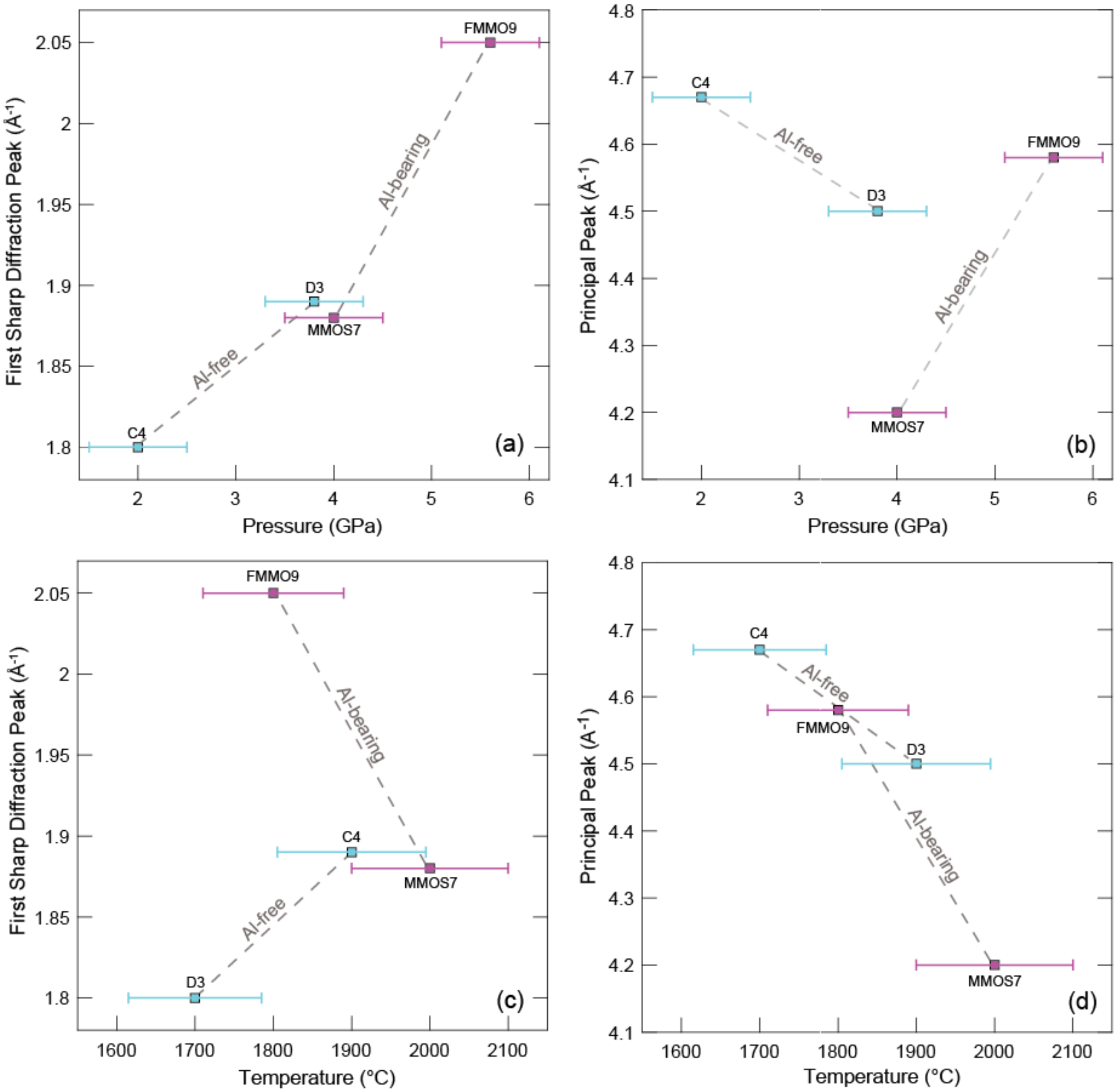

Figure 3.4. First sharp diffraction peak position versus pressure (a), principal peak versus pressure (b), first sharp diffraction peak versus temperature (c), and principal peak versus temperature (d) for each experiment. Experimental pressure and temperature uncertainties, ±0.5 GPa and ±5% °C, respectively, from the Paris-Edinburgh apparatus are included for each analysis. Refer to Mouser et al. (2021) for more detail on the experimental uncertainties.

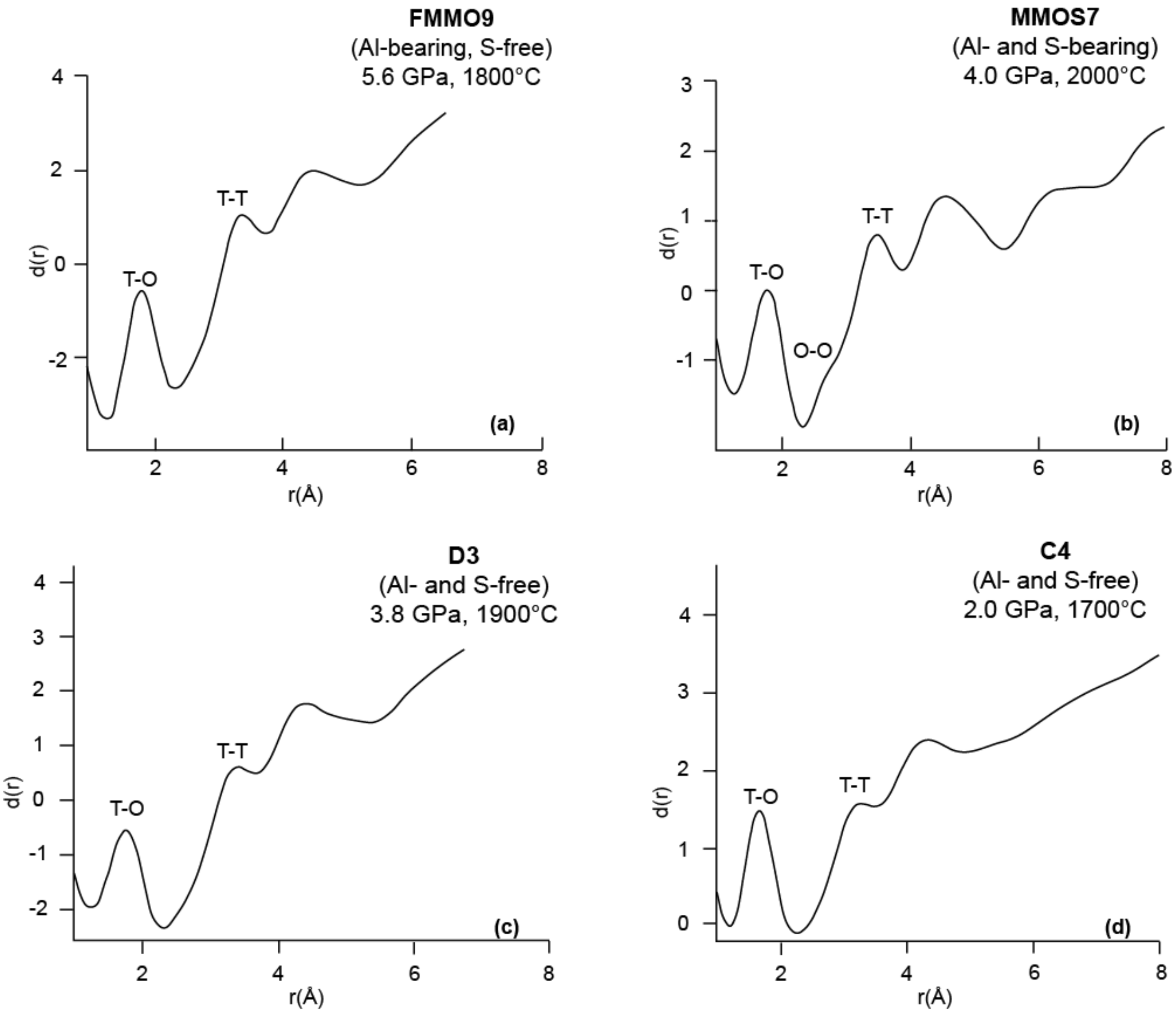

Figure 3.5. Distribution function for (a) FMMO9, (b) MMOS7, (c) D3, (d) C4 with peaks corresponding to the locations of T-O, T-T, and O-O indicated on each figure.

Table 3.4. Bond lengths and bond angles (α and β) for each sample.

Sample	T-T (Å)	T-O (Å)	O-O (Å)	α (°)	β (°)
FMMO9	3.18	1.66	2.60*	146.77	100.27*
MMOS7	3.32	1.66	2.55	179.91	100.27
C4	3.13	1.64	2.60*	156.42	101.99*
D3	3.27	1.65	2.60*	164.44	101.41*

*FMMO9, D3, and C4 did not exhibit an identifiable O-O bond (e.g., Figure 4). To calculate α and β values, previously reported O-O value for silicate liquids similar to MMOS7 were assumed (e.g., Yamada et al., 2011; Zoltov et al., 1989).

To determine the bond angles in a melt, the following equations are used to calculate the α (T-O-T) and β (O-T-O) angles (Figure 3.6):

$$\alpha = 2sin^{-1}\left(\frac{r_{T-T}}{2r_{T-O}}\right), \tag{3.5}$$

$$\beta = 2sin^{-1}\left(\frac{r_{O-O}}{2r_{T-O}}\right), \tag{3.6}$$

Where $r_{T\text{-}T}$ is the peak position for the T-T bonds, $r_{T\text{-}O}$ is the peak position for the T-O bonds, and $r_{O\text{-}O}$ is the peak position for the O-O bonds. The T-T, T-O, and O-O bond angles are listed in Table 3.4 and shown in Figure 3.7. The O-O peak was only apparent in MMOS7, thus reasonable values from analogous liquid compositions were assumed for O-O values in FMMO9, C4, and D3 (2.60 Å, similar to albite liquids and Si glass) for bond angle analysis. The T-O bond lengths for each series are in accordance with the differing cation sizes for Al^{3+} and Si^{4+} in tetrahedral coordination (Figure 3.7a;d), 0.39 Å and 0.26 Å, respectively (Shannon, 1976). Increasing bond lengths between tetrahedral cations (T-T) show a positive correlation with increasing temperature (Figure 3.7e). The same positive correlation with increasing temperature is also seen in the α (T-O-T) bond angles (Figure 3.7f). There is a lack of correlation between the T-T bond length of the two compositional series when plotted against pressure, where the Al-free maintains a positive correlation with pressure and the Al-bearing shows a negative correlation with pressure (Figure 3.7b).

3.3.2. *Raman*

The Raman spectrum of the glasses are a result of Raman scattering. Raman scattering is inelastic, where the energy of the scattered photons have a different energy from that of the incident photons (e.g., Neuville et al., 2014). The scattered photons exhibit a shift in energy which is referred to as Raman shift, and these shifts are due to the chemical structure of a molecule (e.g., Neuville et al., 2014). The intensity of normal Raman bands will depend on the polarizability of the molecule, the intensity of the incident source, and the concentration of the molecules being measured. A wide range of spectral features may be visible utilizing this method (0–4000 cm^{-1}); however, in this study, ranges relevant for silicate features, 600–1700 cm^{-1}, are analyzed.

The Raman spectra (Figure 7) show mid- (700–850cm^{-1}) to high-frequency (850–1300 cm^{-1}) regions (regions as defined in Neuville et al., 2014) of two experimental glasses (sulfur-free and sulfur-bearing), MMOS7 and MMO6. Both the mid- and high-frequency regions are attributed to Si-O stretching in the TO_4 structures, with the mid-frequency region involving oxygen motions (Neuville et al., 2014). Since these regions are associated with silicate features, there are several peak positions that can include important information for the interpretation of silicate materials. ~850–900 cm^{-1}, ~1000 cm^{-1}, ~1100 cm^{-1}, and ~1250 cm^{-1} are peaks seen in the Raman spectra in Figure 3.8 that are associated with different silicate structures, discussed further in section 3.4.3. The O_2 peak seen in both samples is around 1555 cm^{-1} which was used to normalize the spectra. Reflected light images (Figures C4-5) and spectra that have not been smoothed (Figure C6) are reported in Appendix C.

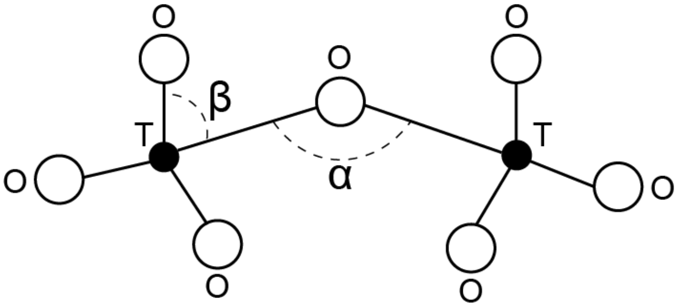

Figure 3.6. Schematic of TO_4 bonds showing the location of α (T-O-T) and β (O-T-O) bond angles. O stands for oxygen and T stands for the tetrahedral cation (e.g., Si^{4+}, Al^{3+}).

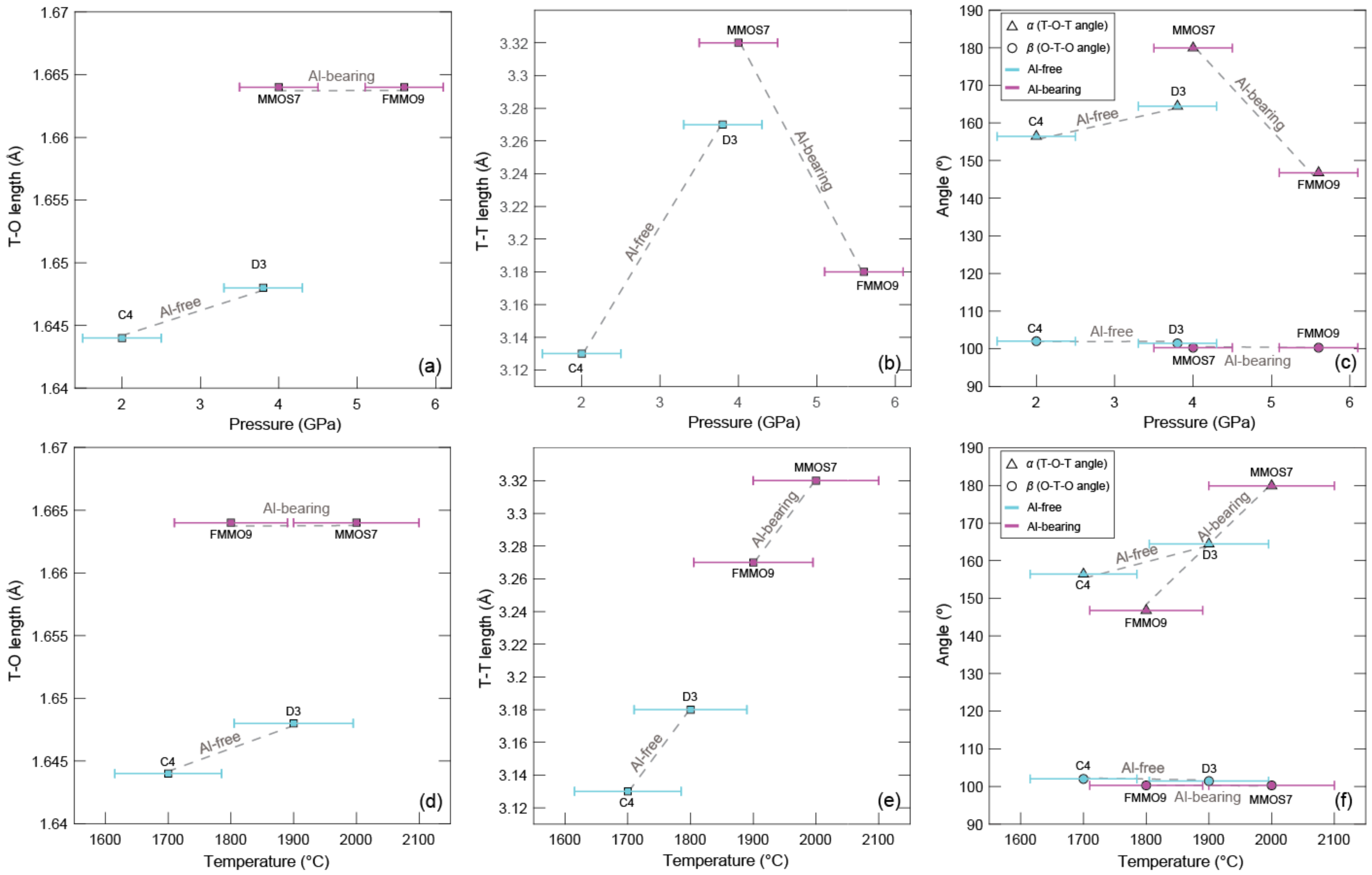

Figure 3.7. Bond length versus pressure for (a) T-O and (b) T-T, and (c) α and β bond angle versus pressure for each experiment determined from EDXD data. Experimental pressure and temperature uncertainties, ±0.5 GPa and ±5% °C, respectively, from the Paris-Edinburgh apparatus are included for each analysis. Refer to Mouser et al. (2021) for more detail on the experimental uncertainties.

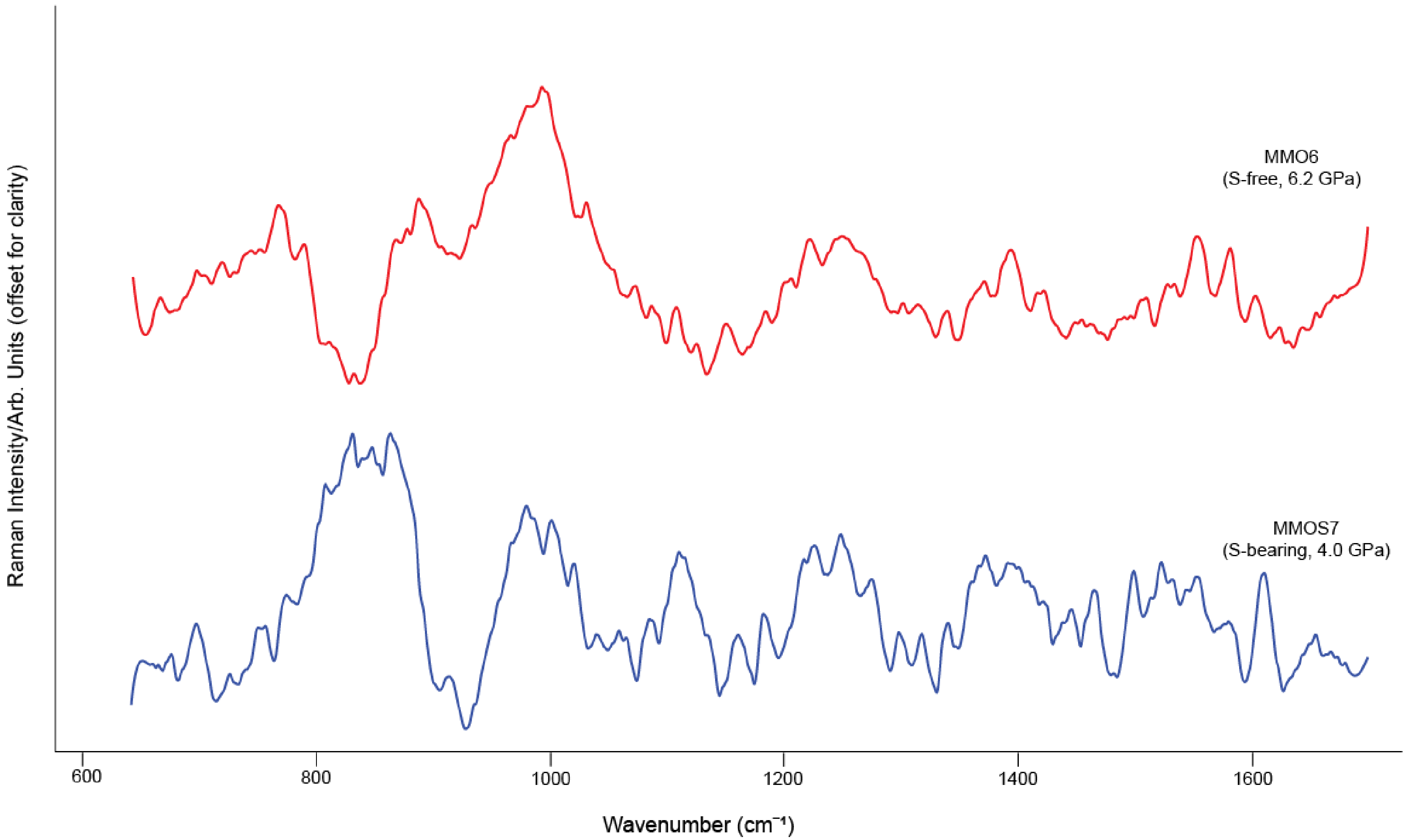

Figure 3.8. Raman spectroscopy of samples MMOS7 and MMO6. A Savitzky-Golay filter has been applied to smooth the spectra.

3.4. Discussion

The viscosities of the sulfur-free (MMO) and sulfur-bearing (MMOS) compositions reported in Mouser et al. (2021) differ at similar pressure and temperature conditions (e.g., Figure 3.1). The sulfur-bearing experiments have lower viscosities at all tested conditions. Both compositions decrease in viscosity with increased temperature or pressure. but the sulfur-bearing system is less pressure and temperature sensitive than the sulfur-free system (see Figure 2a-b in Mouser et al., 2021, and 3.8 this work). The reported viscosities for the two Al-free liquids were lower than the Al-bearing liquids by approximately an order of magnitude. Below we use the EDXD and Raman results to understand how the structural properties of these liquids control viscosity.

3.4.1. *Structure Factor*

Previous work on silicate materials suggests the structure factor is sensitive to pressure and possibly temperature, where the FSDP will show a decrease in amplitude and shift to higher *q* positions at higher pressures (e.g., Elliott, 1991, 1995; Sakamaki, 2018). The trend of increasing FSDP *q* position and increasing pressure is seen in all samples, and therefore is consistent despite the presence or absence of Al (Figure 3.4a). The relationships with pressure and temperature are opposite between FSDP and PP, which has been noted in SiO_2 glasses (Inamura et al., 2001). These features show the effects of the experimental conditions on the intermediate range order of the silicate structure. Densification of the tetrahedral structures due to increasing pressure (FSDP) as well as disruption over the overall extension of the silicate network due to increasing temperature (PP) are systematic despite Al content in these compositions.

3.4.2. *Distribution Function*

Much like the structure factor, we may expect structural transitions to be correlated with pressure and temperature of the experiment (e.g., Suzuki et al., 2002). In general, the bond angle is dependent on the chemistry (e.g., Suzuki et al., 2002) and the breaking of bonds which correlates to smaller T-O-T angles (Navrotsky et al., 1985) and potentially representing a reduction of void space between TO_4 structural units (Crupi et al., 2015; Bonechi et al., 2022) at higher pressures. The type of cation in the tetrahedrally coordinated site has been noted to have a direct effect on the bond length, and therefore the bond angle, in aluminosilicate liquids (Brown et al., 1969), therefore the differences in the T-T bond length and α angles are likely largely influenced by the Al cation in tetrahedral coordination in the Al-bearing liquids, where the radius of Al is 0.39 Å and the radius of Si is 0.26 Å in four-fold coordination (Shannon, 1976). Here, we observe temperature having a consistent effect on the lengths and angles in the tetrahedral structures. The lack of consistent correlation between the Al-free series and Al-bearing series versus pressure may indicate some internal effects of Al on the structure at different pressure conditions.

When comparing the structure factor (FSDP, PP) and the distribution function (bond length and angles) of the four samples, it is apparent that temperature has the strongest correlation to liquid behavior. The only feature that the liquids responded to consistently with pressure was the FSDP (Figure 3.4a) showing a more densified network TO_4 at increasing pressure. The T-T bond lengths increased with increasing temperature in all samples (Figure 3.4e) which is an expected result as bond lengths have been shown to increase with increasing temperature in silicate systems (e.g., Downs et al., 1992; Dove et al., 1997). Therefore, the bond angles exhibiting the same correlation with temperature is to be expected and is observed in these analyses (Figure 3.7f). The shifting PP position with increasing temperature suggests changes to how extended the intermediate range order of the liquid is, and the results from this work suggest a decrease in the intermediate range order with increasing temperature (Figure 3.4d). This is likely correlated to the changes occurring on the local scale of increasing bond angles and bond distances, where the increasing temperature is ultimately decreasing the overall connectivity of the silicate structures.

The presence of Al in the silicate structure appears to have different properties than in an Al-free system as seen by the bond lengths and angles (Figure 3.4 and 3.7) which likely correlates to the viscosity of these liquids. Effects of Al on the viscosity has been noted in previous studies on silicate liquids, where an inverse pressure dependence of Al^{3+} on liquid viscosity that has been attributed to the coordination change of Al from tetrahedral to octahedral at high pressures (e.g., Kushiro, 1976; Suzuki et al., 2002; Liebske et al., 2005). Perhaps the bond length shortening seen in the Al-bearing series (Figure 3.7b) and the observations made from the viscosity measurements of these liquids (Mouser et al., 2021), we can infer that Al can affect the behavior of the silicate structure differently than an Al-free

3.4.3. *Variation in the Silicate Tetrahedral Network*

The peak positions of the various bands in the Raman spectra (Figure 3.8) indicate the variation of the TO_4 units in the glassy structure. The high-frequency region (850–1300 cm^{-1}) exhibits bands responsible for the different TO_4 units, defined as Q^n, where Q refers to the tetrahedrally coordinated cation and n refers to the number of bridging oxygens (e.g., Mysen et al., 1980b; Neuville et al., 2014; Giordano et al., 2020). Depending on the amount of network modifying cations present, the spectral peak location of the features associated with the Q species may vary and is expected to shift peak locations to lower wavenumbers from where the pure SiO_2 network would be expected (e.g., Neuville et al., 2014).

The bands at ~850–900 cm^{-1} for both samples are in the Q^0 region (tetrahedral unit has no bridging oxygens, fully isolated tetrahedra); however, this feature is more prominent in the sulfur-bearing sample than in the sulfur-free (Figure 3.9). The higher presence of isolated tetrahedra correlates to a lower viscosity liquid, as there is little polymerization between the tetrahedral units. The low viscosity data collected for the sulfur-bearing liquids versus the sulfur-free liquids in Mouser et al. (2021) may provide support to the increased presence of isolated units in the sulfur-bearing glass. Additionally, an increased presence of isolated tetrahedral networks will reduce pressure sensitivity in a system due to the low abundance of bridging oxygen bonds to break, therefore the more depolymerized structure of the sulfur-bearing glass may lend some insight into the limited pressure range of this liquid that was measured during viscosity experiments (Figure 2b, Mouser et al., 2021).

The Q^1, Q^2, and Q^3 species are located at ~980, 1050, and 1100 cm^{-1}, respectively, representing one, two, and three bridging oxygen on the tetrahedral units. These three regions appear to contribute to the largest peak in the sulfur-free experiment (Figure 3.9), supporting the higher viscosity sulfur-free composition. These peaks are also present in the sulfur-bearing glass but are less prominent than the Q^0 peak. The final species, Q^4 (~1150-1200cm^{-1}) represents the most connected TO_4 network in silicate systems with four bridging oxygens. Both glasses have a peak offset from 1200 cm^{-1} that appears to relate to the Q^4 species.

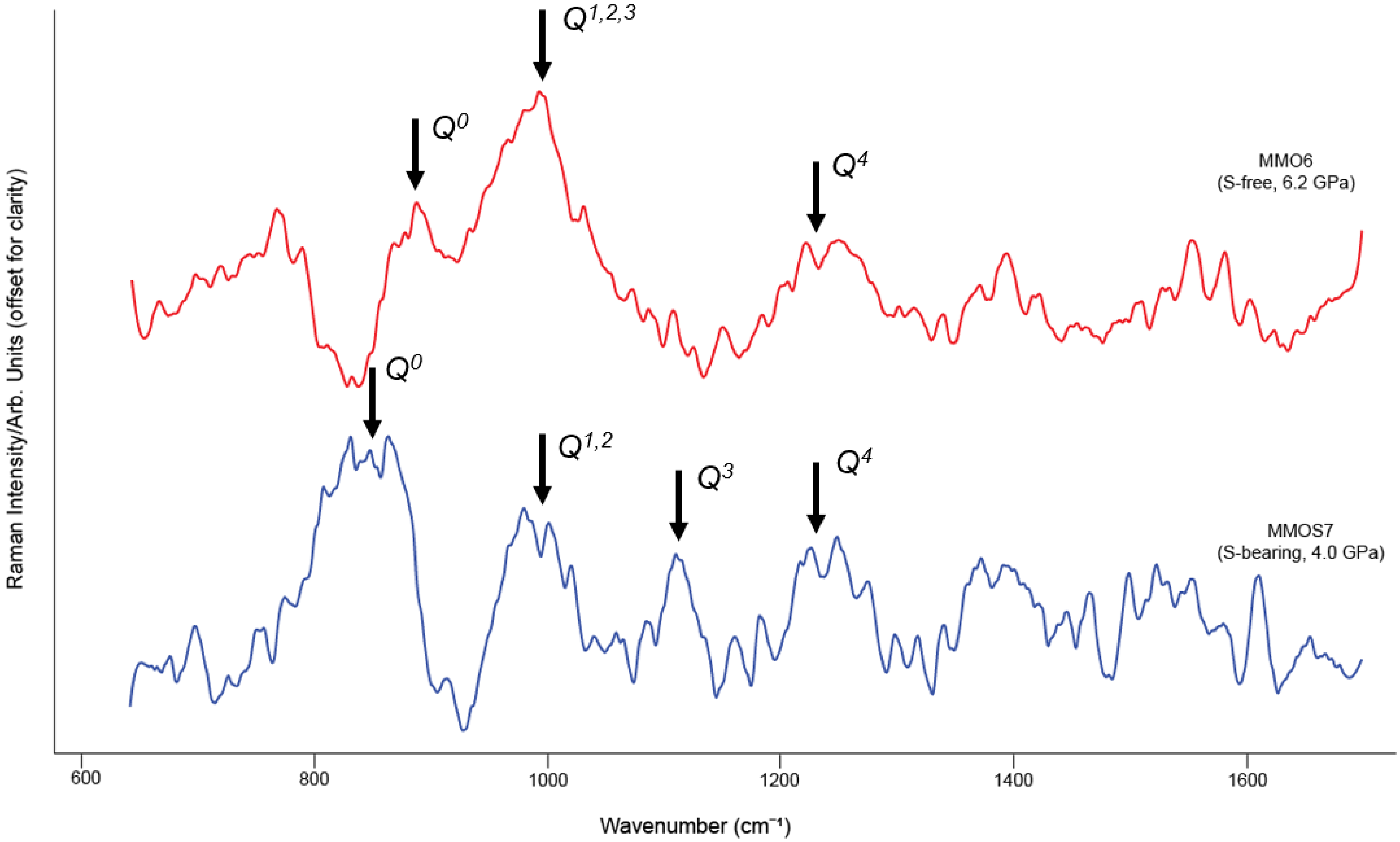

Figure 3.9. Baseline corrected Raman spectra plotted with *Q* species for MMO6 and MMOS7. Peaks correlated to the different *Q* species are indicated on the figure.

An increase in M-O bonds (M being network modifying cations, e.g., Ca^{2+}, Mg^{2+}) may result in the loss of some of the Q^4 band, and an increase in/new appearances of band features at lower Q species (Neuville et al., 2014). The substitution of Al in the tetrahedral site will also be visible in Q units (Q^4, Q^3, and Q^2) (McMillan and Piriou, 1983; Neuville et al., 2008; Licheron et al., 2011); however, the effect of Al is dependent on the network modifying cation involved in the charge balance substitution for Si^{4+}, so the variations in the wavenumber for Al will be the same as the network modifier wavenumber variations (Neuville et al., 2014). It is worth noting that pressure will affect the structure of the silicate units as seen by intensity of the Raman bands decreasing with pressure (e.g., Kubicki et al., 1992), and while we may expect that to occur in these glasses, the lack of data at different pressures for each composition prevents that conclusion from definitively being drawn from the present data.

Comparison of the results from the Raman and PP analysis from the EDXD data provide evidence of the effect of S on the melt structure. The PP reflects the overall connectivity, or periodicity, of the TO_4 structures in the liquid, and the sulfur-free composition had a higher PP value both in peak amplitude and q position than the sulfur-bearing composition. It is likely that the higher PP is a reflection of the more connected TO_4 structures, or Q species, in the sulfur-free liquid observed in the Raman data.

3.4.4. *The Importance of fO_2 and Sulfur*

Fe is the most common fO_2-sensitive element in most geologic systems; under moderately reducing conditions (QFM-IW) it is mostly divalent and under more oxidizing conditions it is mostly trivalent (Schreiber et al., 1987). The lack of Fe and low abundance of other fO_2 sensitive elements in the melt explored here (e.g., Ti) means the effect of fO_2 variations on the overall structure of the melts presented in this study are probably minimal. Under very low fO_2 conditions relevant to the MMOS and D samples, Si may be Si^{3+} (Boujibar et al., 2019). In TO_4 units with Al^{3+} as the tetrahedral cation, the bonds between T and O atoms are generally weaker than they would be with $Si^{4+}O_4$ units due to the presence of an M^+ cation to charge balance the structure (Bottinga and Weill, 1972), thus a similar effect may be expected for TO_4 units with Si^{3+}. While the presence of Si^{3+} may occur in these highly reduced liquids, the effect and/or presence of Si^{3+} likely is not great enough to affect the network as appears to be the case for Al^{3+}. If any features of Si^{3+} do exist, it is likely they are overlapping with or dominated by higher frequency features in the glass and are not the primary cause of structural changes in these liquids.

The sulfur species in these liquids is expected to represent an anion with 2- charge and complex with network modifying metal cations such as Fe and Mg, thus potentially further polymerizing the melt by bonding with 2+ cations that would normally break up the TO_4 units (e.g., Fogel, 1997; McCoy et al., 1999; Anzures et al., 2020). This expected effect of increased polymerization of the sulfur-bearing liquid (higher viscosity) was not exhibited by the viscometric experiments of Mouser et al. (2021), in fact, the sulfur-bearing composition exhibited lower viscosities than the sulfur-free. Sulfide in Raman spectra presents at wavenumbers lower than were measured (S, FeS at 300–400 cm^{-1}; e.g., Kalampounias et al., 2003; Klimm and Botcharnikov, 2010; Namur et al., 2016; Sułowska et al., 2021). Future analysis of these glasses will include exploring these lower wavenumbers to determine any possible effect of sulfides, however; the effect of sulfides cannot be evaluated in the current Raman spectra. Nonetheless, some inferences can be made on the sulfur behavior based on the Q species. In general, the sulfur-bearing composition exhibits more isolated Q species (Q^0) and fewer bonded *Q* species (Q^{1-4}). The greater presence of less connected TO_4 units may be related to reactions that occur in reduced, sulfur-rich systems. Previous work (Namur et al., 2016; Anzures et al., 2020) has suggested that the presence of S^{2-} will enhance the activity of silica in the system, reducing the forsterite stability field in favor of a broader enstatite stability field via the following reaction: $Mg_2SiO_4 + SiO_2 \rightarrow 2MgSiO_3$ (Anzures et al., 2020). This reaction is not in agreement with our current analysis of the *Q* species, where the sulfur bearing glass has a greater abundance of Q^0 which, based on the above reaction, should be significantly reduced in favor of Q^1 or Q^2 species. However, the difference in silicate species produced in these two liquids indicates that sulfur does have an effect on the silicate system, suggesting different silicate stability fields in sulfur-bearing silicate liquids that require further analysis to fully understand.

3.4.5. *Applications to Mercurian Magmas*

The study of the physical properties of silicate liquids is important to understanding the physical evolution of a magmatic body. The data discussed in this work are experiments with compositions relevant to Mercury's magma ocean, where the viscosity data revealed differences between the behavior of sulfur-free and sulfur-bearing liquids (Mouser et al., 2021). In the context of Mercury's magma ocean evolution, if the liquid did contain significant amount of sulfur as proposed due to the presence of sulfur on the surface of the planet (1–4 wt%, Nittler et al., 2011; Evans et al., 2012; Starr et al., 2012; Weider et al., 2012; Peplowski et al., 2014), the liquid will be depolymerized and the viscosity will be on average lower than in a liquid without sulfur, as suggested by the Raman spectroscopic analysis. The low viscosity nature of the sulfur-bearing liquids has implications for the behavior of the resulting volcanism that may be produced from these liquids. Low viscosity liquids on Mercury have been modeled to erupt as thin, laterally extensive flows (Stockstill-Cahill et al., 2012) possibly resulting in the formation of the Borealis Planitia. Therefore, this work on understanding the highly-reduced, sulfur-bearing liquids may provide support for low viscosity volcanism that produced the Borealis Planitia.

3.5. Conclusions

The liquid properties of multi-component silicate liquids were measured at high-temperatures and high-pressures utilizing multi-angle energy-dispersive X-ray diffraction on in situ liquids and Raman spectroscopy on recovered quenched glasses. The work aimed to understand structural differences between liquids of similar compositions to understand the controls on viscosity (e.g., Si/Al content, S). EDXD results showed that temperature has a large effect on the bond length and angles of silicate liquids, regardless of composition, where higher temperatures result in longer bond lengths and angles. The FSDP is the main feature that exhibited sensitivity to pressure, resulting in the densification of the structural units at higher pressures. The differences in bond lengths and valence states between Al and Si in the tetrahedral structure likely effect the overall behavior of the silicates at different pressure and temperature conditions which may correspond to the inverse relationship with pressure that the viscosities of these liquids exhibit.

The viscosity differences between the sulfur-bearing and sulfur-free (Al-bearing) liquids showed that the sulfur-bearing liquid has systematically lower viscosities at all tested pressure and temperature conditions than the sulfur-free liquid (Mouser et al., 2021). Raman data collected from quenched glasses showed a stronger band associated with Q^0 in the sulfur-bearing liquid while the sulfur-free liquid had a stronger band associated with more polymerized *Q* species (Q^1, Q^2, Q^3). These band amplitudes and locations show the possible correlation between fully isolated tetrahedral units (Q^0) expected in low viscosity liquids, and units that are not fully isolated and have some degree of polymerization ($Q^{1–4}$). Future work to better understand these systems could benefit from further analysis of the effects of sulfur anion in a simplified silicate melt to fully understand the possible controls it may have.

3.6. Acknowledgments

Thank you to Grace Sarabia and Blake LaDouceur who assisted with Raman data acquisition and processing.

References

Anzures, B. A., Parman, S. W., Milliken, R. E., Namur, O., Cartier, C., & Wang, S. (2020) Effect of sulfur speciation on chemical and physical properties of very reduced mercurian melts. *Geochimica et Cosmochimia Acta*, *286,* 1-18. https://doi.org/10.1016/j.gca.2020.07.024

Bonechi, B., Stango, V., Kono, Y., Hrubiak, R., Ziberna, L., Andreozzi, G. B., Perinelli, C., & Gaeta, M. (2022). Experimental measurements of the viscosity and melt structure of alkali basalts at high pressure and temperature. *Scientific Reports, 12,* 2599. https://doi.org/10.1038/s41598-022-06551-7

Bottinga, Y. & Weill, D. E. (1972). The Viscosity of Magmatic Silicate Liquids: A Model for Calculation. *American Journal of Science, 272,* 438-475. https://doi.org/10.2475/ajs.272.5.438

Boujibar, A., Habermann, M., Righter, K., Ross, D. K., Pando, K., Righter, M., Chidester, B. A., & Danielson, L. R. (2019). U, Th, and K partitioning between metal, silicate, and sulfide and implications for Mercury's structure, volatile content, and radioactive heat production. *American Mineralogist*, *104*, 1221–1237. https://doi.org/10.2138/am-2019-7000

Brown, G. E., Gibbs, G. V., & Ribbe, P. H. (1969). The nature and the varitation in the length of the Si-O and Al-O bonds in framework silicates. *American Mineralogist*, *54,* 1044-1061.

Campbell, A. J., Danielson, L., Righter, K., Seagle, C. T., Wang, Y., & Prakapenka, V. B. (2009). High pressure effects on the iron-iron oxide and nickel-nickel oxide oxygen fugacity buffers. *Earth and Planetary Science Letters*, *286,* 556-564. https://doi.org/10.1016/j.epsl.2009.07.022

Carey, C., Dyar, M. D., & Giguere, S. (2017). Web-based Software for Preprocessing, Matching, Fitting, Prediction, and Visualization of Spectroscopic Data: The Data Exploration, Visualization, and Analysis of Spectra (DEVAS) Website. *Lunar and Planetary Science Conference XLVIII*, abstract #1097.

Cormier, L., Creux, S., Galoisy, L., Calas, G., & Gaskell, Ph. (1996). Medium range order around cations in silicate glasses. *Chemical Geology,128,* 77-91. https://doi.org/10.1016/0009-2541(95)00164-6

Crupi, C., Carini, G., González, M., & D'Angelo, G. (2015). Origin of the first sharp diffraction peak in glasses. *Physical Review B, 92*, 134206. https://doi.org/10.1103/PhysRevB.92.134206

Deubener, J., Müller, R., Behrens, H., & Heide, G. (2003). Water and the glass transition temperature of silicate melts. *Journal of Non-Crystalline Solids, 330,* 268-273. https://doi.org/10.1016/S0022-3093(03)00472-1

Dingwell, D. B. & Mysen B. O. (1985). Effects of water and fluorine on the viscosity of albite melt at high pressure: a preliminary investigation. *Earth and Planetary Science Letters, 74*, 266-274. https://doi.org/10.1016/0012-821X(85)90026-3

Dove, M. T., Keen, D. A., Hannon, A. C., & Swainson, I. P. (1997). Direction measurement of the Si-O bond length and orientational disorder in the high-temperature phase of cristobalite. *Physics and Chemistry of Minerals, 24*, 311-317. https://doi.org/10.1007/s002690050043

Downs, R. T., Gibbs, G. V., Bartelmehs, K. L., & Boisen Jr., M. B. (1992). Variations of bond lengths and volumes of silicate tetrahedra with temperature. *American Mineralogist, 77,* 751-757.

Elliott, S. R. (1991). Origin of the First Sharp Diffraction Peak in the Structure Factor of Covalent Glasses. *Physical Review Letters, 67,* 711-714. https://doi.org/10.1103/PhysRevLett.67.711

Elliott, S. R. (1995). Extended-range order, interstitial voids and the first sharp diffraction peak of network glasses. *Journal of Non-Crystalline Solids, 182*, 40-48. https://doi.org/10.1016/0022-3093(94)00539-7

Evans, L. G., Peplowski, P. N., Rhodes, E. A., Lawrence, D. J., McCoy, T. J., Nittler, L. R., et al. (2012). Major-element abundances on the surface of Mercury: Results from the MESSENGER Gamma-Ray Spectrometer. *Journal of Geophysical Research, 117*, E00L07. https://doi.org/10.1029/2012JE004178

Fogel, R. A. (1997). On the significance of diopside and oldhamite in enstatite chondrites and aubrites. *Meteoritics & Planetary Science, 32,* 577-591. https://doi.org/10.1111/j.1945-5100.1997.tb01302.x

Giordano, D., Romano, C., Papale, P., & Dingwell, D. B. (2004). The viscosity of trachytes, and comparison with basalts, phonolites, and rhyolites. *Chemical Geology*, 213, 49-61. https://doi.org/10.1016/j.chemgeo.2004.08.032

Giordano, D., Russell, J. K., González-García, D., Bersani, D., Dingwell, D. B., & Del Negro, C. (2020). Raman Spectroscopy from Laboratory and Proximal to Remote Sensing: A Tool for the Volcanological Sciences. *Remote Sensing, 12,* 805. https://doi.org/10.3390/rs12050805

Harke, K. J., Vohra, Y. K., Kono, Y., Wereszczak, A. A., & Patel, P. (2017). White-beam X-ray diffraction and radiography studies on high-boron-containing borosilicate glass at high pressures. *High Pressure Research, 37,* 233-243. https://doi.org/10.1080/08957959.2017.1287263

Henderson, G. S. (2005). The Structure of Silicate Melts: A Glass Perspective. *The Canadian Mineralogist, 43,* 1921-1958. https://doi.org/10.2113/gscanmin.43.6.1921

Ibers, J. A. & Hamilton, W. C. (1974). International tables for X-ray crystallography. *Acta Crystallographica, b31*, 2558. https://doi.org/10.1107/S0567740875008175

Inamura, Y., Arai, M., Nakamura, M., Otomo, T., Kitamura, N., Bennington, S. M., Hannon, A. C., & Buchenau, U. (2001). Intermediate range structure and low-energy dynamics of densified vitreous silica. *Journal of Non-Crystalline Solids, 293-295,* 389-393. https://doi.org/10.1016/S0022-3093(01)00824-9

Kalampounias, A. G., Andrikopoulos, K. S., & Yannopoulos, S. N. (2003). Probing the sulfur polymerization transition *in situ* with Raman spectroscopy. *Journal of Chemical Physics, 118*, 8460-8467. https://doi.org/10.1063/1.1566938

Keiko, N. & Takao, I. (1984). Corrections for Intensity Data in Energy-dispersive X-Ray Diffractometry of Liquids. Application to Carbon Tetrachloride. *Bulletin of the Chemical Society of Japan, 57,* 1750-1759. https://doi.org/10.1246/bcsj.57.1750

Klimm. K. & Botcharnikov, R. E. (2010). The determination of sulfate and sulfide species in hydrous silicate glasses using Raman spectroscopy. *American Mineralogist, 95,* 1574-1579. https://doi.org/10.2138/am.2010.3590

Kono, Y., Irifune, T., Higo, Y., Inoue, T., & Barnhoorn, A. (2010). P-V-T relation of MgO derived by simultaneous elastic wave velocity and in situ X-ray measurements: A new pressure scale for the mantle transition region. *Physics of the Earth and Planetary Interiors, 183,* 196-211. https://doi.org/10.1016/j.pepi.2010.03.010

Kono, Y., Park, C., Kenny-Benson, C., Shen, G., & Wang, Y. (2014). Toward comprehensive studies of liquids at high pressures and high temperatures: Combined structure, elastic wave velocity, and viscosity measurements in the Paris-Edinburgh cell. *Physics of the Earth and Planetary Interiors, 228,* 269-280. http://doi.org/10.1016/j.pepi.2013.09.006

Kono, Y. (2018). Viscosity Measurement. In. Y. Kono and C. Sanloup (Eds.) *Magmas Under Pressure: Advances in High-Pressure Experiments on Structure and Properties of Melts,* Elsevier, Cambridge, Massachusetts, pp 261-277.

Koyama, C., Tahara, S., Kohara, S., Onodera, Y., Småbråten, D. R., Selbach, S. M., Akola, J., Ishikawa, T., Masuno, A., Mizuno, A., Okada, J. T., Watanabe, Y., Nakata, Y., Ohara, K., Tamaru, H., Oda, H., Obayashi, I., Hiraoka, Y., & Sakata, O. (2020). Very shrp diffraction peak in nonglass-forming liquid with the formation of distorted tetraclusters. *NPG Asia Materials, 12,* 1-11. https://doi.org/10.1038/s41427-020-0220-0

Kubicki, J. D., Hemley, R. J., & Hofmeister, A. M. (1992). Raman and infrared study of pressure-induced changes in $MgSiO_3$, $CaMgSi_2O_6$, and $CaSiO_3$ glasses. *American Mineralogist, 77,* 258-269.

Kushiro, I. (1976). Changes in viscosity and structure of melt of NaAlSi2O8 composition at high pressures. *Journal of Geophysical research, 81(35),* 6347-6350. https://doi.org/10.1029/JB08li035p06347

Kress, V. C., & Carmichael, I. S. E. (1991). The compressibility of silicate liquids containing Fe2O3 and the effect of composition, temperature, oxygen fugacity and pressure on their redox states. *Contributions to Mineralogy and Petrology, 108,* 82-92. https://doi.org/10.1007/BF00307328

Licheron, M., Montouillout, V., Millot, F., & Neuville, D. R. (2011). Raman and ^{27}Al NMR structure investigations of aluminate glasses: (1-x)Al_2O_3-xMO, with M=Ca, Sr, Ba and 0.5<x<0.75). *Journal of Non-Crystalline Solids, 357,* 2796-2801. https://doi.org/10.1016/j.jnoncrysol.2011.03.001

Liebske, C., Schmickler, B., Terasaki, H., Poe, B. T., Akio, S., Funakoshi, K., Ando, R., & Rubie, D. C. (2005). Viscosity of peridotite liquid up to 13 GPa: Implications for magma ocean viscosities. *Earth and Planetary Science Letters, 240,* 589-604. https://doi.org/10.1016/j.epsl.2005.10.004

McCoy, T. J., Dickinson, T. L., & Lofgren, G. E. (1999). Partial melting of the Indarch (EH4) meteorite: A textural, chemical, and phase relations view of melting and melt migration. *Meteoritics & Planetary Science, 34,* 735-746. https://doi.org/10.1111/j.1945-5100.1999.tb01386.x

McMillan, P. (1984). Structural studies of silicate glasses and melts- applications and limitations of Raman spectroscopy. *American Mineralogist, 69,* 622-644.

McMillan, P., & Piriou, B. (1983). Raman spectroscopy of calcium aluminate glasses and crystals. *Journal of Non-Crystalline Solids, 55,* 221-242. https://doi.org/10.1016/0022-3093(83)90672-5

Morard, G., Mezour, M., Rey, N., Poloni, R., Merlen, A., Le Floch, S., Toulemonde, P., Pascarelli, S., San-Miguel, A., Sanloup, C., & Fiquet, G. (2007). Optimization of Paris-Edinburgh press cell assemblies for *in situ* monochromatic X-ray diffraction and X-ray absorption. *High Pressure Research, 27,* 223-233. https://doi.org/10.1080/08957950601183553

Mouser, M. D., Dygert, N., Anzures, B. A., Grambling, N. L., Hrubiak, R., Kono, Y., Shen, G., Parman, S. W. (2021). Experimental investigation of Mercury’s magma ocean viscosity:

Implications for the formation of Mercury's cumulate mantle, its subsequent dynamic evolution, and crustal petrogenesis. *Journal of Geophysical Research: Planets, 126,* e2021JE006946 https://doi.org/10.1029/2021JE006946

Mysen, B. O. (1990). Relationships between silicate melt structure and petrologic processes. *Earth-Science Reviews, 27,* 281-365. https://doi.org/10.1016/0012-8252(90)90055-Z

Mysen, B. J., Virgo, D., Scarfe, C. M., & Cronin, D. J. (1985). Viscosity and structure of iron- and aluminum-bearing calcium silicate melts at 1 atm. *American Mineralogist, 70,* 487-498.

Mysen, B. O., Virgo, D., & Kushiro, I. (1981). The structural role of aluminum in silicate melts- a Raman spectroscopic study at 1 atmosphere. *American Mineralogist, 66,* 678-701.

Mysen, B. O., Seifert, F., & Virgo, D. (1980a). Structure and redox equilibria of iron-bearing silicate melts. *American Mineralogist, 65,* 867-884.

Mysen, B. O., Virgo, D., & Scarfe, C. M. (1980b). Relations between the anionic structure and viscosity of silicate melts- a Raman spectroscopic study. *American Mineralogist, 65,* 690-710.

Namur, O., Charlier, B., Holtz, F., Cartier, C., & McCammon, C. (2016). Sulfur solubility in reduced mafic silicate melts: Implications for the speciation and distribution of sulfur on Mercury. *Earth and Planetary Science Letters, 448,* 102-114. https://doi.org/10.1016/j.epsl.2016.05.024

Navrotsky, A., Geisinger, K. L., McMillan, P., & Gibbs, G. V. (1985). The Tetrahedral Framework in Glasses and melts- Inferences from Molecular Orbital Calculations and Implications for Structure, Thermodynamics, and Physical Properties. *Physics and Chemistry of Minerals, 11,* 284-298. https://doi.org/10.1007/BF00307406

Neuville, D. R., Cormier, L., Montouillout, V., Florian, P., Millot, F., Rifflet, J-C., & Massiot, D. (2008). Structure of Mg- and Mg/Ca aluminosilicate glasses: ^{27}Al NMR and Raman spectroscopy investigations. *American Mineralogist, 93,* 1721-1731. https://doi.org/10.2138/am.2008.2867

Neuville, D. R., de Ligny, D., & Henderson, G. S. (2014). Advances in Raman Spectroscopy Applied to Earth and Material Sciences. *Reviews in Mineralogy & Geochemistry, 78,* 509-541. https://doi.org/10.2138/rmg.2013.78.13

Nishikawa, K., & Iijima, T. (1984). Corrections for Intensity Data in Energy-dispersive X-Ray Diffractometry of Liquids. Application to Carbon Tetrachloride. *The Bulletin of the Chemical Society of Japan, 57,* 1750-1759. https://doi.org/10.1246/bcsj.57.1750

Nittler, L. R., Starr, R. D., Weider, S. Z., McCoy, T. J., Boynton, W. V., Ebel, D. S., et al. (2011). The major-element composition of Mercury's surface from MESSENGER x-ray spectrometry. *Science, 333,* 1847–1850. https://doi.org/10.1126/science.1211567

Perrillat, J-P., Meouzar, M., Garbarino, G., & Bauchau, S. (2010). *In situ* viscometry of high-pressure melts in the Paris-Edinburgh cell: application to liquid FeS. *High Pressure Research, 30,* 415-423. https://doi.org/10.1080/08957959.2010.494844

Peplowski, P. N., Evans, L. G., Stockstill-Cahill, K. R., Lawrence, D. J., Goldsten, J. O., McCoy, T. J., et al. (2014). Enhanced sodium abundance in Mercury's north polar region revealed by the MESSENGER Gamma-Ray Spectrometer. *Icarus, 228,* 86–95. https://doi.org/10.1016/j.icarus.2013.09.007

Reinsch, S., Roessler, C., Bauer, U., Müller, R., Deubener, J., & Behrens, H. (2016). Water, the other network modifier in borate glasses. *Journal of Non-Crystalline Solids, 432,* 208-217. https://doi.org/10.1016/j.jnoncrysol.2015.10.010

Richet, P., Lejeune, A-M., Holtz, F., & Roux, J. (1996). Water and the viscosity of andesite melts. *Chemical Geology, 128,* 185-197. https://doi.org/10.1016/0009-2541(95)00172-7

Riebling, E. F. (1966). Structure of Sodium Aluminosilicate Melts Containing at Least 50 mole % SiO2 at 1500°C. *The Journal of Chemical Physics, 44,* 2857-2865. https://doi.org/10.1063/1.1727145

Sakamaki, T., Wang, Y., Park, C., Yu, T., & Shen, G. (2014). Contrasting behavior of intermediate-range order structures in jadeite glass and melt. *Physics of the Earth and Planetary Interiors. 228,* 281-286. https://doi.org/10.1016/j.pepi.2014.01.008

Sakamaki, T. (2018) Structure and Properties of Silicate Magmas. In. Y. Kono and C. Sanloup (Eds.) *Magmas Under Pressure: Advances in High-Pressure Experiments on Structure and Properties of Melts,* Elsevier, Cambridge, Massachusetts, pp 323-366.

Salmon, P. S., Martin, R. A., Mason, P. E., & Cuello, G. J. (2005). Topological versus chemical ordering in network glasses at intermediate and extended length scales. *Nature, 435,* 75-78. https://doi.org/10.1038/nature03475

Scarfe, C. M., & Cronin, D. J. (1986). Viscosity-temperature relationships of melts at 1 atm in the system diopside-albite. *American Mineralogist, 71,* 767-771.

Schreiber, H. D., Merkel Jr., R. C., Schreiber, V. L., & Balazs, G. B. (1987). Mutual interactions of redox couples via electron exchange in silicate melts: Models for geochemical systems. *Journal of Geophysical Research: Solid Earth, 92,* 9233-9245. https://doi.org/10.1029/JB092iB09p09233

Shannon, R. D. (1976). Revised effective ionic radii and systematic studies of interatomic distances in halides and chalcogenides. *Acta Crystallographica, A32,* 751-767. https://doi.org/10.1107/S0567739476001551

Shibazaki, Y., Kono, Y., & Fei, Y. (2015). Microscopic structural change in liquid Fe-C alloy of ~5 GPa. *Geophysical Research Letters, 42,* 5236-5242. https://doi.org/10.1002/2015GL064271

Starr, R. D., Schriver, D., Nittler, L. R., Weider, S. Z., Byrne, P. K., Ho, G. C., et al. (2012). MESSENGER detection of electron-induced X-ray fluorescence from Mercury's surface. *Journal of Geophysical Research, 11,* E00L02. https://doi.org/10.1029/2012JE004118

Stopler, E. (1982). The speciation of water in silicate melts. *Geochimica et Cosmochimica Acta, 46,* 2609-2620. https://doi.org/10.1016/0016-7037(82)90381-7

Sułowska, J., Jeleń, P., Olejniczak, Z., & Szumera, M. (2021). Sulfur speciation and network structural changes in silicate-phosphate glasses. *Journal of Non-Crystalline Solids, 557,* 120645. https://doi.org/10.1016/j.jnoncrysol.2021.120645

Suzuki, A., Ohtani, E., Funakoshi, K., Terasaki, H., & Kubo, T. (2002). Viscosity of albite melt at high pressure and high temperature. *Physics and Chemistry of Minerals, 29,* 159-165. https://doi.org/10.1007/s00269-001-0216-4

Tomozawa, M., Takata, M., Acocella, J., Watson, E. B., & Takamori, T. (1983). Thermal properties of Na2O·3SiO2 glasses with high water content. *Journal of Non-Crystalline Solids, 56,* 343-348. https://doi.org/10.1016/0022-3093(83)90491-X

Waff, H. S. (1975). Pressure-induced coordination changes in magmatic liquids. *Geophysical Research Letters, 2,* 193-196. https://doi.org/10.1029/GL002i005p00193

Wang, Y., Sakamaki, T., Skinner, L. B., Jing, Z., Yu, T., Kono, Y., Park, C., Shen, G., Rivers, M. L., & Sutton, S. R. (2014) *Nature Communications, 5,* 1-10. https://doi.org/10.1038/ncomms4241

Waseda, Y. (1980). Principles of Structural Analysis for Non-crystalline Systems. *The Structure of Non-crystalline Materials- Liquids and Amorphous Solids*. (pp. 1-26) McGraw-Hill, New York.

Weider, S. Z., Nittler, L. R., Starr, R. D., McCoy, T. J., Stockstill-Cahill, K. R., Byrne, P. K., et al. (2012). Chemical heterogeneity on Mercury's surface revealed by the MESSENGER X-Ray Spectrometer. Journal of Geophysical Research, 117, E00L05. https://doi.org/10.1029/2012JE004153

Whitaker, D. A. & Hayes, K. (2018). A simple algorithm for despiking Raman spectra. *Chemometrics and Intelligent Laboratory Systems, 179,* 82-84. https://doi.org/10.1016/j.chemolab.2018.06.009

Whittington, A., Richet, P., Linard, Y., & Holtz, F. (2001). The viscosity of hydrous phonolites and trachytes. *Chemical Geology, 174,* 209-223. https://doi.org/10.1016/S0009-2541(00)00317-X

Wilding, M. C., Benmore, C. J., & Weber, J. K. R. (2008). In situ diffraction studies of magnesium silicate liquids. *Journal of Material Sciences, 43,* 4707-4713. https://doi.org/10.1007/s10853-007-2356-5

Williams, Q., & Jeanloz, R. (1988). Spectroscopic Evidence for Pressure-Induced Coordination Changes in Silicate Glasses and Melts. *Science, 239,* 902-905. https://doi.org/10.1126/science.239.4842.902

Wright, A. C. (1990). Diffraction Studies of Glass Structure. *Journal of Non-Crystalline Solids, 123*, 129-148. https://doi.org/10.1016/0022-3093(90)90779-L

Wright, A. C., Hulme, R. A., Grimley, D. I., Sinclair, R. N., Martin, S. W., Price, D. L., & Galeener, F. L. (1991). The structure of some simple amorphous network solids revisited. *Journal of Non-Crystalline Solids*, *129*, 213-232. https://doi.org/10.1016/0022-3093(91)90098-Q

Xue, A., Stebbins, J. F., Kanzaki, M., McMillan P., & Poe, B. (1991). Pressure-induced silicon coordination and tetrahedral structural changes in alkali oxide-silica melts up to 12 GPa: NMR, Raman, and infrared spectroscopy. *American Mineralogist, 76*, 8-26.

Yamada, A., Wang, Y., Inoue, T., Yang, W., Park, C., Yu, T., & Shen, G. (2011). High-pressure x-ray diffraction studies on the structure of liquid silicate using a Paris-Edinburgh type large volume press. *Review of Scientific Instruments*, *82*, 015103. https://doi.org/10.1063/1.3514087

Yarger, J. L., Smith, K. H., Nieman, R. A., Diefenbacher, J., Wolf, G. H., Poe, B. T., & McMillan, P. F. (1995). Al Coordination Changes in High-Pressure Aluminosilicate Liquids. *Science*, *270*, 1964-1967. https://doi.org/10.1126/science.270.5244.1964

Zotov, N., Dimitrov, V., & Yanev, Y. (1989). X-Ray Radial Distribution Function Analysis of Acid Volcanic Glasses from the Easter Rhodopes, Bulgaria. *Physics and Chemistry of Materials, 16,* 774-782. https://doi.org/10.1007/BF00209701

Appendix C

X-ray Diffraction Data

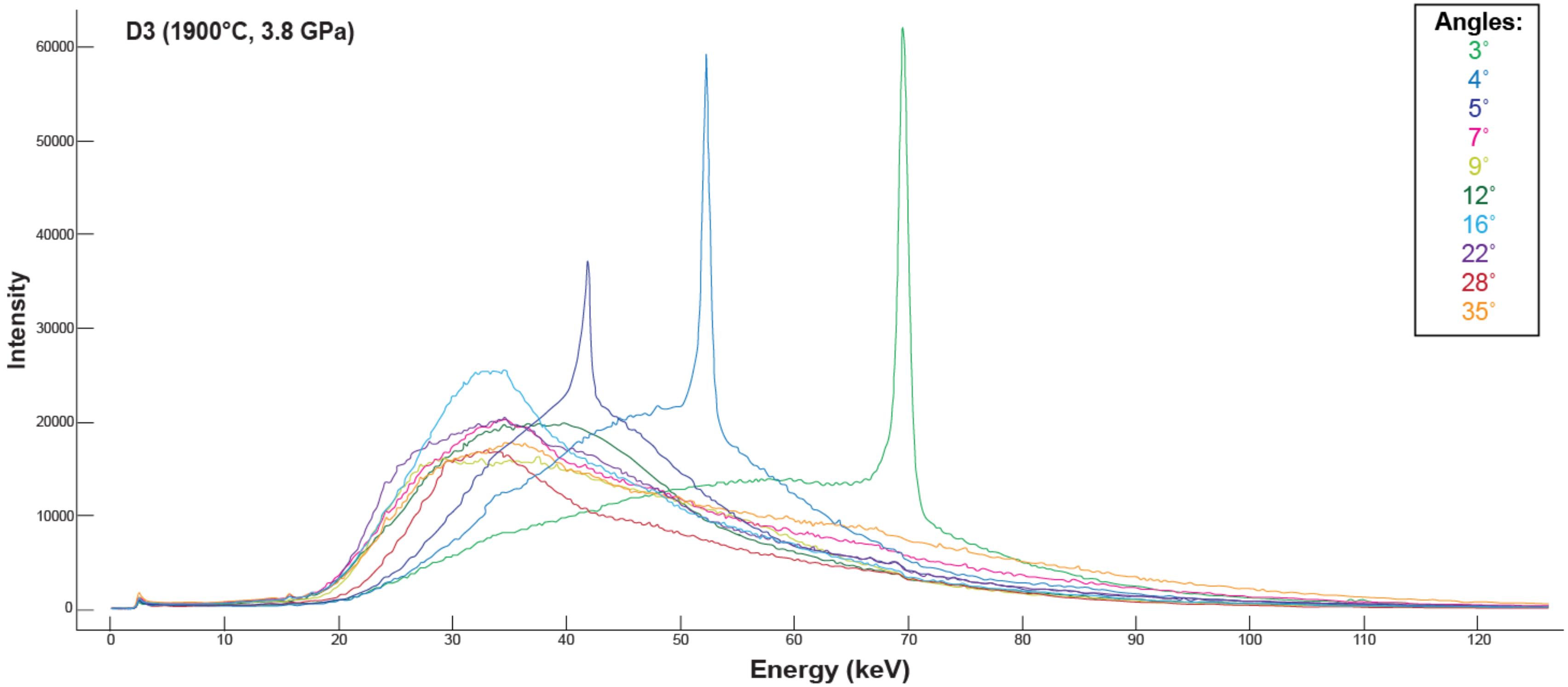

Figure C1. Uncut and unsmoothed spectra of sample D3 featuring peaks associated with the assembly parts.

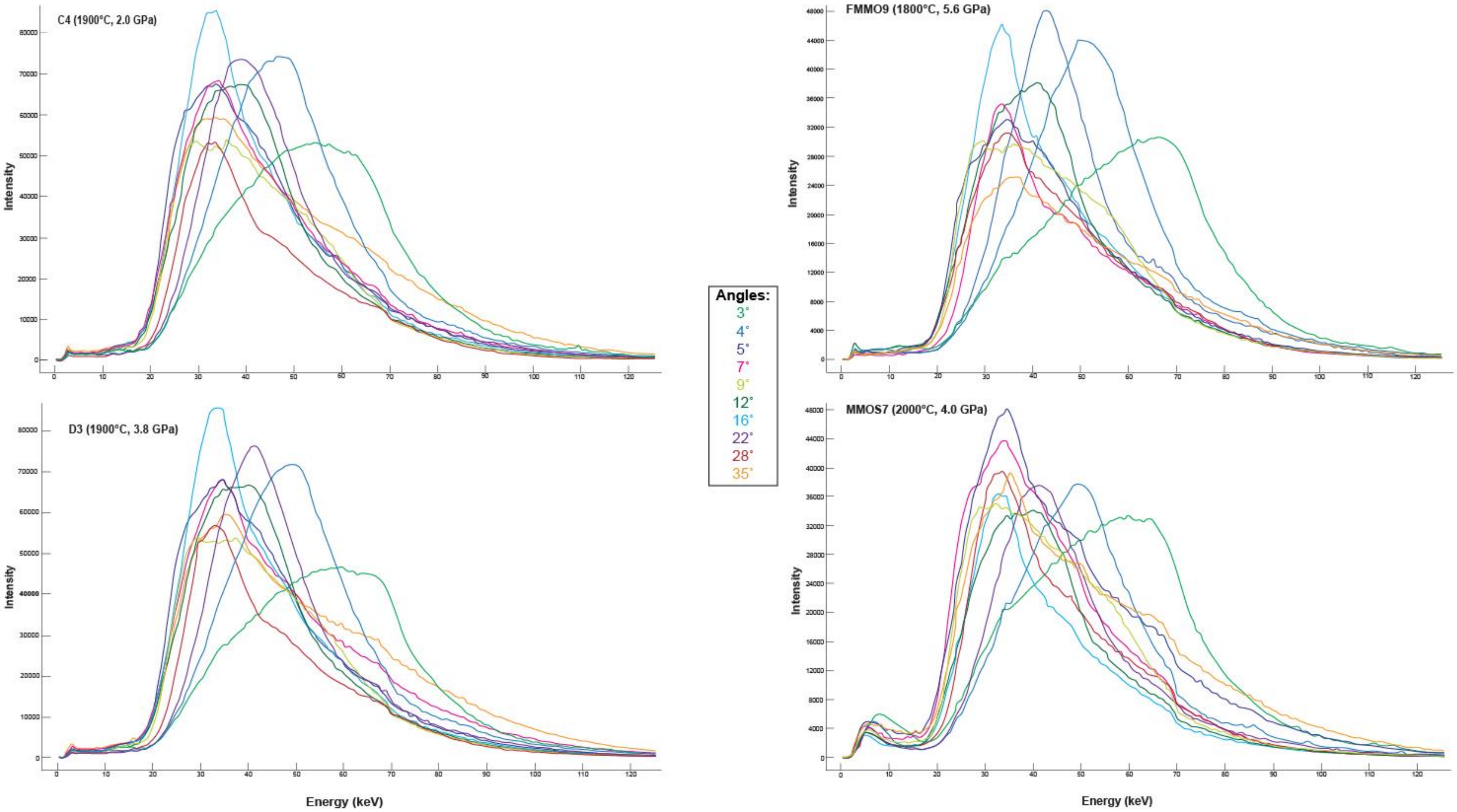

Figure C2. Smoothed melt spectra for samples C4 (a), D3 (b), FMMO9 (c), and MMOS7 (d) at all measured angles. Peaks associated with assembly components were removed from the spectra.

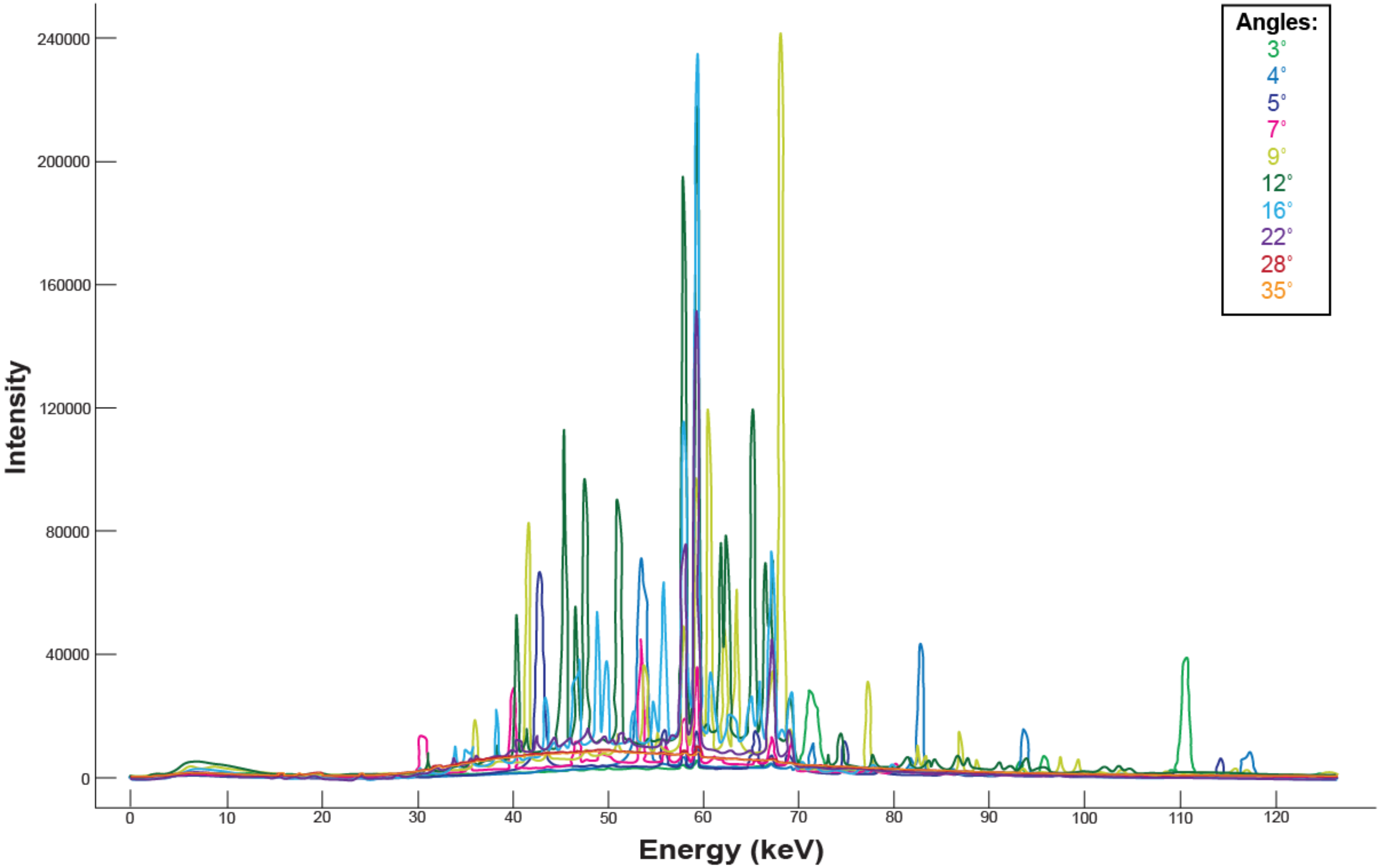

Figure C3. Raw spectra of an experiment with crystalline features.

Raman Spectroscopy Data

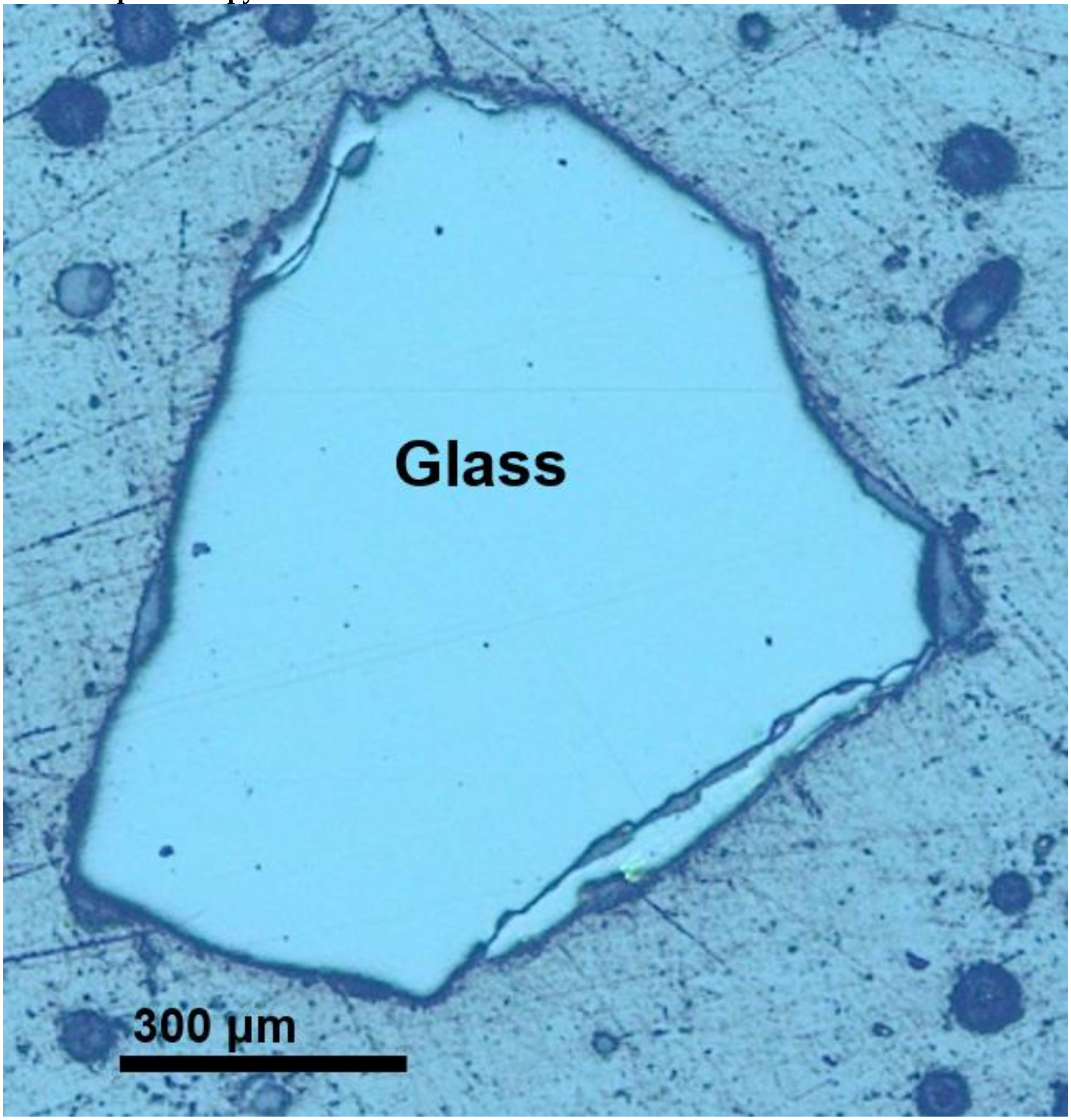

Figure C4. Reflected light image of sample MMOS7.

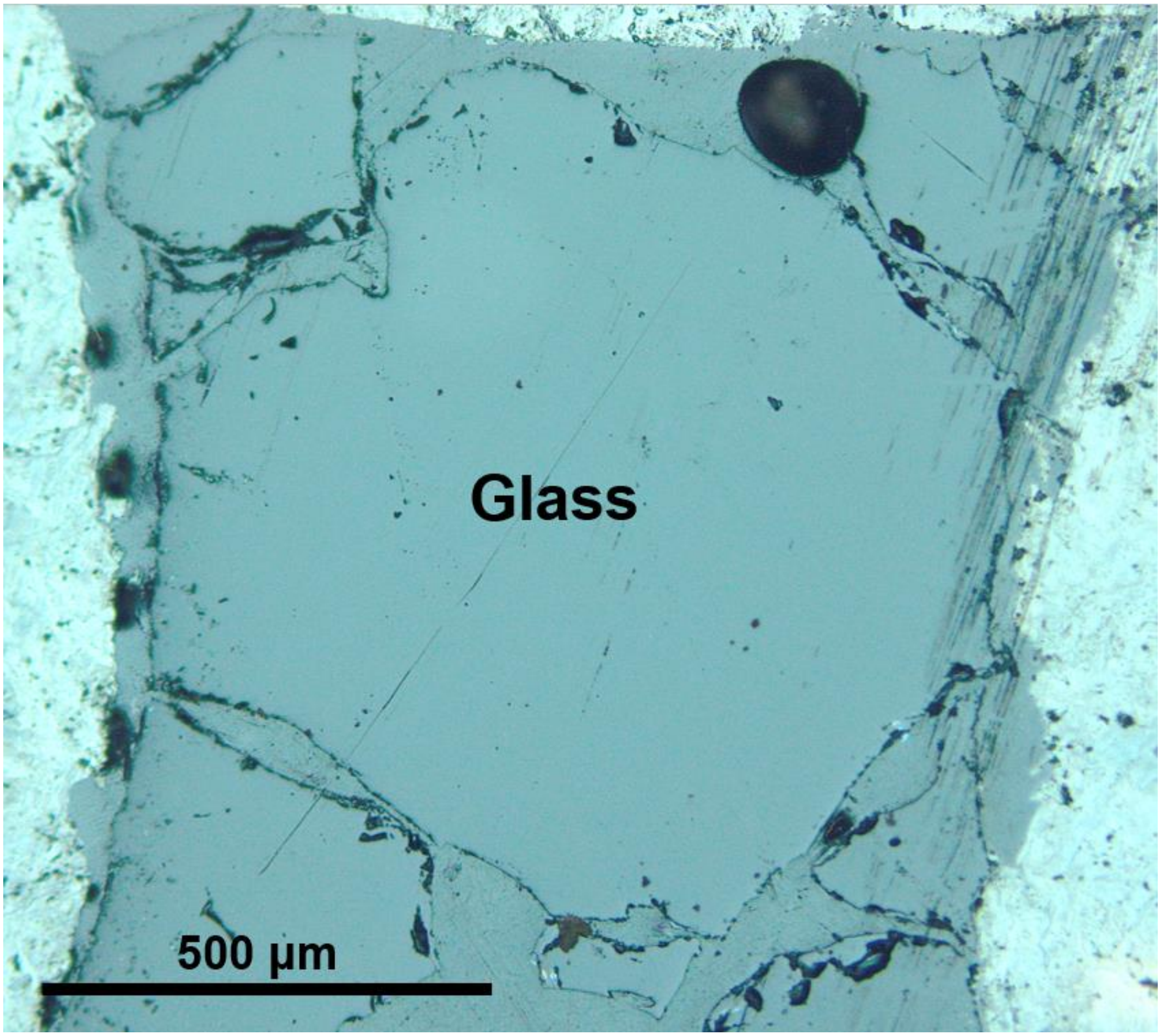

Figure C5. Reflected light image of sample MMO6

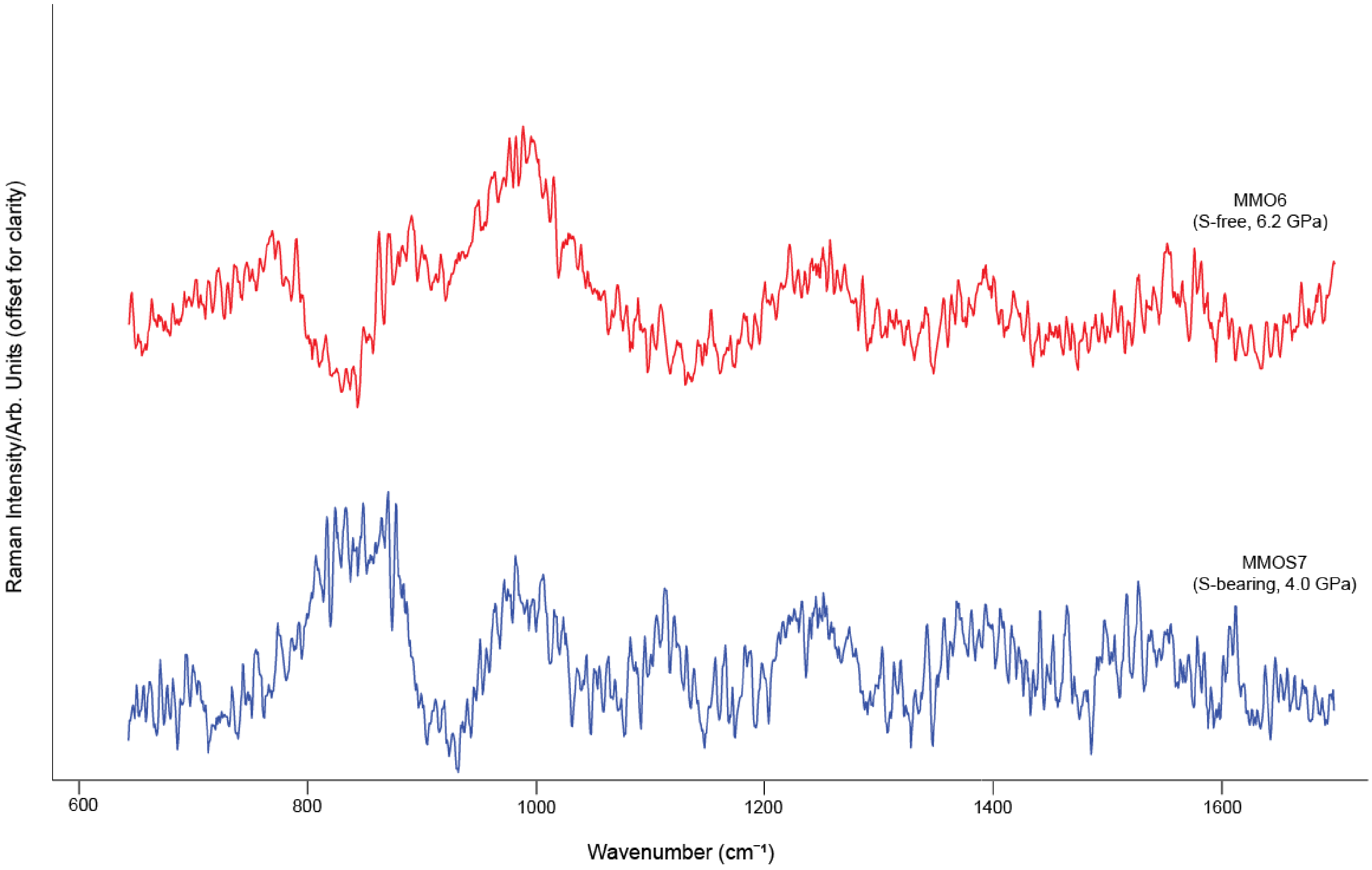

Figure C6. Unsmoothed Raman spectra for glass samples MMO6 (red) and MMOS7 (blue)

CHAPTER IV.

AN EXPERIMENTAL STUDY ON CLINOPYROXENE-MELT TRACE ELEMENT PARTITIONING IN FE-RICH BASALTIC SYSTEMS

Abstract

Trace element partitioning in Fe-rich basaltic systems is understudied but is important for understanding petrogenesis on Fe-rich magmatic bodies in the Solar System. Clinopyroxenes are a major host of incompatible elements in planetary interiors for the study of incompatible trace element inventories as their large M2 crystallographic site allows for elements with a wide variety of cation radii and valence states to enter the site. To investigate crystal chemical controls on trace element partitioning in clinopyroxenes in Fe-rich basalts, an experimental study utilizing two synthetic compositions, an Fe-rich, Mg- and Al-poor composition (ferrobasalt) and a moderate Fe/Mg and Al enriched composition (intermediate basalt), was conducted. Experiments were run in a piston cylinder apparatus at 1 and 2 GPa, testing each endmember and a 50-50 mixture of the endmembers. These experiments reveal that Al substitution into the pyroxene structure in the tetrahedral site influences 3+ cations partitioning into the lattice, with the more aluminous samples, in general, having the highest partition coefficients for high field strength elements (HFSE), large ion lithophile elements (LILE), and rare earth elements (REE) in both the 1 and 2 GPa series. However, the more Fe-rich experiments (ferrobasalt and 50-50 mix) demonstrated an increase in partitioning of heavy REEs, likely into the M1 site in 6-fold coordination where they are more similar to the radius of Fe. Lattice strain models using the experimental trace element partitioning data from this work are used to model and predict the partitioning of elements onto the M1 and M2 lattice sites in Fe-rich clinopyroxenes. The experimental results and predictive models developed from this work can be applied to the petrogenesis Fe-rich basalts (e.g., Nakhlite meteorites, lunar basalts) to better understand magmatic processes in the Solar System.

4.1. Introduction

Trace element compositions of mafic, rock-forming minerals (e.g., olivine, orthopyroxene, clinopyroxene) are records of melting and fractionation processes during igneous petrogenesis. The distribution of incompatible trace elements in these minerals are important for interpretations of the petrogenesis of igneous rocks (Sun and Liang, 2013a), in particular, the rare earth element (REE) group is the most commonly applied in petrogenetic modeling (Gallahan and Nielsen, 1992). In addition to REEs, high field strength elements (HFSEs) are also useful petrogenetic indicators. Both REEs and HFSEs have high valence states (e.g., 3+, 4+) which require coupled substitution when substituting into a crystal lattice site in a mineral that would typically house a 2+ cation (e.g., Mg, Fe). Experiments conducted on terrestrial Mg-rich systems found that coupled substitution of a 3+ cation is correlated with Al^{3+} substituting into the tetrahedrally coordinated site usually occupied by Si^{4+} (e.g., Colson et al., 1989; Gallahan and Nielsen, 1992; Hauri et al., 1994; Gaetani and Grove, 1995), thus a higher trace element content is positively correlated with a higher Al concentration (Sun and Liang, 2013b). Whether this dependence on Al translates to Fe-rich systems is not well understood (Dygert et al., 2014).

Among the major minerals in planetary upper mantles, clinopyroxene has a more favorable structure to host the incompatible trace elements. Clinopyroxene, with a general formula of $(M2)(M1)T_2O_6$, preferentially hosts trace elements because of the large size of the M2 site in the crystal structure. The M2 site normally houses Ca^{2+} and is large enough to accommodate substitution of cations with larger ionic radii and higher valence states (e.g., Cameron and Papike, 1981; McKay et al., 1986; Gallahan and Nielsen, 1992; Olin and Wolff, 2010). The M1 site is a stiffer, less distorted site in the crystal structure that houses cations with smaller valence states and radii, e.g., Mg^{2+}, Fe^{2+} (Blundy and Wood, 2003). Therefore, the M1 site is typically not as important when considering partitioning of elements with larger radii (e.g., REEs) in a clinopyroxene structure with the exception of Fe-rich systems where heavy REEs may partition into the M1 site in 6-fold coordination (Olin and Wolff, 2010). While the most common charge-balancing coupled substitution of REE and HFSE into the M1 site is a substitution of Al^{3+} in the tetrahedral site, there can be other couple substitution mechanisms such as vacancy substitution.

Clinopyroxene-melt trace element partitioning studies have mainly focused on Mg-rich basaltic systems (e.g., Gaetani and Grove, 1995; Sun and Liang, 2012; 2013a; Bédard, 2014; Sun et al., 2017). These studies have found that the main controls on the trace element partitioning in the system are the compositions of the mineral and melt, crystallization fO_2, and the pressure and temperature during crystallization. Composition appears to have a large effect on the trace element partitioning for the Fe-rich clinopyroxene endmembers as well (Olin and Wolff, 2010; Dygert et al., 2014)., where an increase in heavy REE in 6-fold coordination in the M1 site has been noted in Fe-rich clinopyroxenes (Olin and Wolff, 2010). This HREE partitioning could be attributed to the similar ionic radii between HREE in 6-fold coordination and Fe^{2+} (e.g., Lu in 6-fold- 0.861 Å vs. 8-fold- 0.977 Å, and Fe2+ in 6-fold-0.780 Å). While Al does affect the partitioning of 3+ and 4+ cations (e.g., Lundstrom et al., 1998; Schwandt and McKay, 1998; Shearer et al., 2006), the partitioning of HREE in 6-fold is likely more directly influenced by the effect of high Fe abundances in clinopyroxene structure. Existing predictive models for clinopyroxene-melt trace element partitioning (e.g., Sun and Liang, 2012; Dygert et al., 2014) are not suited to accurately model the HREE partitioning onto the M1 lattice site. Establishing the controls of pyroxene Fe and Al composition on trace element partitioning requires new constrains from experiments conducted on high-Fe and low-Al, and low-Fe and high-Al systems which are explored in this work.

4.2. Methods

4.2.1. *Compositions*

A ferrobasalt composition based on FR1290 from Longhi (2003) was used to prepare two endmember basalt compositions to explore the effects of Al and Fe on partitioning in Fe-rich systems. One has no added Al and a higher Fe content (ferrobasalt), while the other has a more moderate Fe content and higher Al (Mg# of approximately 50, where Mg# is defined as 100×Mg/Mg+Fe) resembling an intermediate basalt. These were made from reagent grade oxide powder, ground in an agate mortar and pestle for 6 hours. Both compositions were spiked with a REE/HFSE/alkali earth element mixture of ~ 0.5wt% of the total composition (Table 4.1). After the grinding and doping process, the compositions were decarbonated at 900°C for 24 hours in an alumina crucible. After decarbonation they were conditioned to one log unit below the iron wüstite buffer at Brown University. Major element compositions of glassed samples of both compositions are presented in Table 4.1.

4.2.2. *Piston Cylinder Apparatus*

Experiments were conducted in 150-ton end-loaded piston cylinder (PC) apparatuses at the University of Tennessee in graphite lined Mo capsules. Assemblies used NaCl cells as a confining medium and were placed in ¾” pressure vessels and pressurized before heating. The experiments were run at 1 and 2 GPa. The programs set for each experiment were a rapid ramp to superliquidus temperature (1300°C for 1 GPa, 1350°C for 2 GPa) at a rate of 70°C/min, dwell for 1 hour, a slow cool to final temperature (1120–1150°C for 1 GPa, and 1175°C for 2 GPa) at a rate of 0.1°C/min, and dwelling at the target temperature for at least 48 hours before an isobaric quench (Table 4.2). The range of superliquidus and final dwell temperatures in the 1 GPa experiments were selected to produce appropriate proportions of crystals and glass, with the more magnesian experiments requiring higher temperatures than the ferrobasalt.

4.2.3. *Electron Microprobe Analysis*

After the experiments were quenched, they were mounted in epoxy and polished for electron probe micro analysis (EPMA). Analyses were conducted using the Cameca SX100 electron microprobe at the University of Tennessee. Major elements were analyzed at an accelerating voltage of 15 kV, a beam current of 20 nA, and a 2 um spot size. Backscattered electron images of each experimental charge are shown in Figure 4.1.

4.2.4. *Laser Ablation Inductively Coupled Plasma Mass Spectrometry*

Trace element data were collected by laser ablation inductively coupled plasma mass spectrometry (LA-ICP-MS) at the University of Texas at Austin, on the recovered experimental glasses and pyroxene rims. Spot sizes were 50 μm and data were collected with a laser fluence of 2.03 J/cm^3 at 20 Hz with a 60 second dwell and 30 second gas blank. The reference materials were: NIST612 and NIST610 used primary standards, and NIST610, NIST612, BHVO2G, and BCR-2G used as secondary standards. Reflected light images of the 1 GPa experiments with LA-ICP-MS analysis pits are included in the appendix, Figures D1a-c.

4.3. Results

4.3.1. *Major Element Chemistry*

Major element chemistry of the experimental pyroxenes range from near endmember hedenbergite in the ferrobasalt sample, to augite in the intermediate basalt experiment (Table 4.3, Figure 4.2). The rim compositions of the pyroxenes were used for analysis in this study as they are anticipated to represent the closest approach to equilibrium with the coexisting melt. Measured glass compositions are homogeneous across each sample (Table D1). The 2 GPa intermediate basalt experiment produced garnet in addition to pyroxene, with a resulting composition that is Fe (and somewhat less Ca)-rich almandine (Alm), Figure 4.2b.

4.3.2. *Trace Element Chemistry*

Trace element chemistry of each experimental sample (glass and pyroxene rims) are plotted in the appendix, Table D2. The 1 GPa Al-poor ferrobasalt sample exhibited the lowest concentration of trace elements among the six samples, with the 1 GPa Al-rich intermediate basalt and 2 GPa ferrobasalt samples having the highest concentrations (Figure 4.3). Chondrite normalized REE diagrams of the pyroxene rims and glasses are shown in the appendix, Figures D2 and D3. The 2 GPa intermediate basalt pyroxene was not included in the analysis due to the mantling of garnet around the pyroxene, which appears to have prohibited attainment of equilibrium between pyroxene and the host melt.

Table 4.1. Major element experimental compositions.

	SiO_2	TiO_2	Al_2O_3	MgO	CaO	MnO	FeO	Na_2O	K_2O	P_2O_5	Dopant	Total
Intermediate Basalt	35.85	2.72	5.04	2.69	10.35	0.63	39.44	0.16	0.28	0.53	0.34	98.03
1σ St Dev	0.24	0.04	0.39	0.03	0.07	0.02	0.19	0.02	0.01	0.02	0.02	
Ferrobasalt	34.58	3.68	0.49	1.01	10.70	1.10	44.57	0.10	0.16	0.48	0.33	97.20
1σ St Dev	0.57	0.11	0.01	0.03	0.22	0.03	1.04	0.01	0.01	0.01	0.02	
FR1290[a]	44.16	4.05	8.67	0.26	10.89	0.70	29.86	0.50	0.36	0.40	--	99.85

Compositional data in wt% from glassed Fe- and Al-rich endmember compositions. Total dopant concentrations were calculated from LA-ICP-MS measurements, converted from ppm to wt%. Major elements were analyzed by electron microprobe. [a]For comparison, lunar magma ocean ferrobasalt FR1290 composition from Longhi (2003).

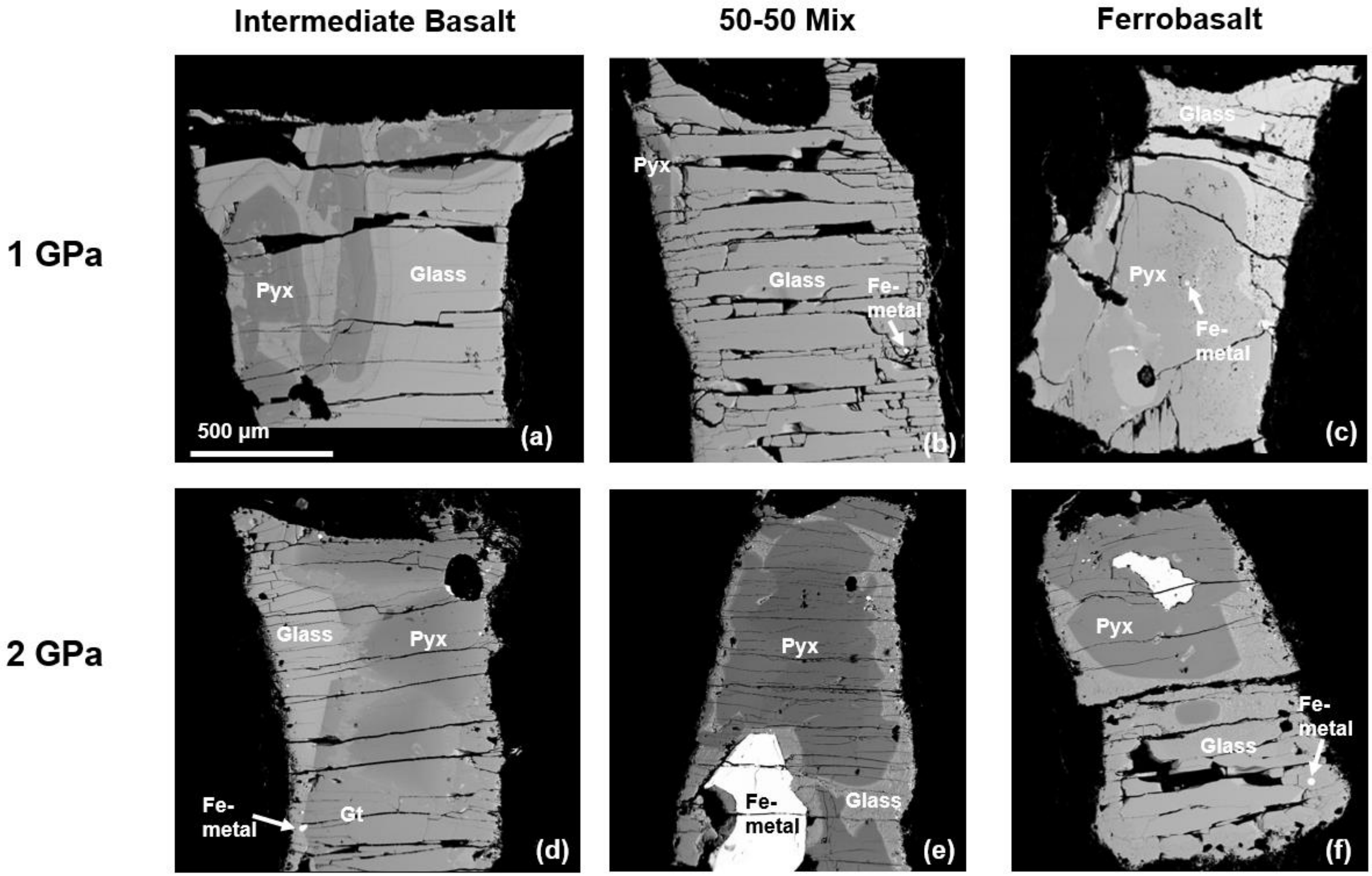

Figure 4.1. Representative backscattered electron micrographs of recovered experiments conducted at 1 GPa (a-c) and 2 GPa (d-f) for intermediate basalt (a;d), 50-50 Mix (b;e), and ferrobasalt (c;f). Pyx= pyroxene, Gt= Garnet.

Table 4.2. Experimental run conditions and phases for all experiments.

Experiment	Composition	Pressure (GPa)	Superliquidus Temperature (°C)	Dwell Temperature (°C)	Dwell Period (hr)	Phases
FR1290-Hd-1	Ferrobasalt	1	1300	1120	48	Pyx + Fe metal + Glass
FR1290-Aug-2	Intermediate Basalt	1	1300	1150	56	Pyx + Glass
FR1290-5050HdAug-1	50-50 Mix	1	1300	1150	51	Pyx + Fe metal + Glass
FR1290-Hd-3	Ferrobasalt	2	1350	1175	59	Pyx + Fe metal + Glass
FR1290-Aug-3	Intermediate Basalt	2	1350	1175	48	Pyx + Gt + Fe metal + Glass
FR1290-5050HdAug-2	50-50 Mix	2	1350	1175	58	Pyx + Fe metal + Glass

Pyx= pyroxene, Gt= garnet

Table 4.3. Pyroxene, garnet, and glass major element composition.

Pyroxene Rims (wt% oxide)													
	SiO_2	**TiO_2**	**Al_2O_3**	**Cr_2O_3**	**MgO**	**CaO**	**MnO**	**FeO**	**Na_2O**	**K_2O**	**P_2O_5**	**Dopant**	**Total**
Intermediate Basalt (1 GPa) n= 4	49.61	0.79	1.70	0.00	9.90	18.70	0.52	18.56	0.04	0.00	0.00	0.04	99.86
1σ StDev	0.44	0.08	0.26	0.00	0.66	0.24	0.02	1.15	0.01	0.00	0.00	0.01	
50-50 Mix (1 GPa) n= 6	48.01	0.91	0.81	0.01	4.79	18.10	0.93	26.18	0.04	0.00	0.00	0.02	99.80
1σ StDev	0.21	0.05	0.09	0.01	0.32	0.21	0.02	0.62	0.01	0.01	0.00	0.00	
50-50 Mix (2 GPa) n= 19	47.77	0.87	1.43	0.01	4.06	16.63	0.92	27.78	0.14	0.00	0.00	0.03	99.64
1σ StDev	0.36	0.08	0.21	0.01	0.53	0.51	0.04	1.02	0.02	0.00	0.00	0.00	
Ferrobasalt (1 GPa) n= 3	47.54	0.96	0.07	0.00	1.83	16.51	1.42	31.85	0.03	0.01	0.00	0.02	100.24
1σ StDev	0.37	0.11	0.01	0.00	0.70	1.53	0.11	2.29	0.00	0.01	0.00	0.00	
Ferrobasalt (2 GPa) n= 37	47.85	1.08	0.19	0.01	2.73	17.33	1.09	29.28	0.33	0.01	0.00	0.05	99.95
1σ StDev	0.72	0.34	0.08	0.01	0.5	1.32	0.13	1.83	0.05	0.01	0.00	0.01	
Garnet (wt% oxide)													
Intermediate Basalt (2 GPa) n= 8	36.05	3.00	18.87	0.01	1.04	9.09	1.21	30.79	0.02	0.00	0.04	0.33	100.45
1σ StDev	0.12	0.40	0.29	0.01	0.03	0.25	0.04	0.12	0.01	0.00	0.01	0.01	
Glass (wt% oxide)													
Intermediate Basalt (1 GPa) n= 8	42.55	3.96	7.75	0.01	2.41	11.06	0.68	28.81	0.21	0.38	0.76	0.51	99.09
1σ StDev	0.75	0.09	0.07	0.01	0.13	0.13	0.01	0.55	0.02	0.01	0.05	0.02	

Table 4.3 Continued

Glass (wt% oxide)													
	SiO_2	**TiO_2**	**Al_2O_3**	**Cr_2O_3**	**MgO**	**CaO**	**MnO**	**FeO**	**Na_2O**	**K_2O**	**P_2O_5**	**Dopant**	**Total**
Intermediate Basalt (2 GPa) n= 15	38.28	6.77	6.11	0.00	0.55	8.27	0.56	34.71	0.31	0.85	0.76	0.92	98.09
1σ StDev	0.64	0.29	0.30	0.00	0.02	0.06	0.01	0.22	0.02	0.02	0.06	0.06	
50-50 Mix (1 GPa) n= 7	41.01	4.87	4.18	0.00	1.11	10.81	1.10	33.65	0.23	0.26	0.75	0.54	98.51
1σ StDev	0.66	0.06	0.03	0.00	0.02	0.05	0.02	0.50	0.02	0.01	0.04	0.00	
50-50 Mix (2 GPa) n= 8	36.61	7.35	3.86	0.01	1.05	9.44	1.09	39.38	0.18	0.04	0.44	0.53	99.98
1σ StDev	4.71	3.38	0.41	0.01	0.23	1.93	0.06	4.70	0.03	0.05	0.02	0.03	
Ferrobasalt (1 GPa) n= 4	35.83	8.32	0.47	0.00	0.30	9.11	1.59	40.95	0.20	0.12	0.99	0.91	98.79
1σ StDev	0.23	0.59	0.04	0.00	0.02	0.21	0.02	0.57	0.03	0.07	0.16	0.05	
Ferrobasalt (2 GPa) n= 15	34.53	6.26	0.46	0.00	0.77	9.41	1.42	43.20	1.14	0.10	0.63	0.67	98.62
1σ StDev	1.19	0.80	0.04	0.00	0.11	0.72	0.72	1.64	0.25	0.08	0.07	0.06	

Averaged major element chemistry (wt% oxide) of pyroxene rims, garnet, and glass for each experiment. Dopant concentration determined from combining the total measured trace element content. n= number of analyses used for average composition; individual point compositions are reported in Table D1.

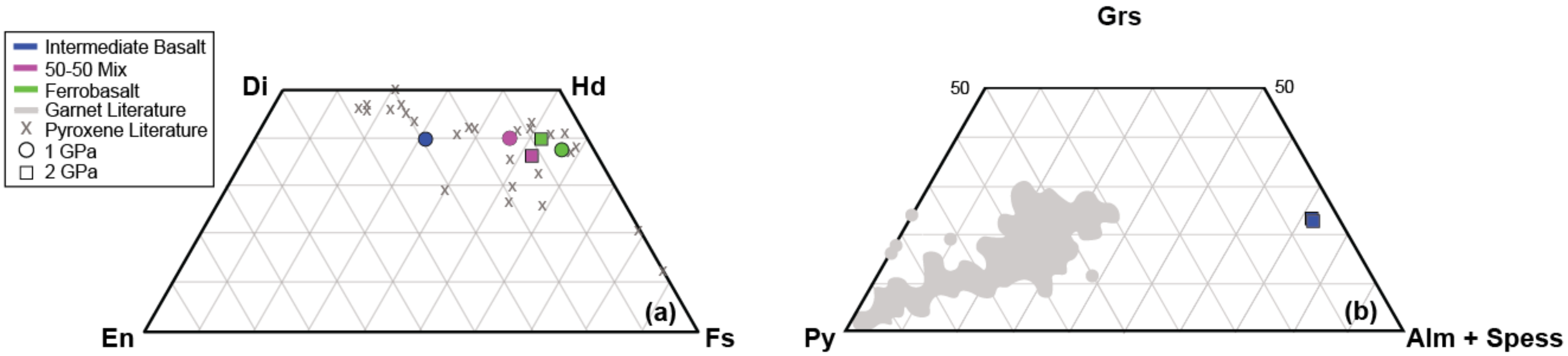

Figure 4.2. (a) Average pyroxene rim composition for each experiment (Di= diopside ($CaMg(Si,Al)_2O_6$), Hd= hedenbergite ($CaFe(Si,Al)_2O_6$), En= enstatite ($MgSiO_3$), Fs= ferrosilite ($FeSiO_3$)). (b) Average garnet composition from the 2 GPa intermediate basalt experiment (Grs= grossular ($Ca_3Al_2(SiO_4)_3$), Py= pyrope ($Mg_3Al_2(SiO_4)_3$), Alm= almandine ($Fe_3Al_2(SiO_4)_3$), Spess= spessartine ($Mn_3Al_2(SiO_4)_3$)). Literature compositions for Fe-rich and intermediate clinopyroxene-melt experiments from Pertermann and Hirschmann (2002); Olin and Wolff (2010); Dygert et al. (2014); Beard et al. (2019); Snape et al. (2022). Published garnet compositions from garnet-melt experiments: Yurimoto and Ohtani (1992); Johnson (1998); Salters and Longhi (1999); van Westrenen et al. (1999); van Westrenen et al. (2000); Klemme et al. (2002); Salters et al., (2002); Bennett et al. (2004); Corgne and Wood (2004); Pertermann et al. (2004); Walter et al. (2004); Draper et al. (2006); Dwarzski et al. (2006); Tuff and Gibson (2007); Corgne et al. (2012); Suzuki et al. (2012).

Elemental concentrations were used to calculate the experimental coefficients ($D^i_{pyroxene-melt}$) of the element:

$$D^i_{pyroxene-melt} = \frac{C^i_{pyroxene}}{C^i_{melt}}, \tag{4.1}$$

where $C^i_{pyroxene}$is the element concentration in the pyroxene, C^i_{melt} is the element concentration in the liquid, and *i* refers to the element. The REE partition coefficients for the experimental pyroxene rims (Figure 4.3a) systematically increase with increasing Al content. In general, all experiments show a depletion in the light REEs (LREE) and a relative enrichment in heavy REEs (HREE). Two features of note in the partition coefficient patterns are the Eu anomalies and the HREE anomalies in the ferrobasalt. First is the Eu anomaly, which is seen in systems where the redox sensitive Eu (Drake, 1975) is in 2+ coordination while the other REEs are 3+, thus causing Eu to partition differently due to its different valence state from the other REEs. The intermediate basalt exhibits a negative Eu anomaly while the 1 GPa ferrobasalt, and to a lesser extent the 1 and 2 GPa 50-50 mix and 2 GPa ferrobasalt, show positive Eu anomalies. Secondly, in the ferrobasalt (and 50-50 mix), there is a significant increase in the HREE (Tm-Lu) not exhibited in the intermediate basalt which has a consistent profile across the HREEs (Figure 4.3b).

The pyroxene partition coefficients for the other trace elements (large ion lithophile elements (LILE), high field strength elements (HFSE), transition metals, and U and Th) are presented in Figure 4.4. The HFSE partition coefficients mimic the trend demonstrated by REE partition coefficients in that pyroxene with a more aluminous composition (intermediate basalt for 1 GPa and 50-50 mix for 2 GPa) exhibit higher partition coefficients compared to the aluminum-poor ferrobasalt. U and Th show similar sensitivity to composition, both being measurable in the aluminous intermediate basalt, both below detection limit in the aluminum-free 1 GPa ferrobasalt. The 1 and 2 GPa 50-50 mix and 2 GPa ferrobasalt contain measurable amounts of Th only (Figure 4.4). Garnet partition coefficients for LILE, HFSE, transition metals, and U and Th are plotted in Appendix D, Figure D4.

4.4. Discussion

4.4.1. *Lattice Strain Models*

The relationship of a partition coefficient to the effective ionic radius of a lattice site can be described using the lattice strain model, which enables prediction of a partition coefficient for a cation of a given size and charge substituting into a specific lattice site if the properties of the site are known (e.g., Blundy and Wood, 2003; Olin and Wolff, 2010). The lattice strain model is defined by the Brice equation (Brice, 1975):

$$D_i = D_0 \times exp\left(\frac{-4\pi E N_A\left(\frac{r_0}{2}\right)(r_0-r_i)^2-\left(\frac{1}{3}\right)(r_0-r_i)^3}{RT}\right), \tag{4.2}$$

where D_0 is the ideal Nernst partition coefficient for strain free substitution into the lattice site (Eq. 4.1), E is the effective Young’s modulus of the lattice site, N_A is Avogadro’s number, r_i is the cation radius, r_0 is the crystal site radius, R is the gas constant, and T is the temperature in K. The lattice strain model is used to define parabola(s) for partitioning groups of isovalent cations into a specific lattice site as a function of their ionic radii. This model has been instrumental in demonstrating controls on trace element partitioning behavior.

The elements in this study were separated into valence states and probable lattice sites (M1 or M2) in the clinopyroxene based on ionic radii (Shannon, 1976) and their observed partitioning behavior. Nonlinear regressions were used to calculate D_0, E, r_0 for the lattice strain equation, Eq (4.2), from each experimental data set with enough observations. Lattice strain model values for the M2 lattice site for 1+, 2+, and 3+ cations, and M1 site for 3+ and 4+ cations are reported in Table 4.4 and the models are plotted with experimental values in Figure 4.5. The fit quality was tested by comparing the modeled partition coefficients to the measured partition coefficients (Figure 4.6). Model predictions for Ba fall off parabolas defined by other divalent elements; however, Ba concentrations are near LA-ICP-MS detection limits (~0.01 ppm) and exhibit considerable uncertainty (Figure 4.6). Lu and Yb are assumed to substitute onto the M1 site in 6-fold coordination for the ferrobasalt and 50-50 mix and the 8-fold coordinated M2 for the intermediate basalt.

4.4.2. *Partition Coefficient Anomalies*

The partition coefficients for the different trace element groups show that, in general, there is a positive correlation with the Al content and higher partition coefficients for trivalent and tetravalent elements substituting onto sites normally occupied by divalent elements (Figure 4.7). This indicates the importance of tetrahedral substitution of Al to balance excess charge on the pyroxene M sites, e.g., $Si^{4+} + Ca^{2+} \leftrightarrow Al^{3+} + REE^{3+}$ (e.g., Lundstrom et al., 1998; Schwandt and McKay; 1998; Shearer et al., 2006). However, the Al-depleted ferrobasalt, and to a lesser extent the 50-50 mix, exhibit some additional unique features including a positive Eu anomaly and relative enrichment of HREEs (Figure 4.3).

The differing Eu anomalies among the samples are likely a direct result of the Al content. Since Eu is predominately 2+ in these fO_2 conditions (~IW-1, Schreiber et al., 1987), the partitioning of the 2+ cations should be similar amongst the three compositions since they generally do not require a coupled substitution to charge balance the structure. The Eu2+ partition coefficients in the 1 GPa samples differ slightly, between 0.048 for the ferrobasalt, 0.076 for the 50-50 mix, and 0.10 for the intermediate basalt (Figure 4.3a). The difference among the samples that makes the Eu anomaly notable is the varying partitioning of the trivalent REEs adjacent to Eu on a spider diagram (Sm and Gd), where Sm and Gd are being directly affected by the presence (or lack thereof) of tetrahedral Al to charge balance their substitution into the structure.

To determine the degree of the anomaly, the measured Eu partition coefficient (D_{Eu}) can be compared to the interpolated Eu partition coefficient (D_{Eu^*}):

$$D_{Eu^*} = \sqrt{D_{Sm} \times D_{Gd}}, \tag{4.3}$$

where D_{Sm} and D_{Gd} are the measured partition coefficients for neighboring elements Sm and Gd, respectively. The values of D_{Eu}/D_{Eu^*} are plotted in Figure 4.8 against Al_T for each experimental pyroxene. A D_{Eu}/D_{Eu^*} value of one indicates no anomaly, anything greater than one is a positive anomaly and anything less than one is a negative anomaly.

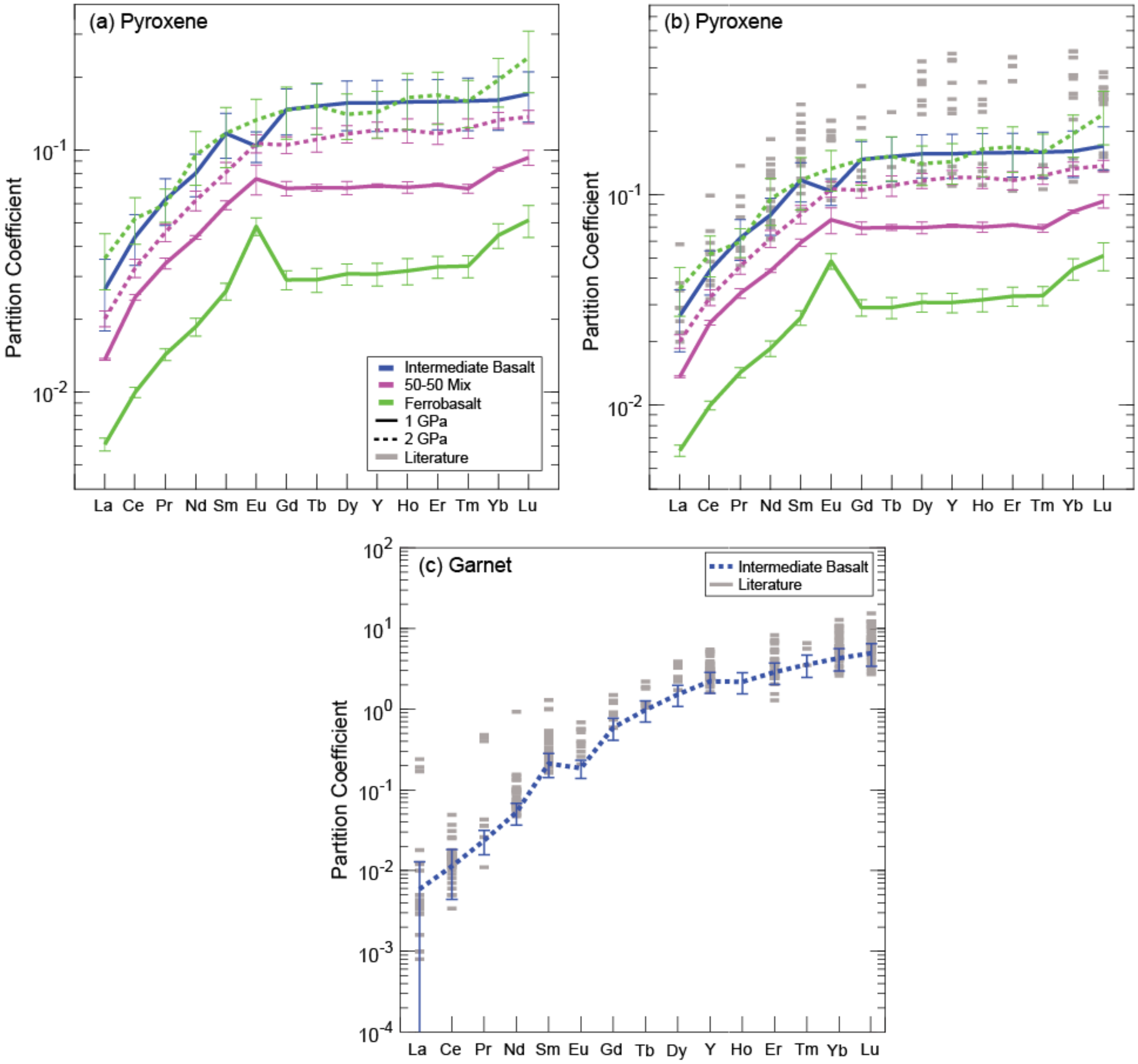

Figure 4.3. REE partition coefficients for 1 and 2 GPa pyroxene rims calculated used Eq (4.1) for (a) experiments only, (b) experiments and relevant clinopyroxene partition coefficients from literature (Pertermann and Hirschmann, 2002; Dygert et al., 2014; Snape et al., 2022), and (c) experimental garnet partition coefficient and partition coefficients from literature (Johnson, 1998; Longhi and Salters, 1999; van Westrenen et al., 1999; van Westrenen et al., 2000; Klemme et al., 2002; Salters et al., 2002; Bennett et al., 2004; Pertermann et al., 2004).

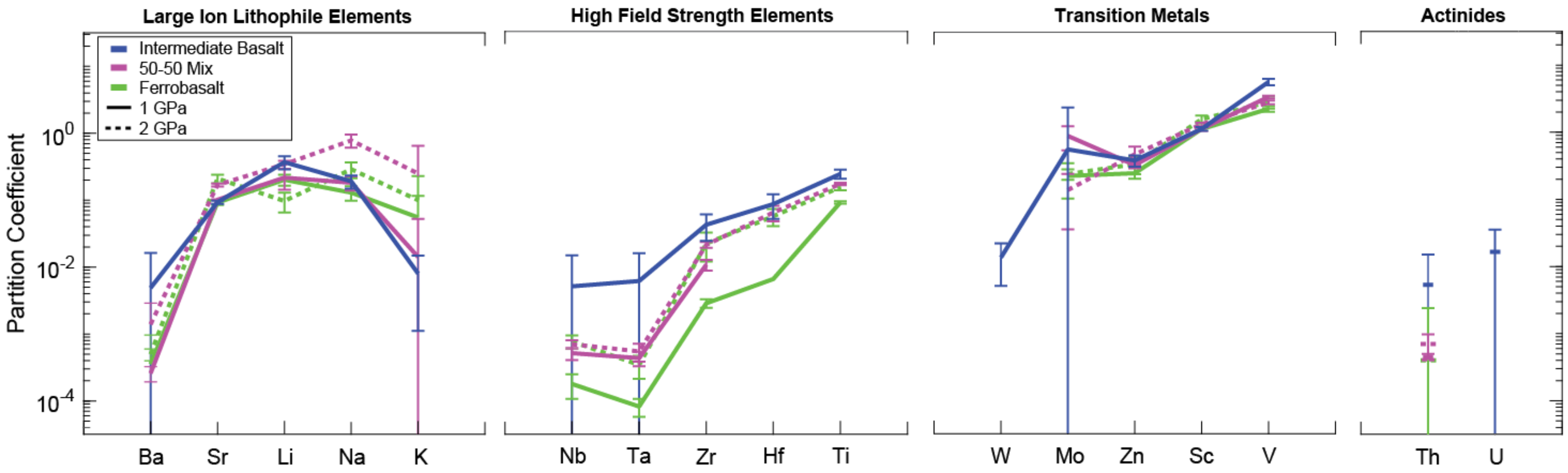

Figure 4.4. Partition coefficients for LILE, HFSE, transition metals, and U and Th for the pyroxene rims calculated using Eq (4.1).

Table 4.4. Pyroxene lattice strain model parameters and uncertainty for 1 and 2 GPa experiment.

	Intermediate Basalt (1 GPa)	1σ	**50-50 Mix (1 GPa)**	1σ	**50-50 Mix (2 GPa)**	1σ	**Ferrobasalt (1 GPa)**	1σ	**Ferrobasalt (2 GPa)**	1σ
M2 (+1)										
D_0	0.37	-	0.23	-	0.79	-	0.27	-	0.29	-
r_0 (Å)	0.75	-	0.85	-	1.05	-	0.17	-	1.07	-
E (GPa)	38.46	-	34.63	-	30.88	-	13.28	-	34.29	-
M2 (2+)										
D_0	1.90	±0.20	1.89	±0.19	1.89	±0.20	2.09	±0.38	1.93	±0.24
r_0 (Å)	0.96	±0.05	0.95	±0.05	0.96	±0.07	0.95	±0.05	0.97	±0.08
E (GPa)	192.38	±92.38	180.52	±80.52	161.81	±62.00	188.16	±88.16	160.21	±61.00
M1 (3+)										
D_0	-	-	3.99	±1.10	2.87	± 2.8	2.30	±1.10	2.86	±2.70
r_0 (Å)	-	-	0.58	±0.70	0.62	± 0.08	0.65	±0.70	0.63	±0.07
E (GPa)	-	-	247.13	±100.00	262.31	±162.50	402.52	±100.00	236.26	±136.50
M2 (3+)										
D_0	0.16	±0.15	0.07	±0.03	0.12	±0.11	0.03	±0.02	0.16	±0.06
r_0 (Å)	1.00	±0.01	1.02	±0.02	1.00	±0.01	1.01	±0.01	1.01	±0.02
E (GPa)	193.73	±93.73	233.16	±33.12	213.15	±110.70	186.70	±86.35	185.19	±85.00
M1 (4+)										
D_0	0.63	-	-	-	1.19	-	0.13	-	0.69	-
r_0 (Å)	0.65	-	-	-	0.65	-	0.63	-	0.65	-
E (GPa)	2530.00	-	-	-	4279.90	-	2414.50	-	3541.20	-

Note that model uncertainty cannot be determined with less than four elements in the inversions, which affects monovalent and tetravalent elements.

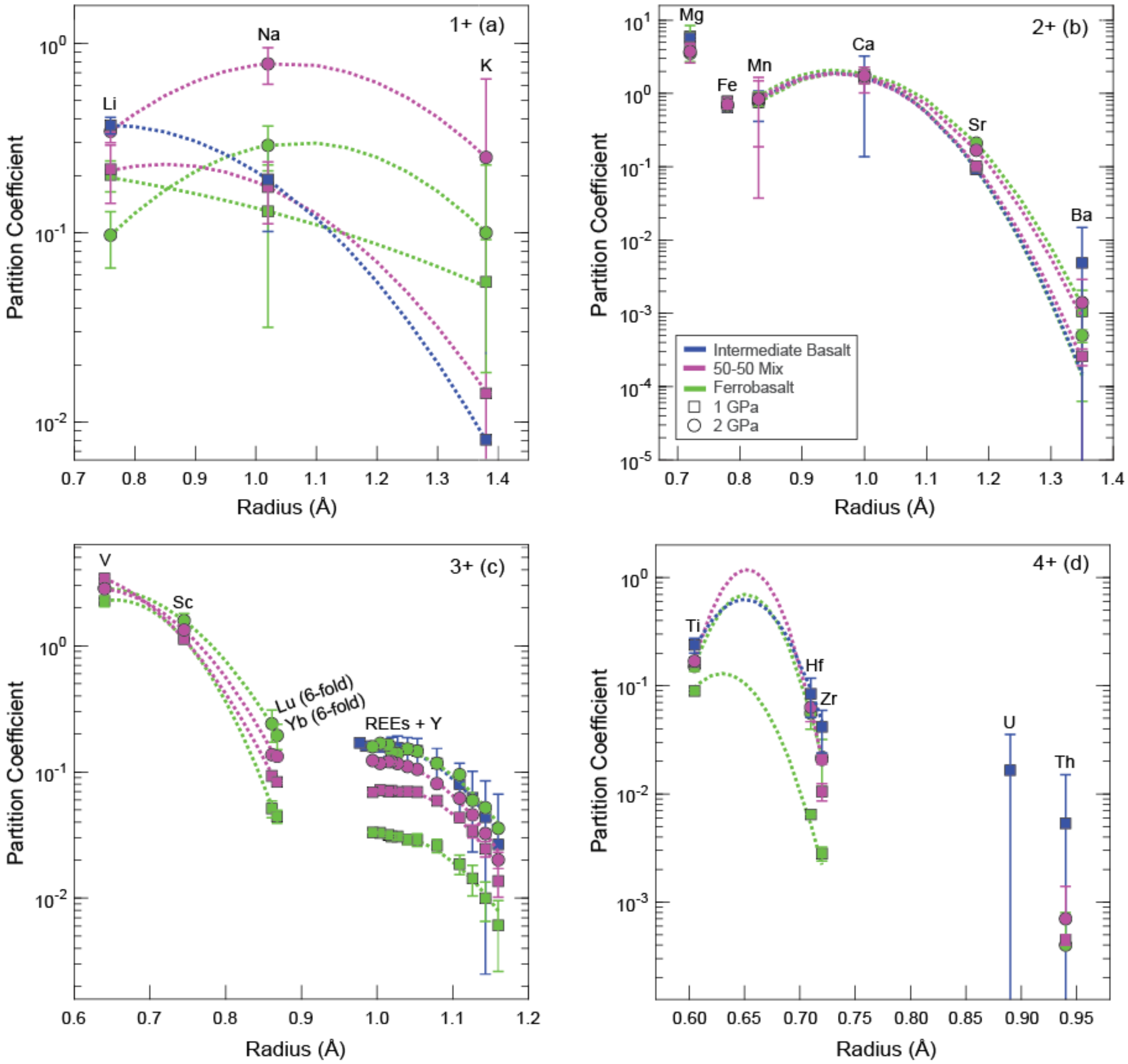

Figure 4.5. Lattice strain model fits to the partitioning data for 1+, 2+, 3+, and 4+ cations, and partition coefficients for 2+ and 4+ cations that do not exhibit parabolic behavior.

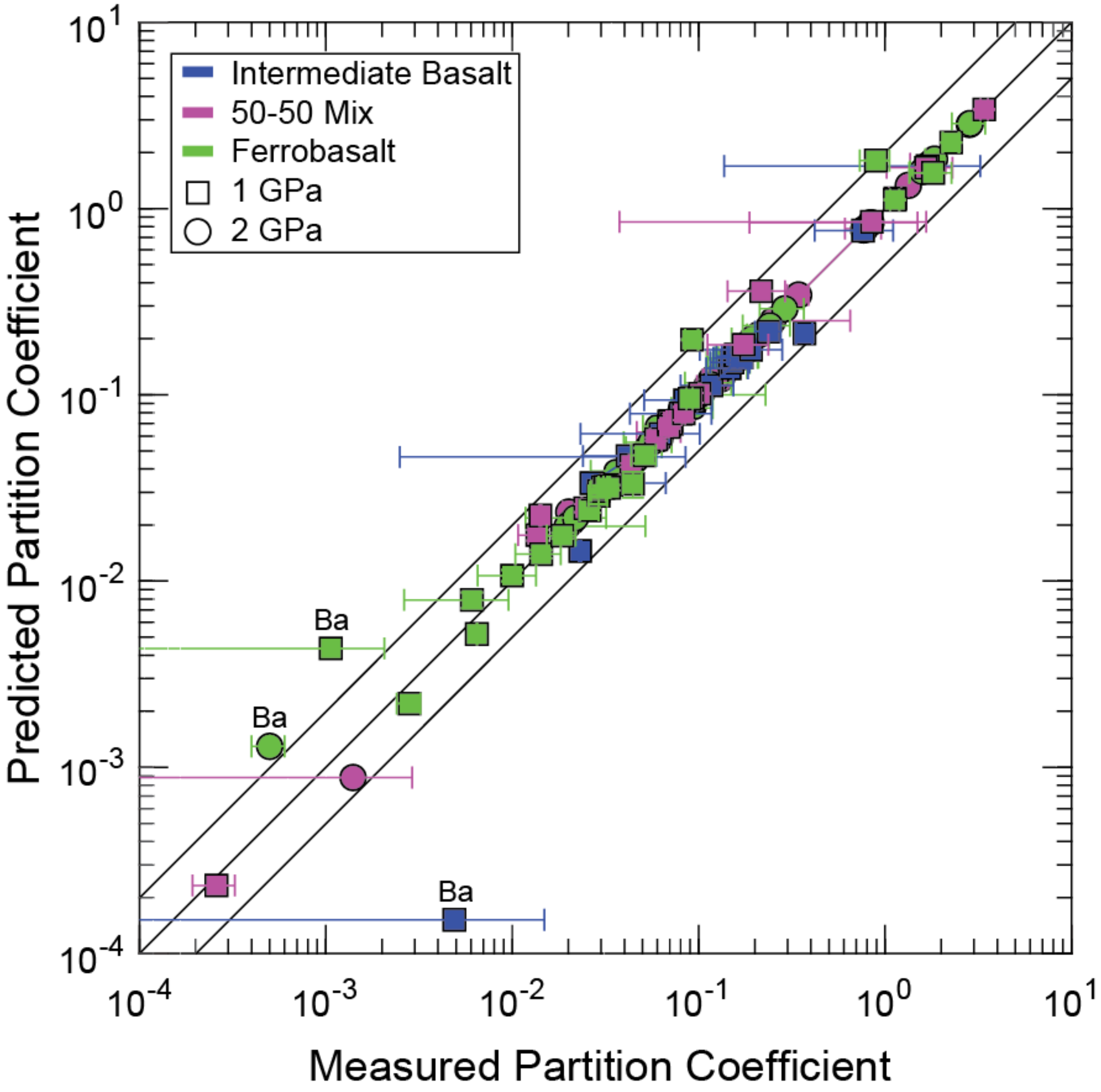

Figure 4.6. Measured vs predicted partition coefficient values to show quality of the lattice strain model fits for each pyroxene experiment.

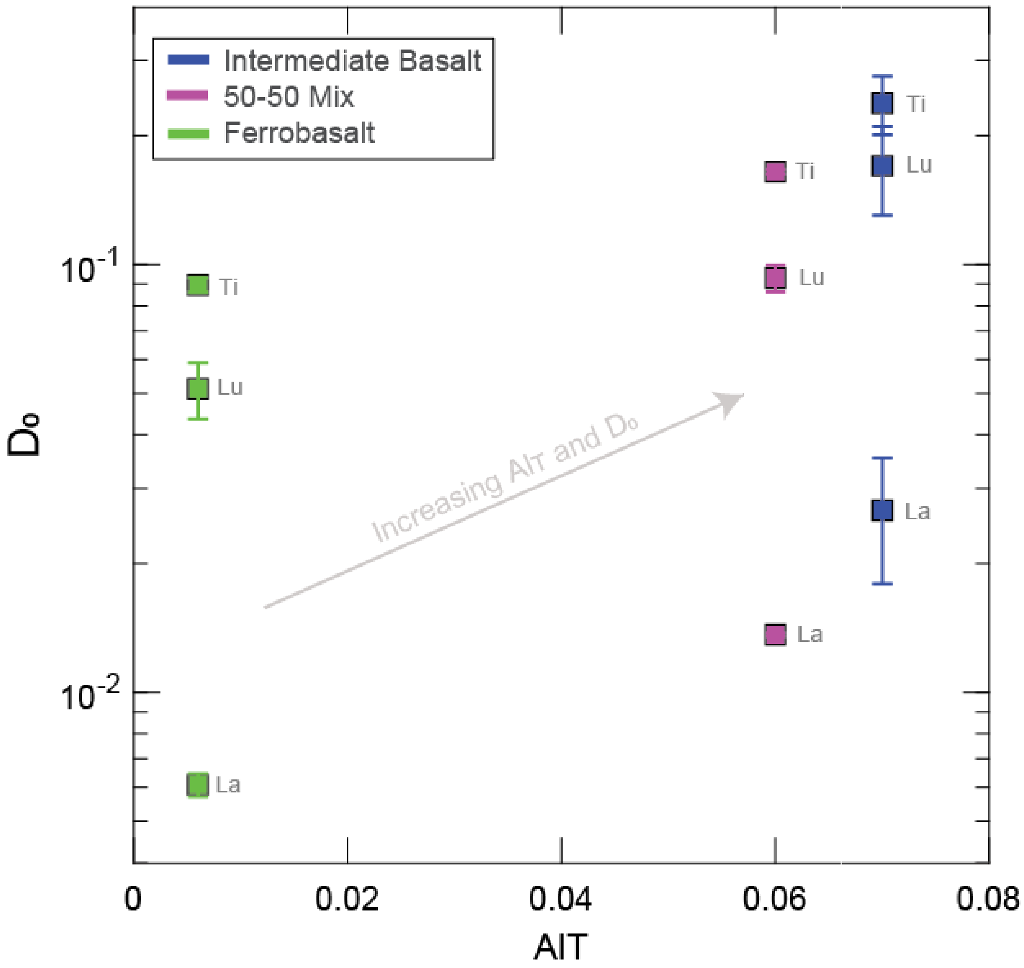

Figure 4.7. Partition coefficients (D_0) for La, Lu, and Ti in the 1 GPa experiments plotted against the tetrahedral Al for each experiment to show positive correlation of increasing partition coefficient with Al_T.

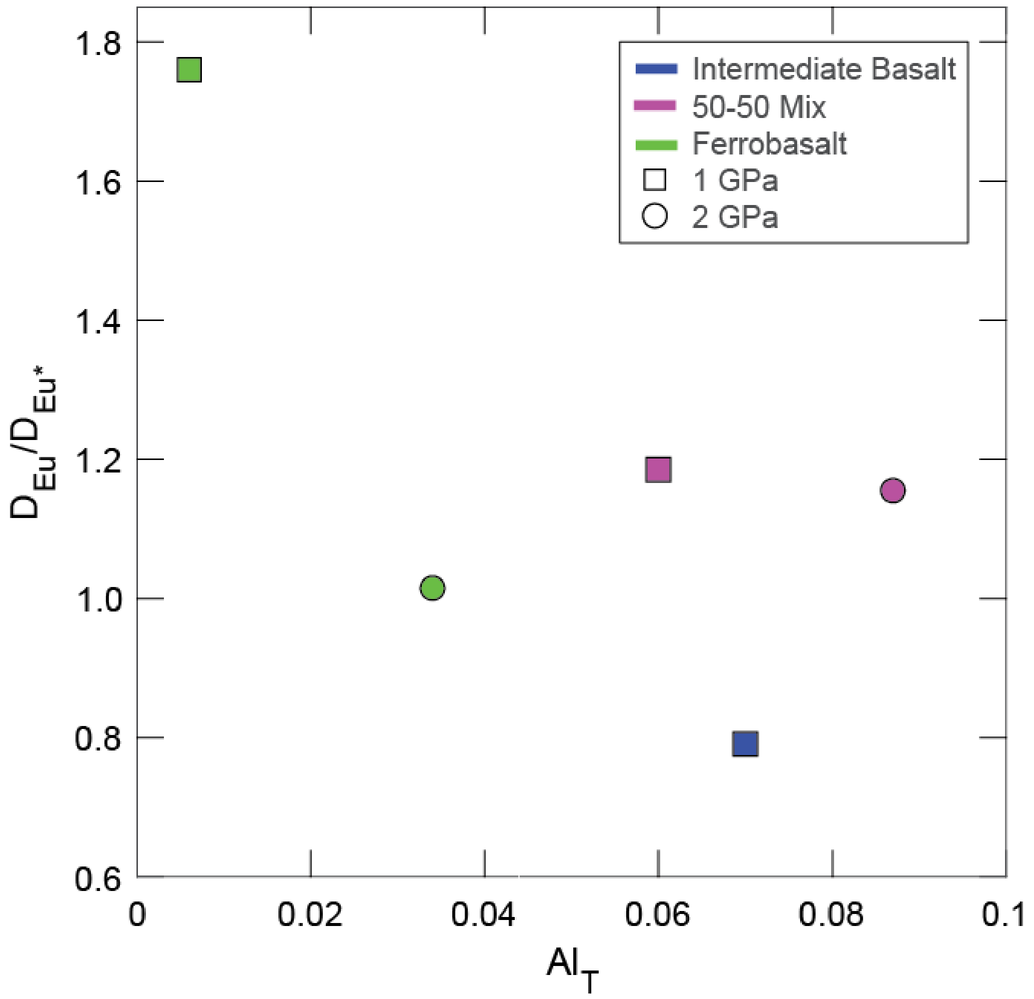

Figure 4.8. Eu anomaly (presented as measured D_{Eu} divided by interpolated D_{Eu^*}) versus tetrahedral Al for 1 and 2 GPa pyroxene partition coefficients.

The Eu anomalies vary between the 1 and 2 GPa series where the 1 GPa series shows a systematic negative to positive anomaly in accordance with the Al_T composition (Figure 4.8). The aluminum-poor 1 GPa ferrobasalt has a positive anomaly ($D_{Eu}/D_{Eu*} = 1.76$), the 1 GPa 50-50 mix with the closest to neutral pattern ($D_{Eu}/D_{Eu*} = 1.18$), and the aluminous 1 GPa intermediate basalt has a negative anomaly ($D_{Eu}/D_{Eu*} = 0.79$). In the 2 GPa experiments, however; the Eu anomaly is effectively absent (Figure 4.8). This change in Eu anomaly between the two experimental and compositional series suggest there are multiple factors that contribute to this change in Eu anomaly: pressure, temperature, and composition. The 2 GPa experiments had increased Al_T content than their 1 GPa counterpart, and it is likely that pressure and temperature also contribute to the partitioning of REE^{3+} in the clinopyroxene structure resulting in a more neutralized Eu anomaly than in a more Al-depleted ferrobasalt pyroxene.

The anomalies increase of HREE partition coefficients in the ferrobasalt (and 50-50 mix) pyroxenes may occur as a result are likely influenced by the Fe content. The 1 GPa ferrobasalt has the lowest Mg#, approximately 9, thus the abundance of larger Fe^{2+} is greater than the slightly smaller Mg^{2+} cation. The 2 GPa ferrobasalt showed an increase in all REE partition coefficients when compared to the 1 GPa experiment, but maintained a similarly sharp increase in HREEs, suggesting temperature, and to a certain effect, pressure, effect on this HREE partitioning. Previous work has suggested the increased presence of Fe and Mn may lead to HREE partitioning in 6-fold coordination onto the M1 site due to enlargement of the M1 site owing to the increased abundance of Fe (Rutstein and Yund, 1969; Olin and Wolff, 2010). In order to charge balance the clinopyroxene structure with a 3+ cation in the M1 site and no tetrahedral Al present, additional substitutions must occur. One such possibility would be the partitioning of a monovalent cation (M^+, e.g., K^+, Na^+) into the M2 site (Harlow, 1997): $(Fe, Mg)^{2+} + Ca^{2+} \leftrightarrow HREE^{3+} + M^+$. Both the ferrobasalt and the 50-50 mix show more elevated Na^+ and K^+ partition coefficients relative to the 1 GPa intermediate basalt (Figures 4.4 and 4.5) , perhaps indicating this type of coupled substitution.

Model parameters for M2 2+, M2 3+, and M1 3+ from this work and from previous studies are compared against temperature, Al_T, and the M1 Fe component, X_{Fe}^{M1} (Figures D5-7). These comparisons reveal that temperature has an influence on the D_0 parameter, where the model parameters from this work and literature show increasing temperature leads to lower D_0 values (Figure 4.9 a;d;f). Thus, there seems to be a general correlation between increasing temperature producing lower D_0 values. Additionally, the M2 2+ D_0 parameters show a strong correlation with X_{Fe}^{M1} where higher Fe component leads to higher D_0 values in this lattice site (Figure 4.9b). This correlation between increasing D_0 for 2+ cations with increasing Fe is to be expected as D_0 is also correlated with decreasing Al_T (Figure 4.9c), suggesting a preferential partitioning of 2+ cations onto the M2 lattice site when there is a lack of Al for coupled substitution with cations of different valence states.

The M1 3+ parameters are correlated with X_{Fe}^{M1} and Al_T. A higher r_0 is associated with a higher Fe content (Figure D5e), suggesting an increased presence of Fe in the crystal lattice will shift r_0 to higher values, thus changing the properties of the lattice site as also seen with the correlation of increasing E values with increasing Fe (Figure D5h). Higher D_0 values are associated with increasing Al_T (Figure 4.9g), which is to be expected as Al is important for the coupled substitution to allow cations of different valence states, in this case 3+, to partition into the M1 site. This same positive correlation of increasing D_0 with increasing Al_T is also seen in the M2 3+ experimental parameters (Figure 4.9e).

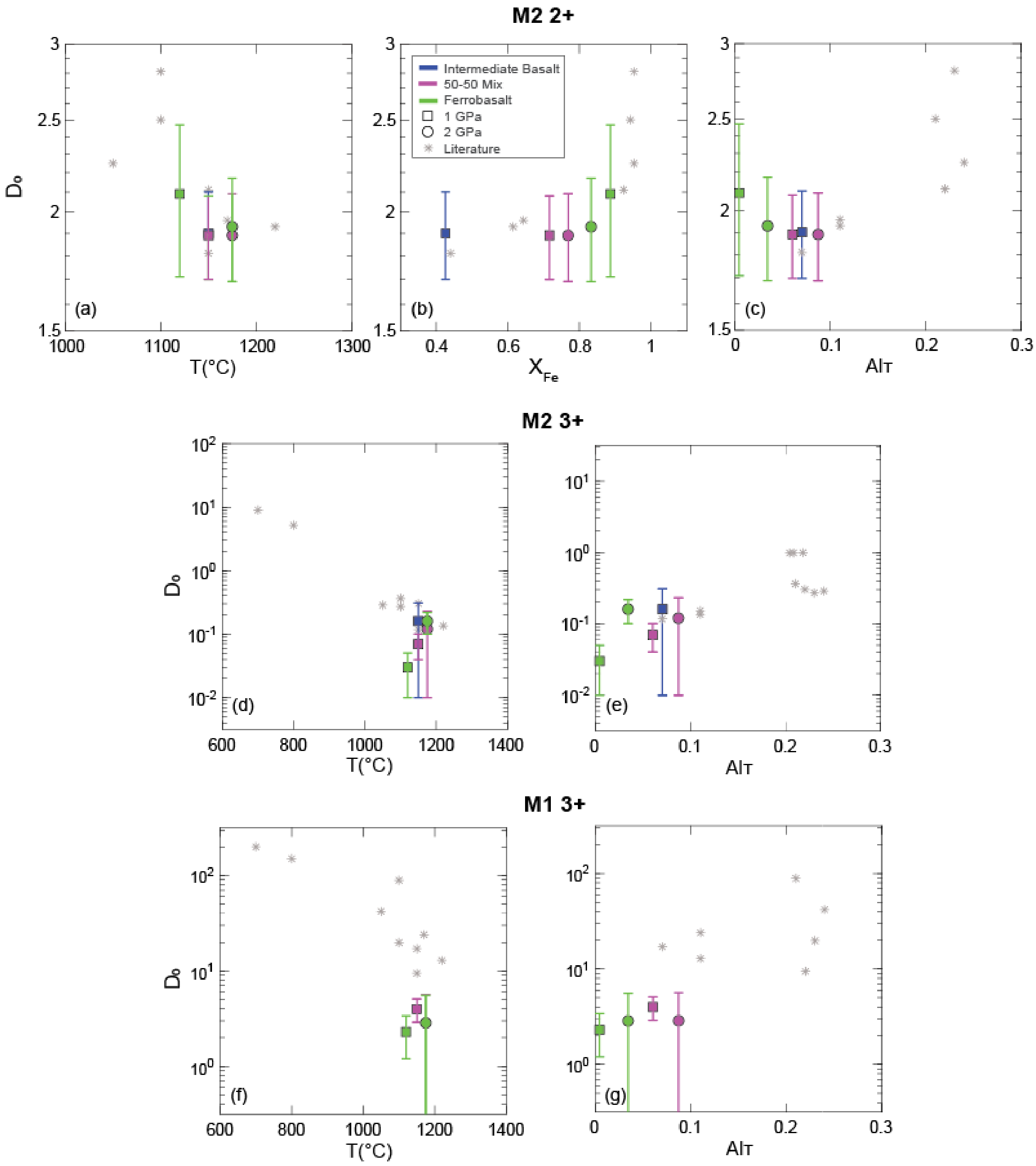

Figure 4.9. Model parameters from this work and literature (Pertermann and Hirschmann, 2002; Dygert et al., 2014) versus (a;d;f) temperature, (b) X_{Fe}^{M1}, and (c;e;g) Al_T. All model parameters versus X_{Fe}^{M1} Al_T, and T are included in Appendix D, Figures D5-7.

4.4.3. *Fe- and Al-based Predictive Model*

Pyroxene compositions most similar to this work are from Dygert et al. (2014). In that study, the authors parameterized Fe- and Al-based predictive lattice strain models. Using these predictive models and comparing the modeled results to the results of this work, both the Fe- and Al-based models from Dygert et al. (2014) successfully predict the more aluminous intermediate basalt to close approximation (Figure 4.10). However, as the composition becomes more Fe-rich and Al-depleted, the models overpredict the partition coefficients and cannot accurately model the behavior of the HREEs (Figure 4.10). Prior to this study, there are no relevant models for these Fe-rich compositions that accurately predict the partitioning behavior of 6-fold HREEs on the M1 site. This necessitates parameterization of a predictive model for HREE substitutions onto the M1 site that is apparent in Fe-rich clinopyroxenes.

Using the M1 3+ cation partition coefficients (V, Sc, Lu, Yb), M1 Fe content, tetrahedral Al content, and temperature data from the 1 and 2 GPa ferrobasalt and 50-50 mix experiments (Figure 4.10a), a predictive model was parameterized. D_0 is calculated as a function of crystal-chemical and temperature effects on the lattice site:

$$D_0 = -a_1 + \frac{a_2}{R \times T} + a_3 \times X_{Fe}^{M1} + a_4 \times X_{Al}^{T}, \tag{4.4}$$

where $X_{Fe}^{M1}$is the Fe component in the M1 lattice site and X_{Al}^{T} is the tetrahedral Al component. Variables a_1, a_2, a_3,and a_4 are parameterized by nonlinear regression through a modified version of Eq (4.2) that includes the expanded D_0 expression from Eq (4.4) utilizing partition coefficients, temperature, X_{Fe}^{M1} and X_{Al}^{T}data from the experiments. E and r_0 from Eq (4.2) are inverted as constants in this expanded lattice strain model.

The resulting E, r_0, and D_0 expression with parameterized values for 3+ cations in the M1 lattice site are: $D_0 = -8.54(\pm 0.46) + \frac{2.76(\pm 0.76) \times 10^5}{R \times T} + 10.64(\pm 0.64) \times X_{Fe}^{M1} + 25.42(\pm 5.42) \times X_{Al}^{T}$, $E = 263.86(\pm 126.85), r_0 = 0.62(\pm 0.04)$. The fit of the model was tested by calculating the M1 parabola with the measured partition coefficients, temperature, X_{Al}^{T}, and X_{Fe}^{M1} component of each experiment (Figure 4.10). Uncertainty for each parameter is in parentheses next to their respective parameter. The model will benefit from more characterization of HREE partitioning in the 6-fold coordinated M1 site, but the current model presented above successfully predict the experimental determinations to close approximation (Figure 4.11). Ongoing work is to pair this with a model to predict the M2 site for 3+ cations.

4.4.4. *Applications to Natural Systems*

4.4.4.1. *Nakhlite Meteorites*

Nakhlite meteorites are cumulate igneous rocks of basaltic origin, believed to have originated from a lava flow on the surface of Mars, forming around 1.3 Ga (e.g., Shih et al., 1999; Treiman, 2005; Bouvier et al., 2009; Udry and Day, 2018). The primary mineralogy of the samples includes augite, olivine, and fine-grained mesostasis (e.g., Imae et al., 2003; Treiman, 2005; Day et al., 2006; Udry et al., 2012). The general composition of the meteorites are rich in Ca and incompatible elements, and depleted in Al (e.g., Harvey and McSween, 1992; Wadhwa and Crozaz, 1995; Treiman, 2005). The geochemistry of these rocks, in particular their rich trace element content relative to common basalts on Earth (Treiman, 2005), suggests that the lave flow they originated from may have endured extensive differentiation such that the remaining liquid contained an elevated incompatible content to produce enriched minerals. The pyroxenes in nakhlites range in composition but are similar to the experimentally produced pyroxenes from this work (Figure 4.12).

The similarities between the experimental pyroxenes, in particular the intermediate basalt and 50-50 mix, and the nakhlite pyroxenes (Figure 4.11) allow for experimental models to be used on the natural sample data to understand the petrogenesis of the meteorites. The experimentally measured crystal-melt partition coefficients can be used with the nakhlite trace element data to predict the composition of the host liquid that the nakhlite pyroxenes would have been in equilibrium with using the following equation:

$$C^{i}_{melt} = \frac{C^{i}_{pyroxene}}{D^{i}_{pyroxene-melt}}, \tag{4.5}$$

where $C^{i}_{melt}$is the predicted concentration an element in the liquid that is in equilibrium with the pyroxene, $C^{i}_{pyroxene}$ is the measured element concentration in the pyroxene, and $D^{i}_{pyroxene-melt}$ is the partition coefficient.

Figure 4.13 shows the predicted liquid concentration in equilibrium with the nakhlite pyroxenes using the partition coefficients from the compositionally relevant intermediate basalt and 50-50 mix experiments. Additionally, predicted equilibrium liquid is modeled using “martian” clinopyroxene partition coefficients determined from melting models (Borg and Draper, 2003). The different partition coefficient models consider a range of Mg#: 24 (50-50 mix), 48 (intermediate basalt), and ~70 (Borg and Draper, 2003). The equilibrium liquid analyses indicates that the liquid will have a higher trace element content in more Fe-rich (or lower Mg#) magmas. This behavior is also likely correlated to the Al content, as the 50-50 mix experiment is the most depleted in Al ($D^{Al}_{cpx-melt} = 0.19$), and the model from Borg and Draper (2003) is the most aluminous out of the compositions being considered here ($D^{Al}_{cpx-melt} = 0.67$).

The increase of HREE partitioning in Fe-rich systems is shown in this work to be an important process, and the model from Borg and Draper (2003) will not model this type of behavior. Therefore, this highlights the importance for using these more Fe-rich models to predict the evolution of nakhlite liquids. Utilizing the experimentally determined partition coefficients ($D_{50\text{-}50}$, $D_{Intermediate}$) from this work allows us to predict the evolution of the nakhlite liquid with better constraints on how the major element chemistry influences the trace element concentrations in Fe-rich clinopyroxenes.

4.4.4.2. *Lunar Basalts*

As shown in Figure 4.12, the experimental pyroxenes from this study are relevant to Fe-rich pyroxenes found in lunar basalts. Lunar basalts range in composition (e.g., Fe, Ti) where the compositional diversity represents the complex early history of the Moon’s interior. Geophysical and petrological constraints from sample analysis suggest that the Moon’s mantle likely formed distinct layers during magma ocean solidification (Ohtani, 1985; Warren, 1985; Shearer and Papike, 1999). One such layer represents the end of the magma ocean solidification (~95-99% crystallization; Shearer and Papike, 1999) where the remaining liquid was highly enriched in incompatible elements such as potassium, REE, phosphorous, uranium, and thorium (commonly referred to as KREEPy trace element pattern; Warren, 1985). Evidence for this layer, rich in ilmenite, is shown through the enrichment of Ti and KREEP in lunar basalt samples (e.g., Walker et al., 1975, Hess et al., 1978; Snyder et al., 1992). The KREEPy late magma ocean cumulates would have been much denser than the underlying cumulates which would have caused gravitational instabilities to form and sink into the interior (e.g., Kesson and Ringwood, 1976; Hess and Parmentier, 1995; Zhang et al., 2017; Li et al., 2019; Yu et al., 2019). This process would have caused the dense ilmenite and KREEP-bearing material to mix with the underlying mafic cumulates forming Ti- and KREEP-rich source regions in the mantle to produce the compositional range of lunar basalts seen on the surface of the Moon today.

Lunar basalts are broken into different categories based on their Ti content: the very low-Ti basalts (<1 wt% TiO_2), low-Ti basalts (1.5-5 wt% TiO_2), and high-Ti basalts (8-14 wt% TiO_2). The trace element abundances in these rocks, in general, correlate to the TiO_2 content in the basalts where the very low-Ti basalts have the lowest REE abundances and the high-Ti basalts have the highest REE abundances (Shearer and Papike, 1999). The three basalt groups exhibit large negative Eu anomalies that correlate with the positive Eu anomalies seen in the highland rocks which are primarily composed of plagioclase (Shearer and Papike, 1999). In addition to the wide range of Ti and REE seen in these basalts, there is also an observed variation in Hf and Nd isotopic compositions (e.g., Unruh et al., 1984; Beard et al., 1998; Münker, 2010) suggesting that processes such as the mantle overturn hybridized the lunar mantle by mixing the ilmenite-bearing, REE enriched material with older mafic layers in the mantle. The hybridized mantle source should show an enrichment in incompatible elements in clinopyroxenes, indicating the need for predictive models to assess this further. While there is a lack of paired major and trace element data on clinopyroxenes in lunar basalts, these trace elements partitioning models may be used to understand and predict the petrogenesis of the incompatible element-rich basalts on the Moon when more data becomes available.

4.4.4.3. *Angrite Meteorites*

Angrite meteorites represent some of the oldest known differentiation in the Solar System, with ages around 4.56 Ga (e.g., Wasserburg et al., 1977; Amelin, 2008; Brennecka and Wadhwa, 2012; Tissot et al., 2017; Zhu et al., 2019). The suite of angrites (currently 35 known meteorites; Sanborn and Wadhwa, 2021) includes both volcanic and plutonic samples. The general composition of these meteorites are Ca, Ti, Fe, and Al rich, producing exotic mineralogy such as kirschsteinite (Ca-rich olivine), various accessory minerals (spinel, sulfides, phosphates), and Al-Ti-bearing diopside-hedenbergites (e.g., Prinz et al., 1977; McKay et al., 1988; Yanai et al., 1994; Mikouchi et al., 1995; Mittlefehldt et al., 2002; Jambon et al., 2005; Keil, 2012). Al-Ti-bearing diopside-hedenbergites contain a higher amount of Al and Ti than in most pyroxenes found in other basaltic systems which skews the clinopyroxene composition towards Wo as seen in Figure 4.12. The trace element composition of pyroxenes found in these meteorites are similar to the experiments (Figure D98), however, angrite pyroxenes are more Ca and Al rich. With modifications to the existing experimental compositions, e.g., more Al and Ca, experiments may be utilized to understand the equilibrium liquid of the natural pyroxenes and provide further insight into angrite petrogenesis and thus some of the earliest magmatic processes in the Solar System.

4.5. Conclusions

Fe-rich basaltic magmas are products of late-stage, or more evolved mafic systems and are common on various terrestrial bodies across the Solar System, such as Mars, the Moon, and meteorite parent bodies. The trace element partitioning behavior in mafic systems are important for understanding the petrogenesis of a rock. This work experimentally studied the trace element partitioning in clinopyroxenes in variable Fe and Al systems to observe the dependence on Fe in the system and how it may differ from Mg-rich systems.

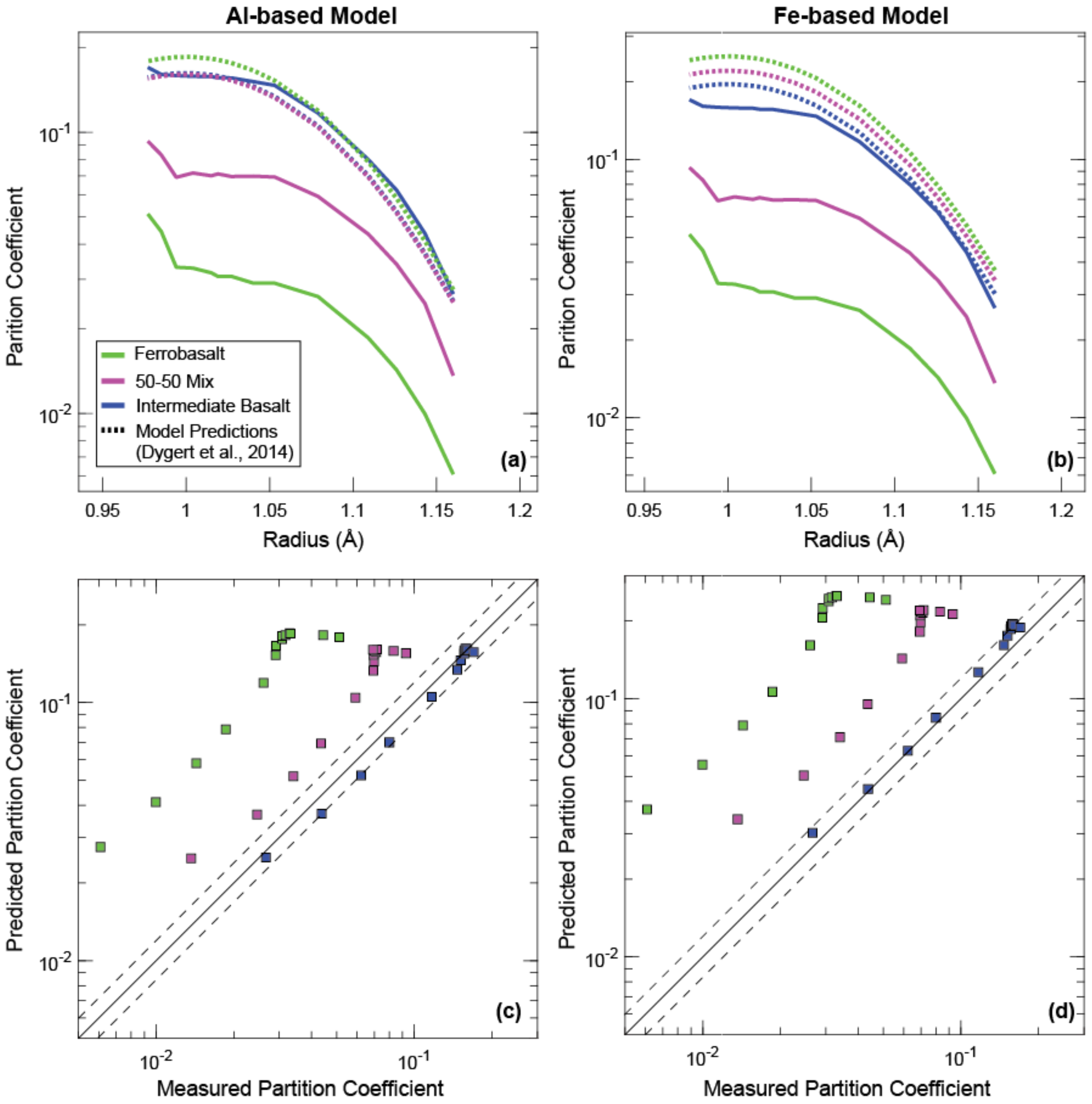

Figure 4.10. REE Al- and Fe-based model predictions from Dygert et al. (2014) for the three compositions and REE experimental measurements. (a-b) lattice strain parabolas, and (c-d) measured versus predicted partition coefficient. Note all REE are plotted in 8-fold coordination.

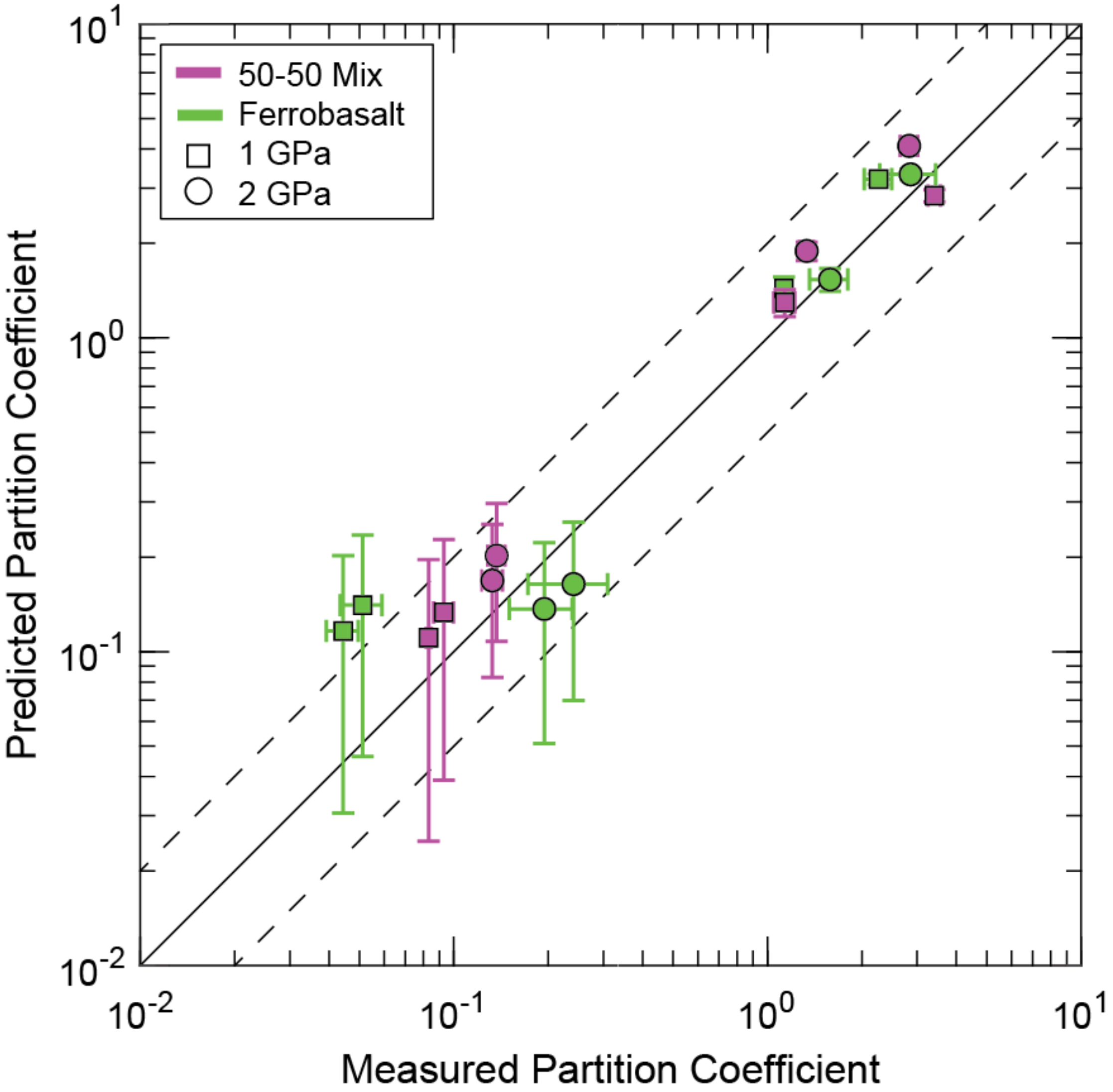

Figure 4.11. Fe-based model predictions for 3+ cations the M1 lattice site (V, Sc, Lu, Yb) versus the measured partition coefficients from the 1 and 2 GPa ferrobasalt and 50-50 mix experiments.

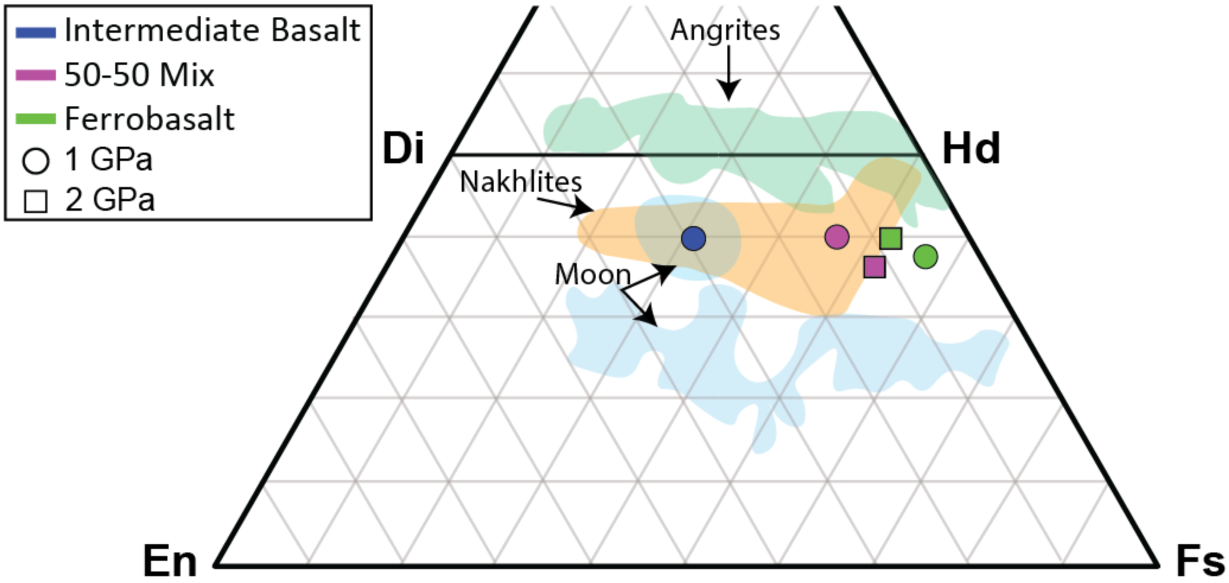

Figure 4.12. Experimental pyroxene rim compositions plotted with regions of nakhlite pyroxenes (peach), angrite pyroxenes (green), and lunar pyroxene compositions from Apollo 12 and 15 pigeonite basalts (light blue). Data are from Brown et al., 1972; Virgo, 1973; Papike et al., 1976; Shearer et al., 1989; Day et al., 2006; Udry et al., 2012; Keil, 2012 and references therein.

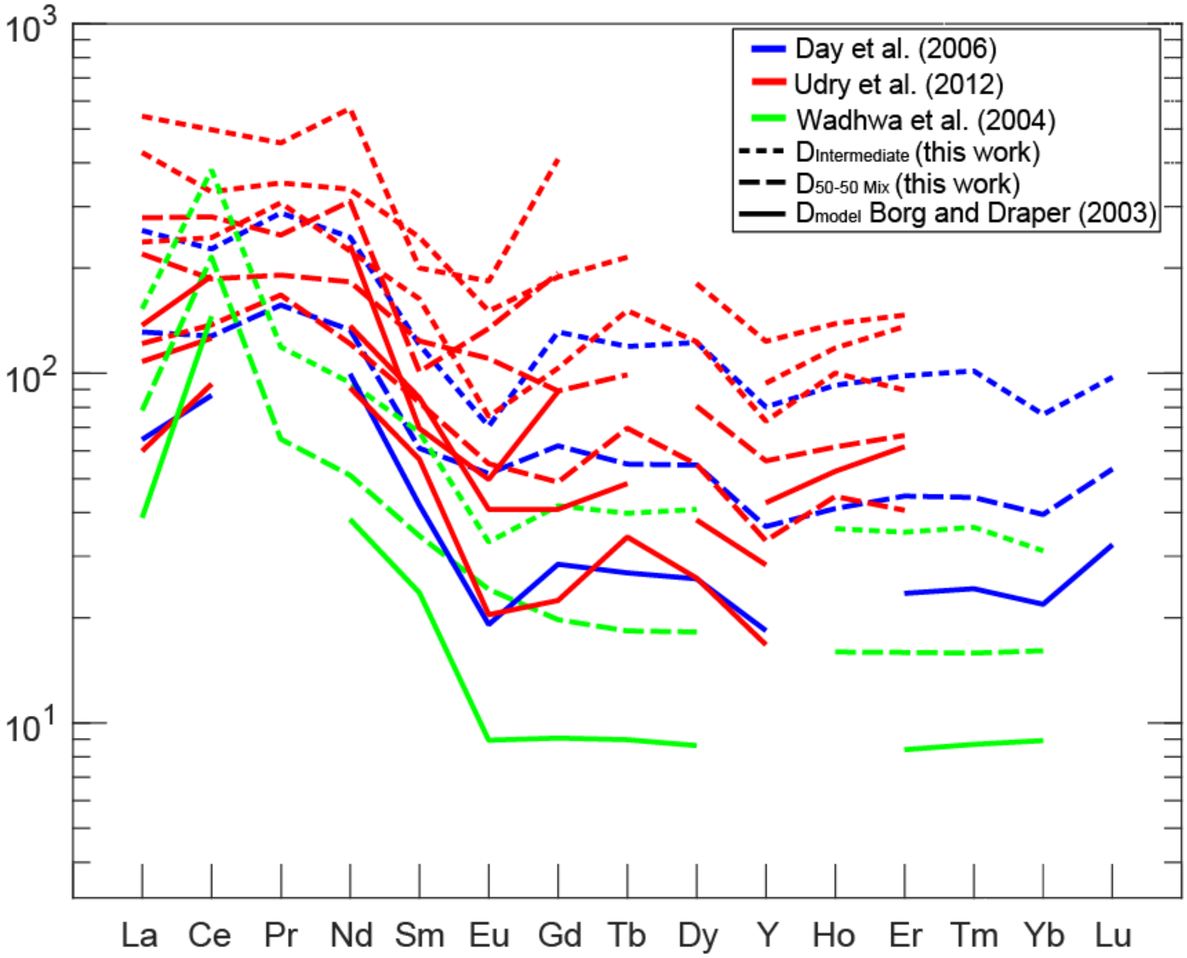

Figure 4.13. Predicted REE concentration in the liquids in equilibrium with measured nakhlite pyroxenes. Dashed lines use the 50-50 mix and intermediate basalt partition coefficients, solid lines use modeled “martian” clinopyroxene partition coefficients (Borg and Draper, 2003). Nakhlite pyroxene REE data are from Wadhwa et al. (2004) (green); Day et al. (2006) (blue); Udry et al. (2012) (red).

The experiments revealed that, much like in Mg-rich systems (e.g., Lundstrom et al., 1998; Schwandt and McKay; 1998; Shearer et al., 2006; Sun and Liang, 2012), Al controls the partitioning of 3+ cations into the M2 site of the clinopyroxene structure via the coupled substitution of a cation on the M2 site with a tetrahedral cation substitution, e.g., $Ca^{2+} + Si^{4+} \leftrightarrow REE^{3+} + Al^{3+}$. The most aluminous sample, the intermediate basalt, had the highest partition coefficients of the three experiments. The most Al-depleted and Fe-rich sample, the ferrobasalt had the lowest partition coefficients, but it did exhibit different behaviors from the Al-rich sample. First, it has a positive Eu anomaly as a result of the depletion of REE^{3+} cations in the structure. Secondly, it showed an enrichment of heavy REE partitioning. This can be explained by the HREEs partitioning onto the M1 site in 6-fold coordination. HREEs in 6-fold coordination are similar to Fe^{2+} and thus may substitute for them in the stiffer M1 crystallographic site in Fe-rich systems.

The partition coefficients from these experiments were used to determine lattice strain parameters to predict the partitioning of trace elements into the clinopyroxenes at 1 and 2 GPa. Using the 3+ M1 lattice site partition coefficients, a new predictive model was parameterized to predict the partitioning nature of $HREE^{3+}$, V, and Sc on the M1 lattice site at different temperature conditions, and variable Al and Fe content. Additionally, the similar composition between these experiments and other systems (e.g., Nakhlites, lunar basalts, angrite meteorites) suggests these partitioning models can be used to model the petrogenetic history of different suites of Fe-rich basalts.

4.6. Acknowledgments

Thank you to Nathan Miller and Allan Patchen for assistance with LA-ICP-MS and EPMA measurements.

References

Amelin, Y. (2008). U-Pb ages of angrites. *Geochimica et Cosmochimica Acta, 72,* 221-232. https://doi.org/10.1016/j.gca.2007.09.034

Anders, E. & Grevesse, N. (1989). Abundances of the elements: Meteoric and solar. *Geochimica et Cosmochimica Acta. 53,* 197-214. https://doi.org/10.1016/0016-7037(89)90286-X

Beard, B. L., Taylor, L. A., Scherer, E. E., Johnson, C. M., & Snyder, G. A. (1998) The source region and melting mineralogy of high-titanium and low-titanium lunar basalts deduced from Lu-Hf isotope data. *Geochimica et Cosmochimica Acta*, *62,* 525-544. https://doi.org/10.1016/S0016-7037(97)00373-6

Beard, C. D., van Hinsberg, V. J., Stix, J., & Wilke, M. (2019). Clinopyroxene/Melt Trace Element Partitioning in Sodic Alkaline Magmas. *Journal of Petrology*, *60,* 1791-1824. https://doi.org/10.1093/petrology/egz052

Bédard, J. H. (2014). Parameterizations of calcic clinopyroxene-Melt trace element partition coefficients. *Geochemistry, Geophysics, Geosystems*, *15,* 303-336. https://doi.org/10.1002/2013GC005112

Bennett, S. L., Blundy, J., & Elliott, T. (2004). The effect of sodium and titanium on crystal-melt partitioning of trace elements. *Geochimica et Cosmochimica Acta, 68,* 2335-2347. https://doi.org/10.1016/j.gca.2003.11.006

Blundy, J. & Wood, B. (2003). Partitioning of trace elements between crystals and melts. *Earth and Planetary Science Letters, 210,* 383-397. https://doi.org/10.1016/S0012-821X(03)00129-8

Borg, L. E. & Draper, D. S. (2003). A petrogenetic model for the origin and compositional variation of the martian basaltic meteorites. *Meteoritics & Planetary Science*, *38,* 1713-1731. https://doi.org/10.1111/j.1945-5100.2003.tb00011.x

Bouvier, A., Blichert-Toft, J., & Albarède (2009). Martian meteorite chronology and the evolution of the interior of Mars. *Earth and Planetary Science Letters. 280,* 285-295. https://doi.org/10.1016/j.epsl.2009.01.042

Brennecka, G. A. & Wadhwa, M. (2012). Uranium isotope compositions of the basaltic angrite meteorites and the chronological implications for the early Solar System. *Proceedings of the National Academy of Sciences*, *109,* 9299-9303. https://doi.org/10.1073/pnas.111404310

Brice, J. C. (1975) Some thermodynamic aspects of the growth of strained crystals. *Journal of Crystal Growth*, *28,* 249-253. https://doi.org/10.1016/0022-0248(75)90241-9

Brown, G. M., Emeleus, C. H., Holland, G. J., Peckett, A., & Phillips, R. (1972). Mineral-chemical variations in Apollo 14 and Apollo 15 basalts and granitic fractions. *Proceedings of the 3rd Lunar Science Conference*, 141-157.

Cameron, M. & Papike, J. J. (1981) Structural and chemical variations in pyroxenes. *American Mineralogist*, *66,* 1-50.

Colson, R. O., McKay, G. A., & Taylor, L. A. (1989) Charge balancing of trivalent trace elements in olivine and low-Ca pyroxene: A test using experimental partitioning data. *Geochimica et Cosmochimica Acta*, *53,* 643-648. https://doi.org/10.1016/0016-7037(89)90007-0

Corgne, A. & Wood, B. J. (2004). Trace element partitioning between majoritic garnet and silicate melt at 25 GPa. *Physics of the Earth and Planetary Interiors*, *143-144,* 407-419. https://doi.org/10.1016/j.pepi.2003.08.012

Corgne, A., Armstrong, L. S., Keshav, S., Fei, Y., McDonough, W. F., Minarik, W. G., Moreno, K. (2012). Trace element partitioning between majoritic garnet and silicate melt at 10-17 GPa: Implications for deep mantle processes. *Lithos*, *148*, 128-141. https://doi.org/10.1016/j.lithos.2012.06.013

Day, J. M. D., Taylor, L. A., Floss, C., & McSween, H. Y. (2006). Petrology and chemistry of MIL 03346 and its significant in understanding the petrogenesis of nakhlites on Mars. *Meteoritics & Planetary Science, 41*, 581-606. https://doi.org/10.1111/j.1945-5100.2006.tb00484.x

Drake, M. J. (1975). The oxidation state of europium of an indicator of oxygen fugacity. *Geochimica et Cosmochimica Acta, 39*, 55-64. https://doi.org/10.1016/0016-7037(75)90184-2

Draper, D. S., duFrane, S. A., Shearer Jr., C. K., Dwarszki, R. E., & Agee, C. B. (2006). High-pressure phase equilibria and element partitioning experiments on Apollo 15 green C picritic glass: Implications for the role of garnet in the deep lunar interior. *Geochimica et Cosmochimica Acta, 70*, 2400-2416. https://doi.org/10.1016/j.gca.2006.01.027

Dwarzski, R. E., Draper, D. S., Shearer, C. K., & Agee, C. B. (2006). Experimental insights on crystal chemistry of high-Ti garnets from garnet-melt partitioning of rare-earth and high-field-strength elements. *American Mineralogist, 91*, 1536-1546. https://doi.org/10.2138/am.2006.2100

Dygert, N., Liang, Y., Sun, C., & Hess, P. (2014) An experimental study of trace element partitioning between augite and Fe-rich basalts. *Geochimica et Cosmochimica Acta, 132*, 170-186. https://doi.org/10.1016/j.gca.2014.01.042

Gaetani, G. A. & Grove, T. L. (1995) Partitioning of rare earth elements between clinopyroxene and silicate melt: Crystal-chemical controls. *Geochimica et Cosmochimica Acta, 59*, 1951-1962. https://doi.org/10.1016/0016-7037(95)00119-0

Gallahan, W. E. & Nielsen, R. L. (1992) The partitioning of Sc, Y, and the rare earth elements between high-Ca pyroxene and natural mafic to intermediate lavas at 1 atmosphere. *Geochimica et Cosmochimica Acta, 56*, 2387-2404. https://doi.org/10.1016/0016-7037(92)90196-P

Floss, C., Crozaz, G., McKay, G., Mikouchi, T., & Killgore, M. (2003). Petrogenesis of Angrites. *Geochimica et Cosmochimica Acta*, *67*, 4775-4789. https://doi.org/10.1016/S0016-7037(03)00310-7

Harlow, G. E. (1997). K in clinopyroxene at high pressure and temperature: An experimental study. *American Mineralogist, 82*, 259-269. https://doi.org/10.2138/am-1997-3-403

Harvey, R. P. & McSween, H. Y. (1992). Petrogenesis of the nakhlite meteorites: Evidence from cumulate mineral zoning. *Geochimica et Cosmochimica Acta*, *56*, 1655-1663. https://doi.org/10.1016/0016-7037(92)90232-8

Hauri, E. H., Wagner, T. P., & Grove, T. L. (1994) Experimental and natural partitioning of Th, U, Pb and other trace elements between garnet, clinopyroxene and basaltic melts. *Chemical Geology*, *117*, 149-166. https://doi.org/10.1016/0009-2541(94)90126-0

Hess, P. C. & Parmentier, E. M. (1995). A model for the thermal and chemical evolution of the Moon's interior: implications for the onset of mare volcanism. *Earth and Planetary Science Letters, 134(3-4)*, 501-514. https://doi.org/10.1016/0012-821X(95)00138-3

Hess, P. C., Rutherford, M. J., & Campbell, H. W. (1978). Ilmenite crystallization in nonmare basalt- Genesis of KREEP and high-Ti mare basalt. *Proceedings of the 9th Lunar and Planetary Science Conference*, *1*, 705-725.

Imae, N., Ikeda, Y., Shinoda, K., Kojima, H., & Iwata, N. (2003). Yamato nakhlites: Petrography and mineralogy. *Antarctic Meteorite Research, 16,* 13-33.

Jambon, A., Barrat, J. A., Boudouma, O., Fonteilles, M., Badia, D., Göpel, C. & Bohn, M. (2005). Mineralogy and petrology of the angrite Northwest Africa 1296. *Meteoritics and Planetary Science, 40,* 361-375. https://doi.org/10.1111/j.1945-5100.2005.tb00388.x

Johnson, K. T. (1998). Experimental determination of partition coefficients for rare earth and high-field-strength elements between clinopyroxene, garnet, and basaltic melt at high pressures. *Contributions to Mineralogy and Petrology, 133,* 60-68.

Keil, K. (2012). Angrites, a small but diverse suite of ancient, silica-undersaturated volcanic-plutonic mafic meteorites, and the history of their parent asteroid. *Chemie der Erde, 72,* 191-218. https://doi.org/10.1016/j.chemer.2012.06.002

Kesson, S. E. & Ringwood, A. E. (1976) Mare basalt petrogenesis in a dynamic Moon. *Earth and Planetary Science Letters, 30,* 155-163. https://doi.org/10.1016/0012-821X(76)90241-7

Klemme, S., Blundy, J. D., & Wood, B. J. (2002). Experimental constraints on major element and trace element partitioning during partial melting of eclogite. *Geochimica et Cosmochimica Acta, 66,* 3109-3123. https://doi.org/10.1016/S0016-7037(02)00859-1

Longhi, J. (2003) A new view of lunar ferroan anorthosites: Postmagma ocean petrogenesis. *Journal of Geophysical Research, 108,* 1-16. https://doi.org/10.1029/2002JE001941

Li, H., Zhang, N., Liang, Y., Wu, B., Dygert, N. J., Huang, J., & Parmentier, E. M. (2019) Lunar Cumulate Mantle Overturn: A Model Constrained By Ilmenite Rheology. *Journal of Geophysical Research: Planets, 124,* 1357-1378. https://doi.org/10.1029/2018JE005905

Lundstrom, C. C., Shaw, H. F., Ryerson, F. J., Williams, Q., & Gill, J. (1998). Crystal chemical control of clinopyroxene-melt partitioning in the Di-Ab-An system: implications for elemental fractionations in the depleted mantle. *Geochimica et Cosmochimica Acta, 62,* 2849-2862. https://doi.org/10.1016/S0016-7037(98)00197-5

McCubbin, F. M., Elardo, S. M., Shearer Jr., C. K., Smirnov, A., Hauri, E. H., Draper, D. S. (2013). A petrogenetic model for the comagmatic origin of chassignites and nakhlites: inferences from chlorine-rich minerals, petrology, and geochemistry. *Meteoritics & Planetary Science, 48,* 819-853. https://doi.org/10.1111/maps.12095

McKay, G., Wagstaff, J., & Yang, S.-R. (1986) Clinopyroxene REE distribution coefficients for Shergottites: The REE content of the Shergotty melt. *Geochimica et Cosmochimica Acta, 50,* 927-937. https://doi.org/10.1016/0016-7037(86)90374-1

McKay, G., Lindstrom, D., Yang, S.-R., & Wagstaff, J. (1988). Petrology of unique achondrite Lewis Cliff 86010. *Lunar and Planetary Science Conference XIX (abstract),* 19, 762-763.

Mikouchi, T., Takeda, H., Miyamoto, M., Oshumi, K., & McKay, G. A. (1995). Exsolution lamellae of kirschsteinite in magnesium-iron olivine from an angrite meteorite. *American Mineralogist, 80,* 593-612. https://doi.org/10.2138/am-1995-5-618

Mittlefehldt, D. W., Killgore, M., & Lee, M. T. (2002). Petrology and geochemistry of D'Orbigny, geochemistry of Sahara 99555, and the origin of angrites. *Meteoritics & Planetary Science, 37,* 345-369. https://doi.org/10.1111/j.1945-5100.2002.tb00821.x

Münker, C. (2010) A high field strength element perspective on early lunar differentiation. *Geochimica et Cosmochimica Acta, 74,* 7340-7361. https://doi.org/10.1016/j.gca.2010.09.021

Ohtani, E. (1985) The primordial terrestrial magma ocean and its implication for stratification of the mantle. *Physics of the Earth and Planetary Interiors, 38,* 70-80. https://doi.org/10.1016/0031-9201(85)90123-2

Olin, P. H. & Wolff, J. A. (2010) Rare earth and high field strength element partitioning between iron-rich clinopyroxenes and felsic liquids. *Contributions to Mineralogy and Petrology, 160*, 761-775. https://doi.org/10.1007/s00410-010-0506-2

Papike, J. J., Hodges, F. N., Bence, A. E., Cameron, M., & Rhodes, J. M. (1976). Mare basalts: Crystal chemistry, mineralogy, and petrology. *Reviews of Geophysics, 14*, 475-540. https://doi.org/10.1029/RG014i004p00475

Pertermann, M. & Hirschmann, M. (2002). Trace-element partitioning between vacancy-rich eclogitic clinopyroxene and silicate melt. American Mineralogist, 87, *1365-1376.* https://doi.org/10.2138/am-2002-1012

Pertermann, M., Hirschmann, M. M., Hametner, K., Günther, D., & Schmidt, M. W. (2004). Experimental determination of trace element partitioning between garnet and silicat-rich liquid during anhydrous partial melting of MORB-like eclogite. *Geochemistry, Geophysics, Geosystems, 5*, 1-23. https://doi.org/10.1029/2003GC000638

Prinz, M., Keil, K., Hlava, P. F., Berkley, J. L., Gomes, C. B., & Curvello, W. S. (1977). Studies of Brazilian meteorites: III. Origin and history of the Angra dos Reis chondrite. *Earth and Planetary Science Letters, 35*, 317-330. https://doi.org/10.1016/0012-821X(77)90134-0

Rutstein, M. S. & Yund, R. A. (1969). Unit-cell parameters of synthetic diopside-hedenbergite solid solutions. *American Mineralogist, 54*, 238-245.

Salters, V. J. M. & Longhi, J. (1999). Trace element partitioning during the initial stages of melting beneath mid-ocean ridges. *Earth and Planetary Science Letters, 166*, 15-30. https://doi.org/10.1016/S0012-821X(98)00271-4

Salters, V. J. M., Longhi, J. E., & Bizimis, M. (2002). Near mantle solidus trace element partitioning at pressures up to 3.4 GPa. *Geochemistry, Geophysics, Geosystems, 3,* 1-23. https://doi.org/10.1029/2001GC000148

Sanborn, M. E. & Wadhwa, M. (2021). Trace element geochemistry of coarse-grained angrites from Norwthwest Africa: Implications for their petrogenesis on the angrite parent body. *Meteoritics & Planetary Science, 56*, 482-499. https://doi.org/10.1111/maps.13631

Schwandt, C. S. & McKay, G. A. (1998). Rare earth element partition coefficients from enstatite/melt synthesis experiments. *Geochimica et Cosmochimica Acta, 62*, 2845-2848. https://doi.org/10.1016/S0016-7037(98)00233-6

Shannon, R. D. (1976). Revised effective ionic radii and systematic studies of interatomic distances in halides and chalcogenides. *Acta Crystallographica, A32,* 751-767. https://doi.org/10.1107/S0567739476001551

Shearer, C. K., Papike, J. J., Simon, S. B., & Shimizu, N. (1989). An ion microprobe study of the intra-crystalline behavior of REE and selected trace elements in pyroxene from mare basalts with different cooling and crystallization histories. *Geochimica et Cosmochimica Acta, 53*, 1041-1054. https://doi.org/10.1016/0016-7037(89)90209-3

Shearer, C. K. & Papike, J. J. (1999) Magmatic evolution of the Moon. *American Mineralogist, 84*, 1469-1494. https://doi.org/10.2138/am-1999-1001

Shearer, C. K., Papike, J. J., & Karner, J. M. (2006). Pyroxene europium valence oxybarometer: Effects of pyroxene composition, melt composition, and crystallization kinetics. *American Mineralogist, 91*, 1565-1573. https://doi.org/10.2138/am.2006.2098

Shih, C-Y., Nyquist, L. E., & Wiesmann, H. (1999). Samarium-neodymium and rubidium-strontium systematics of nakhlite Governador Valadares. *Meteoritics & Planetary Science, 34*, 647-655. https://doi.org/10.1111/j.1945-5100.1999.tb01370.x

Snape, J. F., Nemchin, A. A., Johnson, T., Luginbühl, S., Berndt, J., Klemme, S., Morrissey, L. J., & van Westrenen, W. (2022). Experimental constraints on the long-lived radiogenic isotope evolution of the Moon. *Geochimica et Cosmochimica Acta, 326,* 119-148. https://doi.org/10.1016/j.gca.2022.04.008

Snyder, G. A., Taylor, L. A., & Neal, C. R. (1992). A chemical model for generating the sources of mare basalts: Combined equilibrium and fractional crystallization of the lunar magmasphere. *Geochimica et Cosmochimica Acta*, *56,* 3809-3823. https://doi.org/10.1016/0016-7037(92)90172-F

Sun, C., Graff, M., & Liang, Y. (2017) Trace element partitioning between plagioclase and silicate melt: The importance of temperature and plagioclase composition, with implications for terrestrial and lunar magmatism. *Geochimica et Cosmochimica Acta, 206*, 273-295. https://doi.org/10.1016/j.gca.2017.03.003

Sun, C. & Liang, Y. (2012) Distribution of REE between clinopyroxene and basaltic melt along a mantle adiabat: effects of major element composition, water, and temperature. *Contributions to Mineralogy and Petrology*, *163*, 807-823. https://doi.org/10.1007/s00410-011-0700-x

Sun, C. & Liang, Y. (2013a) The importance of crystal chemistry on REE partitioning between mantle minerals (garnet, clinopyroxene, orthopyroxene, and olivine) and basaltic melts. *Chemical Geology*, *358,* 23-56. https://doi.org/10.1016/j.chemgeo.2013.08.045

Sun, C. & Liang, Y. (2013b) Distribution of REE and HFSE between low-Ca pyroxene and lunar picritic melts around multiple saturation points. *Geochimica et Cosmochimica Acta, 119,* 340-358. https://doi.org/10.1016/j.gca.2013.05.036

Suzuki, T., Hirata, T., Yokoyama, T. D., Imai, T., & Takahashi, E. (2012). Pressure effect on element partitioning between minerals and silicate melt: Melting experiments on basalt up to 20 GPa. *Physics of the Earth and Planetary Interiors, 209-209,* 59-73. https://doi.org/10.1016/j.pepi.2012.07.008

Tissot, F. L. H., Dauphas, N., & Grove, T. L. (2017). Distinct 238U/235U ratios and REE patterns in plutonic and volcanic angrites: Geochronologic implications and evidence for U isotope fractionation during magmatic processes. *Geochimica et Cosmochimica Acta, 213*, 593-617. https://doi.org/10.1016/j.gca.2017.06.045

Treiman, A. H. (2005) The nakhlite meteorites: Augite rich igneous rocks from Mars. *Chemie der Erde*, *65*, 203-270. https://doi.org/10.1016/j.chemer.2005.01.004

Tuff, J. & Gibson, S. A. (2007). Trace-element partitioning between garnet, clinopyroxene and Fe-rich picritic melts at 3 to 7 GPa. *Contributions to Mineralogy and Petrology, 153,* 369-387. https://doi.org/10.1007/s00410-006-0152-x

Udry, A. & Day, M. D. (2018). 1.34 billion-year-old magmatism on Mars evaluated from the co-genetic nakhlite and chassignite meteorites. *Geochimica et Cosmochimica Acta*, *238,* 292-315. https://doi.org/10.1016/j.gca.2018.07.006

Udry, A., McSween, H. Y., Lecumebrri-Sanchez, P., & Bodnar, R. J. (2012). Paired nakhlites MIL 090030, 090032, 090136, and 03346: Insights into the Miller Range parent meteorite. *Meteoritics & Planetary Science*, *47*, 1575-1589. https://doi.org/10.1111/j.1945-5100.2012.01420.x

Unruh, D. M., Stille, P., Patchett, P. J., & Tatsumoto, M. (1984) Lu-Hf and Sm-Nd evolution in lunar mare basalts. *Journal of Geophysical Research, 89,* B459-B477. https://doi.org/10.1029/JB089iS02p0B459

van Westrenen, W., Blundy, J., & Wood, B. (1999). Crystal-chemical controls on trace element partitioning between garnet and anhydrous silicate melt. *American Mineralogist, 84,* 838-847. https://doi.org/10.2138/am-1999-5-618

van Westrenen, W., Blundy, J. D., & Wood, B. J. (2000). Effect of Fe^{2+} on garnet-melt trace element partitioning: experiments in FCMAS and quantification of crystal chemical controls in natural systems. *Lithos, 53,* 189-201. https://doi.org/10.1016/S0024-4937(00)00024-4

Virgo, D. (1973). Clinopyroxene from Apollo 15: Fe2+, Mg intercrystalline distributions (abstract). *4th Lunar Science Conference,* 749-751.

Wadhwa, M. & Crozaz, G. (1995). Trace and minor elements in minerals of nakhlites and Chassigny: Clues to their petrogenesis. *Geochimica et Cosmochimica Acta, 59,* 3629-3645. https://doi.org/10.1016/0016-7037(95)00228-R

Wadhwa, M., Crozaz, G., & Barrat, J-A. (2004). Trace element distributions in the Yamato 00593/000749, NWA 817 and NWA 998 nakhlites: Implications for their petrogenesis and mantle source on Mars. *Antarctic Meteorite Research, 17,* 97-116.

Walker, D., Longhi, J., Stopler, E. M., Grove, T. L., & Hays, J. F. (1975). Origin of titaniferous lunar basalts. *Geochimica et Cosmochimica Acta, 39,* 1219-1235. https://doi.org/10.1016/0016-7037(75)90129-5

Walter, M. J., Nakamura, E., Trønnes, R. G., & Frost, D. J. (2004). Experimental constraints on crystallization differentiation in a deep magma ocean. *Geochimica et Cosmochimica Acta, 68,* 4267-4284. https://doi.org/10.1016/j.gca.2004.03.014

Warren, P. H. (1985) The Magma Ocean Concept and Lunar Evolution. *Annual Reviews Earth and Planetary Science, 13,* 201-240.

Wasserburg, G. J., Tera, F., Papanastassiou, D. A., & Huneke, J. C. (1977). Isotopic and chemical investigations on Angra do Reis. *Earth and Planetary Science Letters, 35,* 294-316. https://doi.org/10.1016/0012-821X(77)90133-9

Wood, B. J. & Blundy, J. D. (2001). The effect of cation charge on crystal-melt partitioning of trace elements. *Earth and Planetary Science Letters, 188,* 59-71. https://doi.org/10.1016/S0012-821X(01)00294-1

Yanai, K. (1994). Comparative studies of three angrites; Angra dos Reis, LEW87051 and Asuka-881371 meteorites. *Antarctic Meteorites XIX (abstract),* 51-54.

Yu, S., Tosi, N., Schwinger, S., Maurice, M., Breuer, D., & Xiao, L. (2019) Overturn of Ilmenite-Bearing Cumulates in a Rheologically Weak Lunar Mantle. *Journal of Geophysical Research: Planets, 124,* 418-436. https://doi.org/10.1029/2018JE005739

Yurimoto, H. & Ohtani, E. (1992). Element partitioining between majorite and liquid: A secondary ion mass spectrometric study. *Geophysical Research Letters, 19,* 17-20. https://doi.org/10.1029/91GL02824

Zhang, N., Dygert, N., Liang, Y., & Parmentier, E. M. (2017) The effect of ilmenite viscosity on the dynamics and evolution of an overturned lunar cumulate mantle. *Geophysical Research Letters*, *44*, 6543-6552. https://doi.org/10.1002/2017GL073702

Zhu, K., Moynier, F., Wielandt, D., Larsen, K. K., Barrat, J-A., & Bizzarro, M. (2019). Timing and Origin of the Angrite Parent Body Inferred from Cr Isotopes. *The Astrophysical Journal Letters*, *877,* 1-8. https://doi.org/10.3847/2041-8213/ab2044

Appendix D

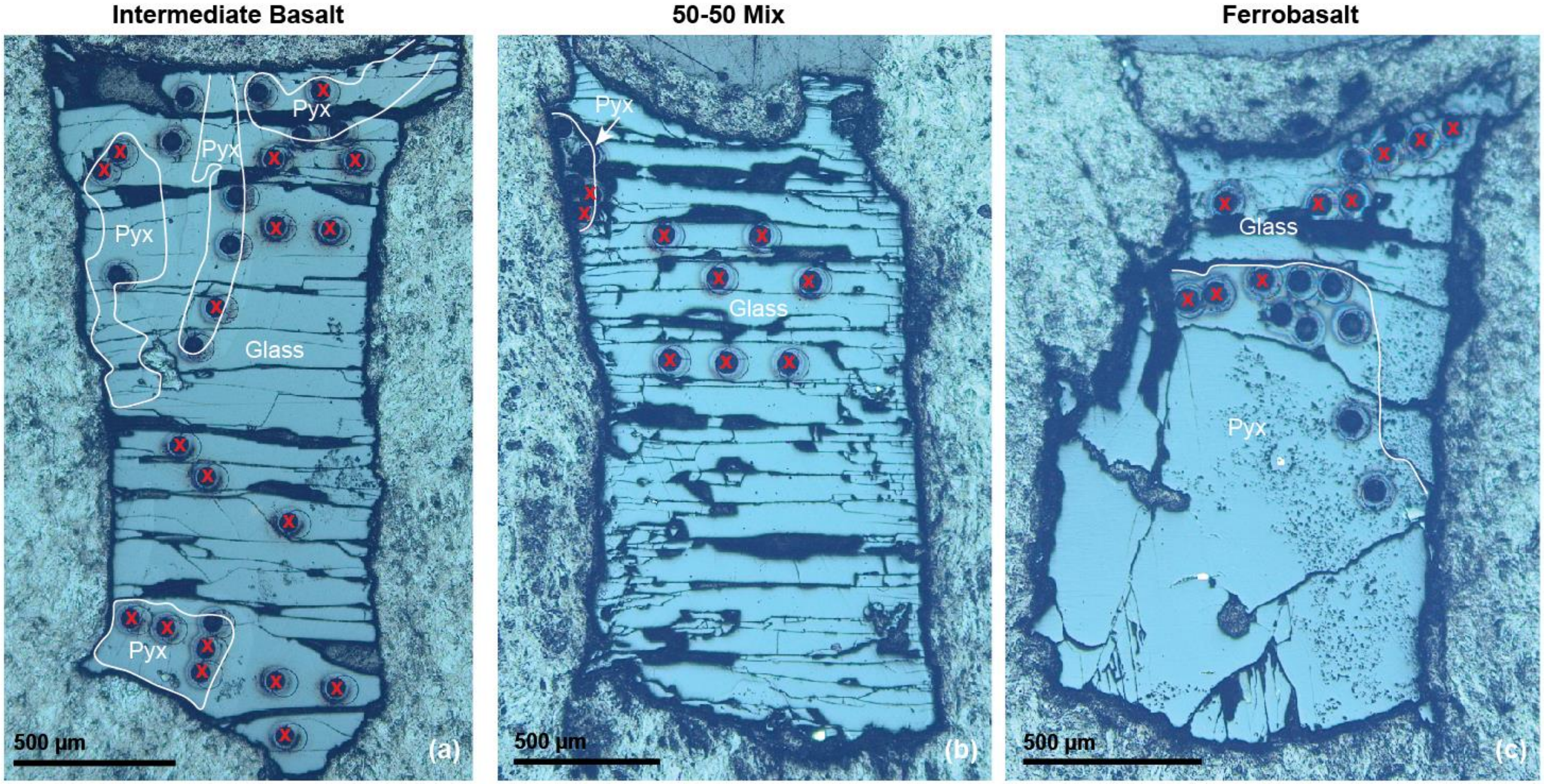

Figure D1. Reflected light images of 1 GPa intermediate basalt (a), 50-50 mix (b), and ferrobasalt (c) experimental charges with LAICP-MS analysis locations on pyroxenes and glass. Red 'x' on images indicate glass and pyroxene points averaged to calculate partition coefficients.

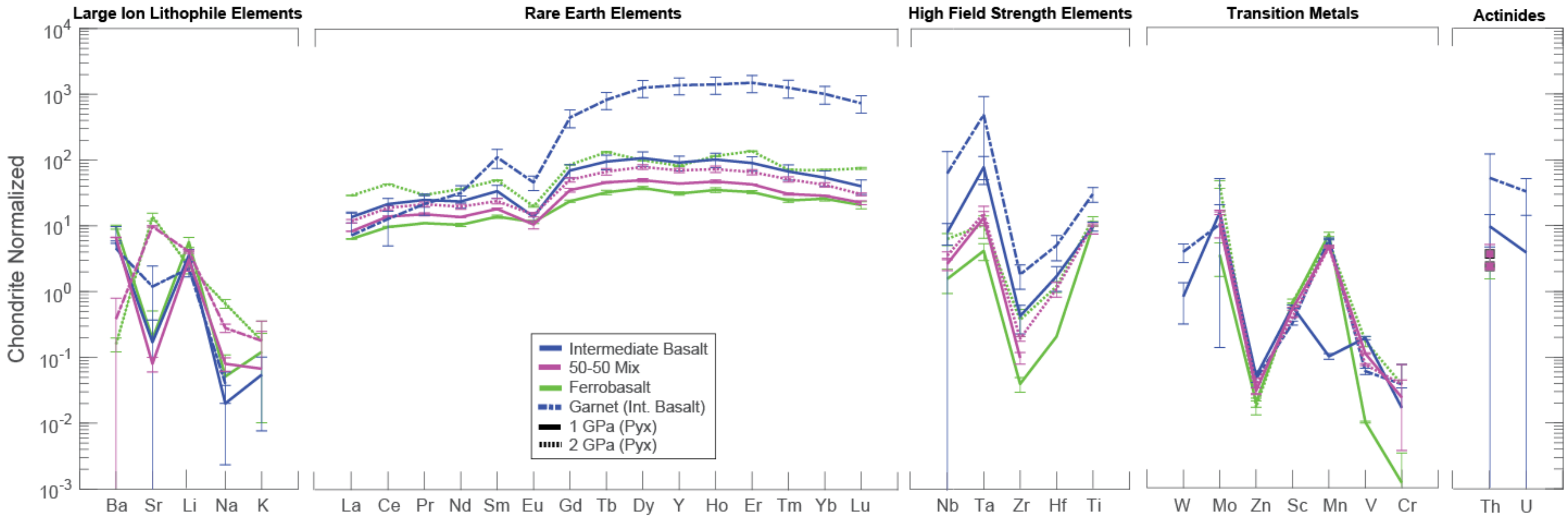

Figure D2. Chondrite normalized REE concentrations for experimental pyroxene and garnet rims. Normalization is from Anders and Grevesse (1989).

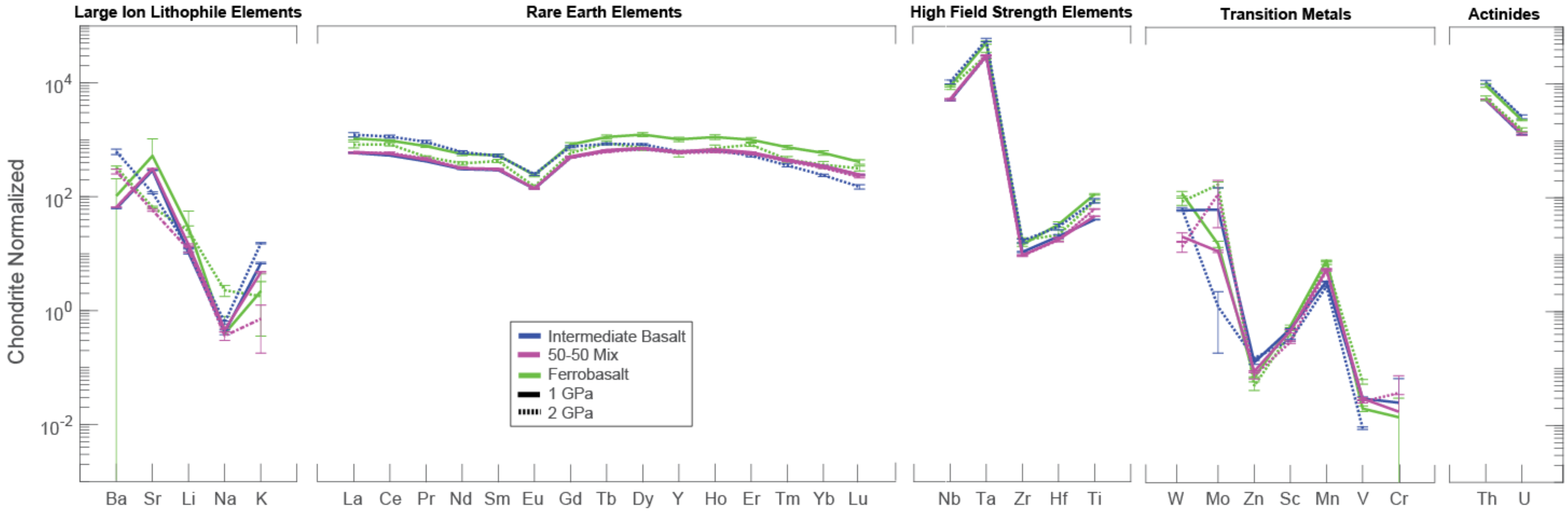

Figure D3. Chondrite normalized REE concentrations for experimental glasses. Normalization is from Anders and Grevesse (1989).

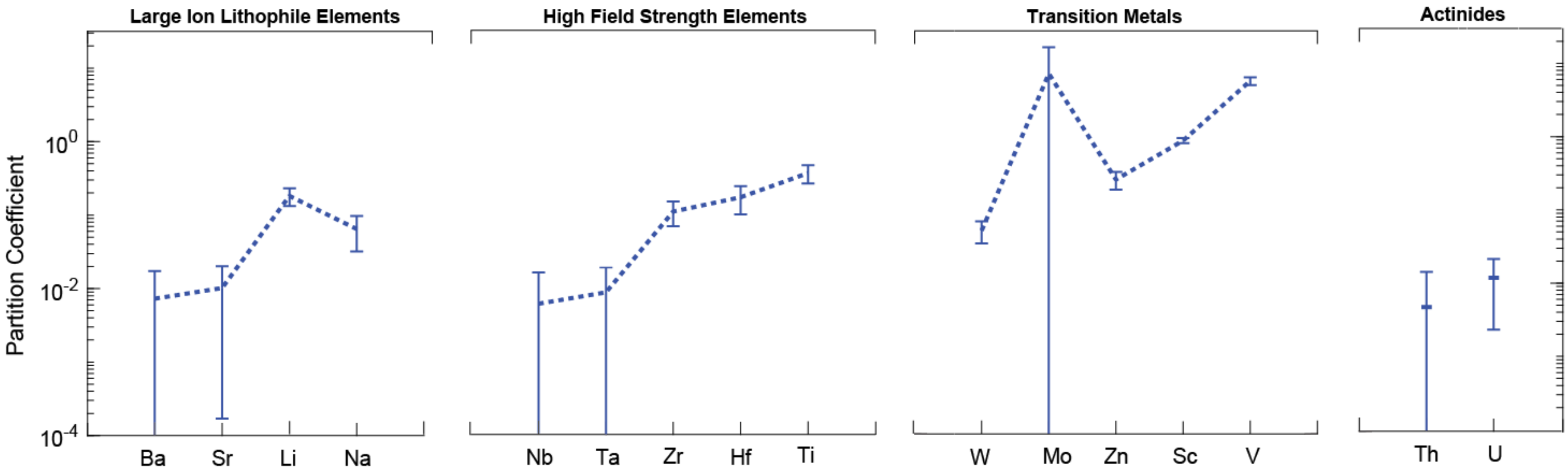

Figure D4. Partition coefficients for LILE, HFSE, Transition metals, and actinides for 2 GPa intermediate basalt garnet.

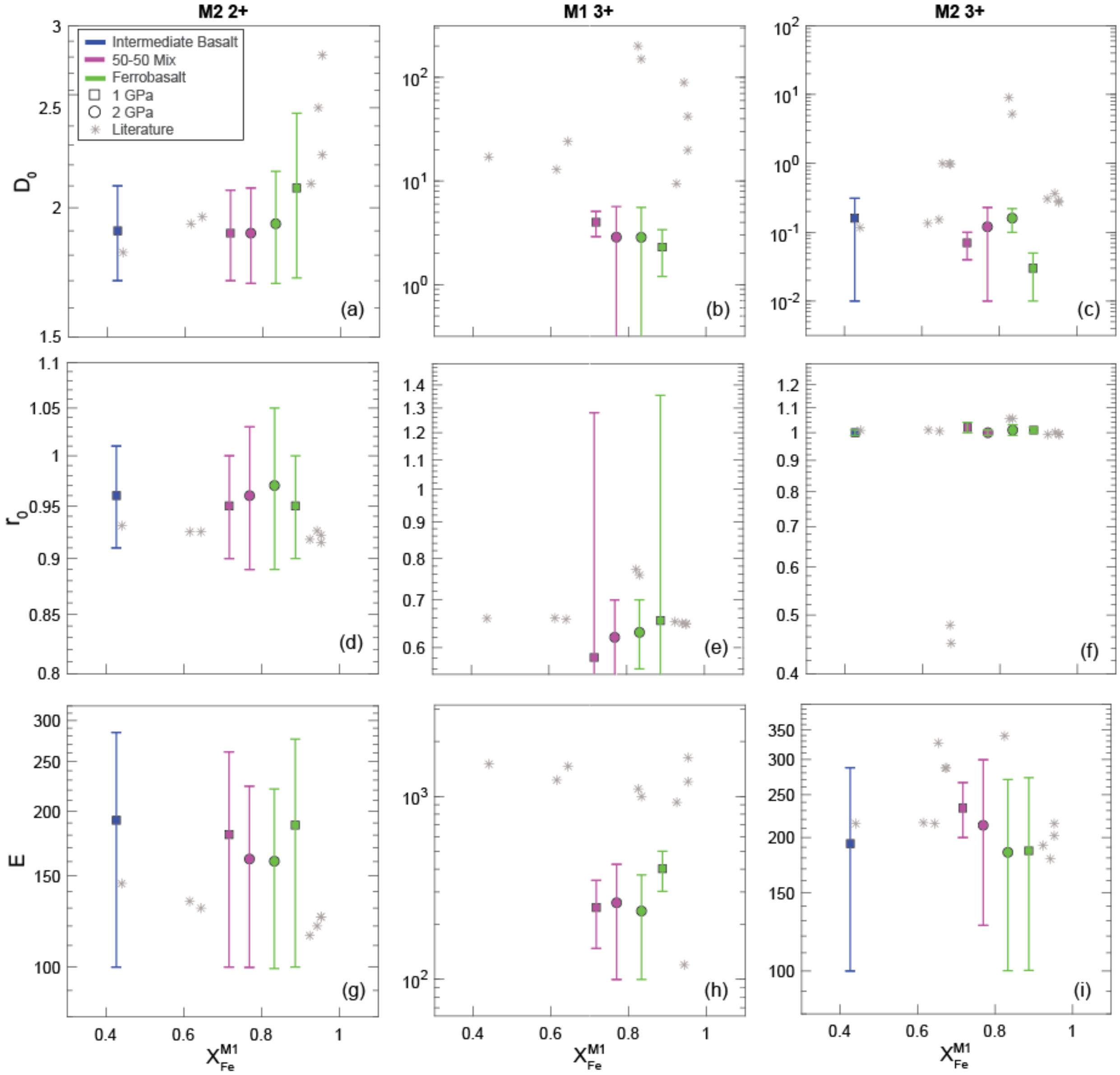

Figure D5. One and two GPa pyroxene model parameters versus X_{Fe}^{Mi}. Gray markers indicate lattice strain model parameters from literature (Pertermann and Hirschmann, 2002; Olin and Wolff, 2010; Dygert et al., 2014).

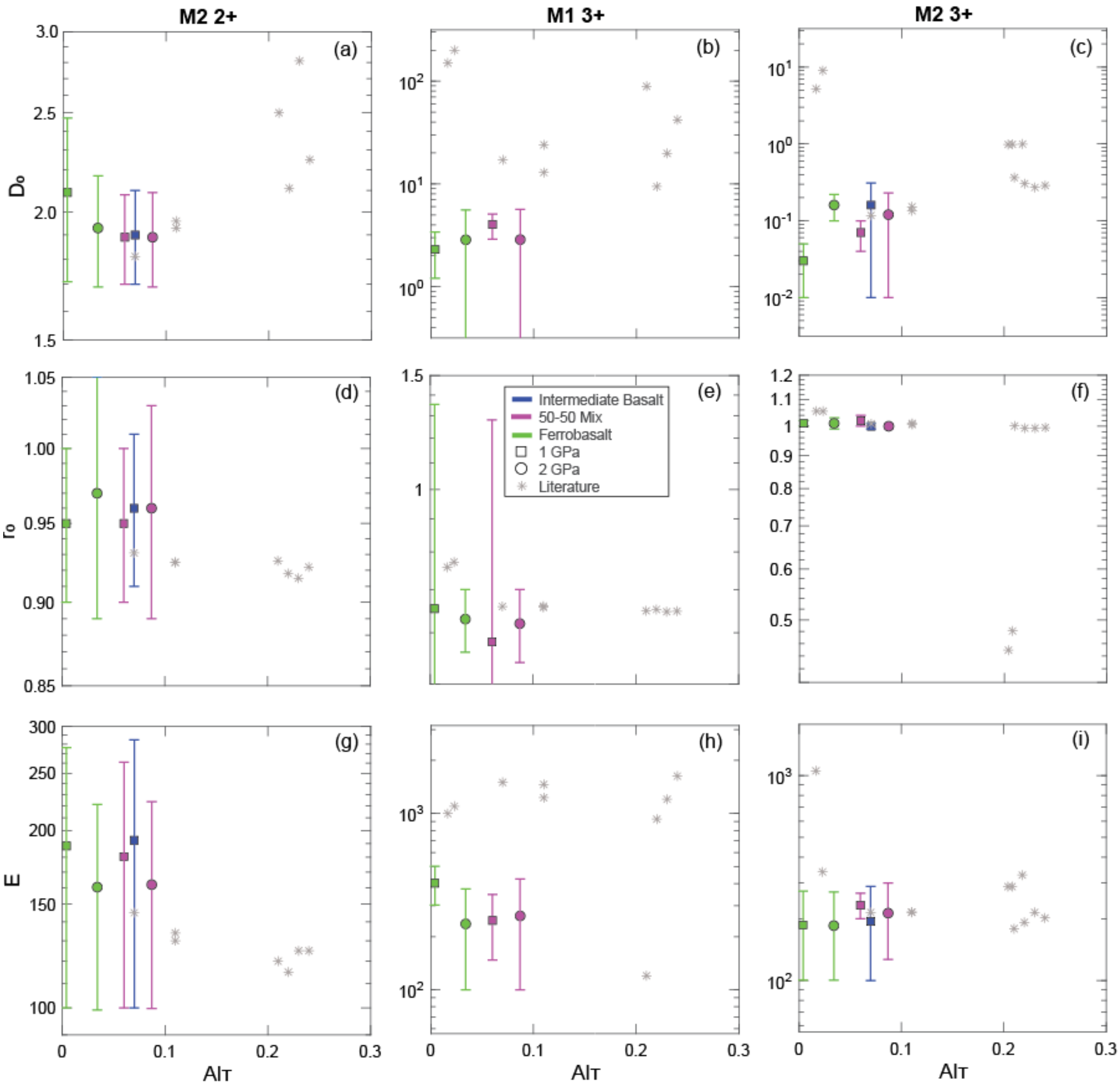

Figure D6. One and two GPa pyroxene model parameters versus Al_T. Gray markers indicate lattice strain model parameters from literature (Pertermann and Hirschmann, 2002; Olin and Wolff, 2010; Dygert et al., 2014).

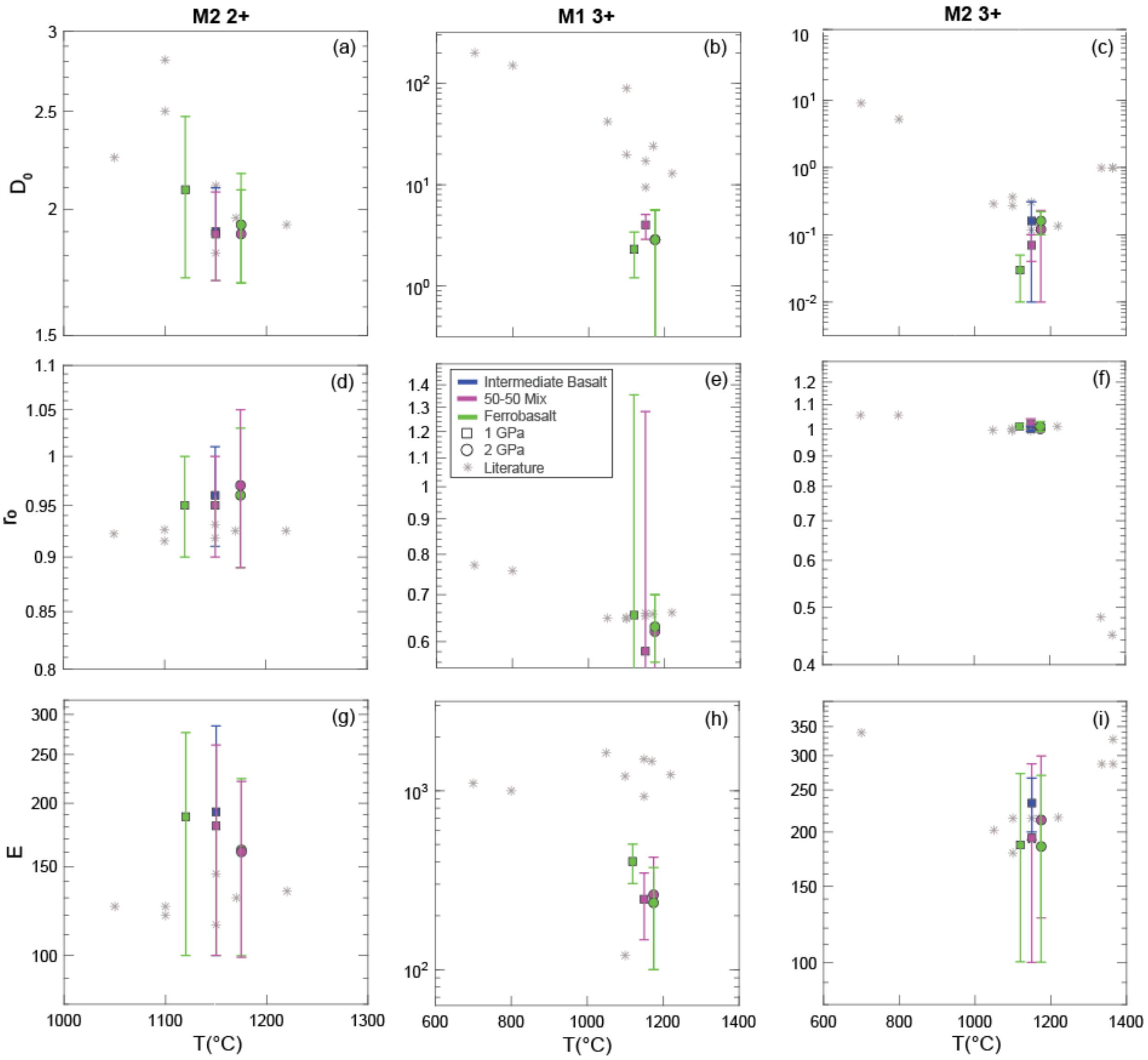

Figure D7. One and two GPa pyroxene model parameters versus temperature. Gray markers indicate lattice strain model parameters from literature (Pertermann and Hirschmann, 2002; Olin and Wolff, 2010; Dygert et al., 2014).

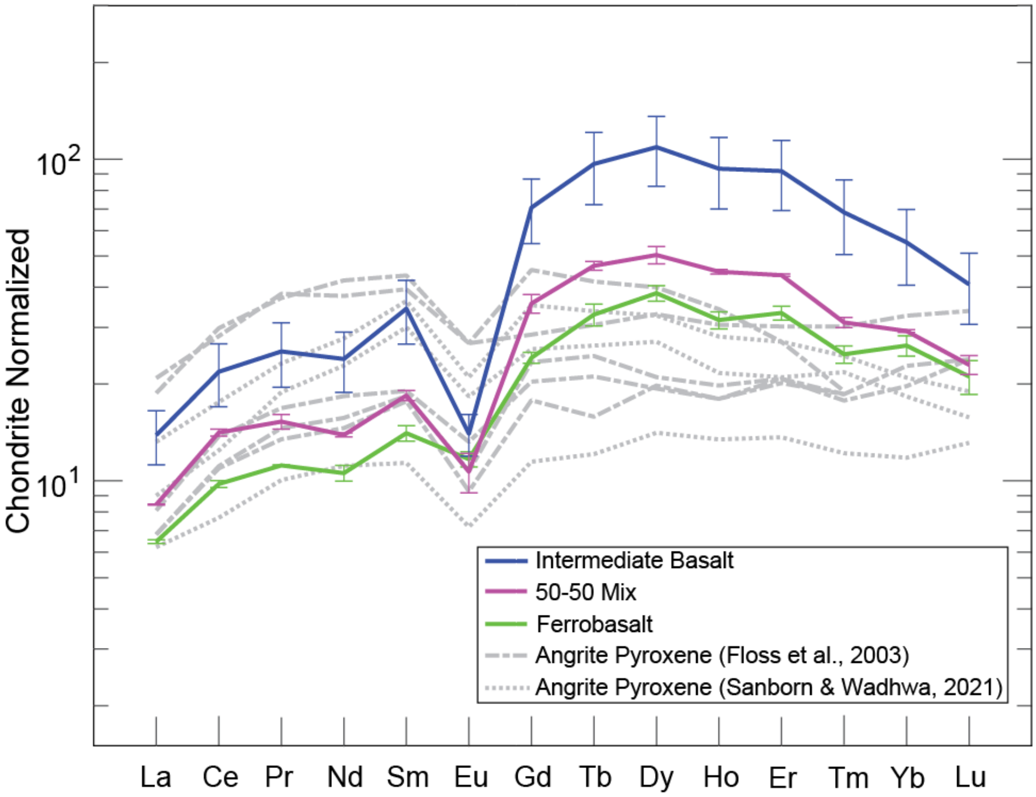

Figure D8. Chondrite normalized REE concentrations in experimental pyroxenes and angrite pyroxenes. Angrite REE data are from meteorites LEW 87051, Sahara 99555, Asuka 881371, D’Orbingy (Floss et al., 2003) and NWA 2999, 4590, and 4801 (Sanborn and Wadhwa, 2021). Normalization from Anders and Grevesse (1989).

CONCLUSION

Experimental methods are valuable tools for understanding petrogenetic processes in igneous rocks. This work presented applications of different high-temperature, high-pressure methods, in combination with analytical techniques and models, that were used to study the liquid properties and crystallization of silicate materials.

Mercury's Magma Ocean and Subsequent Mantle Formation

The viscosity of Mercury-relevant magma ocean compositions were tested via falling sphere viscometry on the Paris-Edinburgh apparatus at the Advanced Photon Source, Argonne National Laboratory. The viscosity results revealed that for a sulfur-bearing (S-bearing) composition, the viscosity was lower at all tested pressure and temperature conditions than a sulfur-free (S-free) composition. The viscosity measurements were used to develop predictive viscosity models to predict Mercurian magma ocean liquid viscosities at different pressure and temperature conditions. The viscosity models were combined with crystallization models to predict crystallization styles in Mercury's cooling magma ocean. The crystallization of the cooling magma ocean was evaluated at two different solidification timescales, one at ~3000 years in the case with a 1 km thick graphite flotation crust and one at ~20 years in the case without a flotation crust. The results from these models suggest that without a flotation crust, the mantle would be compositionally homogeneous as a result of batch crystallization during a short solidification time period. For the case with a graphite flotation crust, the mantle structure is predicted to be compositionally stratified, as a result of fractional crystallization during a longer cooling period.

Considering the internal source regions that produced the surface volcanism seen on Mercury today, if the mantle was homogeneous, perhaps the surface volcanism could have been produced form different periods of partial melting during Mercury's early history. If the mantle was compositionally heterogeneous, other physical processes such as cumulate mantle overturn could have occurred to produce distinct geochemical reservoirs for the surface volcanism. The timing and extent of overturn in a compositionally stratified mantle was predicted using fluid dynamic scaling relations. The presence of sulfur in Mercury's mantle could influence the overturn process whether enhancing gravitational instabilities with the presence of denser sulfides or neutralizing them with the presence of lighter sulfides. Additionally, the lighter sulfides could be primary reservoirs of heat producing elements such as U, Th, and K which, if concentrated to a specific geochemical horizon in the mantle, could produce significant heating over millions of years. This heating could cause partial melting in the sulfide-bearing layer, leading to migration of sulfides in accordance with their buoyancy. This work suggests that overturn in Mercury's mantle could have occurred within 100 million years of magma ocean solidification, creating a possible lherzolite source from mixing between a pyroxenite and a harzburgite.

Structural Analysis of High-pressure, High-Temperature, Fe-free Silicate Liquids

In addition to measuring the viscosity of the Mercurian magma ocean liquids, the structure of the liquids were measured, in situ, by multi-angle energy-dispersive X-ray diffraction (EDXD). The results from the viscosity experiments showed a difference in viscosity between the two liquids, where the S-bearing had lower viscosities than the S-free at all tested pressure and temperature conditions. The EDXD analysis on the liquids were combined with

Raman analysis on recovered glasses to observe the amorphous silicate structure of the sulfur-free, sulfur-bearing, and Al-free liquids to understand the different chemical controls on viscosity. The Raman analysis on the experimental glasses showed that the S-bearing composition had a more depolymerized silicate structure (more Q^0 species) than the S-free composition, supporting the viscosity measurements. This suggests that the addition of sulfur has a depolymerizing effect on the silicate network by forming different abundances of silicate species as a result of sulfide formation than seen in the S-free glass.

The EDXD measurements showed that the presence of Al as a tetrahedral component affects the bonding of the TO_4 structure by increasing bond lengths between tetrahedral and oxygen atoms. The Al-bearing liquids also exhibited differences in the bond lengths and overall network structure when compared to pressure and temperature. The T-T bond length between the Al-free and Al-bearing series were consistent with increasing T-T length with increasing temperature.

Trace Element Partitioning in Fe-rich Pyroxenes

The trace element partitioning in Fe-rich systems was explored using a lunar relevant mafic composition doped with REE/HFSE/LILE at mantle relevant pressure and temperature conditions on the piston cylinder apparatus. Six experiments run at 1 and 2 GPa were conducted on endmember compositions (ferrobasalt (Fe-rich, Al-poor), and intermediate basalt (moderate Fe and Al)) and a mixture of the endmembers. Clinopyroxenes were formed in each experiment, with the 2 GPa intermediate basalt also forming garnet. Major and trace element abundances were conducted on each experiment via EMPA and LA-ICP-MS, respectively. The major element compositions showed a consistent enrichment in Fe from the intermediate basalt to the ferrobasalt, in accordance with their bulk compositions. The trace element analysis revealed that the amount of Al directly correlated to the partition coefficients of 1+, 3+, and 4+ cations, where more aluminous pyroxenes had higher partition coefficients due to the coupled substitution of an incompatible element in the M2 site with Al^{3+} replacing Si^{4+} in the tetrahedral site.

The ferrobasalt, and to a lesser extent the 50-50 mix, in both the 1 and 2 GPa experiments, exhibited different partitioning behaviors from the intermediate basalt. There was an increase of partitioning of the heavy REEs in comparison to the REEs. This partitioning behavior correlates to the presence of Fe, where the HREEs in 6-fold coordination are more similar to the radius of Fe and can therefore partition onto the M1 site. Existing predictive lattice strain models cannot accurately predict the behavior of this HREE partitioning in Fe-rich systems, thus the results from these experiments were used to parameterize a model to predict the M1 lattice site behavior for 3+ cations as a function of temperature and crystal chemistry. The results and predictive models developed from this work are critical to understanding the partitioning behavior in Fe-rich basaltic systems which will be useful for understanding the petrogenetic processes occurring on other Fe-rich bodies, such as Mars and the Moon.

VITA

Megan Mouser was born in Albuquerque, New Mexico and grew up on her family's cattle ranch in the Manzano Mountains. She found her love for geology and planetary science through an introductory astronomy course as a freshman in college which lead to her to pursing a geology major. She earned her Bachelor of Science in Earth and Planetary Sciences, with honors, in 2017 from the University of New Mexico (UNM). During her time at UNM she discovered her interest in experimental work after working on a research project running 1-bar gas mixing furnace experiments to understand the crystallization history of angrite meteorite Sahara 99555. After completing her bachelor's, she interned with the Lunar and Planetary Institute where she worked on the geochemical analysis of Apollo 12 and 15 felsite samples. After her internship, she worked in the experimental petrology group at NASA Johnson Space center where she ran 1-bar gas mixing furnace and piston cylinder experiments for a variety of projects. Megan started graduate school at the University of Tennessee (UT) in spring 2018 working with Dr. Nicholas Dygert, continuing to explore her interests in high-pressure high-temperature experimental work with planetary applications. Her Ph.D. work included several trips to the Advanced Photon Source, Argonne National Laboratory both as a user and a graduate research intern. Megan earned her concurrent master's degree from UT in the fall of 2020. She has presented her work at multiple conferences including the Lunar and Planetary Science Conference and the American Geophysical Union Fall Meeting and was an invited speaker at the 2022 Geological Society of America Annual Meeting.